

# **THE INTERACTION BETWEEN RADIATION AND TURBULENT NATURAL CONVECTION IN SQUARE AND RECTANGULAR ENCLOSURES**

By

**Abdulmaged Khalifa Abdullah Shati**

*A dissertation submitted to the University of Sheffield for the degree of Doctor  
Philosophy*

January 2013

Department of Mechanical Engineering  
The University of Sheffield  
Mappin Street, Sheffield, S1 3JD  
United Kingdom

# Summary

Heat transfer by natural convection inside enclosed spaces with radiation interaction is of practical interest in many engineering applications, such as design of buildings for thermal comfort, nuclear reactors, solar collectors, and the cooling of electronic equipment. In the natural convection studies inside enclosed spaces, mostly two simple enclosed spaces are considered; first the square enclosure and secondly the rectangular cavity both with heated and cooled walls.

In this study the effects of natural convection with and without the interaction of surface radiation in square and rectangular enclosures has been studied, numerically, theoretically and experimentally. The analyses were carried out over a wide range of enclosure aspect ratios ranging from 0.0625 to 16, including square enclosures in sizes from 40cm to 240cm, with cold wall temperatures ranging from 283 to 373 K, and hot to cold temperature ratios ranging from 1.02 to 2.61. The work was carried out using four fluids (Argon, Air, Helium and Hydrogen; whose properties vary with temperature).

The numerical model used is explained in detail and validated using previous experimental and numerical results and also the author's experiments. FLUENT software was used to carry out the numerical study. In the numerical study, turbulence was modelled using the RNG k- $\epsilon$  model with a non-uniform grid and using the Discrete Transfer Radiation Model (DTRM) for radiation. 2D and 3D numerical calculations were performed for square and rectangular enclosures (and for the range of parameters mentioned above) to produce the constants of the derived correlation equation and to compare them with experimental results.

A dimensional analysis was established to produce correlation equations controlling the flow inside square and rectangular enclosures for pure natural convection and natural convection with radiation. This study starts from the partial differential equation which explaining the flow inside the cavities. The correlation equations for the new dimensionless group, which is the ratio between natural convection to radiation heat transfer, were provided for both square and rectangular enclosures. Also the correlation equations for the average Nusselt number with and without radiation were provided for square and rectangular enclosures. The constants, as a function of temperature ratio, of all the derived correlation equations are given along with these equations. These

constants are correlated and a polynomial equations for each constant as a function of absolute temperature ratio is given. All these equations are valid for a different temperature ratio, different enclosure size, different aspect ratio and different fluid properties.

This provides a generalised equation for heat transfer in square and rectangular enclosures both with and without radiation. These can be used to calculate Nusselt numbers for pure natural convection and natural convection with radiation interaction and also to calculate the ratio between convection to radiation heat transfer for both square and rectangular enclosures.

To validate the numerical results, an experimental study was performed for square and rectangular enclosures. This was for three aspect ratios 2.0, 1.0 and 0.5. Tests were carried out for hot wall temperatures ranging from 50°C to 75°C and for a Rayleigh number ranging from  $9.6 \times 10^7 \leq Ra \leq 8 \times 10^9$ . This allows the calculation of total heat transfer from the hot and cold walls using six thermocouples in each side. Experimental measurements of the velocity and turbulence intensity profiles were performed using the laser Doppler velocimetry for three aspect ratios 2.0, 1.0 and 0.5 and hot wall temperature ranging from 50°C to 75°C.

The results of this study are expected to contribute to the literature in this field and enhance the understanding of the natural convection with radiation interaction in rectangular enclosures. Also this will be a useful technique, as, by using the results it is possible to generalise the heat transfer in square and rectangular cavities filled with ideal gases.

# Dedication

To my mother,  
To my father,  
To my sister Rabiha,  
To my wife Esmahan,  
To my elder son Abdurhman,  
To my daughter Omama,  
To my younger son Ahmed,  
To my sweetheart Rahma,  
To all my family in Libya.



# Acknowledgement

Praise and thanks are sent to God for the completion of this study. I would like to express my sincere gratitude to my supervisors Professor S.B.M. Beck and Dr. S. G. Blakey for their excellence advice, guidance and encouragements throughout the research study. They have substantially contributed to my professional development.

I would like to thank Dr. R. Woolley who has given me valuable comments and assistance for the experiments work. I would like also to thank Malcolm Nettleship for his support and comments during the lab work.

I would like also to thank my country Libya the University of Sheffield and the mechanical engineering department to give me this chance to get my PhD.

Most important, I would like to appreciate and thank all my family; my mother, my father, my sister Rabiha, my wife Esmahan, my elder son Abdurhman, my daughter Omama, my younger son Ahmed, and sweetheart Rahma for their support, encouragement and faith, and giving me the most essential force during my study.

I would like to thank all the PhD students, especially Libyan students, who supported me with their valuable comments and assistance.

# Table of Contents

Summary .....	ii
Dedication .....	iv
Acknowledgement.....	v
Table of Contents .....	vi
List of Figures .....	x
List of Tables.....	xvi
Nomenclatures.....	xviii
 CHAPTER 1 .....	 1
1.1 Introduction .....	1
1.2 Research objectives and aims of this study .....	5
1.3 Outline of this thesis .....	6
CHAPTER 2 .....	8
LITERATURE REVIEW.....	8
2.1 Introduction .....	8
2.2 Pure natural convection in square and rectangular enclosures .....	8
2.3 Correlation equations for pure natural convection on flat plates .....	11
2.3.1 Vertical flat plate.....	11
2.3.2 Parallel flat plates .....	12
2.3.3 Inclined parallel plates .....	13
2.4 Correlation equations for pure natural convection in rectangular enclosures ..	13
2.4.1 Horizontal enclosures.....	14
2.4.2 Inclined enclosures.....	16
2.4.3 Vertical enclosures .....	18
2.5 Interaction between radiation and natural convection in square and rectangular enclosures .....	22
2.6 Correlation equations for natural convection with radiation interaction in square enclosure .....	23
2.7 The use of turbulence models for modelling natural convection .....	24
2.8 Dimensional analysis of natural convection in enclosures.....	25
2.9 Experimental studies of natural convection in enclosures .....	26
2.10 Conclusion .....	27
CHAPTER 3 .....	28

THEORETICAL BACKGROUND .....	28
3.1 Convection heat transfer.....	28
3.1.1 Convection boundary layers.....	28
3.1.2 Equations of motion for natural convection.....	31
3.1.3 Dimensional numbers.....	35
3.2 Radiation heat transfer.....	37
3.2.1 Radiation fundamentals.....	37
3.2.2 The view factor .....	39
CHAPTER 4 .....	42
DIMENSIONAL ANALYSIS OF HEAT TRANSFER IN CAVITIES.....	42
4.1 Introduction .....	42
4.2 Producing dimensionless correlation equations .....	43
4.2.1 First analysis method .....	44
4.2.2 Second analysis method for square enclosure.....	45
4.2.3 Second analysis method for rectangular enclosure .....	49
4.3 Producing the new dimensionless group from the provided dimensionless equations .....	50
4.3.1 For square enclosures .....	50
4.3.2 For rectangular enclosures .....	51
4.4 Summary and discussion .....	53
CHAPTER 5 .....	54
TURBULENCE MODELLING AND NUMERICAL RESULTS.....	54
5.1 Introduction .....	54
5.2 Turbulence models .....	55
5.3 The RNG k- $\epsilon$ turbulent model and the free convection in cavity.....	58
5.3.1 Mathematical model.....	58
5.3.2 Boundary conditions .....	67
5.3.3 Grid independence .....	74
5.4 Model validation.....	74
5.5 Numerical results.....	75
5.5.1 Square enclosure .....	76
5.5.2 Rectangular enclosure .....	83
5.5.3 The 3D numerical results .....	88
5.6 Summary and Conclusions .....	103
CHAPTER 6 .....	106
Experimental Rig and Results.....	106
6.1 Introduction .....	106

6.2	Test cavity .....	106
6.2.1	Specifications and cavity design .....	107
6.2.2	Hot side loop .....	111
6.2.3	Cold side loop .....	116
6.2.4	Calculation of measurement uncertainty.....	118
6.3	Thermal calculations and results .....	119
6.3.1	Different aspect ratios .....	120
6.3.2	Different hot wall temperatures .....	120
6.4	Laser Doppler Velocimetry specifications and principles.....	125
6.4.1	Introduction .....	125
6.4.2	Advantages .....	125
6.4.3	Components and Principles.....	126
6.4.4	The measuring volume .....	127
6.4.5	Signal processing .....	129
6.4.6	Determination the sign of the flow direction .....	129
6.4.7	Two and three component measurements .....	129
6.4.8	Seeding particles .....	130
6.4.8.1	.....	131
6.4.8.2	.....	131
6.5	LDV experiments and results .....	132
6.5.1	LDV experiments preparation.....	132
6.5.2	Collecting the data using the LDV .....	135
6.5.3	Velocity and turbulent intensities profiles for different aspect ratios .....	135
6.6	Summary and Conclusions .....	148
CHAPTER 7 .....		151
CORRELATION EQUATIONS FOR HEAT TRANSFER IN CAVITIES .....		151
7.1	Producing the correlation equations for pure natural convection in square and rectangular enclosures .....	151
7.1.1	Providing the correlation equation for square enclosures .....	151
7.1.2	Providing the correlation equation for rectangular enclosures .....	153
7.2	Providing the correlation equations for natural convection with radiation interaction in square and rectangular enclosures .....	154
7.2.1	The correlation equations for square enclosures .....	154
7.2.2	The correlation equations for rectangular enclosures .....	157
7.3	Producing polynomial equations .....	160
7.4	Comparison between numerical results and the derived correlation equations.....	165
7.4.1	Pure natural convection inside a square enclosure.....	165

7.4.2	Natural convection with radiation in square enclosure .....	168
7.4.3	Pure natural convection inside rectangular enclosure .....	168
7.4.4	Natural convection with radiation in a rectangular enclosure.....	171
7.5	Using the provided polynomial correlation equations.....	171
7.6	Summary and discussion .....	181
CHAPTER 8 .....		184
RESULTS COMPARISON AND DISCUSSION .....		184
8.1	Introduction .....	184
8.2	Comparison between numerical and experimental results .....	184
8.2.1	Comparison between the present and the previous correlation equations.....	185
8.2.2	Comparison between the derived correlation equations and the experimental results .....	186
8.2.3	Comparison between the 3D numerical calculations and the experimental results .....	189
8.3	Summary and Conclusions .....	198
CHAPTER 9 .....		204
FINAL FINDINGS AND FUTURE WORK.....		204
9.1	Final conclusions .....	204
9.2	Future work .....	208
References .....		208
Appendix A: Additional Numerical Results .....		214
Appendix B: Additional Experimental Results.....		222
Appendix C: Additional Comparison between Experimental and Numerical Results .		230
Appendix D: List of publications .....		246

# List of Figures

Figure 1-1:	Schematic diagram of the heat transfer inside rectangular enclosure.....	2
Figure 2-1:	Schematic diagram of the considered enclosure .....	9
Figure 2-2:	Isothermal lines and stream lines for an enclosure.....	15
Figure 3-1:	Velocity boundary layer development on a flat plate .....	29
Figure 3-2:	Thermal boundary layer development on an isothermal flat plate. ....	30
Figure 3-3:	Natural convection over a vertical plate with temperature and velocity profiles .....	33
Figure 3-4:	Forces acting on a differential volume in natural convection over a vertical plate.....	33
Figure 3-5:	Incident, absorbed and reflected heat transfer on a surface of an absorptivity .....	39
Figure 3-6:	Heat transfer between two surfaces one completely surrounding the other .....	39
Figure 3-7:	Radiation heat transfer depends on orientation between surfaces ...	40
Figure 4-1:	Two-dimensional rectangular enclosure with isothermal side walls.....	43
Figure 5-1:	Velocity at point x for laminar and turbulent flows.....	56
Figure 5-2:	Velocity profiles for laminar and turbulent flows.....	56
Figure 5-3:	Schematic diagram of the rectangular enclosure .....	59
Figure 5-4:	The three layers near the wall region.....	63
Figure 5-5:	Near wall treatment. ....	64
Figure 5-6:	Angles $\theta$ and $\Phi$ about a point P .....	66
Figure 5-7:	Non-uniform grid used in the simulation model for aspect ratio four .....	71
Figure 5-8:	Non-uniform grid used in the simulation model for square	72

enclosure.....	
Figure 5-9: Non-uniform grid used in the simulation model for aspect ratio quarter .....	73
Figure 5-10: The average Nusselt number as a function of temperature ratio .....	78
Figure 5-11: Relation between $Q_c/Q_r$ with respect to $T_h/T_c$ .....	79
Figure 5-12: Relation between $Ra^{1/3}/Nu$ with respect to $T_h/T_c$ .....	81
Figure 5-13: Resultant collapsed curves .....	82
Figure 5-14: Flow profiles for aspect ratios 16, 8, 4, 2, 1.5, 1.0, 0.75 and 0.5 .....	84
Figure 5-15: The average Nusselt number for rectangular enclosure as a function of temperature ratio .....	86
Figure 5-16: Relation between heat transfer ratio and temperature ratio. ....	87
Figure 5-17: Schematic diagram for the three dimensional enclosure .....	89
Figure 5-18: Total heat transfer inside the enclosure for aspect ratios 2, 1.0 and 0.5 .....	90
Figure 5-19: Velocity profiles at mid-height for aspect ratio 2.0 and 75°C hot wall temperature .....	91
Figure 5-20: Velocity profiles for aspect ratio 2.0 and hot wall temperatures 60°C.....	92
Figure 5-21: Velocity profiles for aspect ratio 2.0 and hot wall temperatures 75°C.....	93
Figure 5-22: Velocity profiles for aspect ratio 1.0 and hot wall temperatures 60°C.....	94
Figure 5-23: Velocity profiles for aspect ratio 1.0 and hot wall temperatures 75°C.....	95
Figure 5-24: Velocity profiles for aspect ratio 0.5 and hot wall temperatures 60°C.....	96
Figure 5-25: Velocity profiles for aspect ratio 0.5 and hot wall temperatures 75°C.....	97
Figure 5-26: Velocity profiles near the hot wall for aspect ratios .....	99
Figure 5-27: Turbulent intensity profiles for aspect ratio 2.0 and for hot wall temperature. ....	100

Figure 5-28:	Turbulent intensity profiles for aspect ratio 1.0 and for hot wall temperature .....	101
Figure 5-29:	Turbulent intensity profiles for aspect ratio 0.5 and for hot wall temperature. ....	102
Figure 5-30:	Velocity profiles near the hot wall for aspect ratios .....	104
Figure 6-1:	Polystyrene board of thickness 120mm .....	107
Figure 6-2:	The polystyrene four side walls for aspect ratio 0.5 .....	108
Figure 6-3:.	The cavity with aspect ratio 0.5 after assembling all the walls.....	109
Figure 6-4:	Using the band clamp to connect the cavity walls together.....	110
Figure 6-5:	Schematic diagram of the enclosure with the hot and cold side walls and all insulation layers.....	111
Figure 6-6:	The steel frame used to fix and support the radiator.....	112
Figure 6-7:	Schematic diagram of radiator hot water side. ....	113
Figure 6-8:	The insulated thermocouples at the hot side exit.....	115
Figure 6-9:	The rotameter chart 10 metric.....	116
Figure 6-10:	The NESLAB CFT-75 recirculating chiller.....	117
Figure 6-11:	Draw and discharge the air in the cooling unit .....	117
Figure 6-12:	Enclosure final shape for aspect ratios 2.0, 1.0 and 0.5.....	121
Figure 6-13:.	The thermocouples collected data of about two days for hot and cold side .....	123
Figure 6-14:	Thermal results of total heat transfer from three aspect ratios for hot side and cold side.....	124
Figure 6-15:	LDV principles. ....	127
Figure 6-16:	The Bragg cell used as a beam splitter .....	127
Figure 6-17:	The probe and the measuring volume.....	128
Figure 6-18:	Doppler frequency to velocity for a frequency shifted LDV system. ....	130



Figure 6-19: LDV optics for measuring three velocity components. ....	131
Figure 6-20: The Six-Jet atomizer. ....	132
Figure 6-21: Exchanging the side wall by a Perspex surface .....	133
Figure 6-22: Velocity profiles for aspect ratio 2.0 and hot wall temperatures 60°C between hot and cold walls and near the hot wall .....	137
Figure 6-23: Velocity profiles for aspect ratio 2.0 and hot wall temperatures 75°C between hot and cold walls and near the hot wall. ....	138
Figure 6-24: Velocity profiles for aspect ratio 1.0 and hot wall temperatures 60°C between hot and cold walls and near the hot wall. ....	139
Figure 6-25: Velocity profiles for aspect ratio 1.0 and hot wall temperatures 75°C between hot and cold walls and near the hot wall .....	140
Figure 6-26: Velocity profiles for aspect ratio 0.5 and hot wall temperatures 60°C between hot and cold walls and near the hot wall. ....	141
Figure 6-27: Velocity profiles for aspect ratio 0.5 and hot wall temperatures 75C between hot and cold walls and near the hot wall.....	142
Figure 6-28: The repeatability of the LDA measurement for aspect ratio 2.0 and hot wall temperature 50°C and 75°C. ....	143
Figure 6-29: Velocity profiles near the hot wall for aspect ratios 2.0, 1.0 and 0.5 .....	144
Figure 6-30: Turbulence intensity profiles for aspect ratio 2.0 and for hot wall temperature 60°C and 75°C. ....	145
Figure 6-31: Turbulence intensity profiles for aspect ratio 1.0 and for hot wall temperature 60°C and 75°C. ....	146
Figure 6-32: Turbulence intensity profiles for aspect ratio 0.5 and for hot wall temperature 60°C and 75°C. ....	147
Figure 6-33: Turbulence intensity profiles near the hot wall for aspect ratios 2.0, 1.0 and 0.5. ....	149
Figure 7-1 : Constants values as a function of $T_h/T_c$ for Natural convection with and without radiation. ....	152
Figure 7-2: Constants as a function of temperature ratio .....	155
Figure 7-3: Constants as a function of temperature ratio .....	156
Figure 7-4: Constants as a function of temperature ratio .....	158
Figure 7-5: Constants as a function of temperature ratio .....	160

Figure 7-6:	Comparison between numerical and calculated results for the average Nusselt number in square enclosure.....	167
Figure 7-7:	Comparison between numerical and calculated results of the new dimensionless group in square enclosure.....	169
Figure 7-8:	Comparison between numerical and empirical calculated average Nusselt number of pure natural convection in rectangular enclosure.....	170
Figure 7-9:	Comparison between numerical and empirical calculated results of natural convection with radiation interaction in rectangular enclosure.....	172
Figure 7-10:	Graphical solution for example 18 showing the iteration number...	177
Figure 8-1:	Comparison between the derived correlation equations and previous experimental results.....	187
Figure 8-2:	Comparison between calculated heat transfer and experimental results for aspect ratio 2.0, 1.0 and 0.5 .....	188
Figure 8-3:.	Comparison between 3D thermal results and experimental results for aspect ratio 2.0, 1.0 and 0.5.....	190
Figure 8-4:	Comparison of velocity profiles between experimental and numerical results for aspect ratio 2.0 and hot wall temperature 60 °C between the two walls, near the hot side and near the cold side.....	191
Figure 8-5:	Comparison of velocity profiles between experimental and numerical results for aspect ratio 2.0 and hot wall temperature 75 °C between the two walls, near the hot side and near the cold side.....	192
Figure 8-6:	Comparison of velocity profiles between experimental and numerical results for aspect ratio 1.0 and hot wall temperature 60 °C between the two walls, near the hot side and near the cold side.....	193
Figure 8-7:	Comparison of velocity profiles between experimental and numerical results for aspect ratio 1.0 and hot wall temperature 75 °C between the two walls, near the hot side and near the cold side.....	194
Figure 8-8:	Comparison of velocity profiles between experimental and numerical results for aspect ratio 0.5 and hot wall temperature 60 °C between the two walls, near the hot side and near the cold side.....	195
Figure 8-9:	Comparison of velocity profiles between experimental and numerical results for aspect ratio 0.5 and hot wall temperature 75°C between the two walls, near the hot side and near the cold side.....	196

Figure 8-10: Velocity profiles at $x = 4\text{mm}$ near the hot wall side at $70^\circ\text{C}$ and for aspect ratio 2.0, 1.0 and 0.5.....	199
Figure 8-11: Velocity profiles at $x = 4\text{mm}$ near the hot wall side at $75^\circ\text{C}$ and for aspect ratio 2.0, 1.0 and 0.5.....	200
Figure 8-12: Turbulence profiles near the hot wall side for $60^\circ\text{C}$ and aspect ratio 2.0, 1.0 and 0.5. ....	201
Figure 8-13: Turbulence profiles near the hot wall side for $75^\circ\text{C}$ and aspect ratio 2.0, 1.0 and 0.5. ....	202

# List of Tables

Table 2.1:	Relationships of Nusselt number for inclined rectangular enclosure .....	17
Table 2.2:	Critical angle for inclined rectangular enclosures .....	17
Table 5.1:	Average Nusselt number as a comparison with others for natural convection in a square enclosure.....	75
Table 5.2:	Average and mid height Nusselt number for natural convection in a square enclosure at $Ra=5 \times 10^{10}$ as a comparison with reference and experimental results.....	75
Table 7.1:	The values of constants $p_1, p_2, p_3$ and $p_4$ for the polynomial equations of $k_l, a_l$ and $b_l$ for the case of pure natural convection in square enclosure, equation 44 .....	161
Table 7.2:	The values of constants $p_1, p_2, p_3$ and $p_4$ for the polynomial equations of $k_{a1}, k_{a2}, k_{a3}, k_{a4}$ and $k_{b1}, k_{b2}, k_{b3}, k_{b4}, k_{b5}$ for the case of pure natural convection in a rectangular enclosure, equations 46 and 47.....	162
Table 7.3:	The values of constants $p_1, p_2, p_3$ and $p_4$ for the polynomial equations of $k_2, a_2, b_2$ and $c_2$ for the case of natural convection with radiation interaction in square enclosure equation 48.....	163
Table 7.4:	The values of constants $p_1, p_2, p_3$ and $p_4$ for the equations of $k_{c1}, k_{c2}, k_{c3}, k_{c4}$ and $k_{d1}, k_{d2}, k_{d3}, k_{d4}, k_{d5}$ for the case of natural convection with radiation interaction in rectangular enclosure, equations 51 and 52.....	164
Table 7.5:	The values of constants $p_1, p_2$ and $p_3$ for the polynomial equations of a, b, c and d for the case of natural convection with radiation interaction in square enclosure equation 49.....	165
Table 7.6:	The values of constants $p_1, p_2$ and $p_3$ for the equations of $g_1, g_2, g_3, g_4$ and $h_1, h_2, h_3, h_4, h_5$ for the case of natural convection with radiation interaction in rectangular enclosure, equations 54 and 55.....	166
Table 7.7:	Results for examples 1 to 6 for pure natural convection using the explicit method.....	174
Table 7.8:	Results for examples 7 to 12 for natural convection with radiation interaction using the explicit method.....	175
Table 7.9:	Results for example 13: a square enclosure for natural convection with radiation interaction, cold wall temperature supplied .....	177

Table 7.10:	Results for example 14: a square enclosure for natural convection with radiation interaction, cold wall temperature supplied and using the iterative method.....	178
Table 7.11:	Results for example 15: a square enclosure for natural convection with radiation interaction, cold wall temperature supplied and using the iterative method.....	178
Table 7.12:	Results for example 16: a rectangular enclosure with aspect ratio equal to 8 for natural convection with radiation interaction, cold wall temperature supplied .....	178
Table 7.13:	Results for example 17: a rectangular enclosure with aspect ratio equal to 0.125 for natural convection with radiation interaction, cold wall temperature supplied and using the iterative method.....	179
Table 7.14:	Results for example 18: : a square enclosure for pure natural convection, cold wall temperature supplied and using the iterative method.....	179
Table 7.15:	Results for example 19: a square enclosure for natural convection with radiation interaction, hot wall temperature supplied and using the iterative method.....	179
Table 7.16:	Results for example 20: a square enclosure for natural convection with radiation interaction, hot wall temperature supplied and using the iterative method.....	180
Table 7.17:	Results for example 21: a square enclosure for natural convection with radiation interaction, hot wall temperature supplied and using the iterative method.....	180
Table 7.18:	Results for example 22: : a rectangular enclosure with aspect ratio equal to 8 for natural convection with radiation interaction, hot wall temperature supplied and using the iterative method.....	180
Table 7.19:	Results for example 23: a rectangular enclosure with aspect ratio equal to 0.125 for natural convection with radiation interaction, hot wall temperature supplied and using the iterative method.....	181

# Nomenclature

$C_p$	Specific heat capacity	(Jkg <sup>-1</sup> K <sup>-1</sup> )
$g$	Gravitational acceleration	(ms <sup>-2</sup> )
$H$	Heat transfer rate	(W)
$h$	Heat transfer coefficient	(Wm <sup>-2</sup> K <sup>-1</sup> )
	Radiation heat transfer intensity	(Wm <sup>-2</sup> )
$K$	Thermal conductivity of the fluid	(Wm <sup>-1</sup> K <sup>-1</sup> )
$L$	Enclosure wall length	(m)
$Q_{cond}$	Conduction heat transfer	(W)
$Q_{conv}$	Convection heat transfer	(W)
$Q_{rad}$	Radiation heat transfer	(W)
$T$	Temperature	(K)
$u_\tau$	Shear velocity = $\sqrt{\tau_w/\rho}$	(ms <sup>-1</sup> )
$x, y$	Horizontal and vertical coordinates	(m)
$S_h$	Any other heat sources	(Wm <sup>-3</sup> )
$\rho$	Density	(kgm <sup>-3</sup> )
$\mu$	Viscosity	(Nsm <sup>-2</sup> )
$\alpha$	Thermal diffusivity	(m <sup>2</sup> s <sup>-1</sup> )
$\vartheta$	Kinematic Viscosity	(m <sup>2</sup> s <sup>-1</sup> )
$\beta$	Thermal expansion coefficient	(K <sup>-1</sup> )
$\varepsilon$	Surface emissivity	(-)
$\sigma$	Stefan-Boltzman constant = $5.672 \times 10^{-8}$	(Wm <sup>-2</sup> K <sup>-4</sup> )
$\tau_w$	Local wall shear stress	(Nm <sup>-2</sup> )
$\Omega$	Hemispherical solid angle	(rad)

$$\Delta T \quad \text{Temperature difference between hot and cold walls} \quad (\text{K})$$

### Dimensionless groups

$$Br \quad \text{Brinkman number} = \frac{\mu U^2}{K \Delta T} \quad (-)$$

$$Gr \quad \text{Grashof number} = \frac{\beta g \Delta T L^3 \rho^2}{\mu^2} \quad (-)$$

$$Nu_c \quad \text{Convection Nusselt number} = \frac{Q_{conv}}{Q_{cond}} = \frac{hH}{K} \quad (-)$$

$$N_{RC} \quad \text{Radiation Conduction parameter} = \frac{Q_{rad}}{Q_{cond}} = \frac{\sigma T_H^4 L}{k(T_H - T_C)} \quad (-)$$

$$Nu_r \quad \text{Radiation equivalent Nusselt number} = \frac{Q_{rad}}{Q_{cond}} \quad (-)$$

$$Nu_t \quad \text{Total Nusselt number} = \frac{Q_{conv} + Q_{rad}}{Q_{cond}} \quad (-)$$

$$Pl \quad \text{Planck number} Pl = \frac{Q_{cond}}{Q_{rad}} \quad (-)$$

$$Pr \quad \text{Prandtl number} = \frac{\mu C_p}{K} \quad (-)$$

$$Ra \quad \text{Rayleigh number} = \frac{g \beta \Delta T L^3}{\nu \alpha} \quad (-)$$

$$RC_n \quad \text{The new dimensionless group} = \frac{Nu_c}{Nu_r} = \frac{Q_{conv}}{Q_{rad}} = Nu_c \times Pl \quad (-)$$

$$T_r \quad \text{Absolute temperature ratio} = \frac{T_h}{T_c} \quad (-)$$

$$y^+ \quad \text{Dimensionless distance} = \frac{\rho u_\tau y}{\mu} \quad (-)$$

# CHAPTER 1

## INTRODUCTION

### 1.1 Introduction

Heat transfer is a mechanism, which is responsible for energy transfer from one object to another when the two objectives have a temperature difference. This heat transfer has three modes, conduction, convection and radiation. Conduction heat transfer occurs when a stationary medium (a solid or a fluid) has a temperature gradient between its two surfaces. Convection heat transfer occurs between a surface and a moving fluid both at different temperature [1].

Convection heat transfer can be divided into two types according to the nature of flow. The first is called forced convection when the flow is driven by external agent (pressure difference), such as a fan or pump. The second class is called free or natural convection, which will be explained in detail in this study. Natural convection flow is generated by density difference in different sections of a fluid. This density difference, along with the effect of the gravity, causes a buoyancy force which causes the heavier molecules in the fluid to move downward and those lighter in the fluid to move upward, producing buoyancy driven flow. The density differences in natural convection flows may result from a temperature difference or from the differences in the concentration of chemical species or from the presence of multiple phases in the fluid. In the present study, only natural convection flows caused by a temperature difference are considered.

The natural convection which results from the density difference caused by temperature difference can be sub-divided into main categories. The first category when the temperature gradient is parallel to the direction of gravity (heated from top or below) and the second category is when the temperature gradient is perpendicular to the direction of the gravity (heated from side) [1]. Natural convection has an important effect in the atmospheric flows and heat transfer processes in nature as well as many technical applications. The use of natural convection is preferable in many engineering and industrial applications, because of its simplicity and low cost. The main two



important geometries considered in natural convection studies are, the first geometry, single isothermal vertical plate and the second geometry, is the enclosed cavity with heated and cooled walls. The former geometry of natural convection flows is much easier for analysis than the enclosed cavities. For the second geometry there are two different types of buoyant flow, two vertical differentially heated and cooled walls and the two horizontally differentially heated and cooled walls. In a vertical enclosure, which is heated from one vertical wall and cooled from another vertical wall, the fluid adjacent to the hot wall rises up and the fluid adjacent to the cold wall falls down, producing a re-circulating flow motion within the enclosure, as shown in figure 1. This flow motion enhances the heat transfer through the enclosure when compared to pure conduction through the fluid.

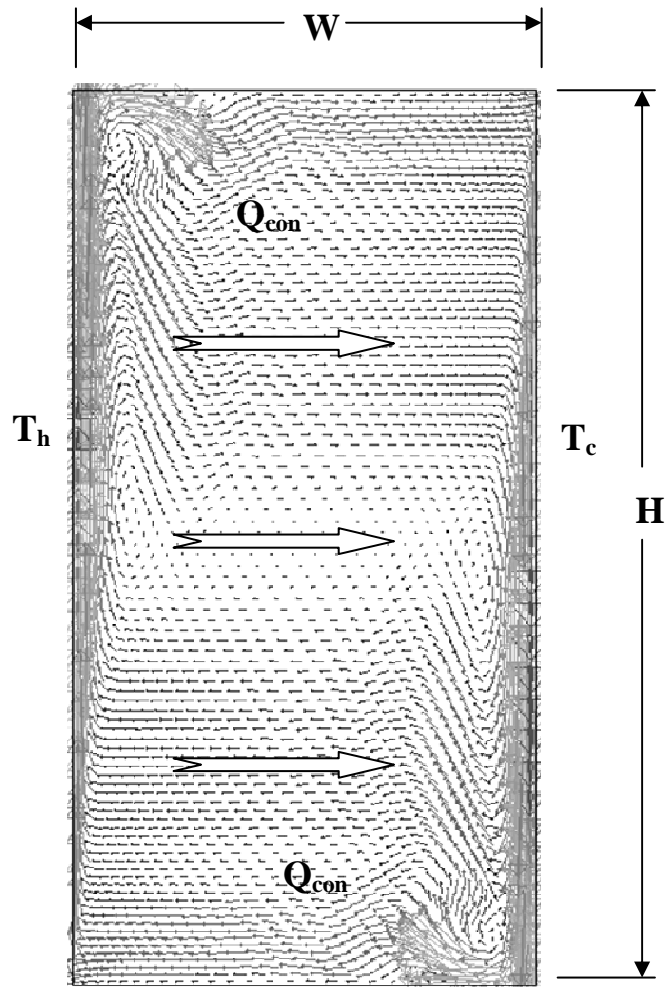


Figure 1.1 Schematic diagram of the heat transfer inside rectangular enclosure.

In a horizontal enclosure, the hot wall can be either at the top or the bottom. When the hot wall is at the top of the horizontal enclosure, the hot fluid will be always on the top of the cold fluid, this cause no flow motion inside the enclosure, which means no heat transfer by convection. In this case the heat transfer will be only by pure conduction. On the other hand when the hot wall inside the horizontal enclosure is at the bottom, the hot fluid will be at the bottom of the cold fluid, this causes the hot fluid to rise up and the cold fluid to fall down. The heat transfer at the beginning of this case is only by pure conduction, this continues until the buoyancy force overcomes the viscous force, where the natural convection occurs.

The heat transfer inside enclosures depends strongly on the flow regimes. These flow regimes depend on the value of the Rayleigh number. The first flow regime is the conduction regime where heat is transferred by pure conduction. This regime occurs at low Rayleigh numbers and obviously has a Nusselt number equal to unity. The second flow regime is the laminar regime, this occurs as the Rayleigh number increases, which causes large temperature gradients near the wall indicating the growth of the boundary layers on the two vertical surfaces. Further increase of the Rayleigh number led to unsteady motion indicating the transition to turbulent regime.

The numerical analysis of natural convection inside enclosures requires the solution of the Navier-Stokes equations including the energy equation. The results obtained by many researchers for the natural convection inside enclosed cavities are either by numerical methods or by experimental methods. These numerical methods have a certain advantage over experimental ones; in the flexibility of different geometries and boundary conditions.

The natural convection of the internal flow in an enclosed space can be dominated by buoyancy forces. The strength of the buoyancy flow can be measured using the Rayleigh number, which is the ratio of buoyancy forces to the viscous forces acting on a fluid. The value of the Rayleigh number can indicate whether the flow can be considered as laminar or turbulent [2]. The Rayleigh number is the product of Grashof and Prandtl numbers. It plays the same role in natural convection that the Reynolds number plays in forced fluid flow. The combination effects between free and forced convection must be considered when the ratio between Grashof and Reynolds numbers

$(Gr_L/Re_L^2) \approx 1$ . When  $(Gr_L/Re_L^2) \ll 1$ , the free convection effects may be neglected. Conversely, when  $(Gr_L/Re_L^2) \gg 1$ , the forced convection effects may be neglected [3].

The convective heat transfer coefficient (which controls the rate at which heat is transported across enclosures) is the most important quantity that needs to be accurately predicted inside the enclosures, this coefficient depends on the accurate evaluation of the Nusselt number values. The Nusselt number represents the enhancement of heat transfer by convection relative to conduction. That means the larger the Nusselt number the more effective convection heat transfer.

Most of these past studies were for pure natural convection, while in reality heat transfer inside enclosed spaces is through a combination of natural convection and radiation. Radiation is the energy emitted by a body in the form of electromagnetic waves. The energy transferred by radiation does not require the presence of an intervening medium, which would allow for conduction and convection. The most studies in radiation heat transfer use thermal radiation, which is the form of radiation emitted by bodies because of their temperatures [3]. The thermal surface radiation occurs between two or more surfaces at different temperatures, and it becomes extremely important if the temperature difference is high, due to the fourth order dependence of the radiation, which implies that radiation will dominate at high temperature differences.

However, heat transfer by natural convection inside enclosed spaces with radiation interaction is of practical interest in many engineering applications, such as the design of buildings for thermal comfort, nuclear reactors, solar collectors, and the cooling of electronic equipment.

The evaluation of the Nusselt number for laminar natural convection in enclosures has been extensively investigated by many researchers both numerically and experimentally. These studies concentrated on a certain range of some important parameters which affect the flow inside the enclosures and thus produced a correlation equations to calculate Nusselt number, which controlled by these parameters ranges. In reality there are many parameters that affect the heat transfer inside the enclosures which need to be investigated simultaneously to get reasonably accurate results. These parameters are the enclosure sizes, aspect ratios, wall temperature values and variable properties. Studying the effect of these parameters in account with the effect of radiation

is expecting to give good results. That means the generality for effecting of these parameters on the problem (heat transfer inside enclosures) needs to be investigated.

Hence, the effect of real conditions on the natural convection with surface radiation inside enclosures will be investigated in this work. This study will focus on the generality of the problem (for a wide range of parameters), by producing a new dimensionless group which defines the relation between heat transfer by convection and radiation inside square and rectangular enclosures. It also aims to provide correlation equations to calculate the total and convection Nusselt numbers inside the enclosures for natural convection with radiation interaction and pure natural convection respectively. Finally the study will validate the numerical results and the results using the derived correlation equations by comparing them to the produced experimental results for different aspect ratios and hot wall temperatures.

Using the results of this study is expected to give useful information and enhance the understanding of the flow inside enclosures, as, by using these results it is possible to generalise the heat transfer inside square and rectangular cavities filled with ideal gases.

## **1.2 Research objectives and aims of this study**

The main objective of this study is to find a general relation between natural convection and radiation heat transfer inside enclosures. This study will be focusing on the dimensional analysis of the governing equations by producing a new dimensionless group that defines the relation between the natural convection and radiation heat transfer inside cavities. The analysis uses the RNG k epsilon model as a turbulent model to find out the results inside cavities. To generalize the result the analysis were carried out over a wide range of enclosure sizes from 40cm square to 240cm square, aspect ratios for rectangular enclosures ranging from 16 to 0.0625, with cold wall temperatures from 283 to 373 K, and temperature ratios ranging from 1.02 to 2.61. The work was carried out using four fluids (Argon, Air, Helium and Hydrogen; with properties varying with temperature).

The aims of the present study to achieve these objectives are:

- I. Choosing the suitable turbulent model for this case, that can predict the heat transfer inside enclosures and produce accurate results, by validating the model with existing numerical and experimental data available in the literature.

- II. Identify the boundary conditions that can simulate the flow process inside the enclosures to get the most accurate results.
- III. Derive a new dimensionless group by non-dimensionalisation of the governing equations.
- IV. Study the pure natural convection and natural convection with radiation interaction inside square and rectangular enclosure.
- V. Find out the effect of all realistic conditions (such as aspect ratio, variable properties, and absolute temperature ratio and enclosure size) on the natural convection flow with and without radiation inside square and rectangular enclosure.
- VI. Produce correlation equations to provide the convection and total Nusselt numbers in square and rectangular enclosures for the whole range of parameters.
- VII. Experimentally validate the produced correlation equations and the numerical results by comparing them within a certain range of parameters.

In order to achieve these aims, the analysis involves using the chosen turbulent model with different grid sizes and the suitable conditions to capture all the turbulent effects. Also using the experimental results to validate the numerical results by comparing the thermal results for different aspect ratios and different hot wall temperatures and it also involves comparing the velocity and turbulence intensity profiles which collected using the laser Doppler velocimetry.

Hence, the results of this study are expected to contribute to the literature in this field and enhance the understanding of natural convection with radiation interaction in rectangular enclosures.

### **1.3 Outline of this thesis**

In this thesis, the results of a numerical and theoretical study of natural convection heat transfer flows with and without radiation inside differentially heated square and rectangular enclosures are discussed and described in detail. The analysis was carried out over a wide range of enclosure sizes from 40cm square to 240cm square, aspect ratios for rectangular enclosures ranging from 16 to 0.0625, with cold wall temperatures ranging from 283 to 373 K, and temperature ratios ranging from 1.02 to 2.61. The work

was carried out using four fluids (Argon, Air, Helium and Hydrogen; with properties varying with temperature). Also in this thesis the results of our experimental study for heat transfer inside square and rectangular enclosures are explained in detail. The experimental analysis was carried out over a range of hot wall temperatures ranging from 50°C to 70°C with 5°C increment and three aspect ratios 2.0, 1.0 and 0.5. The thesis is organized in several chapters as follows:

**Chapter 1** provides an introduction about natural convection and radiation heat transfer and the importance of the study carried out in this thesis and it also includes the objectives and aims of this study.

**Chapter 2** discusses the literature review of the natural convection heat transfer with and without radiation interaction in square and rectangular enclosures. It also discusses the literature review of the used turbulence model, the dimensional analysis and the experimental work for such type of flow in enclosures.

**Chapter 3** explains the theoretical background of the natural convection heat transfer with and without radiation interaction inside enclosures and also it discusses the dimensional analysis.

**Chapter 4** provides and explaining the dimensional analysis starting from the governing equations for the case of natural convection heat transfer with and without radiation interaction inside enclosures.

**Chapter 5** discusses and explain the used numerical model and its governing equations and boundary conditions. It also discusses the numerical results for both square and rectangular enclosures for the two cases of study pure natural convection and natural convection with radiation interaction. Also it discusses the 3D numerical results which will be used to be compared with the experimental results.

**Chapter 6** explains the experimental results, which include explaining the test apparatus, method and results.

**Chapter 7** discusses the dimensional analysis with the numerical results which used to produce the correlation equations for the natural convection heat transfer with and without radiation interaction in square and rectangular enclosures.

**Chapter 8** discusses and compares the final results between the experimental results and both the numerical results and the results using the derived correlation equations.

**Chapter 9** summarizes the important findings and the final conclusions from this study and the proposed future work.

# CHAPTER 2

## LITERATURE REVIEW

### 2.1 Introduction

Heat transfer by natural convection inside enclosed spaces with radiation interaction is of practical interest in many engineering applications, such as design of buildings for thermal comfort, nuclear reactors, solar collectors, and the cooling of electronic equipment [4]. In square and rectangular enclosures with natural convection as shown in figure 2.1, the internal flow is dominated by buoyancy forces. The most important dimensionless group in natural convection inside these enclosures is the Rayleigh number (which is the ratio of buoyancy forces to viscous forces acting on a fluid,) and is analogous to the Reynolds number, but for buoyancy dominated flows. The value of the Rayleigh number can indicate whether the flow can be considered as laminar or turbulent [5]. Inside square and rectangular enclosures transition from laminar to turbulent flow occurs when the Rayleigh number is greater than one million [2, 6].

### 2.2 Pure natural convection in square and rectangular enclosures

In the pure natural convection studies inside enclosed spaces, mostly two simple enclosed spaces are considered; first the square enclosure and secondly the rectangular cavity both with heated and cooled walls. The interest in this problem over the last four decades has led to many numerical and experimental studies. Elsherbiny et al. [7], reported experimentally the laminar natural convection across vertical and inclined air layers for different enclosure aspect ratios. They derived correlation equations to calculate Nusselt numbers. Davis [8], provided a bench-mark numerical solution for the natural convection of air in a square cavity using a mesh refinement for  $10^3 \leq Ra \leq 10^6$ . He [9], also provided a comparison to confirm the accuracy of the bench mark solution in [8] by compared this to 37 other pieces of work. Barletta et al. [10], numerically studied the laminar natural convection in a 2-D enclosure. A good

agreement between the solutions was found by comparison to the bench-mark [8] results. Ramesh and Venkateshan[11], investigated experimentally the natural convection in a square enclosure using a differential interferometer and again provided a correlation equation to calculate the average convection Nusselt number. Lankhorst et al.[12], experimentally studied the buoyancy induced flows in a differentially heated air filled square enclosure at high Rayleigh numbers. They found that the core stratification has a significant influence on the regimes and the characteristics of the flow. Schmidt et al. [13], compared the experimental and predicted results for laminar natural convection in a water filled enclosure.

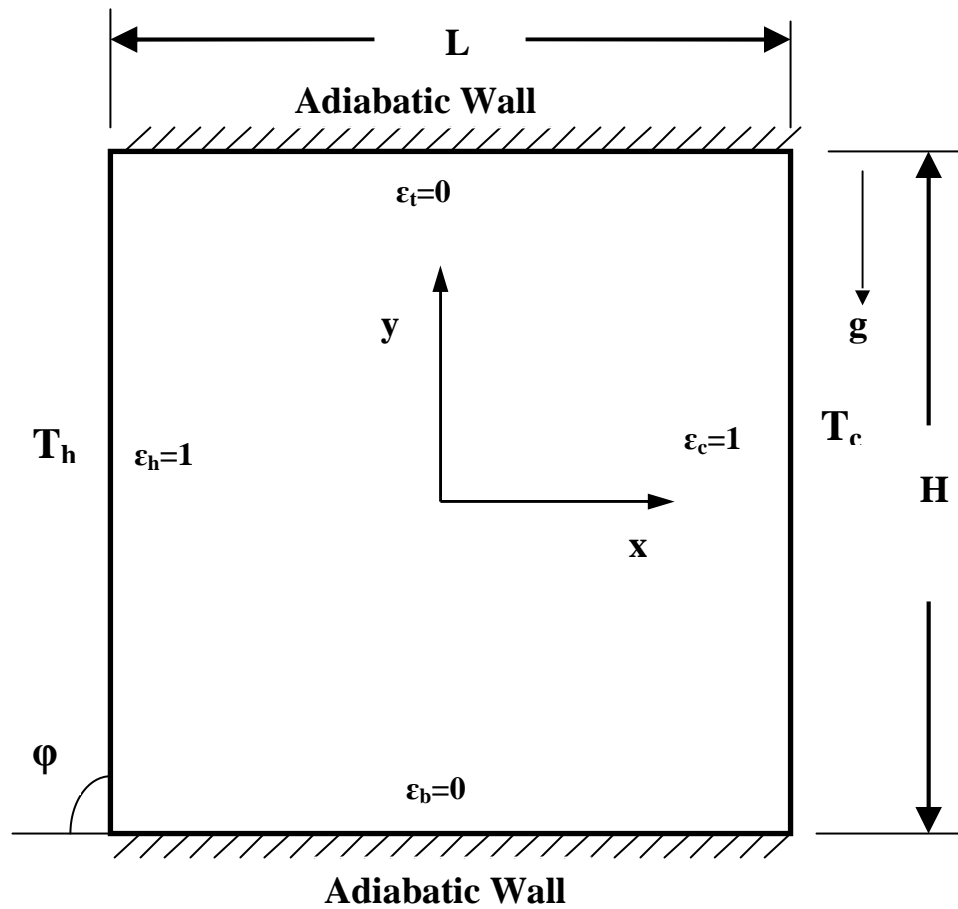


Figure 2.1 Schematic diagram of the considered enclosure

Many papers have been published that discuss the turbulent natural convection in the absence of radiation in enclosures. Henekes et al. [14], studied numerically the laminar and turbulent natural convection flow in a two dimensional square cavity using three different turbulence models. They have shown that the  $k-\epsilon$  model gives too high a



prediction, whereas the low Reynolds number models are reasonably close to the experiment. Markatos and Pericleous[6], have reported on laminar and turbulent buoyancy driven flows and heat transfer in an enclosed cavity. Henkes and Hoogendoorn[15], published a numerical reference solution for turbulent natural convection in a differentially heated enclosure at  $Ra = 5 \times 10^{10}$ , by a comparison of the computational results of 10 different groups. These groups studied the turbulent natural convection in a square, differentially heated enclosure with adiabatic horizontal walls and the detailed results of these ten groups are described in [16].

Some researchers have discussed the effect of aspect ratio on the natural convection inside enclosures. Patterson and Imberger[17] studied the transient natural convection in a cavity of aspect ratios less than one. They provide a scaling analysis of the heat transfer inside a rectangular enclosure. Bejan et al. [18] experimentally studied the turbulent natural convection in shallow enclosures. Their experimental study focused on the flow and temperature patterns in the core region. Bejan[19] explained the pure natural convection heat transfer flow regimes in tall, square and shallow enclosures. He claims that the relationship between Nusselt number and Rayleigh number in enclosures with different aspect ratios is more complicated and cannot be expressed by just a power law.

There has been some research conducted on natural convection, which also included the effect of variable fluid properties. Zhong et al. [20], studied the laminar natural convection in a square enclosure. They have observed that; with the effect of variable properties, when the temperature increases, the addition of this parameter slows down the vertical velocities in the hot wall region and increases these velocities in the core but at the same time, the total heat transfer rate is seen to increase. Also, they pointed out the necessity of solving realistic physical cases (i.e. by including the thermal radiation effects with the variable properties). Fusegi and Hyun [21], reported the effects of complex and realistic conditions such as variable properties and three-dimensionality on laminar and transitional natural convection in an enclosure. They have thrown light on the discrepancies between the numerical prediction and the experimental measurements; to the unexplored aspects of realistic flows. Nithyadevi et al. [22], investigated the effect of aspect ratio on the natural convection in a rectangular cavity with partially active side walls. They found that, the heat transfer rate increases with an increase in the aspect ratio.

## 2.3 Correlation equations for pure natural convection on flat plates

### 2.3.1 Vertical flat plate

Kato et al.[23], studied the turbulent heat transfer by free convection from a vertical plate. They provided a correlation equation to calculate the local Nusselt number as a function of Prandtl and Grashof numbers.

$$Nu_y = 0.149[(Pr)^{0.175} - 0.55](Gr_y)^{0.36} \quad (1)$$

Vliet and Liu[24], experimentally studied the turbulent natural convection boundary layers on a flat plate in a water tank. They derived correlation equations that fit their experimental data for both the laminar and turbulent regimes.

$$Nu_y = 0.61(Gr_y Pr)^{1/5} \quad \text{for } Ra_y < 3 \times 10^{12} \quad (2)$$

$$Nu_y = 0.568(Gr_y Pr)^{0.22} \quad \text{for } 2 \times 10^{13} < Ra_y < 1 \times 10^{16} \quad (3)$$

A correlation equation for the Nusselt number was provided by Churchill and Chu [25] Holman [26] claimed to be applicable for a wide ranges of Rayleigh numbers

$$\overline{Nu_L} = \left\{ 0.825 + \frac{0.387 Ra_L^{1/6}}{\left[ 1 + (0.492/Pr)^{9/16} \right]^{8/27}} \right\}^2 \quad \text{for } Ra_L < 1 \times 10^{12} \quad (4)$$

For laminar flow, another equation provided by them [25] to obtain slightly better accuracy than the previous equation[27]

$$\overline{Nu_L} = 0.68 + \frac{0.67 Ra_L^{1/4}}{\left[ 1 + (0.492/Pr)^{9/16} \right]^{4/9}} \quad \text{for } Ra_L \leq 10^9 \quad (5)$$

Siebers et al [28], studied the effect of variable fluid properties and boundary conditions on natural convection heat transfer in air over a large electrically heated vertical plate. They derived correlation equations for the local Nusselt number for both laminar and turbulent natural convection regimes.

For laminar regime

$$Nu_y = C Gr_y^{1/4} \left( \frac{T_W}{T_\infty} \right)^{-0.04} \quad (6)$$

Where the value of the constant  $C$  in equation 6 is 0.404 for a uniform heat flux plate surface and 0.356 for a uniform temperature plate surface.

Furthermore they declared that for the turbulent regime

$$Nu_y = 0.098 Gr_y^{1/3} \left( \frac{T_W}{T_\infty} \right)^{-0.14} \quad (7)$$

### 2.3.2 Parallel flat plates

For the case of vertical channels many researchers studied the natural convection heat transfer between two parallel plates. Elenbass[29], in a bench mark paper provided a correlation equation to calculate the Nusselt number for symmetrically heated isothermal plates as;

$$\overline{Nu}_L = \frac{1}{24} Ra_L \left( \frac{L}{H} \right) \left\{ 1 - \exp \left[ - \frac{35}{Ra_L \left( \frac{L}{H} \right)} \right] \right\}^{3/4} \quad (8)$$

Where

$$Ra_L = \frac{g\beta(T_s - T_\infty)L^3}{\alpha\vartheta} \quad (9)$$

Bar-Cohen and Rohsenow[30] obtained Nusselt number correlation equations for both isothermal and isoflux conditions. The correlation equations for the symmetric isothermal plates and adiabatic isothermal plates respectively are of the form:

$$\overline{Nu}_L = \left[ \frac{576}{\left(Ra_L \left(\frac{L}{H}\right)\right)^2} - \frac{2.87}{\left(Ra_L \left(\frac{L}{H}\right)\right)^{1/2}} \right]^{-1/2} \quad (10)$$

$$\overline{Nu}_L = \left[ \frac{144}{\left(Ra_L \left(\frac{L}{H}\right)\right)^2} - \frac{2.87}{\left(Ra_L \left(\frac{L}{H}\right)\right)^{1/2}} \right]^{-1/2} \quad (11)$$

### 2.3.3 Inclined parallel plates

Azevedo and Sparrow [31] experimentally studied the natural heat transfer between inclined symmetric isothermal plates and isothermal insulated plates in water for  $0 \leq \theta \leq 45^\circ$ . They provided a correlation equation for the Nusselt number for all the experiments to within 10% using this correlation [27]

$$\overline{Nu}_L = 0.645 \left[ Ra_L \left(\frac{L}{H}\right) \right]^{1/4} \quad \text{for} \quad Ra_L \left(\frac{L}{H}\right) > 200 \quad (12)$$

## 2.4 Correlation equations for pure natural convection in rectangular enclosures

The heat transfer by natural convection inside enclosed spaces with radiation interaction is of practical interest in many engineering applications, such as design of building for thermal comfort, nuclear reactors, solar collectors, and the cooling of electronic equipment. The heat transfer inside an enclosed space is a complicated case because the fluid conditions inside the enclosure do not stay stationary. In a vertical enclosure, which is heated from one vertical wall and cooled from another vertical wall; at very low Rayleigh numbers, heat transfer mainly occurs by conduction across the enclosure. Then as the Rayleigh number increases, the fluid adjacent to the hot wall rises up and the fluid adjacent to the cold wall falls down, producing a rotation in the fluid motion within the enclosure as shown in figure 2.2-a for both isothermal lines left of the figure and streamlines right of the figure. Due to its momentum, this flow motion enhances the

heat transfer through the enclosure. In a horizontal enclosure, the hot wall could be at the top or at the bottom. When the hot wall is at the top of the horizontal enclosure, the hot fluid will be always on the top of the cold fluid this causes no flow motion inside the enclosure that means no heat transfer by convection. For this case the heat transfer will be only by pure conduction this can be seen for both isothermal lines and stream lines in figure 2.2-b. On the other hand when the hot wall inside the horizontal enclosure is at the bottom, the hot fluid will be at the bottom of the cold fluid, this cause the hot fluid tend to rise up and the cold fluid to fall down as it can be seen in figure 2.2-c. The heat transfer at the beginning of this case is only by pure conduction, this is continues until the buoyancy force overcomes the viscous force, where the natural convection occurs.

### 2.4.1 Horizontal enclosures

The natural heat transfer inside horizontal enclosures has been studied and correlation equations to calculate Nusselt number inside these enclosures have been provided. For a horizontal enclosure filled with air, Jakob[32], provided two correlation equations for different Rayleigh numbers in the form

$$Nu_L = 0.195Ra_L^{1/4} \quad \text{for} \quad 10^4 \leq Ra_L \leq 4 \times 10^5 \quad (13)$$

$$Nu_L = 0.068Ra_L^{1/3} \quad \text{for} \quad 4 \times 10^5 \leq Ra_L \leq 10^7 \quad (14)$$

Globe and Dropkin[33] from their experimental results using water, silicon oil and mercury in a horizontal enclosure heated from below provided a correlation equation to calculate Nusselt number as

$$Nu_L = 0.069Ra_L^{1/3}Pr^{0.074} \quad \text{for} \quad 3 \times 10^5 \leq Ra_L \leq 7 \times 10^9 \quad (15)$$

This equation applies only for a horizontal enclosure heated from below and for values of L/H sufficiently small [27]. Hollands et al [34], provides a correlation equation to calculate Nusselt number based on the experimental results of air in a horizontal enclosure, of the form

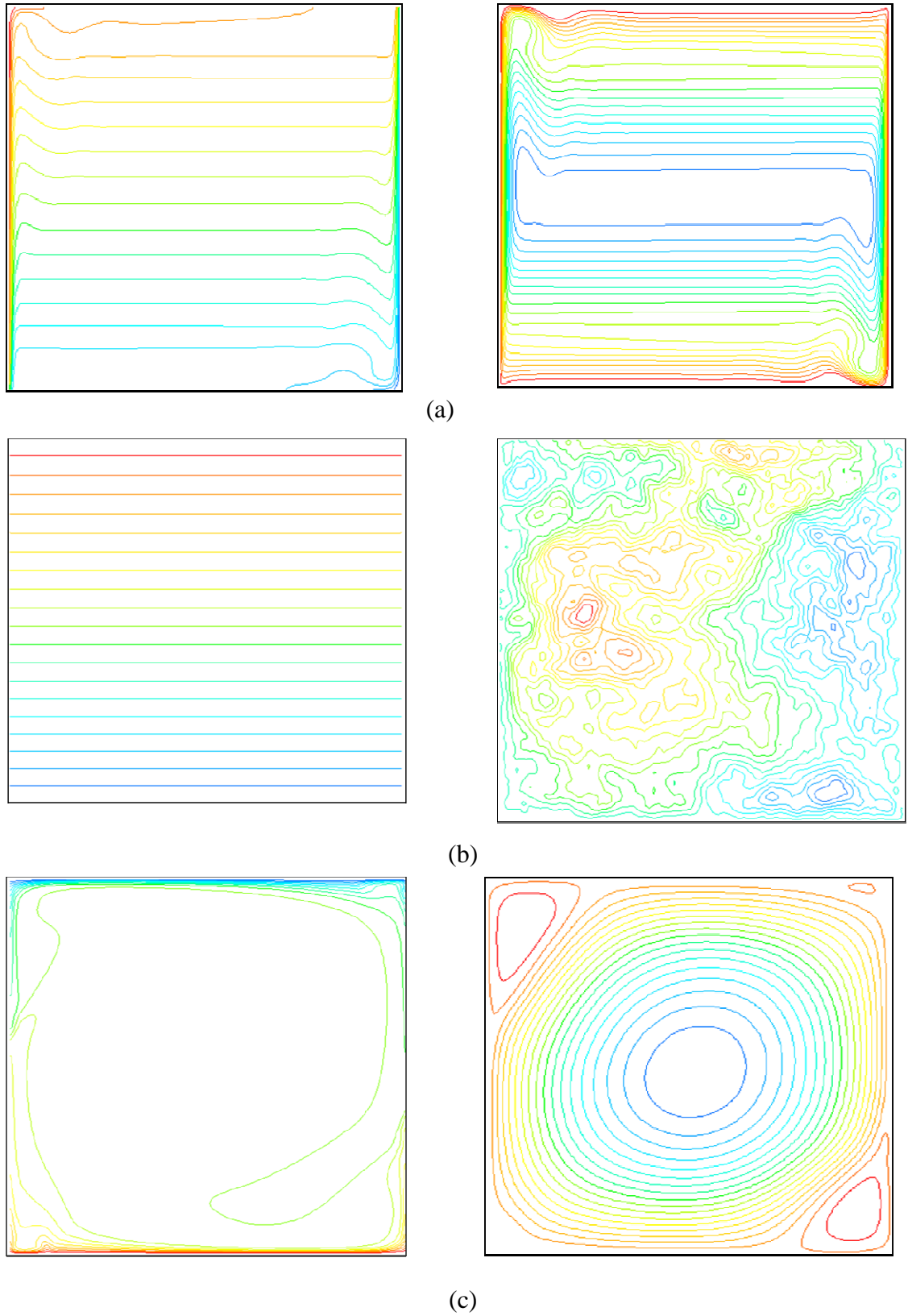


Figure 2.2 Isothermal lines and stream lines for enclosure heated from a) side wall, b) top wall and c) bottom wall. This was for  $\Delta T = 70$  and  $Ra = 9.2 \times 10^8$

$$Nu_L = 1 + 1.44 \left[ 1 - \frac{1708}{Ra_L} \right]^+ + \left[ \frac{Ra_L^{1/3}}{18} - 1 \right]^+ \quad (16)$$

The notation + indicate that if the quantity in the bracket is negative, it should be set to zero. This equation is applied for air in horizontal enclosure and for  $Ra_L < 10^8$  and  $H/L \geq 12$ .

### 2.4.2 Inclined enclosures

For the case of an inclined rectangular enclosure, De Graaf and Van Der Held [35] derived some relationships for the Nusselt number for pure laminar natural convection with different angles of inclination. Table 2.1 shows these relationships for Nusselt number as a function of Grashof number and for different angle of inclination of rectangular enclosure and also given the range of application of each relationship.

Hollands et al [34], provides a correlation equation to calculate Nusselt number based on the experimental results of air in the form

$$Nu_L = 1 + 1.44 \left[ 1 - \frac{1708}{Ra_L \cos \theta} \right]^+ \left( 1 - \frac{1708 (\sin 1.8 \theta)^{1.6}}{Ra_L \cos \theta} \right) + \left[ \frac{(Ra_L \cos \theta)^{1/3}}{18} - 1 \right]^+ \quad (17)$$

This equation is applied for  $Ra_L < 10^8$ ,  $0 < \theta < \theta_{cr}^\circ$  and  $H/L \geq 12$  and again the notation + indicate that if the quantity in the bracket is negative, it should be set to zero,  $\theta_{cr}$  is the critical angle which depends on the aspect ratio as shown in table 2.2. Also this equation is the same as equation (16, above) when  $\theta = 0^\circ$ .

Catton [36] provided a correlation equation to calculate Nusselt number for small aspect ratios:

$$Nu_L = Nu_L(\theta = 0^\circ) \left[ \frac{Nu_L(\theta = 90^\circ)}{Nu_L(\theta = 0^\circ)} \right]^{\theta/\theta_{cr}} (\sin \theta_{cr})^{\theta/4\theta_{cr}} \text{ for } \left[ \begin{array}{l} \frac{H}{L} \leq 12 \\ 0 < \theta \leq \theta_{cr} \end{array} \right] \quad (18)$$

Table 2.1 Relationships of Nusselt number for inclined rectangular enclosure [35]

Angle of inclination	Nusselt number equation	Range of application
20°	$Nu_L = 1$	$Gr_L < 2 \times 10^3$
	$Nu_L = 0.0507Gr_L^{0.4}$	$2 \times 10^3 < Gr_L < 3 \times 10^4$
	$Nu_L \approx 3.6$	$4 \times 10^4 < Gr_L < 2 \times 10^5$
	$Nu_L = 0.0402Gr_L^{0.37}$	$2 \times 10^5 < Gr_L$
30°	$Nu_L = 1$	$Gr_L < 3 \times 10^3$
	$Nu_L = 0.0588Gr_L^{0.37}$	$3 \times 10^3 < Gr_L < 5 \times 10^4$
	$Nu_L = 0.0390Gr_L^{0.37}$	$2 \times 10^5 < Gr_L$
45°	$Nu_L = 1$	$Gr_L < 4 \times 10^3$
	$Nu_L = 0.0503Gr_L^{0.37}$	$4 \times 10^3 < Gr_L < 5 \times 10^4$
	$Nu_L = 0.0372Gr_L^{0.37}$	$2 \times 10^5 < Gr_L$
60°	$Nu_L = 1$	$Gr_L < 5 \times 10^3$
	$Nu_L = 0.0431Gr_L^{0.37}$	$5 \times 10^3 < Gr_L < 5 \times 10^4$
	$Nu_L = 0.0354Gr_L^{0.37}$	$2 \times 10^5 < Gr_L$
70°	$Nu_L = 1$	$Gr_L < 6 \times 10^3$
	$Nu_L = 0.0384Gr_L^{0.37}$	$10^4 < Gr_L < 8 \times 10^4$
	$Nu_L = 0.0342Gr_L^{0.37}$	$2 \times 10^5 < Gr_L$

Table 2.2 Critical angle for inclined rectangular enclosures[34]

(H/L)	1	3	6	12	>12
$\theta_{cr}$	25°	53°	60°	67°	70°

Ayyaswamy and Catton [37] and Arnold et al. [38] provided two correlation equations beyond the critical tilt angle of [36] to calculate Nusselt numbers for all aspect ratios according to the values of the tilt angle.



$$Nu_L = Nu_L(\theta = 90^\circ)(\sin\theta_{cr})^{1/4} \quad \text{for } \theta_{cr} < \theta \leq 90^\circ \quad (19)$$

$$Nu_L = 1 + [Nu_L(\theta = 90^\circ) - 1]\sin\theta \quad \text{for } 90^\circ < \theta \leq 180^\circ \quad (20)$$

Sharma et al. [4], provided a correlation equation to calculate Nusselt number for the interaction of turbulent natural convection and surface thermal radiation in inclined square enclosures.

$$Nu_L = [0.017N_{RC}^{-0.97} + 0.021\sin(\theta^2) + 0.142]Ra_L^{1/3} \left[ \begin{array}{c} 10^8 \leq Ra_L \leq 10^{12} \\ 15^\circ \leq \theta \leq 90^\circ \\ 4 \leq N_{RC} \leq 85 \end{array} \right] \quad (21)$$

This equation is applied only for inclined square enclosure and with the above conditions.

### 2.4.3 Vertical enclosures

For the vertical enclosure heated from one side and cooled from the other side, Eckert and Carlson [39], studied the natural convection in vertical enclosure with large aspect ratio (AR=30). They provided a correlation equation to calculate Nusselt number

$$Nu_L = 0.119Gr_L^{0.3} \quad (22)$$

This equation is applies for a rectangular cavity filled with air and with an aspect ratio of 30 and small values of Grashof number.

De Graaf and Van Der Held [35] derived the following relationships from their experiments for Nusselt number in vertical enclosure for pure laminar natural convection

$$\begin{aligned} Nu_L &= 1 & \text{for } Gr_L < 7 \times 10^3 \\ Nu_L &= 0.038Gr_L^{0.37} & \text{for } 1 \times 10^4 < Gr_L < 8 \times 10^4 \\ Nu_L &= 0.032Gr_L^{0.37} & \text{for } 2 \times 10^5 < Gr_L \end{aligned} \quad (23)$$

MacGregor and Emery [40], studied experimentally the effect of Prandtl number with the aspect ratio inside rectangular enclosure. They provided a correlation equation to calculate the Nusselt number for a wide range of Prandtl number and aspect ratios

$$Nu_L = 0.046Ra_H^{1/3} \quad for \quad \left[ \begin{array}{c} 1 \times 10^7 < Ra_L < 1 \times 10^9 \\ 1 < Pr < 20 \\ 1 < \frac{H}{L} < 40 \end{array} \right] \quad (24)$$

Seki et al. [41], provided experimentally a correlation equation for Nusselt number in rectangular enclosure with the effect of aspect ratio and Prandtl number for the laminar regime

$$Nu_H = 0.36Ra_H^{0.25}Pr^{0.051}\left(\frac{H}{L}\right)^{-0.11} \quad for \quad \left[ \begin{array}{c} 1 \times 10^7 < Ra_H < 4 \times 10^9 \\ 3 < Pr < 40000 \\ 5 < \frac{H}{L} < 47.5 \end{array} \right] \quad (25)$$

They [41], also suggested a correlation equations for Nusselt number in the turbulent regime

$$Nu_H = 0.084Ra_H^{0.3}Pr^{0.051} \quad for \quad \left[ \begin{array}{c} 4 \times 10^9 < Ra_H < 4 \times 10^{12} \\ 1 < Pr < 200 \\ 5 < \frac{H}{L} < 47.5 \end{array} \right] \quad (26)$$

$$Nu_H = 0.039Ra_H^{1/3} \quad for \quad \left[ \begin{array}{c} Ra_H > 2 \times 10^{12} \\ 1 < Pr < 4 \\ 5 < \frac{H}{L} < 47 \end{array} \right] \quad (27)$$

All these correlation equations are for natural convection in rectangular enclosure with aspect ratio greater than 5.

Catton [36], provided two correlation equations to calculate the Nusselt number as

$$Nu_L = 0.18 \left( \frac{Pr}{0.2 + Pr} Ra_L \right)^{0.29} \quad for \quad \left[ \begin{array}{c} \frac{Ra_L Pr}{(0.2 + Pr)} > 10^3 \\ 10^{-3} < Pr < 10^5 \\ 1 < \frac{H}{L} < 2 \end{array} \right] \quad (28)$$

$$Nu_L = 0.22 \left( \frac{Pr}{0.2 + Pr} Ra_L \right)^{0.28} \left( \frac{H}{L} \right)^{-1/4} \quad for \quad \left[ \begin{array}{c} 10^3 < Ra_L < 10^{10} \\ Pr < 10^5 \\ 2 < \frac{H}{L} < 10 \end{array} \right] \quad (29)$$

Cowan et al. [42], experimentally studied the turbulent natural convection in vertical cavities filled with water. They provided a correlation equation from the resulting data to calculate Nusselt number

$$Nu_L = 0.043Ra_L^{1/3} \quad for \quad \left[ \begin{array}{c} 2 \times 10^5 < Ra_L < 2 \times 10^{11} \\ 1.5 < \frac{H}{L} < 60.8 \end{array} \right] \quad (30)$$

This correlation is quite similar to that of MacGregor's correlation[43].

Ziai[44], carried out an experimental study of turbulent natural convection in a rectangular air cavity of aspect ratio 6. He provided a correlation equation to calculate Nusselt number

$$Nu_L = 0.045Ra_L^{1/3} \quad for \quad Gr_L > 10^5 \quad (31)$$

His correlation agrees well with both correlations of[40] and [43].

Markatos and Pericleous[6], provided three correlation equations for laminar and turbulent natural convection in an enclosed cavity (square enclosure) according to the value of Rayleigh number. These correlation equations are in the form:

$$Nu_L = 0.143Ra_L^{0.299} \quad for \quad 10^3 \leq Ra_L \leq 10^6 \quad (32)$$

$$Nu_L = 0.082Ra_L^{0.329} \quad for \quad 10^6 \leq Ra_L \leq 10^{12} \quad (33)$$

$$Nu_L = 1.325Ra_L^{0.245} \quad for \quad 10^{12} \leq Ra_L \leq 10^{16} \quad (34)$$

For large aspect ratios Macgregor and Emery [43] provided two correlation equations to calculate the Nusselt number

$$Nu_L = 0.42Ra_L^{1/4}Pr^{0.012}\left(\frac{H}{L}\right)^{-0.3} \quad for \quad \left[ \begin{array}{c} 10^4 < Ra_L < 10^7 \\ 1 < Pr < 2 \times 10^4 \\ 10 < \frac{H}{L} < 40 \end{array} \right] \quad (35)$$

$$Nu_L = 0.046Ra_L^{1/3} \quad \text{for} \quad \left[ \begin{array}{l} 10^6 < Ra_L < 10^9 \\ 1 < Pr < 20 \\ 1 < \frac{H}{L} < 40 \end{array} \right] \quad (36)$$

Ramesh and Venkateshan[11], experimentally studied the natural convection in a square enclosure, filled with air, using differential interferometer and they provided a correlation equation to calculate the Nusselt number that match the experimental results. The correlation equation as a function of Grashof number is

$$Nu_L = 0.56Gr^{0.195} \quad \text{for} \quad 5 \times 10^4 \leq Gr \leq 2 \times 10^6 \quad (37)$$

Trias et al. in part-I [45] and in part-II [46] studied the numerical methods and heat transfer inside a differentially heated cavity of aspect ratio 4 with Rayleigh numbers up to  $10^{11}$  using the direct numerical simulation. They provided two correlation equations to calculate Nusselt number for the studied range of Rayleigh number.

$$Nu_L = 0.182Ra_L^{0.275} \quad \text{for} \quad 6.4 \times 10^8 \leq Ra \leq 10^{11} \quad (38)$$

$$Nu_L = C_1 \left( 1 - \exp(aRa_L^b) \right) Ra_L^{1/3} + C_2 \exp(aRa_L^b) Ra_L^{1/4} \quad (39)$$

For  $6.4 \times 10^8 \leq Ra \leq 10^{11}$  where,  $C_1 = 4.6847 \times 10^{-2}$ ,  
 $C_2 = 3.2101 \times 10^{-1}$ ,  $a = -1.5104 \times 10^{-4}$  and  $b = 3.1874 \times 10^{-1}$

All these correlation equations have limitations and used for a certain range of parameters which must be carefully noted before they are applied. First and most important, is the geometry which is a major factor. For example external flow over a flat plate is not the same as flow inside an enclosure. Thus, each correlation equation is valid for a specific geometry. Second important, limitations on the range of parameters used, such as the Rayleigh, Prandtl and Grashof numbers, for which a correlation equation is valid, are determined by the availability of data.

## **2.5 Interaction between radiation and natural convection in square and rectangular enclosures**

The importance of surface radiation with natural convection in square and rectangular enclosures has also been studied and investigated by many researchers. Balaji and Venkateshan[47], numerically investigated the interaction of surface radiation with laminar free convection in a square cavity. They elucidated the importance of surface radiation even at low emissivities and provide some reasons for the discrepancies noted between the experimental and theoretical correlations. They [48] derived correlation equations to calculate convection and radiation Nusselt numbers in square enclosures. Sen and Sarkar[49], have considered the effects of variable properties on the interaction of laminar natural convection and surface radiation in a differentially heated square cavity. They discovered that, the presence of both radiation at low emissivity ( $\epsilon = 0.1$ ) and variable properties, affect intensively the thermal stratification of the core and the symmetry of the mid-plane vertical velocity as well as temperature profiles. Akiyama and Chong [50], analysed the interaction of laminar natural convection with surface thermal radiation in a square enclosure filled with air. They found that the presence of surface radiation significantly altered the temperature distribution and the flow patterns and affected the values of average convective and radiation Nusselt numbers.

Velusamy et al. [51], studied the turbulent natural convection with the effect of surface radiation in square and rectangular enclosures. They pointed out that, the radiation heat transfer is significant even at low temperatures and low emissivities. Colomer et al. [52], looked at the three-dimensional numerical simulation of the interaction between the laminar natural convection and the radiation in a differentially heated cavity for both transparent and participating media. Their work reveals that in a transparent fluid, the radiation significantly increases the total heat flux across the enclosure. Ridouane and Hasnaui[53], investigated the effect of surface radiation on multiple natural convection solutions in a square cavity partially heated from below. They found that, the surface radiation alters significantly the existence ranges of the resultant solutions. Sharma et al. [54], studied the turbulent natural convection with surface radiation in air filled rectangular enclosures heated from below and cooled from other walls. Their results emphasise the need for coupling radiation and convection to get an accurate prediction of heat transfer in enclosures. Also Sharma et al. [4], investigated and analysed

turbulent natural convection with thermal surface radiation in inclined square enclosures. They reported that, for the case of angle of inclination  $\phi = 90^\circ$ , the circulation rate in the enclosure increases significantly and the turbulent viscosity is three times that of the non-radiating case.

This work focuses on the effect of aspect ratio and realistic conditions (which include the effect of different enclosure size, changing the cold and hot wall temperatures, and using different fluids, for all properties vary with temperature) on the turbulent natural convection with and without surface radiation reports a correlation equation for the natural convection for both types of (square and rectangular enclosures). The analysis uses a new dimensionless group which demonstrates the relation between the convection and radiation heat transfer inside the rectangular and square enclosures.

## 2.6 Correlation equations for natural convection with radiation interaction in square enclosure

Balaji and Venkateshan[48], numerically studied the interaction of surface radiation with free convection in a square enclosure. They provided two correlation equations to calculate convection and radiation Nusselt numbers.

$$Nu_C = 0.149Gr^{0.294}(1 + \varepsilon_H)^{-0.279}(1 + \varepsilon_C)^{0.182}(1 + \varepsilon_B)^{-0.135} \\ (1 + \varepsilon_T)^{0.115} \left( \frac{N_{RC}}{N_{RC} + 1} \right)^{0.272} \left[ \begin{array}{l} 10^3 < Gr < 10^6 \\ 0.73 < Tr < 0.95 \\ 4 < N_{RC} < 22 \end{array} \right] \quad (40)$$

$$Nu_R = 0.657Gr^{-0.0093}\varepsilon_H^{0.808}\varepsilon_C^{0.342}(1 + \varepsilon_B)^{0.199}(1 + \varepsilon_T)^{-0.039} \\ (1 - Tr^4)^{1.149} N_{RC}^{1.051} \left[ \begin{array}{l} 10^3 < Gr < 10^6 \\ 0.73 < Tr < 0.95 \\ 4 < N_{RC} < 22 \end{array} \right] \quad (41)$$

Where  $Nu_C$  is the convection Nusselt number,  $Nu_R$  is the radiation Nusselt number,  $\varepsilon_H$  is the emissivity of the hot wall,  $\varepsilon_C$  is the emissivity of the cold wall,  $\varepsilon_B$  is the emissivity of the bottom wall,  $\varepsilon_T$  is the emissivity of the top wall, and  $N_{RC} = \frac{\sigma T_H^4 L}{k(T_H - T_L)}$ .

Akiyama and Chong [50], investigated the numerical analysis of natural convection with surface radiation in a square enclosure, they provided a correlation equation to calculate Nusselt number to within an average deviation of 7.32% and a maximum deviation of 14.82% compared to their numerical results. Their correlation equation is

$$Nu_L = 0.529Ra_L^{0.3065}\epsilon^{0.3497} \quad for \quad 10^4 \leq Ra_L \leq 10^6 \quad (42)$$

Velusamy et al. [51], provided two correlation equations to calculate Nusselt number for the case of interaction between surface radiation and turbulent natural convection in square enclosures. The two correlation equations respectively are for the total Nusselt number for coupled natural convection with surface radiation and the total Nusselt number for decoupled natural convection with radiation.

$$Nu_T = 0.17Ra_L^{0.3365} \quad for \quad 10^9 \leq Ra \leq 10^{12} \quad (43)$$

$$Nu_T = 0.142Ra_L^{0.3414} \quad for \quad 10^9 \leq Ra \leq 10^{12} \quad (44)$$

## 2.7 The use of turbulence models for modelling natural convection

The geometry that was solved is shown schematically in figure2.1. This is a two dimensional flow of an ideal gas in an enclosure of side H and width L. The two vertical hot and cold walls are heated isothermally and the other two (horizontal) walls are adiabatic. To simplify the problem and focus on the heat transfer between the hot and cold walls the adiabatic wall surfaces are taken as zero emissivities which is similar to a highly shiny, insulated surface. It is appreciated that changing this will alter the rest of this analysis, and this could form the basis of future work. The turbulent flow in the enclosure is analysed using the commercial code (FLUENT 6.3) and by using the RNG k- $\epsilon$  model with the Boussinesq approximation for the density.

The RNG k- $\epsilon$  model was derived using a rigorous statistical method (called renormalization group theory). It involved the improvement in the accuracy of the k- $\epsilon$  model in rapidly strained flows by adding another term to the  $\epsilon$  equation, and enhancing the accuracy of the swirling flows by including the effect of swirl on turbulence. It also

accounts for low-Reynolds numbers effects by providing an analytical differential formula for effective viscosity, which depends on an appropriate treatment of the near wall region [55]. These features make the RNG  $k$ - $\epsilon$  model more accurate and reliable for a wider class of fully enclosed airflows than the standard  $k$ - $\epsilon$  model. Zhang et al. [56] have compared four turbulence models for the turbulent natural convection in enclosures they have found that the RNG  $k$ - $\epsilon$  model agreed better with the experimental results of [57, 58] than the other models. Gan[59] has also studied the turbulent buoyant flow in a tall air cavity using the standard  $k$ - $\epsilon$  and the RNG  $k$ - $\epsilon$  models. He pointed out, by using the RNG  $k$ - $\epsilon$  model, an improvement in the predicted results was achieved compared to the standard  $k$ - $\epsilon$  model. Zhang et al. [60] have compared eight turbulence models for predicting airflow and turbulence in enclosed environments they have found that between the RANS models, the RNG  $k$ - $\epsilon$  model produced the best results. Coussirat et al. [61] studied and analysed the influence and performance of five numerical models on the simulation of free and forced convection in double-glazed ventilated facades, they found that the RNG  $k$ - $\epsilon$  model performed better for predicting heat transfer than the other turbulence models, compared with experimental results. Omri et al. [62], studied the turbulent natural convection in non-partitioned cavities using three different CFD models. They found that all the models give satisfactory predictions compared with the experimental benchmark values [63]. For these reasons the RNG  $k$ - $\epsilon$  model was chosen in this work.

## **2.8 Dimensional analysis of natural convection in enclosures**

Patterson and Imberger[17] studied the transient natural convection in a cavity of aspect ratio less than one. They provide a dimensionless analysis of the heat transfer inside a rectangular enclosure. Bejan[19] explained the pure natural convection heat transfer flow regimes in tall, square and shallow enclosures. He provides an extendable dimensionless analysis of the heat transfer inside enclosures based on the dimensional analysis of [17]. He claims that the relationship between Nusselt number and Rayleigh number in enclosures with different aspect ratios is more complicated and cannot be expressed by just a power law. Johnstone and Thring[64] studied the scale up methods of general heat transfer. They provide a dimensional analysis of different heat transfer cases.



This study focuses on the dimensional analysis for two cases of natural convection, pure natural convection and natural convection with interaction of surface thermal radiation. Both problems have been analysed and correlation equations for both cases will be provided.

## **2.9 Experimental studies of natural convection in enclosures**

Many researchers experimentally studied the velocity profiles inside the cavities. They tried to find out the position of the peak velocity and flow reversals and how that effected the thickness of the boundary layer. In this study the velocity boundary layer was considered to be the region of velocity values which extends from the wall to the first zero or near to zero velocity value and does not include the region of reversed flow. Also the core of the enclosure is defined relative to the velocity or thermal boundary layers and by noticing that the temperature fluctuations are more dependent on velocity fluctuations not vice versa. Therefore the definition of the core based on the velocity boundary layer is more preferable. King [57], defines the core as that region which exists beyond the velocity boundary layer which ends at the first position of zero velocity.

Kutaleladze et al [65] studied the turbulent natural convection on a vertical flat plate. They observed that the lateral position of the peak mean velocity increases as the height increases. They also showed that increasing the cavity width will increase the boundary layer thickness and significantly decrease the velocity value. Schmidt and Wang [66] experimentally studied the turbulent natural convection in an enclosure filled with water. They observed the flow reversals just outside of the boundary layer for about 60% upstream of each wall. They noticed that the peak of the velocity values start to decrease and moved away from the wall (increasing the boundary layer thickness) after the enclosure mid-height. Giel and Schmidt [67] experimentally studied the turbulent natural convection in an enclosure filled with water. They observed the velocity reversals to occur at upstream of 70% of the heated and cooled walls. They claimed that the boundary layer thickness was being constant except at the corner regions. King [57] studied the turbulent natural convection in air cavity. He observed that the boundary layer thickness and the peak of the mean velocity were at its minimum at the bottom of the heated wall than it starts to increase up to the mid-height then it start to decrease again. Lankhorst et al [12] experimentally studied the buoyancy induced flow in a

square enclosure filled with air. They used laser Doppler velocimetry to obtain the velocity and turbulence intensity profiles inside the enclosure. They found that as the flow proceed downstream the peak velocity shifts away from the wall causing a growth of the boundary layer. Also they noticed that the turbulent intensities are nearly symmetric in the hot and cold boundary layers at similar heights of the boundary layer growth. Ayinde et al [68] experimentally investigated the turbulent convection flow in a channel using the particle image velocimetry. They found that the peak of the velocity value increases as the aspect ratio or the Rayleigh number increase.

This study focuses on the thermal analysis of heat transfer inside square and rectangular enclosures using three aspect ratios. Also in this study the velocity and turbulence intensity profiles using the Laser Doppler Velocimetry (LDV) will be discussed and compared with the numerical results.

## **2.10 Conclusion**

From the published literature it is clear that the problems of both natural convection with radiation effects and with the effect of realistic conditions (which include the effect of enclosure sizes, different wall temperatures, aspect ratios and variable fluid properties) needs be studied in detail. Also, the work of Jonstone and Thring [64] shows that while many physical problems can be approached through dimensional analysis, this problem has not been looked at from this aspect, and can profitably be studied in detail.

Therefore this study will focus on examining how the dimensional analysis of this problem and the effect of the realistic conditions can lead to some general outcomes and empirically reduce the problem to some simple relationships. To this end, the study will aim to provide correlation equations for Nusselt number for the two cases of pure natural convection and natural convection with radiation interaction; both with the effect of realistic conditions. Also this study will provide the variables needed to use a new dimensionless equation which describes the relation between natural convection and radiation heat transfer inside enclosures.

# CHAPTER 3

## THEORETICAL BACKGROUND

### 3.1 Convection heat transfer

The heat transfer by convection between a wall surface and a fluid can be calculated using Newton's law of cooling [2]:

$$\dot{Q}_{conv} = hA(T_w - T_{\infty}) \quad (1)$$

Where  $\dot{Q}_{conv}$  is the heat transfer rate by convection between a surface of area  $A$  at a temperature  $T_w$  and a fluid of temperature  $T_{\infty}$ . The quantity  $h$  is called the convection heat transfer coefficient. For some convection heat transfer systems the convection heat transfer coefficient can be calculated analytically but for more complex systems the convection heat transfer coefficient must be determined experimentally [2].

#### 3.1.1 Convection boundary layers

Conceptually, there are two boundary layers, velocity boundary layer and temperature boundary layer. To define these two boundary layers it is best to consider the flow over a flat plate as shown in figure 3.1. A flow region develops starting at the leading edge of the considered plate, where the effects of the viscous force are dominant. This effecting viscous force is a function of shear stress between fluid layers. This shear stress is proportional to the normal velocity gradient[2, 3].

$$\tau = \mu \frac{du}{dy} \quad (2)$$

Where  $\tau$  = Shear stress

$\mu$  = Dynamic viscosity

$\frac{du}{dy}$  = Velocity gradient

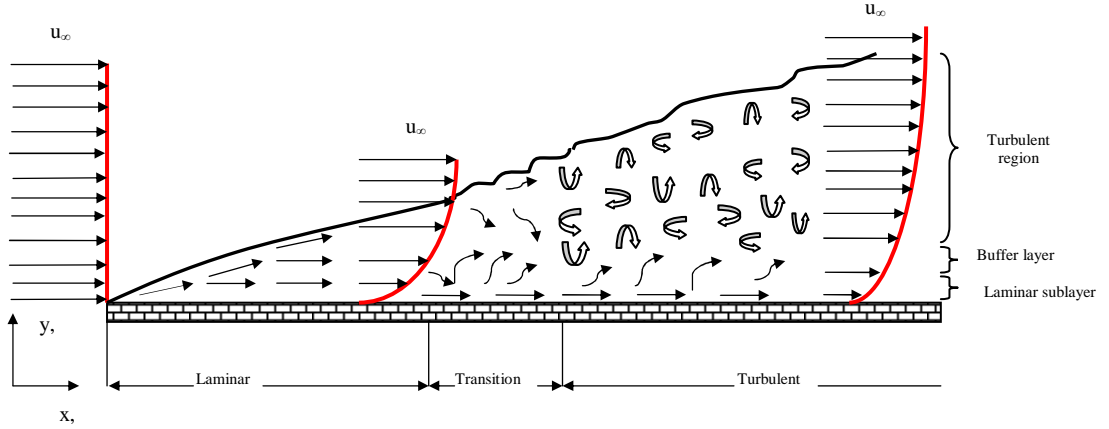


Figure 3.1 Velocity boundary layer development on a flat plate

The region of the flow in which the effects of the viscosity are observed to start develop from the leading edge of the plate; this region is called the boundary layer. This boundary layer ends at a distance on the y coordinate where the velocity becomes 99 percent of the free stream value.

At the beginning the boundary layer development is laminar and as the flow developed from the leading edge a transition process starts and with increasing distance, the laminar layers are no longer stable and the flow becomes turbulent. The transition from laminar to turbulent flow on a flat plate occurs when Reynolds number [2]

$$Re_x = \frac{\rho u_{\infty} x}{\mu} > 5 \times 10^5 \quad (3)$$

Where  $u_{\infty}$  = Free stream velocity

$x$  = Distance from leading edge

$\rho$  = Fluid density

The thermal boundary layer develops when the plate surface temperature and the fluid free stream temperature are different. Also it defines as the region where the temperature gradients are present in the flow. This temperature gradient caused by heat exchange between the plate surface and the fluid. The thermal boundary layer ends at a distance y where  $(T_s - T) = 0.99(T_s - T_{\infty})$ .

Here, the Prandtl number is the ratio between the thicknesses of velocity to thermal boundary layer.

Consider the flow over a flat plate as shown in figure 3.2. The temperature of the surface is  $T_s$ , the temperature of the fluid far from the surface is  $T_\infty$  and the thickness of the thermal boundary layer is  $\delta_t$ . At the plate surface the heat transfer occurs only by conduction because there is no fluid motion. Thus the local heat flux is

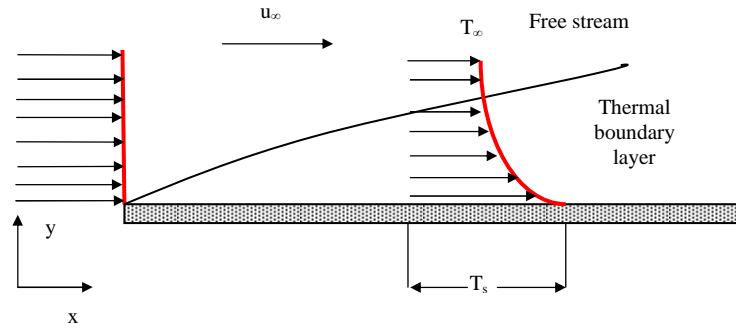


Figure 3.2 Thermal boundary layer development on an isothermal flat plate.

$$q = -k \left. \frac{\partial T}{\partial y} \right|_{surface} \quad (4)$$

Combining this equation with Newton's law (equation one above) result:

$$h = \frac{-k(\partial T / \partial y)_{surface}}{(T_s - T_\infty)} \quad (5)$$

This means that to find the heat transfer coefficient the temperature gradient at the plate surface need to be found.

In this study the velocity boundary layer was considered to be the region of velocity values which extends from the wall to the first zero or near to zero velocity value and does not include the region of reversed flow. The temperature boundary layer is considered to be the region of temperature values which extends from the wall to the position where the fluid temperature reaches that of the fluid at the cavity centre and  $(T_w - T)$  is a maximum.

### 3.1.2 Equations of motion for natural convection

From the physical mechanism of natural convection in a gravitational field, the buoyancy force exerted by the fluid on a body will be equal to the weight of the fluid displaced by the body[3].

$$F_{buoyancy} = \rho_{fluid} g V_{body} \quad (6)$$

Where  $\rho_{fluid}$  is the average fluid density,  $g$  is the gravitational acceleration and  $V_{body}$  is the volume of the body portion immersed in the fluid. The net force acting on this body will be[3]:

$$F_{net} = W - F_{buoyancy} = \rho_{body} g V_{body} - \rho_{fluid} g V_{body} = (\rho_{body} - \rho_{fluid}) g V_{body} \quad (7)$$

The force shown in equation 7 is proportional to the density difference of the fluid and the body immersed in this fluid. In heat transfer studies, however, the most important variable is the temperature; hence the buoyancy forces need to be expressed in terms of temperature difference instead of density difference. The property, which represents the relation between temperature difference and density difference at constant pressure, is called the volume expansion coefficient  $\beta_{(T^{-1})}$ , which is defined as [3, 69]:

$$\beta = \frac{1}{v} \left( \frac{\partial v}{\partial T} \right)_p = -\frac{1}{\rho} \left( \frac{\partial \rho}{\partial T} \right)_p \quad (8)$$

The approximate value of this volumetric coefficient is produced by replacing the differential quantity by a difference quantity as in:

$$\beta \approx -\frac{1}{\rho} \frac{\Delta \rho}{\Delta T} = -\frac{1}{\rho} \frac{\rho_{\infty} - \rho}{T_{\infty} - T} \quad (9)$$

Or

$$\rho_{\infty} - \rho = \rho \beta (T - T_{\infty}) \quad (10)$$

Where  $\rho_{\infty}$  and  $T_{\infty}$  are the bulk density and temperature of the fluid respectively, which are measured far away from the surface so, these properties not be affected by local conditions.

The equation of motion of the natural convection flow in the boundary layer for a vertical hot plate can be derived[3]. By assuming that, the flow shown in figure 3.3 is steady and two dimensional and that the fluid is Newtonian (with constant properties except for density) then, the Boussinesq approximation for density can be applied. The basic approach in this approximation is to treat the density as constant in the continuity equation and the inertia term of the momentum equation, but allow it to change with temperature in the gravity term[70]. The temperature and velocity profiles on the vertical plate will be as shown in figure 3.3. The fluid velocity out of the boundary layer is zero as well as at the plate surface, which differs from forced convection, because here the fluid's outer the boundary layer is motionless[3]. The velocity magnitude increases from zero at the plate surface to a maximum value then starts to decrease again to a zero value at a distance far from the plate. The fluid temperature is a maximum value at the plate surface which in turn is equal to the plate temperature this then starts to decrease until it is the same as the surrounding fluid temperature at a certain distance from the plate surface.

Now, consider a differential volume of height  $dx$ , length  $dy$ , and a unit depth in the  $z$  direction, where the forces acting on this volume element are shown in figure 3.4. By applying Newton's second law of motion in the vertical  $x$  direction:

$$F_x = \delta m \cdot a_x \quad (11)$$

Where  $\delta m$  is the mass of the fluid element  $\delta m = \rho(dx \cdot dy \cdot 1)$ . The acceleration in the  $x$  direction will be

$$a_x = \frac{du}{dt} = \frac{\partial u}{\partial x} \frac{dx}{dt} + \frac{\partial u}{\partial y} \frac{dy}{dt} = u \frac{\partial u}{\partial x} + v \frac{\partial u}{\partial y} \quad (12)$$

And the associated force is:

$$F_x = \left( u \frac{\partial u}{\partial x} + v \frac{\partial u}{\partial y} \right) \rho(dx \cdot dy \cdot 1) \quad (13)$$

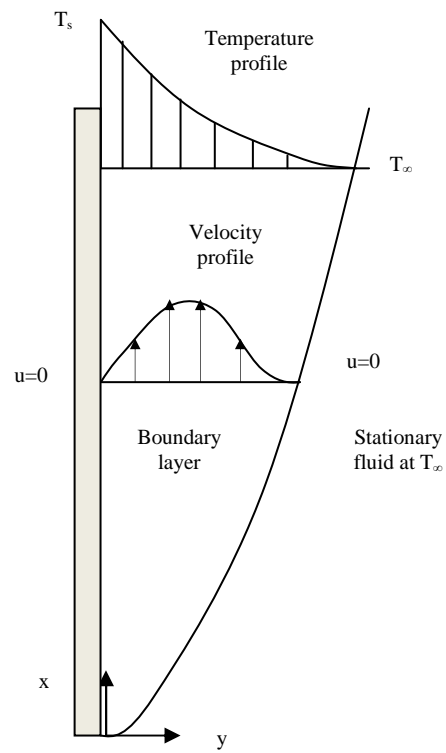


Figure 3.3 Natural convection over a vertical plate with temperature and velocity profiles

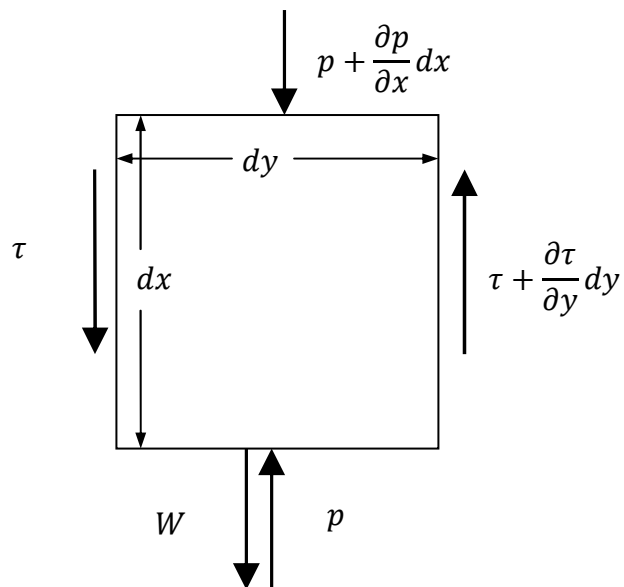


Figure 3.4 Forces acting on a differential volume in natural convection over a vertical plate



The forces acting on the fluid element in the vertical direction are the pressure forces, the shear stresses and the force of gravity. The net forces acting on the element from figure 3.4 will be:

$$\begin{aligned} F_x &= \left( \frac{\partial \tau}{\partial y} dy \right) (dx.1) - \left( \frac{\partial p}{\partial x} dx \right) (dy.1) - \rho g (dx.dy.1) \\ &= \left( \mu \frac{\partial^2 u}{\partial y^2} - \frac{\partial p}{\partial x} - \rho g \right) (dx.dy.1) \end{aligned} \quad (14)$$

From equations 13 and 14 the conservation equation of momentum in the vertical direction

$$\left( u \frac{\partial u}{\partial x} + v \frac{\partial u}{\partial y} \right) \rho (dx.dy.1) = \left( \mu \frac{\partial^2 u}{\partial y^2} - \frac{\partial p}{\partial x} - \rho g \right) (dx.dy.1) \quad (15)$$

Dividing by  $(dx.dy.1)$  gives

$$\rho \left( u \frac{\partial u}{\partial x} + v \frac{\partial u}{\partial y} \right) = \left( \mu \frac{\partial^2 u}{\partial y^2} - \frac{\partial p}{\partial x} - \rho g \right) \quad (16)$$

Equation 16 can be applied to the fluid far from the boundary layer by setting  $u = 0$  to get

$$\frac{\partial p_\infty}{\partial x} = -\rho_\infty g \quad (17)$$

By knowing that  $v \ll u$  in the boundary layer and  $\frac{\partial v}{\partial x} \approx \frac{\partial v}{\partial y} \approx 0$  also assuming that there are no body forces in the  $y$  direction, so the force balance in the  $y$  direction gives,  $\frac{\partial p}{\partial y} = 0$ .

Therefore, the pressure in the boundary layer in the  $x$  direction will be equal to that in the surrounding fluid; from equation 17

$$\frac{\partial p}{\partial x} = \frac{\partial p_\infty}{\partial x} = -\rho_\infty g \quad (18)$$

Subtracting equation 18 from equation 16 gives

$$\rho \left( u \frac{\partial u}{\partial x} + v \frac{\partial u}{\partial y} \right) = \mu \frac{\partial^2 u}{\partial y^2} + (\rho_\infty - \rho)g \quad (19)$$

Substituting equation 10 into equation 19 and dividing both sides by  $\rho$  gives

$$u \frac{\partial u}{\partial x} + v \frac{\partial u}{\partial y} = \nu \frac{\partial^2 u}{\partial y^2} + g\beta(T - T_\infty) \quad (20)$$

This gives equation 20 which is the momentum equation that controls the fluid motion in the boundary layer due to the effect of buoyancy.

### 3.1.3 Dimensional numbers

The governing equations in natural convection are normally non-dimensionlised and the variables are combined together to produce a non-dimensional numbers to reduce the total number of variables.

#### 3.1.3.1 Nusselt number

Consider the heat transfer from a fluid layer of side area  $A$ , a thickness  $L$  and a temperature difference between two sides of  $\Delta T = T_1 - T_2$ . If the fluid is moving, from equation 1 the heat transfer by convection will be as:

$$Q_{conv} = hA(T_1 - T_2) \quad (21)$$

If the fluid is motionless the heat will be transferred by a pure conduction according to this equation:

$$Q_{cond} = \frac{kA(T_1 - T_2)}{L} \quad (22)$$

The two equations can be non-dimensionlised by taking the ratio of the two equations:

$$\frac{Q_{conv}}{Q_{cond}} = \frac{[hA(T_1 - T_2)]}{\left[\frac{kA(T_1 - T_2)}{L}\right]} = \frac{hL}{k} = Nu \quad (23)$$

The dimensionless group produced is called the Nusselt number [71], which represents the number of times that the heat transfer is enhanced by convection relative to that of conduction. That means that the larger the Nusselt number the, more effective the convection heat transfer.

### 3.1.3.2 Grashof number

The governing equations of natural convection heat transfer can be non-dimensionalised using some suitable constant quantities. These constant quantities are [3]:

$$x^* = \frac{x}{L_c}, \quad y^* = \frac{y}{L_c}, \quad u^* = \frac{u}{V}, \quad v^* = \frac{v}{V}, \quad T^* = \frac{T - T_\infty}{T_s - T_\infty}, \quad \text{where } V = \frac{Re_L v}{L}$$

Substituting these into equation 19 gives

$$u^* \frac{\partial u^*}{\partial x^*} + v^* \frac{\partial u^*}{\partial y^*} = \frac{1}{Re_L} \frac{\partial^2 u^*}{\partial y^{*2}} + \left( \frac{g\beta(T_s - T_\infty)L^3}{\vartheta^2} \right) \frac{T^*}{Re_L} \quad (24)$$

Where the dimensionless parameter shown between the brackets is called the Grashof number  $Gr_L$  [71]

$$Gr_L = \frac{g\beta(T_s - T_\infty)L^3}{\vartheta^2} \quad (25)$$

Where the Grashof number is the ratio between the buoyancy force and viscous force and the magnitude of which allows the flow to be considered as laminar or turbulent.

The product of the Grashof number and Prandtl numbers is called the Rayleigh number [72]:

$$Ra_L = Gr_L Pr = \frac{g\beta(T_s - T_\infty)L^3}{\vartheta^2} \cdot Pr \quad (26)$$

Where Prandtl number is

$$Pr = \frac{\mu C_p}{k} = \frac{\nu}{\alpha} \quad (27)$$

The Rayleigh number in natural convection is analogous to the Reynolds number in forced convection and is a measure by which the flow can be calculated as laminar or turbulent. Inside enclosures, the transition from laminar to turbulent flow occurs when the Rayleigh number is greater than one million [2, 6].

## 3.2 Radiation heat transfer

Radiation is the energy emitted by a body in the form of electromagnetic waves. The energy transferred by radiation does not require the presence of an intervening medium such as conduction and convection. The most interested studies in radiation heat transfer is the thermal radiation, which is the form of radiation emitted by bodies because of their temperatures [3]. All bodies emit and absorb electromagnetic waves all the time, by decreasing or increasing their temperatures and the strength of this emission is depending on the temperature of this body [73]. The thermal surface radiation occurs between two or more surfaces at different temperatures, and it becomes extremely important if the temperature difference is high, due to the fourth order dependence of the radiation, which implies that radiation will dominate at high temperature differences.

### 3.2.1 Radiation fundamentals

A surface at an absolute temperature  $T_s$  emits a maximum rate of radiation according to the Stefan-Boltzmann law as [3]

$$\dot{Q}_{rad-max} = \sigma A_s T_s^4 \quad (28)$$

Where  $\sigma = 5.67 \times 10^{-8} \text{ W/m}^2 \cdot \text{K}^4$ , is the Stefan-Boltzmann constant,  $A_s \text{ m}^2$  is the surface area and  $T_s \text{ K}$  is the absolute surface temperature. The surface which emitted

radiation by a maximum rate as in equation 28 is called a black body. All the other surfaces at the same temperature of the black body are emitted radiation less than the black body according to this equation

$$\dot{Q}_{rad} = \varepsilon \sigma A_s T_s^4 \quad (29)$$

Where  $\varepsilon$  is the emissivity of the surface and its value is in the range of  $0 \leq \varepsilon \leq 1$ . The emissivity value for the black body is  $\varepsilon = 1$  and its value is less than one for the other surfaces, which depend on how close that body emittance to the black body.

There is another surface radiation property, the absorptivity  $\alpha$  its value is in the range of  $0 \leq \alpha \leq 1$ . The black body absorptivity value is  $\alpha = 1$  that means it absorb all the incident radiation on it. From Kirchhoff's law the emissivity and the absorptivity of a surface are equal at a given temperature and wavelength. Any surface as shown in figure 3.5 absorbs radiation according to the following equation

$$\dot{Q}_{absorbed} = \alpha \dot{Q}_{incident} \quad (30)$$

Where  $\dot{Q}_{absorbed}$  is the portion of the heat absorbed by the surface and  $\dot{Q}_{incident}$  is the incident heat radiation on this surface. There is a portion of the incident radiation reflected back by the opaque surfaces as shown in figure 3.5.

Calculating the net radiation heat transfer between two surfaces is complicated, because it depends on many parameters such as the properties of the surfaces, their location relative to each other and the interaction of the fluid between the two surfaces with radiation [2]. For example when a surface of emissivity  $\varepsilon$  and surface area  $A_s$  at an absolute temperature  $T_s$  is completely enclosed by a large surface at absolute temperature  $T_{surr}$  separated by a gas that does not intervene with radiation as shown in figure 3.6, in this case the net radiation heat transfer between the two surfaces will be as

$$\dot{Q}_{rad} = \varepsilon \sigma A_s (T_s^4 - T_{surr}^4) \quad (31)$$

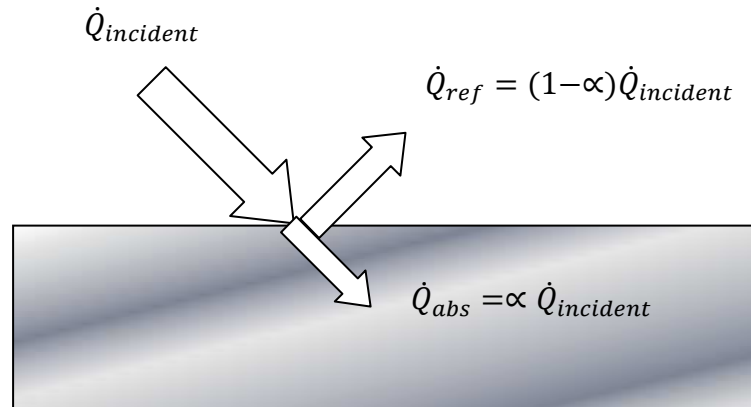


Figure 3.5 Incident, absorbed and reflected heat transfer on a surface of an absorptivity  $\alpha$ .

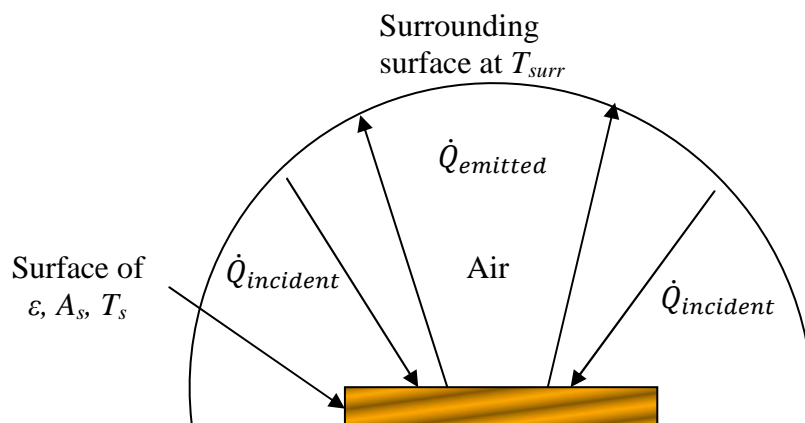


Figure 3.6 Heat transfer between two surfaces one completely surrounding the other.

### 3.2.2 The view factor

Radiation heat transfer between two surfaces depends on the radiation properties of the two surfaces one of these properties is the orientation of the two surfaces relative to each other as shown in figure 3.7. To show the effect of the orientation of the two surfaces relative to each other on the radiation heat transfer between the two surfaces a parameter called the view factor is defined. It is a purely geometric quantity and it is independent of the temperature and the surface properties. The view factor is defined as the fraction of the radiation leaving surface  $i$  to a surface  $j$  that strikes surface  $j$  directly

and is denoted by  $F_{i \rightarrow j}$  or just  $F_{ij}$ . Where  $F_{12}$  represents the fraction of radiation leaving surface one that strikes surface two directly.

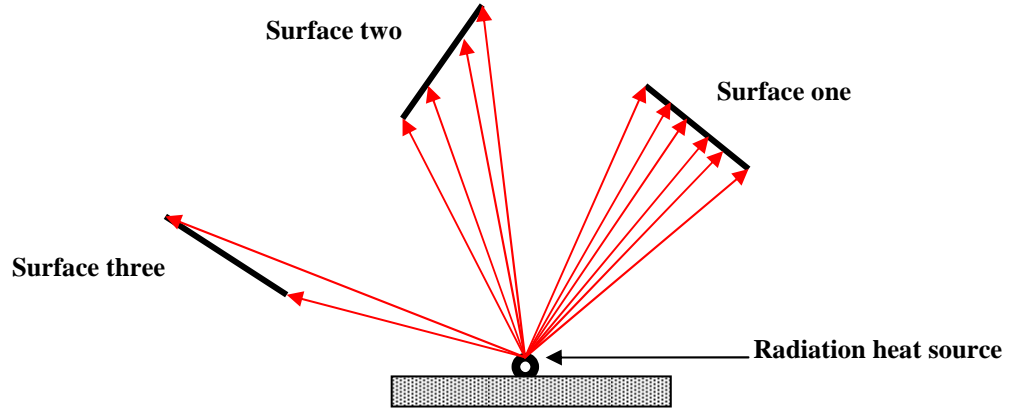


Figure 3.7 Radiation heat transfer depends on orientation between surfaces.

This view factor can be calculated using the following equation

$$F_{12} = F_{A_1 \rightarrow A_2} = \frac{\dot{Q}_{A_1 \rightarrow A_2}}{\dot{Q}_{A_1}} = \frac{1}{A_1} \int_{A_2} \int_{A_1} \frac{\cos \theta_1 \cos \theta_2}{\pi r^2} dA_1 dA_2 \quad (32)$$

Where  $r$  is the distance between  $dA_1$  and  $dA_2$  and  $\theta_1$  and  $\theta_2$  are the angles between the normals of the two surfaces and the line connects  $dA_1$  and  $dA_2$  respectively.

There are some rules controlling the relation between view factors:

- The reciprocity rule  $A_i F_{i \rightarrow j} = A_j F_{j \rightarrow i}$  (33)

- The summation rule  $\sum_{j=1}^N F_{i \rightarrow j} = 1$  (34)

- The superposition rule  $F_{1 \rightarrow (2,3)} = F_{1 \rightarrow 2} + F_{1 \rightarrow 3}$  (35)

- The symmetry rule (if surfaces  $j$  and  $k$  are symmetric about the surface  $i$  then)

$$F_{i \rightarrow j} = F_{i \rightarrow k} \quad (36)$$

The radiation heat transfer between two surfaces forming an enclosure can be calculated using this equation

$$\dot{Q}_{12} = \frac{\sigma(T_1^4 - T_2^4)}{R_1 + R_{12} + R_2} = \frac{\sigma(T_1^4 - T_2^4)}{\frac{1-\varepsilon_1}{A_1\varepsilon_1} + \frac{1}{A_1F_{12}} + \frac{1-\varepsilon_2}{A_2\varepsilon_2}} \quad (37)$$

Where the term  $R_i = \frac{1-\varepsilon_i}{A_i\varepsilon_i}$  is the surface resistance to radiation and  $R_{ij} = \frac{1}{A_iF_{ij}}$  is the space resistance to radiation.



# **CHAPTER 4**

## **DIMENSIONAL ANALYSIS OF HEAT TRANSFER IN CAVITIES**

### **4.1 Introduction**

The dimensions of any physical quantities can be manipulated algebraically and the results can be used to provide useful information for the physical processes considered. This study is the so-called dimensional analysis [74]. Others define dimensional analysis as a process for eliminating extraneous information from a relation between different physical quantities [75]. Palmer [76], defines it as a technique that can be used to represent and elucidate relationships between physical quantities. There are two basic approaches to establish the dimensionless relations that characterize the behaviour of a system [77]. The first approach is to study the general equations that control the behaviour of the system. The second approach is to study the specific equations that control the behaviour of the system.

For any equation to meaningfully express properties of a physical system, this equation must have numerical equality and dimensional homogeneity between its two sides [78]. Dimensional analysis is concerned only with the nature of the properties involved in the situation and not on their numerical values, particularly where the numerical value of the dimensional quantity is a dependant on the system of units used for its measurement [79]. This study focuses on the dimensional analysis of two cases of natural convection, pure natural convection and natural convection with interaction of surface thermal radiation. Both problems are analysed and correlation equations for both cases provided. The analyses use two methods to find the dimensional correlation equations that control the heat transfer inside enclosures, as shown in figure 4.1. The first method is through the use of dimensional methods to get the final correlation equations, while the second method starts from the governing equations. It should be

noted that the same groups can be found using both dimensional analysis techniques, though the second method is far more rigorous.

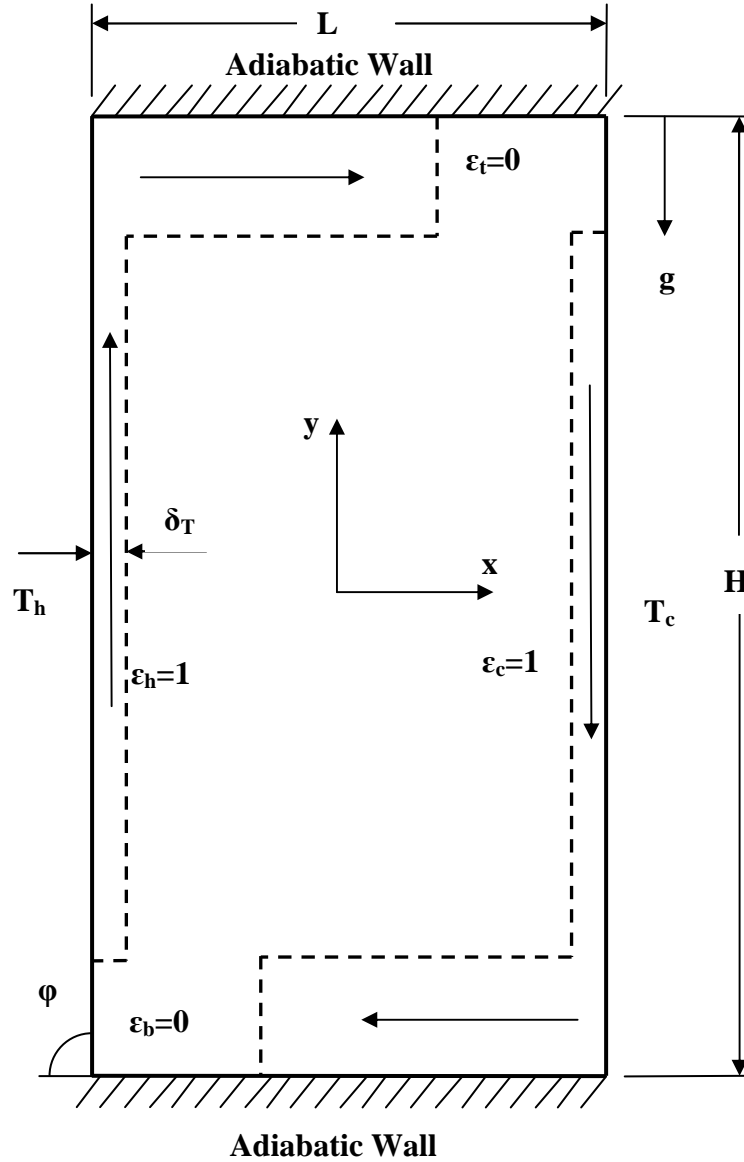


Figure 4.1 Two-dimensional rectangular enclosure with isothermal side walls.

## 4.2 Producing dimensionless correlation equations

The dimensional analysis correlation equations for both square and rectangular enclosures will be produced in this section using two analysis methods and for two cases pure natural convection and natural convection with radiation. The first method starts using the produced dimensional analysis of the energy equation by Johnstone and

Thring[64]. The second method starts from the governing equations for square and rectangular enclosures.

#### 4.2.1 First analysis method

Using dimensional analysis of the energy equation, Johnstone and Thring[64], found that, for the process of heat transfer by pure natural convection they could derive the following equation

$$\frac{H}{KL\Delta T} = \phi \left( \frac{\beta g \Delta T L^3 \rho^2}{\mu^2}, \frac{\mu C_p}{K} \right) (1)$$

The same equation has been derived by Ipsen[77], for the case of pure natural convection, which states  $Nu$  number in terms of  $Gr$  and  $Pr$  numbers.

They [64] also have found that the dimensional analysis for the case of pure radiation led to this equation

$$\frac{H}{\sigma \epsilon L^2 T^4} = \phi \left( \frac{T_1}{T_2} \right) (2)$$

Which is the heat transfer ratio in terms of the absolute temperature ratio.

Then for the case under consideration, which includes both natural convection and radiation heat transfer, the two previous equations 1 and 2 can be coupled together to form the following new dimensionless equation

$$\frac{H}{\sigma \epsilon L^2 T^4} = \phi \left( \frac{H}{KL\Delta T}, \frac{\beta g \Delta T L^3 \rho^2}{\mu^2}, \frac{\mu C_p}{K}, \frac{T_h}{T_c} \right) (3)$$

Which is, heat transfer ratio in terms of Nusselt number, Grashof number, Prandtl number and absolute temperature ratio.

As mentioned in their book Johnstone and Thring found that [64], the rate of heat transfer in terms of heat transfer coefficient was given as

$$H = hL^2\Delta T \quad (4)$$

Substituting equation 4 into equation 3 gives

$$\frac{hL^2\Delta T}{\sigma\epsilon L^2T^4} = \frac{Q_{conv}}{Q_{rad}} = \frac{h}{\sigma\epsilon T^3} = \phi\left(\frac{hL}{K}, \frac{\beta g\Delta TL^3\rho^2}{\mu^2}, \frac{\mu C_p}{K}, \frac{T_h}{T_c}\right) \quad (5)$$

Where this equation is the heat transfer ratio between convection and radiation (new dimensional group) as a function of Nusselt, Grashof and Prandtl numbers and temperature ratio.

#### 4.2.2 Second analysis method for square enclosure

The governing equations for the mass, momentum and energy conservation within the enclosure (as shown in figure 4.1) can be described as in equations 6, 7, 8 and 9 below.

##### Continuity equation

The continuity equation is a differential equation that describes the conservation of mass. The general form of the continuity equation for a two dimensional turbulent flow is:

$$\frac{\partial(\rho)}{\partial t} + \frac{\partial(\rho u)}{\partial x} + \frac{\partial(\rho v)}{\partial y} = 0 \quad (6)$$

Where  $\rho$  is the fluid density,  $t$  is the time,  $u$  is the x velocity and  $v$  is the y velocity components.

##### Momentum equations

From Newton's second law the rate of change of momentum of a fluid particle equals to the sum of the forces on the particle. The general form of the momentum equation in the x and y coordinates for a turbulent flow is:

##### x-component of the momentum equation

$$\frac{\partial(\rho u)}{\partial t} + \frac{\partial(\rho uu)}{\partial x} + \frac{\partial(\rho uv)}{\partial y} = -\frac{\partial p}{\partial x} + \frac{\partial}{\partial y}\left[\mu\left(\frac{\partial u}{\partial y} + \frac{\partial v}{\partial x}\right)\right] \quad (7)$$

Where  $p$  is the static pressure and  $\mu$  is the viscosity.

### y-component of the momentum equation

$$\frac{\partial(\rho v)}{\partial t} + \frac{\partial(\rho uv)}{\partial x} + \frac{\partial(\rho vv)}{\partial y} = -\frac{\partial p}{\partial y} + \frac{\partial}{\partial x} \left[ \mu \left( \frac{\partial v}{\partial x} + \frac{\partial u}{\partial y} \right) \right] + \rho \beta g (T - T_o) \quad (8)$$

Where  $\rho \beta g (T - T_o)$  is the Boussinesq approximation for buoyancy,  $\beta$  is the thermal expansion coefficient and  $g$  is the gravitational acceleration.

### Energy equation

The energy equation in the case of heat transfer in a two dimensional coordinate is:

$$\frac{\partial(\rho C_p T)}{\partial t} + \frac{\partial(\rho u C_p T)}{\partial x} + \frac{\partial(\rho v C_p T)}{\partial y} = \frac{\partial}{\partial x} \left[ k \frac{\partial T}{\partial x} \right] + \frac{\partial}{\partial y} \left[ k \frac{\partial T}{\partial y} \right] \quad (9)$$

By multiplying equation 7 by  $\frac{\partial}{\partial y}$  and equation 8 by  $\frac{\partial}{\partial x}$  then the pressure terms can be eliminated and the momentum equations combined to produce a single momentum equation:

$$\begin{aligned} \frac{\partial}{\partial x} \left( \frac{\partial v}{\partial t} + u \frac{\partial v}{\partial x} + v \frac{\partial v}{\partial y} \right) - \frac{\partial}{\partial y} \left( \frac{\partial u}{\partial t} + u \frac{\partial u}{\partial x} + v \frac{\partial u}{\partial y} \right) \\ = \vartheta \left[ \frac{\partial}{\partial x} \left( \frac{\partial^2 v}{\partial x^2} + \frac{\partial^2 v}{\partial y^2} \right) - \frac{\partial}{\partial y} \left( \frac{\partial^2 u}{\partial x^2} + \frac{\partial^2 u}{\partial y^2} \right) \right] + g \beta \frac{\partial T}{\partial x} \end{aligned} \quad (10)$$

Which contains three momentum groups that control the flow of air in the enclosure; these groups are, from left: inertia, viscous friction, and buoyancy.

Based on Fourier's law, the heat transfer balance at the boundary can be defined as:

$$-k \frac{\partial T}{\partial x} \Big|_{wall1} = -k \frac{\partial T}{\partial x} \Big|_{wall2} = h(T_{wall1} - T_{wall2}) + f_{(L,\varepsilon)} \sigma (T_{wall1}^4 - T_{wall2}^4) \quad (11)$$

Where  $f_{(L,\varepsilon)}$  is a function of the geometry and separation of the walls and their emissivities,  $\sigma$  is the Stephan-Boltzmann constant.

The above equations of motion can be simplified with dimensional analysis. Patterson and Imberge[17], proposed that the energy equation can be converted to dimensionless groups at a time just after  $t = 0$  when the fluid beside each wall is motionless ( $u = v =$

0) and the thermal boundary layer thickness,  $\delta_T$  is much smaller than the enclosure height so that:

$$\frac{\partial^2 T}{\partial y^2} \ll \frac{\partial^2 T}{\partial x^2}$$

Therefore the energy equation 9 can be simplified to:

$$\frac{\partial T}{\partial t} = \alpha \left( \frac{\partial^2 T}{\partial x^2} \right) \quad (12)$$

Or

$$\frac{\Delta T}{t} \propto \alpha \frac{\Delta T}{\delta_T^2}$$

This equation indicates that following  $t = 0$  the thermal boundary layer increases proportionally to:

$$\delta_T \sim (\alpha t)^{1/2} \quad (13)$$

Referring to equation 10, Bejan[19] argues that by assuming  $u \ll v$  the initial vertical velocity scale will be as:

$$v \approx \frac{g\beta\Delta T\alpha t}{\vartheta} \quad (14)$$

As time passes, a steady state situation occurs, where the flow is dominated by buoyancy effects. There will be a time,  $t = t_f$  when the boundary layer reaches its maximum thickness and an energy balance occurs between heat conducted from the wall and the heat carried away by the buoyancy. From the energy equation 9, it is possible to define this time as:

$$t_f = \left( \frac{\vartheta H}{g\beta\Delta T\alpha} \right)^{1/2} \quad (15)$$

The governing equations can be non-dimensionalised using the following scale groups from [19], with the exception of  $\theta$ , where the hot and cold wall temperatures are used:

$$X = \frac{x}{\delta_T}, \quad Y = \frac{y}{H}, \quad \theta = \frac{T_h(T - T_c)}{T_c(T_h - T_c)}, \quad U = \frac{u}{(\delta_T/H)v_f} \text{ and } V = \frac{v}{v_f}$$

The resulting non-dimensionless governing equations are as [19]:

$$\frac{\partial U}{\partial X} + \frac{\partial V}{\partial Y} = 0 \quad (16)$$

$$\begin{aligned} & \frac{1}{Pr} \left[ \frac{\partial}{\partial X} \left( U \frac{\partial V}{\partial X} + V \frac{\partial V}{\partial Y} \right) - Gr^{-\frac{1}{2}} Pr^{-\frac{1}{2}} \frac{\partial}{\partial Y} \left( U \frac{\partial U}{\partial X} + V \frac{\partial U}{\partial Y} \right) \right] \\ &= \frac{\partial}{\partial X} \left( \frac{\partial^2 V}{\partial X^2} + Gr^{-\frac{1}{2}} Pr^{-\frac{1}{2}} \frac{\partial^2 V}{\partial Y^2} \right) - Gr^{-\frac{1}{2}} Pr^{-\frac{1}{2}} \frac{\partial}{\partial Y} \left( \frac{\partial^2 U}{\partial X^2} + Gr^{-\frac{1}{2}} Pr^{-\frac{1}{2}} \frac{\partial^2 U}{\partial Y^2} \right) \\ & \quad + T_r^{-1} \frac{\partial \theta}{\partial X} \end{aligned} \quad (17)$$

$$U \frac{\partial \theta}{\partial X} + V \frac{\partial \theta}{\partial Y} = \frac{\partial^2 \theta}{\partial X^2} + Gr^{-\frac{1}{2}} Pr^{-\frac{1}{2}} \frac{\partial^2 \theta}{\partial Y^2} \quad (18)$$

And from the heat transfer at the boundary shown in equation 11:

$$-\frac{\partial \theta}{\partial X} \Big|_{wall} = \left( \frac{\delta_T}{H} \right) \left( \frac{T_h}{T_c} \right) [Nu_c + Nu_r] \quad (19)$$

Where  $Nu_c$  is the convection Nusselt number:

$$Nu_c = \frac{hH}{k} \quad (20)$$

And  $Nu_r$  is the Radiation equivalent Nusselt number:

$$Nu_r = \frac{f_{(L,\varepsilon)} \sigma H (T_h^4 - T_c^4)}{k(T_h - T_c)} \quad (21)$$

The two numbers of Nusselt numbers could be combined into a new dimensionless group  $RC_n$ , which is the ratio of convection heat transfer to surface radiation:

$$RC_n = \frac{Nu_c}{Nu_r} = \frac{Q_{conv}}{Q_{rad}} = \frac{h(T_h - T_c)}{f_{(L,\varepsilon)} \sigma (T_h^4 - T_c^4)} = Nu_c Pl \quad (22)$$

From equation 19 the total Nusselt number is

$$Nu_t = Nu_c + Nu_r \quad (23)$$

Which is the total Nusselt number as a function of convection Nusselt number and radiation equivalent Nusselt number.

### 4.2.3 Second analysis method for rectangular enclosure

This analysis focuses on the effect of aspect ratio on the dimensional analysis for two cases of natural convection, pure natural convection and natural convection with radiation interaction.

From the mathematical model described above the governing equations from 6 to 9 can be non-dimensionalised using the following scale groups:

$$X = \frac{x}{\delta_T}, \quad Y = \frac{y}{H}, \quad \theta = \frac{(H/L)T_h(T - T_c)}{T_c(T_h - T_c)}, \quad U = \frac{u}{(\delta_T/H)v_f} \text{ and } V = \frac{v}{v_f}$$

The resulting non-dimensional governing equations are as:

$$\frac{\partial U}{\partial X} + \frac{\partial V}{\partial Y} = 0 \quad (24)$$

$$\begin{aligned} \frac{1}{Pr} \left[ \frac{\partial}{\partial X} \left( U \frac{\partial V}{\partial X} + V \frac{\partial V}{\partial Y} \right) - Gr^{-\frac{1}{2}} Pr^{-\frac{1}{2}} \frac{\partial}{\partial Y} \left( U \frac{\partial U}{\partial X} + V \frac{\partial U}{\partial Y} \right) \right] = \\ \frac{\partial}{\partial X} \left( \frac{\partial^2 V}{\partial X^2} + Gr^{-\frac{1}{2}} Pr^{-\frac{1}{2}} \frac{\partial^2 V}{\partial Y^2} \right) - Gr^{-\frac{1}{2}} Pr^{-\frac{1}{2}} \frac{\partial}{\partial X} \left( \frac{\partial^2 U}{\partial X^2} + Gr^{-\frac{1}{2}} Pr^{-\frac{1}{2}} \frac{\partial^2 U}{\partial Y^2} \right) \\ + AR^{-1} T_r^{-1} \frac{\partial \theta}{\partial X} \end{aligned} \quad (25)$$

$$U \frac{\partial \theta}{\partial X} + V \frac{\partial \theta}{\partial Y} = \frac{\partial^2 \theta}{\partial X^2} + Gr^{-\frac{1}{2}} Pr^{-\frac{1}{2}} \frac{\partial^2 \theta}{\partial Y^2} \quad (26)$$

And at the boundary:

$$-\frac{\partial \theta}{\partial X} \Big|_{wall} = \frac{\delta_T T_h}{H T_c} (Nu_c + Nu_r) \quad (27)$$



Where  $Nu_c$  is the modified convection Nusselt number:

$$Nu_c = \frac{hL}{K} * AR \quad (28)$$

And  $Nu_r$  is again the modified radiation equivalent Nusselt number:

$$Nu_r = \frac{f_{(L,\epsilon)} \sigma H (T_h^4 - T_c^4)}{k(T_h - T_c)} * AR \quad (29)$$

Where AR is the aspect ratio

$$AR = \frac{H}{L} \quad (30)$$

The ratio of the two Nusselt numbers from equations (28) and (29) can be combined into a new dimensionless group  $RC_n$ , as before:

$$RC_n = \frac{Nu_c}{Nu_r} = \frac{Q_{conv}}{Q_{rad}} = \frac{h(T_h - T_c)}{f_{(L,\epsilon)} \sigma (T_h^4 - T_c^4)} = Nu_c Pl \quad (31)$$

### 4.3 Producing the new dimensionless group from the provided dimensionless equations

#### 4.3.1 For square enclosures

Thus dimensionless groups defined from the two sections 4.2.1 and 4.2.2 above can be combined into the following generalised dimensionless equation:

$$Nu_t = \varphi(RC_n, Gr, Pr, T_r) \quad (32)$$

And

$$RC_n = \varphi(Nu_t, Gr, Pr, T_r) \quad (33)$$

Where  $RC_n$  is the heat transfer ratio in terms of total Nusselt number, Grashof number, Prandtl number and absolute absolute temperature ratio (the new dimensionless group).

Equation 32 can be compared to Johnstone and Thring's[64] dimensionless equation for a general heat transfer problem involving radiation, convection and conduction using the Thring number,  $(Th = \frac{\rho c_p v}{\sigma \epsilon T^3})$ :

$$Nu = \varphi(Re, Gr, Pr, Th, T_r) \quad (34)$$

For the case of natural convection without radiation interaction; by setting  $Nu_r$  to zero from equation 23 and hence omitting  $RC_n$  from equation 32 it gives:

$$Nu_c = \varphi(Gr, Pr, T_r) \quad (35)$$

Which is the convection Nusselt number as a function of Grashof number, Prandtl number and temperature ratio.

The same sort of result can be provided using the Pi theorem for the case of pure natural convection heat transfer. This analysis has been shown in appendix A.

Even though, many correlation equations have been provided in the literature using Nusselt number as a function of Grashof and Prandtl numbers without the temperature ratio. In our wide range of parameters used it was found to be impossible to collapse all the results curves together without using the temperature ratio. This will be shown in chapter 5 when the ratio of  $Ra^{1/3}/Nu$  compared for the different parameters as a function of the temperature ratio figure 5.12. It is appreciated that providing all other parameters remain the same, the heat transfer rate will be a function of the temperature difference, not the temperature ratio.

### 4.3.2 For rectangular enclosures

The dimensionless groups of this problem as discussed in section 4.2.3 above can be related in the following generalised dimensionless equation:

$$Nu_t = \varphi(RC_n, Gr, Pr, T_r, AR) \quad (36)$$

And

$$RC_n = \varphi(Nu_t, Gr, Pr, T_r, AR) \quad (37)$$

Where  $RC_n$  is the heat transfer ratio in terms of total Nusselt number, Grashof number, Prandtl number, absolute absolute temperature ratio and the aspect ratio (the new dimensionless group).

For the case of natural convection without radiation interaction; by omitting  $Nu_r$  from Eq. (23) and  $RC_n$  from Eq. (37) it gives:

$$Nu_c = \phi(Gr, Pr, T_r, AR) \quad (38)$$

Which is the convection Nusselt number as a function of Grashof number, Prandtl number, absolute absolute temperature ratio and aspect ratio.

From equation 23 the total Nusselt number for the case of natural convection with radiation interaction, can be defined as

$$Nu_t = \phi(Nu_c, Nu_r) \quad (39)$$

Note that, here the Nusselt numbers, for both convection and radiation, are needed. The correlation equation for the total Nusselt number for natural convection with radiation interaction in a rectangular enclosure can be found by comparing equations 38 and 39 and also using the definition of Planck number as given below:

$$Pl = \frac{Q_{cond}}{Q_{rad}} \quad (40)$$

From the definition of the equivalent radiation Nusselt number equation 29 and Planck number equation 40 gives:

$$Nu_r = Pl^{-1} \quad (41)$$

Where  $Nu_r$  is the radiation equivalent Nusselt number and  $Pl$  is the Planck number.

From equations 38, 39 and 41 the dimensionless groups which control the total Nusselt number in a rectangular enclosure is:

$$Nu_t = \phi(Gr, Pr, Pl, T_r, AR) \quad (42)$$

For the case of a square enclosure, from equation 42, by putting the aspect ratio equal to unity equation 42 will be:

$$Nu_t = \emptyset(Gr, Pr, Pl, T_r) \quad (43)$$

## 4.4 Summary and discussion

A review and explanation of the dimensional analysis and the relations to provide the correlation equations are established in this chapter. The analysis method to provide the dimensional relations which will be used to produce the correlation equations for square and rectangular enclosures is provided in this chapter. Using these relations the correlation equations for the new dimensionless group, which is the ratio between natural convection to radiation heat transfer, will be provided for both square and rectangular enclosures in the next chapters. Also using these relations from the dimensional analysis the correlation equations for pure natural convection, which is the average Nusselt number, will be provided for square and rectangular enclosures. For the case of natural convection with radiation interaction, the correlation equations for the total Nusselt number will be provided for both square and rectangular enclosure using these dimensional relations along with the numerical results in the next chapters.

# CHAPTER 5

## TURBULENCE MODELLING AND NUMERICAL RESULTS

### 5.1 Introduction

The flow regime defined as a Laminar flow when the flow is smooth and the adjacent layers of the fluid move past each other in a systematic manner [80]. Douglas [81], defines laminar flow as a flow in which the fluid particles move in a systematic way and retain the same relative positions in sequential cross sections. In laminar flow there is no macroscopic mixing of adjacent fluid layers, where a thin string of ink injected into a laminar flow appears as a single line [82]; as seen in figure 5.1a. For example in the laminar flow in pipes the fluid moves in parallel layers and the velocity profile is parabolic for a Newtonian fluid [83, 84]; as shown in figure 5.2a. Laminar flow is smooth and steady and its theory is well developed and many solutions are known [85-87].

In 1883 Osborne Reynolds, a British engineering professor, showed that transition from laminar to turbulent flow can be visualized experimentally, and he defined these two types of flow which are known as Laminar and Turbulent. Which of these occurs depends on the dimensionless parameter  $\rho Vd/\mu$ , which called the Reynolds number. In circular pipes running full transition occur at  $Re \approx 2300$ , while between two parallel plates when  $Re \approx 2000$ [85].

Turbulent flows occur in many processes in nature as well as in many industrial applications. There are many important and interesting physical phenomena connected with turbulent flows including those of the large flow structures (very large eddies) and very small flow structures (very small eddies) [88]. When the flow motion becomes substantially unsteady even, with constant boundary conditions, and the velocity and all other flow properties change with time, it is known as turbulent flow [89]; as can be seen in figures 5.1b and 5.2b. Turbulent flows are irregular, diffusive, rotational, dissipative and occur at high Reynolds numbers [90]. Among the important

characteristics of turbulent flows are their abilities to transport and mix fluids more effectively than laminar flows, and also that the fluid velocity field varies significantly and irregularly in both position and time [91].

Turbulence is a property of the flow, not the fluid, where the flow originally is laminar, then the turbulence regime comes from the instabilities that develop as the Reynolds number increases [92]. Lesieur[93], defines turbulent flow as a flow which is disordered in time and space and able to mix transport quantities. Scientists, engineers and applied mathematicians have developed analytical methods (models) to predict the flow fields of practical devices, these models can be solved in computational fluid dynamics codes [94]. Turbulent flows are known by the movement of the velocity fields. This movement causes the transport parameters to fluctuate.

As mentioned before in chapter one, for the flow inside cavities, the natural convection flow in an enclosed space can be dominated by the buoyancy forces. The strength of the buoyant flow can be measured using the Rayleigh number, which is the ratio of buoyancy forces and the viscous forces acting on a fluid ( $R_a = g\beta\Delta TL^3/\nu\alpha$ ). The value of the Rayleigh number can indicate whether the flow can be considered as laminar or turbulent [2]. The Rayleigh number is the product of Grashof and Prandtl numbers. It plays the same role in natural convection that the Reynolds number plays in forced fluid flow. Also as mentioned in chapter two, inside square and rectangular enclosures transition from laminar to turbulent flow occurs when the Rayleigh number is greater than one million [2, 95].

## 5.2 Turbulence models

The fluctuation of momentum and energy is computationally expensive to be directly simulated. Therefore, the governing equations can be time averaged to produce a set of modified equations containing additional unknown variables that need to be solved using the turbulence models. This process is known as the Reynolds Averaging Navier-Stokes equations (RANS). In this process the turbulent averaging is introduced to obtain the laws of motion for the mean turbulent quantities [96]. For example the turbulent velocity as shown in figure 5.1b can be defined as the following equation [97, 98]:

$$u = \bar{u} + u' \tag{1}$$

Where  $u$  is the x component velocity,  $u'$  is the fluctuating velocity and  $\bar{u}$  is the mean velocity which can be defined as the following equation:

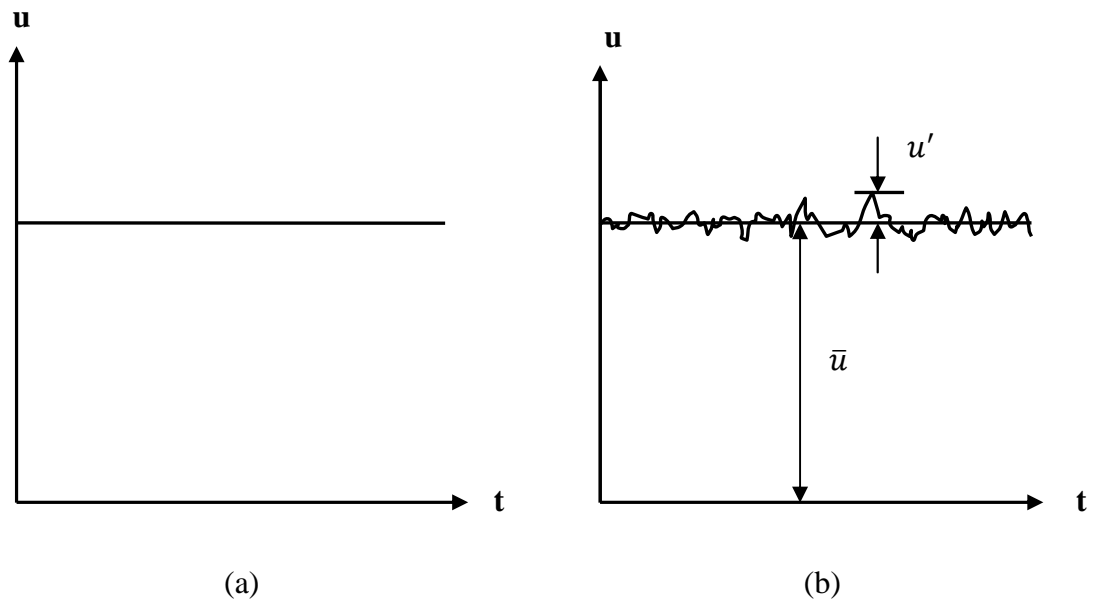


Figure 5.1 Velocity at point x a)- Laminar flow and b)- Turbulent flow

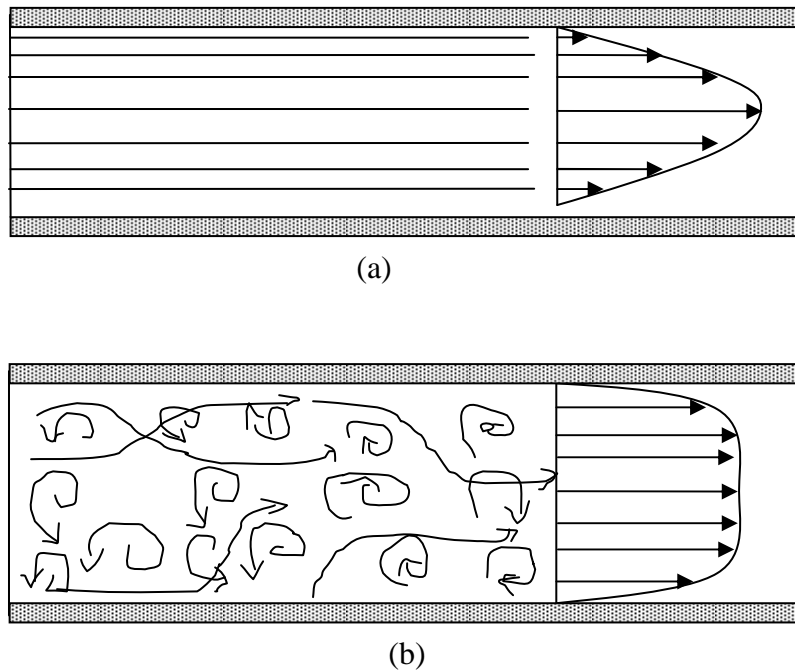


Figure 5.2 Velocity profiles a)- Laminar flow and b)- Turbulent flow

$$\bar{u} = \frac{1}{\Delta T} \int_{t_o}^{t_o + \Delta T} u' dt \quad (2)$$

Where  $t_o$  is the starting time and  $\Delta T$  is the interval time of change.

Substituting these equations into the instantaneous continuity and momentum equations producing additional terms represent the effect of turbulence. These additional terms called Reynolds stress ( $-\rho_i \bar{u}_i' \bar{u}_j'$ ), these terms must be modelled to close the problem.

The Boussinesq approach is used to model the Reynolds stresses related to mean velocity gradients as

$$\text{Reynolds Stresses} = -\rho_i \bar{u}_i' \bar{u}_j' = \mu_t \left( \frac{\partial u_i}{\partial x_j} + \frac{\partial u_j}{\partial x_i} \right) \quad (3)$$

This approach is used in many turbulent models including the RNGk- $\epsilon$  model which used in the present study.

The numerical solution starts from dividing the domain into sub-volumes called cells and for which algebraic equations are written which derived from the exact partial differential equations. Then these algebraic equations are solved for the values of the dependent variables at a discrete number of positions in the domain (the cell centre positions). This process of changing the partial differential equations to algebraic equations is called discretisation.

One process of replacing the exact unsolvable equations by approximate solvable equations is called modelling [99]. The main task of turbulent modelling is to develop computational procedures to predict the extra Reynolds stresses results from the time averaging of the transport equations [89]. There is no single turbulence model that can be used for all different classes of problems and that selected will depend on the physics of the flow. Therefore to solve the turbulent fluid flow and heat transfer problems, using the Fluent CFD software package, it is necessary to use and choose a suitable turbulent model.



## **5.3 The RNG k- $\epsilon$ turbulent model and the free convection in cavity**

The system that was solved in this research is shown schematically in Figure 5.3. This is the two dimensional flow of an ideal gas in a rectangular enclosure of height  $H$  and length  $L$ . The two vertical hot and cold walls are heated isothermally and the other two (horizontal) walls are adiabatic. To simplify the problem and focus on the heat transfer between the hot and cold walls the adiabatic wall surfaces are taken to have a zero emissivity, which is similar to a highly shiny, insulated surface. The turbulent flow in the enclosure is analysed using the commercial code (FLUENT 6.3) and by using the RNG k- $\epsilon$  model with the Boussinesq approximation for the density [55].

The RNG k- $\epsilon$  model was derived using a rigorous statistical method (called renormalization group theory) [55, 80]. It involves improvement of the accuracy of the k- $\epsilon$  model for rapidly strained flows by adding another term to the  $\epsilon$  equation, and enhancing its accuracy in swirling flows by including the effect of swirl on turbulence. It also accounts for low-Reynolds numbers effects by providing an analytical differential formula for effective viscosity, which depends on an appropriate treatment of the near wall region [55]. These features make the RNG k- $\epsilon$  model more accurate and reliable for a wider class of fully enclosed airflows than the standard k- $\epsilon$  model. Also as it has been shown in chapter two that many researchers [56, 59-62] compared up to eight turbulent models for a wider class of a fully enclosed airflows; they found that the RNG k- $\epsilon$  turbulent model gives better and more acceptable results compared to the other turbulent models.

For these reasons the RNG k- $\epsilon$  model was chosen for the work described in this thesis.

### **5.3.1 Mathematical model**

#### **5.3.1.1 Governing equations**

For the case of flow with heat transfer, FLUENT solves conservation equations for mass, momentum and energy equations. Also, the additional transport equations for the case of turbulent flow are involved in the solution, which is turbulent kinetic energy and turbulent dissipation equations. In this case, which is the turbulent heat transfer inside a

cavity, the equations used by the RNG k- $\epsilon$  model in the steady two dimensional Cartesian coordinates [55, 89, 100] are given as below:

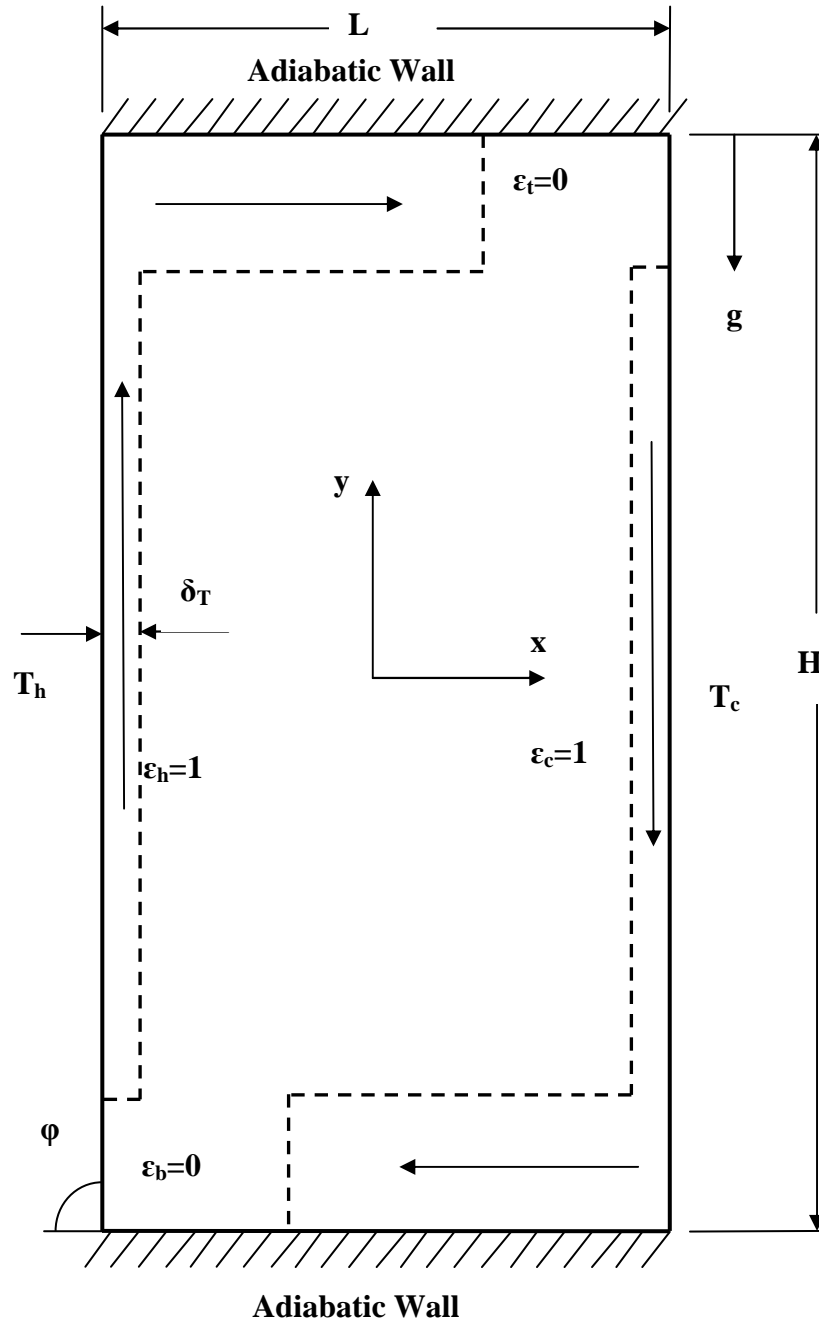


Figure 5.3 Schematic diagram of the rectangular enclosure

### Continuity equation

The continuity equation is a differential equation that describes the conservation of mass. The general form of the continuity equation for a steady two dimensional turbulent flow is:

$$\frac{\partial(\rho u)}{\partial x} + \frac{\partial(\rho v)}{\partial y} = 0 \quad (3)$$

Where  $\rho$  is the fluid density,  $u$  is the x velocity and  $v$  is y velocity components.

### Momentum equations

From Newton's second law the rate of change of momentum of a fluid particle equals to the sum of the forces on the particle. In the case considered here, the general form of the momentum equation in the x and y coordinates for a turbulent flow is:

#### x-component of the momentum equation

$$\frac{\partial(\rho uu)}{\partial x} + \frac{\partial(\rho uv)}{\partial y} = -\frac{\partial p}{\partial x} + \frac{\partial}{\partial y} \left[ \mu_{eff} \left( \frac{\partial u}{\partial y} + \frac{\partial v}{\partial x} \right) \right] + \frac{\partial}{\partial x} \left[ 2\mu_{eff} \frac{\partial u}{\partial x} \right] \quad (4)$$

Where  $p$  is the static pressure and  $\mu_{eff}$  is the turbulent viscosity.

#### y-component of the momentum equation

$$\begin{aligned} \frac{\partial(\rho uv)}{\partial x} + \frac{\partial(\rho vv)}{\partial y} = & -\frac{\partial p}{\partial y} + \frac{\partial}{\partial x} \left[ \mu_{eff} \left( \frac{\partial v}{\partial x} + \frac{\partial u}{\partial y} \right) \right] + \frac{\partial}{\partial y} \left[ 2\mu_{eff} \frac{\partial v}{\partial y} \right] \\ & + \rho\beta g(T - T_o) \end{aligned} \quad (5)$$

Where  $\rho\beta g(T - T_o)$  is the Boussinesq approximation for buoyancy,  $\beta$  is the thermal expansion coefficient and  $g$  is the gravitational acceleration.

### Energy equation

From the first law of thermodynamics the rate of change of energy of a fluid particle is equal to the rate of heat addition to the fluid particle plus the rate of work done on the particle; from this the energy equation can be derived. In the case of turbulent heat transfer in a two dimensional cavity the energy equation is:

$$\frac{\partial(\rho u C_p T)}{\partial x} + \frac{\partial(\rho v C_p T)}{\partial y} = \frac{\partial}{\partial x} \left[ K_{eff} \frac{\partial T}{\partial x} \right] + \frac{\partial}{\partial y} \left[ K_{eff} \frac{\partial T}{\partial y} \right] + S_h \quad (6)$$

Where  $C_p$  is the specific heat,  $T$  is the temperature and  $K_{eff}$  is the effective conductivity and it equal to  $(K + K_t)$  where  $K_t$  is the turbulent thermal conductivity.

By omitting the species diffusion and viscous dissipation terms, where the species diffusion is omitted because there is no combustion in this case and the viscous dissipation is neglected as no diffusion occurs and it depends on the value of Brinkman number

Viscous heating can be neglected if the Brinkman number, Br is less than unity.

$$Br = \frac{\mu U^2}{K \Delta T} \quad (7)$$

$S_h$  in this case represents the radiation source terms, which will be discussed later.

### Turbulent kinetic energy equation

The derived transport equations of the RNG k- $\epsilon$  model for the turbulent kinetic energy ( $k$ ) and its dissipation rate ( $\epsilon$ ) are:

$$\frac{\partial(\rho k u)}{\partial x} + \frac{\partial(\rho k v)}{\partial y} = \frac{\partial}{\partial x} \left[ (\alpha_k \mu_{eff}) \frac{\partial k}{\partial x} \right] + \frac{\partial}{\partial y} \left[ (\alpha_k \mu_{eff}) \frac{\partial k}{\partial y} \right] + G_k + G_b - \rho \epsilon \quad (8)$$

### Dissipation rate equation

The kinetic energy of turbulent motion is dissipated into heat under the influence of viscosity [97]. The dissipation rate ( $\epsilon$ ) of the turbulent kinetic energy ( $k$ ) is:

$$\begin{aligned} \frac{\partial(\rho \epsilon u)}{\partial x} + \frac{\partial(\rho \epsilon v)}{\partial y} = & \frac{\partial}{\partial x} \left[ (\alpha_\epsilon \mu_{eff}) \frac{\partial \epsilon}{\partial x} \right] + \frac{\partial}{\partial y} \left[ (\alpha_\epsilon \mu_{eff}) \frac{\partial \epsilon}{\partial y} \right] \\ & + C_{1\epsilon} \frac{\epsilon}{k} (G_k + C_{3\epsilon} G_b) - C_{2\epsilon}^* \rho \frac{\epsilon^2}{k} \end{aligned} \quad (9)$$

Where the effective viscosity is calculated from

$$\text{In the low Reynolds limit} \quad d \left( \frac{\rho^2 k}{\sqrt{\epsilon \mu}} \right) = 1.72 \frac{\hat{v}}{\sqrt{\hat{v}^3 - 1 + C_v}} d\hat{v}, \quad \hat{v} = \frac{\mu_{eff}}{\mu}$$

Where  $C_v \approx 100$

$$\text{In the high Reynolds limit} \quad \mu_t = \rho C_\mu \frac{k^2}{\epsilon}$$

Where  $C_\mu = 0.0845$

The inverse effective Prandtl numbers  $\alpha_k$  and  $\alpha_\epsilon$  are calculated using the following analytical formula

$$\left| \frac{\alpha - 1.3929}{\alpha_0 - 1.3929} \right|^{0.6321} \left| \frac{\alpha + 2.3929}{\alpha_0 + 2.3929} \right|^{0.3679} = \frac{\mu_{mol}}{\mu_{eff}}$$

Where  $\alpha_0 = 1.0$ . In the high Reynolds limit  $\frac{\mu_{mol}}{\mu_{eff}} \ll 1$ ,  $\alpha_k = \alpha_\epsilon \approx 1.3929$

$$\text{Turbulent production } G_k = \frac{\mu_t}{2} \left( \frac{\partial u_i}{\partial x_j} + \frac{\partial u_j}{\partial x_i} \right)^2,$$

$$\text{Generation of turbulence due to buoyancy } G_b = \beta g_i \frac{\mu_t}{Pr_t} \frac{\partial T}{\partial x_i},$$

Where  $Pr_t = \frac{1}{\alpha}$ , and with  $\alpha_0 = 1/Pr$

The addition term to the turbulent dissipation rate to account for the effects of rapid

$$\text{strained and streamline curvature flows } C_{2\epsilon}^* = C_{2\epsilon} + \frac{C_\mu \rho \eta^3 (1 - \frac{\eta}{\eta_o})}{1 + \beta \eta^3},$$

$$\eta = S \frac{k}{\epsilon}, \eta_o = 4.38, \beta = 0.012$$

$$\text{Effect of buoyancy on the turbulence dissipation rate } C_{3\epsilon} = \tanh \left| \frac{v}{u} \right|,$$

$$\text{The effective thermal conductivity } K_{eff} = \alpha Cp \mu_{eff}$$

The RNG k- $\epsilon$  model employs values of the following constants:

$$C_v = 100, \quad \eta_o = 4.38, \quad C_\mu = 0.0845, \quad C_{1\epsilon} = 1.42, \quad C_{2\epsilon} = 1.68$$

In the case of calculating  $\alpha$  for  $K_{eff}$ ,  $\alpha_0 = 1/Pr$ .

### 5.3.1.2 Treatment of the near wall

In the near wall region, the solution variables change greatly with large gradients and the turbulent flows are significantly affected. Near walls, the viscous damping reduces the tangential velocity fluctuations and the kinematic blocking reduces the normal fluctuations. Away from the near wall region, the turbulence is significantly increased due to the severe gradient of the mean velocity. The numerical solutions are highly affected by the near wall region as the wall is the main source of turbulence. Therefore, to successfully determine and predict this turbulent flow, precise representations of the flow in the near wall region were needed [55].

The turbulent model described above is valid for turbulent flows far from walls. Therefore special considerations are needed to make this model appropriate for flows near walls. The near wall region can be divided into three layers as shown in Figure 5.4. The first one very close to the wall called “viscous sub-layer”, the flow here is

influenced by the viscous effects. The second layer is between the viscous sub-layer and the fully turbulent layer called “buffer layer”, where both the turbulence effects and viscous effects are important. The third layer is the fully turbulent layer and it comes far from the wall and after the first and second layers; in this region, turbulence is dominant and plays the major role [101].

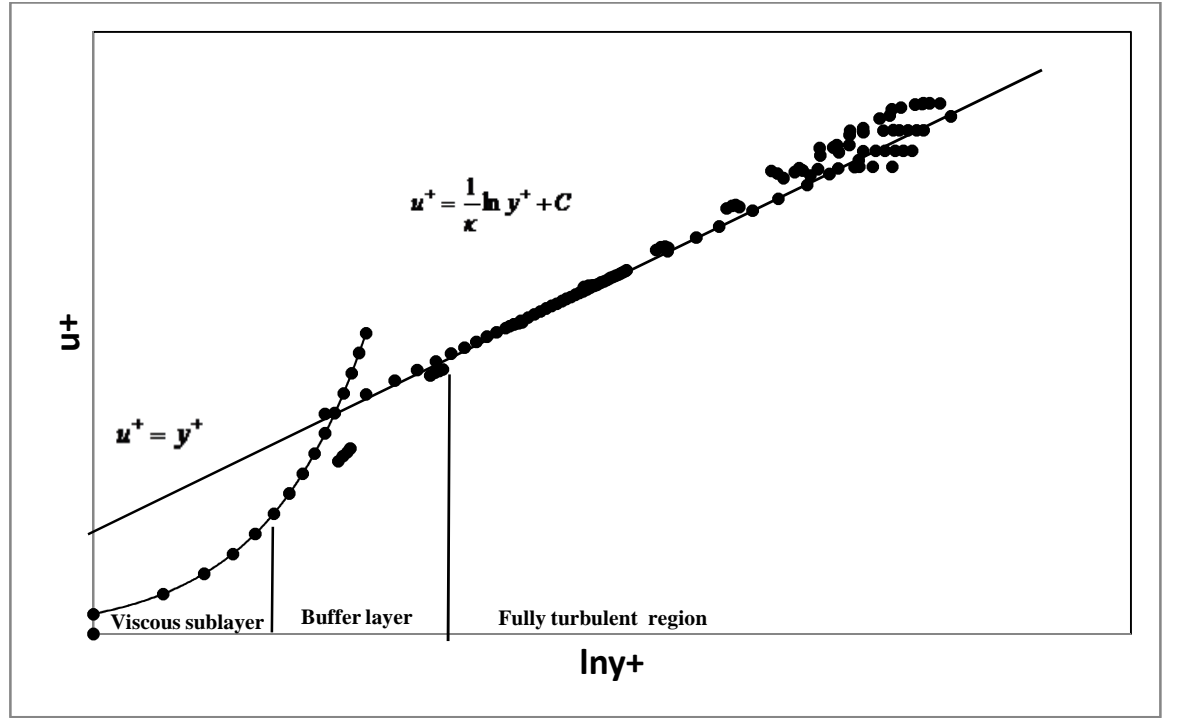


Figure 5.4 The three layers near the wall region

There are two approaches to represent and solve the flow in the near wall region. In the first approach, the first two layers near the wall, which are the viscous sub-layer and the buffer layer are not resolved. For this approach, the turbulence model does not need to be modified to account the near wall region, where semi-empirical formulas called “wall functions” are used to bridge or link the solution variables of the viscosity affected region between the wall and the fully turbulent region [102, 103]. For the second approach, the turbulence model needs to be modified to account and resolve the viscous sub-layer and the buffer layer using a sufficiently dense mesh resolution. The two approaches of near wall solutions are represented schematically in Figure 5.5. So, to represent and capture the critical importance of the buoyancy flow features in the simulation model used in this study, the two-layer model (which is the second approach) was employed for the near-wall treatment with the RNG  $k-\epsilon$  model. In this

model the domain is divided into two main regions, a viscosity affected region and a fully turbulent region. Where the two regions are determined by the value of a wall distance called “turbulent Reynolds number”.

$$Re_y = \frac{\rho \sqrt{k} y}{\mu} \quad (10)$$

Where  $y$  is the normal distance from the wall at the cell centres.

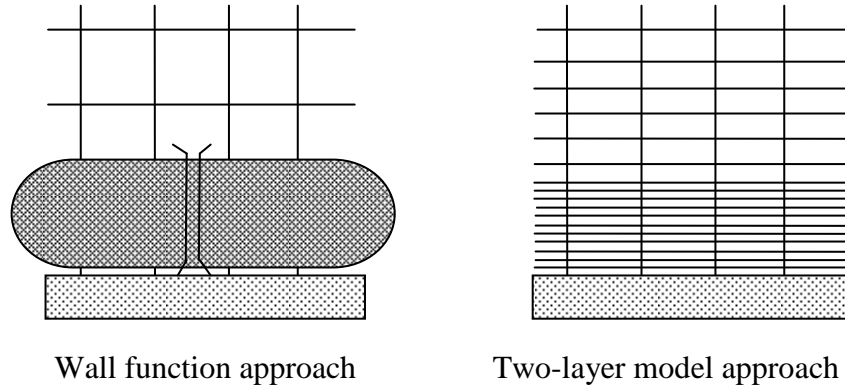


Figure 5.5 Near wall treatment

The near-wall grid can be checked by calculating the value of  $y^+$  equation (11) or the value of turbulent Reynolds number equation (10). As it can be seen from equations 10 and 11 both  $y^+$  and  $Re_y$  are geometrical quantities and also both solution dependent. Each of them has special strategies that need to be followed to know the accuracy of the results and to check the grid used.

$$y^+ = \frac{\rho u_\tau y}{\mu} \quad (11)$$

Where,  $u_\tau = \sqrt{\tau_w / \rho}$  is the shear velocity and  $\tau_w$  is the local wall shear stress.

Depending on the value of turbulent Reynolds number the fully turbulent region which starts at  $Re_y > 200$  is solved using RNG  $k-\epsilon$  model, while in the viscous-affected near-wall region at  $Re_y < 200$  is solved using the one equation model of Wolfstein[104].

The one equation model keeps the momentum equations and the turbulent kinetic energy equation the same while:

The turbulent viscosity is computed from

$$\mu_t = \rho C_\mu \sqrt{k} \ell_\mu \quad (12)$$

The dissipation rate is computed from

$$\epsilon = \frac{k^{\frac{3}{2}}}{\ell_\epsilon} \quad (13)$$

Where the length scales are computed from [105]

$$\ell_\mu = C_l y \left[ 1 - \exp\left(-\frac{Re_y}{A_\mu}\right) \right] \quad (14)$$

$$\ell_\epsilon = C_l y \left[ 1 - \exp\left(-\frac{Re_y}{A_\epsilon}\right) \right] \quad (15)$$

The model constants are  $C_l = \kappa C_\mu^{-\frac{3}{4}}$ ,  $A_\mu = 70$  and  $A_\epsilon = 2C_l$

### 5.3.1.3 Radiation model

The Discrete Transfer Radiation Model (DTRM), which is used in the present study, is a relatively simple model which, is used for calculating radiation and can be used both with and without participating fluid. It applies to a wide range of optical thicknesses, and its accuracy can be increased by increasing the number of rays [55]. The model calculates the change in radiation intensity,  $dI$ , along a path  $ds$ .

$$\frac{dI}{ds} + aI = \frac{a\sigma T^4}{\pi} \quad (16)$$

Where  $a$  is the gas absorption coefficient and  $I$  the radiation intensity.

Equation 16 is then integrated along a series of rays emanating from boundary faces so that the radiation intensity is:

$$I(s) = \frac{\sigma T^4}{\pi} (1 - e^{-as}) + I_o e^{-as} \quad (17)$$

Where  $I_o$  is the radiant intensity at the start of the incremental path, which is determined by the appropriate boundary conditions.



The ray tracing technique used in the DTRM can provide a prediction of radiation heat transfer between surfaces without explicit view factor calculations. The accuracy of the model depends on the number of rays traced and the computational grid [55].

The ray paths are calculated and stored before the flow calculations. At each radiation face the rays are calculated for different values of the polar angles  $\theta$  and  $\Phi$ . Where,  $\theta$  is from 0 to  $\frac{\pi}{2}$  and  $\Phi$  from 0 to  $2\pi$  as seen in Figure 5.6. Each ray is then traced to determine the control volumes it intercepts as well as its length within each control volume. This information is stored in a file and it must be read in before the flow calculations start.

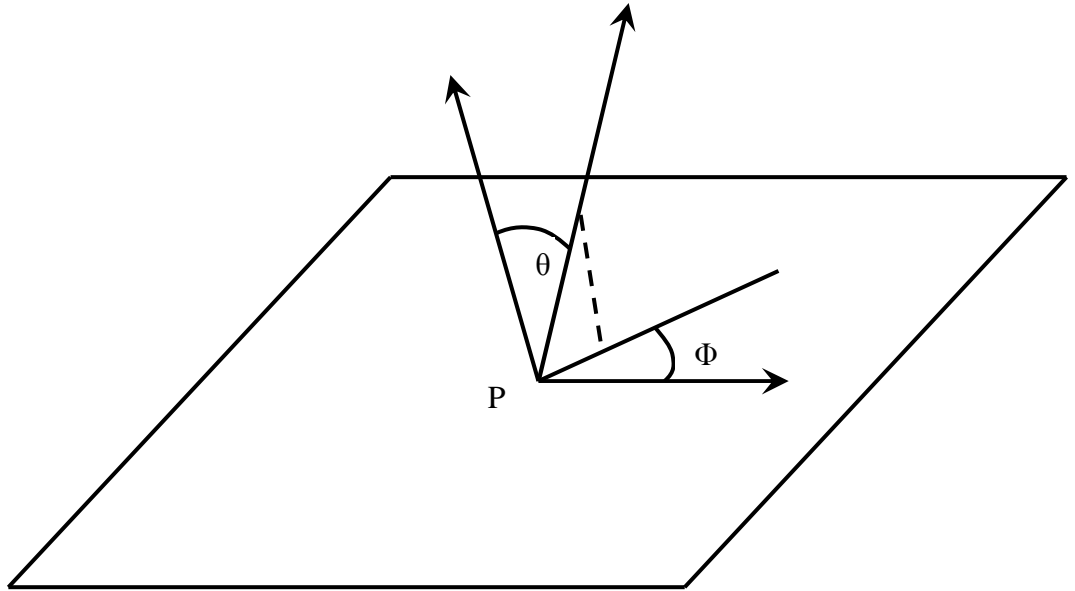


Figure 5.6 Angles  $\theta$  and  $\Phi$  about a point P.

For the ray tracing method, the incident radiation heat flux on a wall surface is

$$q_{in} = \int_{s \cdot n > 0} I_{in} S \cdot n d\Omega \quad (18)$$

Where,  $I_{in}$  is the intensity of the incoming ray,  $S$  is the ray direction vector and  $n$  is the normal pointing out of the domain.

The net radiation heat flux from the surface is the sum of the reflected portion of  $q_{in}$  and the emissive power of the surface:

$$q_{out} = (1 - \varepsilon_w) q_{in} + \varepsilon_w \sigma T_w^4 \quad (19)$$

Where,  $T_w$  is the surface temperature of the point P on the surface and  $\varepsilon_w$  is the wall emissivity from the boundary condition. Equation 19 is used in the prediction of the wall surface temperature  $T_w$  and also provides the boundary radiation intensity  $I_o$  as:

$$I_o = \frac{q_{out}}{\pi} \quad (20)$$

### 5.3.2 Boundary conditions

#### 5.3.2.1 Model inputs

For the case of turbulent flow, as in this study, the turbulent portion of the viscous model menu is activated, which in this case is the RNG k- $\epsilon$  model. The flow involves the walls; so in this case, the two layer model is chosen as a near wall treatment. In the model options, the differential formula for the effective viscosity model is selected to include the low-Reynolds number effects.

The effect of swirl on turbulence is included in the RNG model, enhancing accuracy for swirling flows. The RNG model provides an option to account for the effects of swirl or rotation by modifying the turbulent viscosity appropriately. Depending on whether the flow is swirl-dominated or only mildly swirling, some swirl flow options in the RNG model need to be modified [55].

The boundary condition for the turbulent kinetic energy and turbulent dissipation rate at the walls are taken by default by FLUENT and they must only be provided in the cases that have inlet boundaries. Using the segregated solver, Fluent under-relaxes the energy equation using the defined under-relaxation parameter which is one as a default value. In the cases where the energy field impacts the fluid flow via temperature dependent properties or buoyancy the under-relaxation factor should be in the range of 0.8-1.0 [55], as in this study, where the under-relation factor for energy is defined as 0.8.

The buoyancy forces which drive the flow due to the density variations in a natural convection can be either included or ignored in the turbulent model by examining the ratio between the Grashof and Reynolds numbers

$$\frac{G_r}{Re^2} = \frac{\Delta\rho gh}{\rho v^2} \quad (21)$$

When this number approaches or exceeds one, a strong buoyancy contribution can be expected in the flow. On the other hand when this number is quite small, the buoyancy effects may be neglected in the simulation. To include the buoyancy effects in the RNG k- $\epsilon$  model, the gravity in the FLUENT *operating conditions* panel should be turned on and gravitational acceleration should be entered in the appropriate Cartesian coordinate direction. The generation of turbulent kinetic energy due to buoyancy is included by default while the effect of buoyancy on the turbulent dissipation rate needs to be included by activating the *full buoyancy* option under the *viscous model* menu.

For the case of natural convection flow; using the Boussinesq model for density can accelerate the convergence. This model takes density as a constant value in all solved equations, except for the buoyancy term in the momentum equation, as it mentioned in chapter three. In the *materials* panel the Boussinesq model is selected as a method for the *material density* and the operating temperature in the operating condition panel was specified. Also in the *materials* panel, the *thermal expansion coefficient* and *density* were specified. For the case of heat transfer there are some options in the model that need to be activated, such as activate the calculation of *energy equation*. The boundary conditions at the walls need to be defined and finally the *material properties* need to be defined as constant or as a function of temperature. In this study the walls thermal conditions are set as constant temperatures and have a certain value of emissivity. The fluid properties are set as a function of temperature. The discretization methods are selected to be second order upwind scheme for both energy and momentum and PRESTO (pressure staggering option) for pressure.

In the second order accuracy upwind scheme, quantities at cell faces are computed using a multidimensional linear reconstruction approach [55]. In this approach, using a Taylor series expansion of the cell centred solutions about the cell centroid, high order accuracy is achieved at the cell faces. The discretization of the convection term in momentum equation turns out to have a problem. This is because the level of the momentum in a cell is sensitive to the momentum upstream as the convection terms are concerned and if this is not represented in the discretization, numerical problems arise. The upwind scheme solves the problem by approximating the values at the cell faces in the convection terms by simply taking the value at the nearest cell centre upstream from the face. This works brilliantly to stabilise the iteration process so that a converged solution to the discrete equations is easily reached. The second order upwind gives a

good accuracy and for the first order upwind need to have small grid size to have the same accuracy.

The PRESTO discretization method for pressure is recommended [55], to be used when a quadrilateral or hexahedral mesh is used and also with using the segregated solver. The scheme uses the discrete continuity balance for a staggered control volume about the face to compute the staggered pressure. This procedure is similar to the staggered-grid schemes used with structured grids[55]. The scheme is well suited for steep pressure gradients involved in rotating flows. It provides improved pressure interpolation in situations where large body forces or strong pressure variations are present as in swirling flows.

The compressibility effects are neglected because the flow has low velocity, low Mach number, ( $M < 0.1$ ) and the pressure variations is very small. Therefore the flow in this study is treated as incompressible.

### **5.3.2.2 Turbulent simulations and grid generation**

In turbulent flow, especially in the near wall region, the solution variables change greatly and have large gradients. Therefore to successfully determine and predict the turbulent flow features with high accuracy, precise representations of the flow in the near wall region are needed [55].

Turbulence has a strong interaction with the mean flow features, so, the turbulent flow results tend to be grid dependant. Thus, a sufficiently fine grid is needed in the regions where the mean flow features have severe changes.

For the case of using the wall function approach to solve the near wall region, the value of  $y^+$  should be in the range  $y^+ > 30 \sim 60$ . The wall function approach is still valid up to  $y^+ > 11.225$ . When the mesh has a value of  $y^+ < 11.225$  FLUENT applies a laminar stress strain relationship instead of using the logarithmic law.

The Low-Reynolds-Number method resolves the details of the boundary layer profile by using very small mesh length scales in the direction normal to the wall. Note that the low-Re method does not refer to the device Reynolds number, but to the turbulent Reynolds number, which is low in the viscous sub-layer. This method can therefore be

used even in simulations with very high device Reynolds numbers, as long as the viscous sub-layer has been resolved [55].

The computations are extended through the viscosity-affected sub-layer close to the wall. The low-Re approach requires a very fine mesh in the near-wall zone and correspondingly large number of nodes. Computer-storage and runtime requirements are higher than those of the wall-function approach and care must be taken to ensure good numerical resolution in the near-wall region to capture the rapid variation in variables [55].

For the case of using the two-layer turbulent model as in this study the dimensionless distance  $y^+$  must be  $y^+ < 5$  to get acceptable results [55]. For the ideal case, it should have at least 10 mesh cells inside the viscosity near wall region. In the present study all the simulations were in the range of  $y^+ < 5$ .

#### **5.3.2.3 Model convergence**

To accelerate the convergence of the model it is recommended to start with a laminar model then after it has converged somewhat, turn on the turbulent model. Changing the under relaxation factors for the energy and momentum equations also may result in faster convergence of the model. Solving the flow equations first by turning off the energy equation until the flow field solution has converged, then turning on the energy equation to complete the heat transfer solution that will accelerate the solution. The convergence can be judged by monitoring some important parameters, solution residuals and checking the heat balance through all boundaries.

For the cases of high Rayleigh numbers and to speed the convergence, it is recommended to start with lower value of Rayleigh number and then run the simulation until convergence by using the first order scheme, then the resultant data of low Rayleigh number can be used as an initial guess for the high Rayleigh number. Convergence can then be achieved by changing to the second order scheme.

#### **5.3.2.4 Grid formation**

For the models used in this study, different non-uniform mesh sizes were used as shown in Figure 5.7 for aspect ratio equal four, Figure 5.8 for a square enclosure and Figure 5.9 for aspect ratio equal to a quarter. These have a sufficiently fine grid near the

walls and a relatively coarse grid at the core, to get acceptable results while keeping the total grid size down.

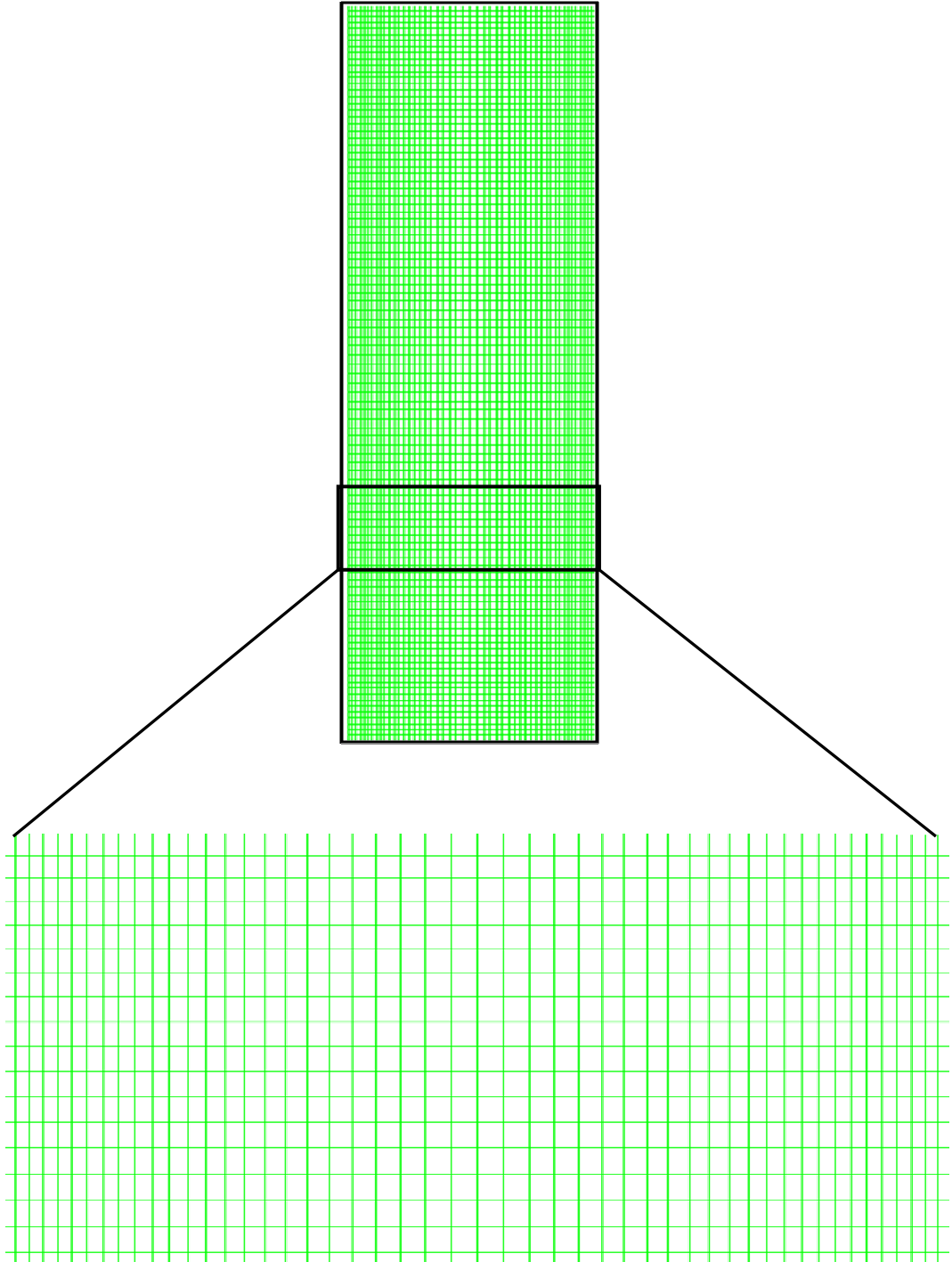


Figure 5.7 Non-uniform grid used in the simulation model for aspect ratio four

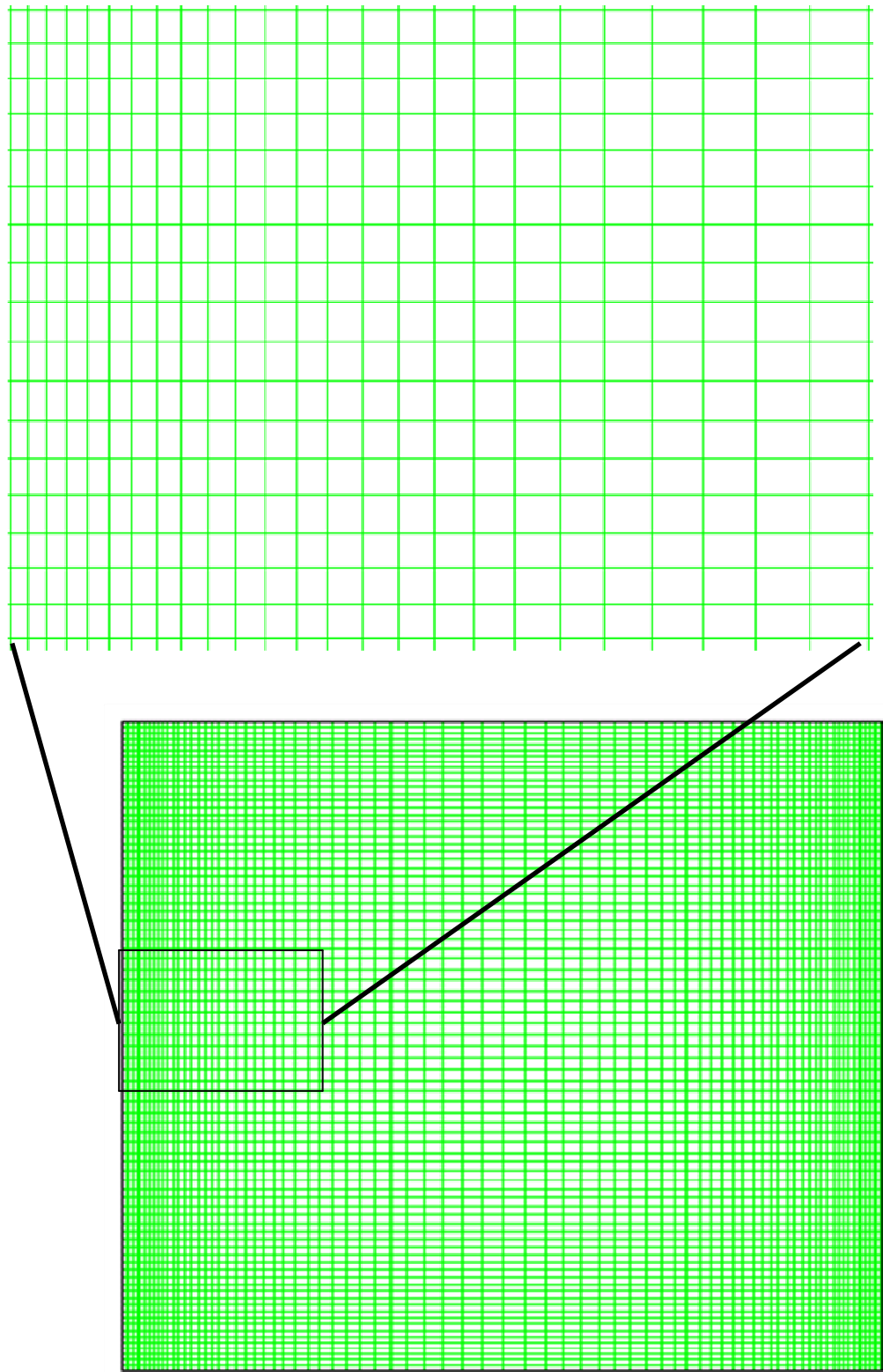


Figure 5.8 Non-uniform grid used in the simulation model for square enclosure

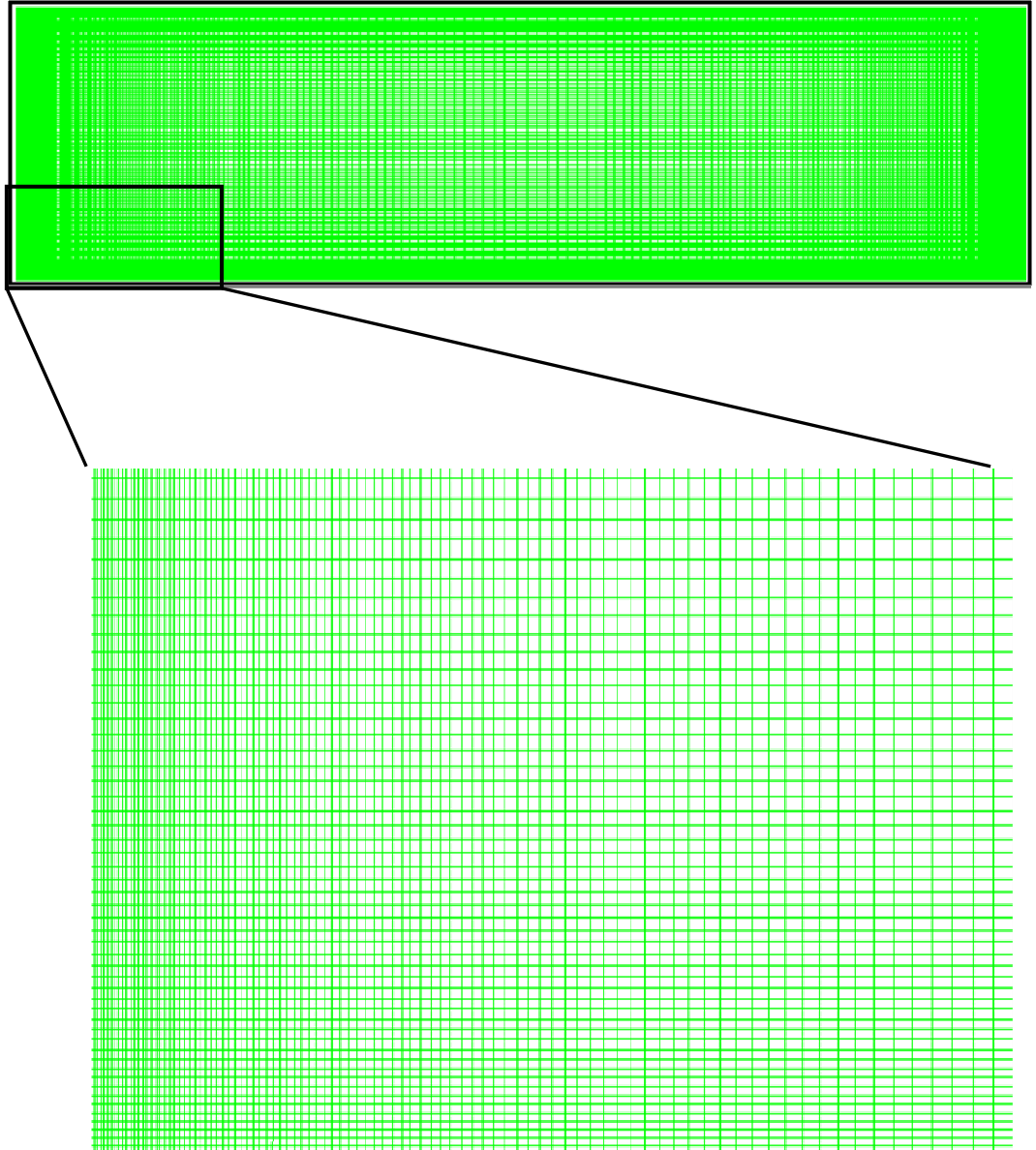


Figure 5.9 Non-uniform grid used in the simulation model for aspect ratio quarter

The grid size for the square enclosure varied from  $67 \times 67$  up to  $200 \times 200$  for the three different groups (where, the first group is for different cold wall temperatures, the second group for different enclosure sizes and the third group for different gas properties). While the non-uniform grid size for the rectangular enclosure, was from  $100 \times 19$  for the aspect ratio equal to 16 up to  $100 \times 400$  for an aspect ratio of 0.0625. The height of the enclosure was kept the same for all aspect ratios.



### 5.3.3 Grid independence

The grid independence has been studied for the case of an absoluteabsolute temperature ratio of  $T_r = 2.6$  and an enclosure size of 240cm square using Hydrogen as a working fluid. The analysis was done for three non-uniform grid patterns 80×80, 100×100 and 150×150 nodes, taking the total average Nusselt number as the parameter to be compared.

The average values of Nusselt numbers were 286.3, 281.71 and 280.5 and the maximum values of  $y^+$  were 5, 2.25 and 0.9 for the three grids respectively. So, the maximum error for the average Nusselt number which calculated at  $y^+ = 5$  (which is in the present study range) and grid pattern 80×80 is 1.6% and 2% compared to the average Nusselt numbers at  $y^+ = 2.25$  and 0.9 and grid patterns 100×100 and 150×150 respectively. Hence, the maximum error in the present study will be less than 3% due to the mesh size employed.

The grid independence has been studied also for the case of a rectangular enclosure and an absoluteabsolute temperature ratio of  $T_r = 2.6$  and an enclosure aspect ratio 16 using Air as a working fluid. The analysis was done for three non-uniform grid patterns 100×19, 150×29 and 200×39 nodes, taking the total average Nusselt number as the parameter to be compared. The results varied by less than 1.2%. So the grid sizes mentioned in grid formation section 5.3.2.4 were used for both square and rectangular enclosures. These have values of  $y^+ \leq 5$ .

## 5.4 Model validation

To validate the computational model described above, the average Nusselt number results of the numerical solutions found in the present study have been compared with the predicted results of Markatos and Pricleous[95]. The results are also compared with the correlation equation obtained from the experimental results by Elsherbiny et al. [7], these are all displayed in Table 5.1, where it can be seen that the present results are more consistent with the experimental correlation than the other numerical results [95].

Table 5.1 Comparison of average Nusselt number for natural convection in a square enclosure

Ra	Present results	Elsherbiny et al. [7]	Markatos and Pericleous[95]
$10^8$	31.42	28.78	38.06
$10^9$	66.16	62	74.96
$10^{10}$	135.15	133.57	159.89

For further validation of the model used, the problem of natural convection without radiation interaction in a square enclosure was solved for a high Rayleigh Number ( $5 \times 10^{10}$ ). The results were compared with the experimental results provided by both Cheesewright et al. [58] and King [57] and also with a reference solution from 10 research groups provided by Heneks and Hoogendoorn[15] as shown in Table 5.2. The results were compared for the average Nusselt number and for the local Nusselt number at the mid height of the enclosure. It can be seen from Table 5.2 that the present results agree better with the average value of the experimental results of [57, 58] than the reference solution [15].

Table 5.2 Average and mid height Nusselt number for natural convection in a square enclosure at  $Ra=5 \times 10^{10}$  as a comparison with reference and experimental results.

Quantity	Present results	Reference solution [15]	Experimental results [57, 58]
Average Nu	194.9	256	154-210(average=182)
Mid height Nu	205	261	133-241(average=187)

## 5.5 Numerical results

The numerical calculations and results using the RNG k- $\epsilon$  model for square and rectangular enclosures are discussed in detail in this chapter. The calculations are established for a wide range of different temperatures, enclosure sizes and gases with and without radiation interaction. The numerical results are explained and discussed in two main categories: the first category comprises square enclosures and the second are rectangular enclosures.

Under each of these two main categories the numerical results are discussed and explained using two other categories, which are pure natural convection and natural convection with radiation interaction. Also in this chapter the 3D numerical results are explained for the thermal results and velocity and turbulent intensity profiles which will be discussed and compared with the experimental results in the next chapter.

### 5.5.1 Square enclosure

The interaction effects of turbulent natural convection with and without surface thermal radiation on fluid flow in a square enclosure are studied in detail. The study has been carried out over the following range of parameters, cold wall temperature,  $T_c = 283 \text{ to } 373K$ , enclosure size: 40cm square to 240cm square and with different gases including: Argon, Air, Helium and Hydrogen.

In order to make the preceding analysis more useful and general, a large number of simulations were performed to extract the numerical relationship between the dimensionless numbers. To this end, the interaction effects of turbulent natural convection with and without surface thermal radiation on fluid flow in a square enclosure are studied in detail.

The results are divided to three groups:

1. different cold wall temperatures (ranging from 283 to 373K),
2. different enclosure sizes (ranging from 40cm square to 240cm square) and
3. different gas properties (Argon, Air, Helium and Hydrogen).

For all of the three groups the ratio between the hot and cold wall temperatures was in the range of ( $T_r = \frac{T_h}{T_c} = 1.02 \text{ to } 2.61$ ) and the modelling was conducted with all the fluid properties as a function of temperature.

#### 5.5.1.1 Pure natural convection inside a square enclosure

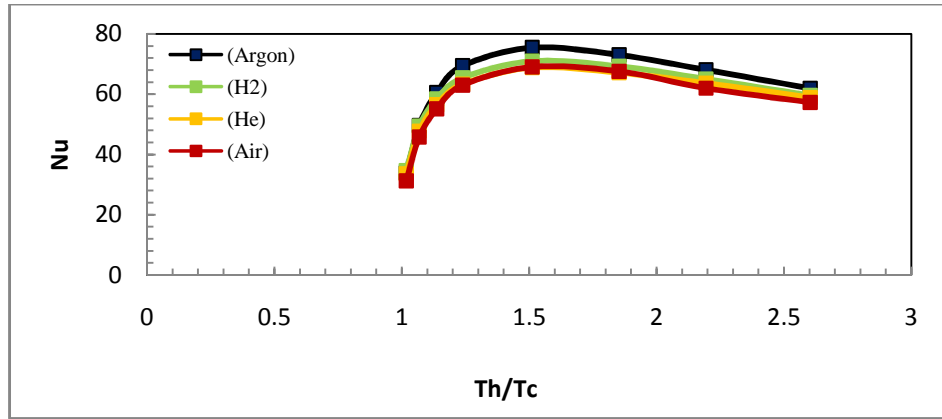
The turbulent natural convection without radiation interaction in the square enclosure has been analysed and investigated numerically. The average Nusselt number at each absolute temperature ratio for each case in the three different groups was reported.

The numerical results of the three different groups for the calculated average Nusselt number inside square enclosure are shown in figure 5.10. From the figure it can be seen that the average Nusselt number increases as a function of absolute absolute temperature ratio  $T_r$  up to a certain value of  $T_r$  (which is around 1.2) then it starts to slightly decrease. Also from Figure 5.10-a, the values of average Nusselt number are very close for the different fluids and the deviation between them was less than 7%. More over from Figures 5.10-b and 5.10-c it can be seen that the Nusselt number increases as the size of the enclosure increase and decreases as the temperature increase.

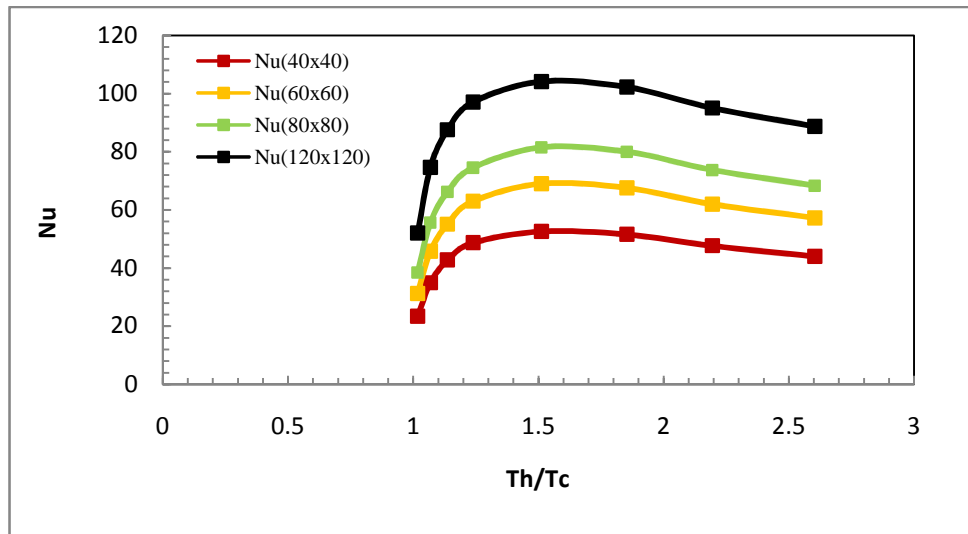
### 5.5.1.2 Natural convection with radiation in square enclosure

Turbulent natural convection with radiation interaction in square enclosures has been analysed and investigated numerically. Figure 5.11 shows the numerical results of the relationship between  $(Q_{conv}/Q_{rad})$  and  $(T_r = \frac{T_h}{T_c})$  (the ratio between hot and cold wall temperatures) for the three different groups. It can be seen from the Figure that, as the  $T_r$  increases the  $(Q_{conv}/Q_{rad})$  increases at the same time up to a value of  $T_r$  which is around 1.2. Then for  $T_r > 1.2$ , the  $(Q_{conv}/Q_{rad})$  decreases as  $T_r$  increases. This means that as  $T_r$  increases up to  $T_r = 1.2$ , convection increases more than the radiation heat transfer for all groups, then radiation heat transfer become dominant and as  $T_r > 1.2$  the radiation increases more than the convection and the ratio  $(Q_{conv}/Q_{rad})$  decreases.

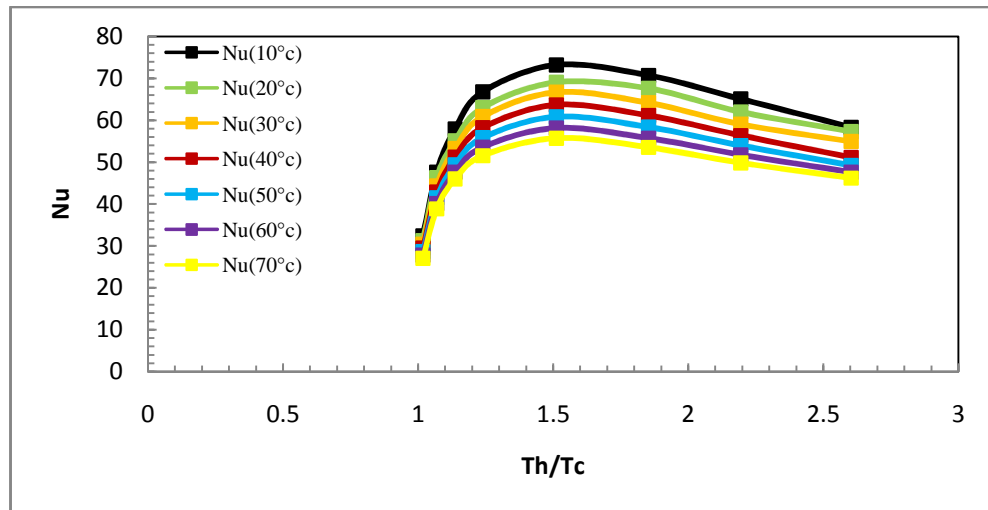
This trade off in heat transfer modes occurs because increasing the temperature will increase the viscosity of the fluid which will slow down the velocity in the hot wall region, this result in a reduction of the convection heat transfer. At the same time, increasing the temperature will increase the thermal conductivity which results in an increase of the convection heat transfer. It can be seen from Figures (5.11-a) and (5.11-b) increasing the temperature and the size will increase the radiation more than the convection heat transfer, this results in a decrease of the overall trend of  $(Q_{conv}/Q_{rad})$  as a function of  $T_r$ . This is because the radiation heat transfer is a function of  $T^4$  and the convection heat transfer is a function of  $T$ . Furthermore as shown in Figure (5.11-c), increasing the thermal conductivity from 0.017 for Argon to 0.18 for Hydrogen will increase the convection heat transfer results increasing the overall of  $(Q_c/Q_r)$  as a function of  $T_r$ .



(a)

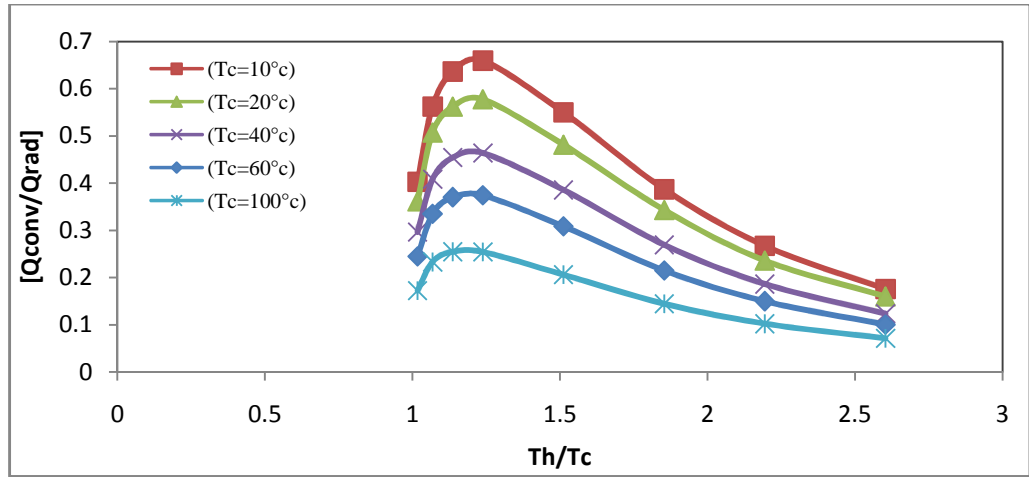


(b)

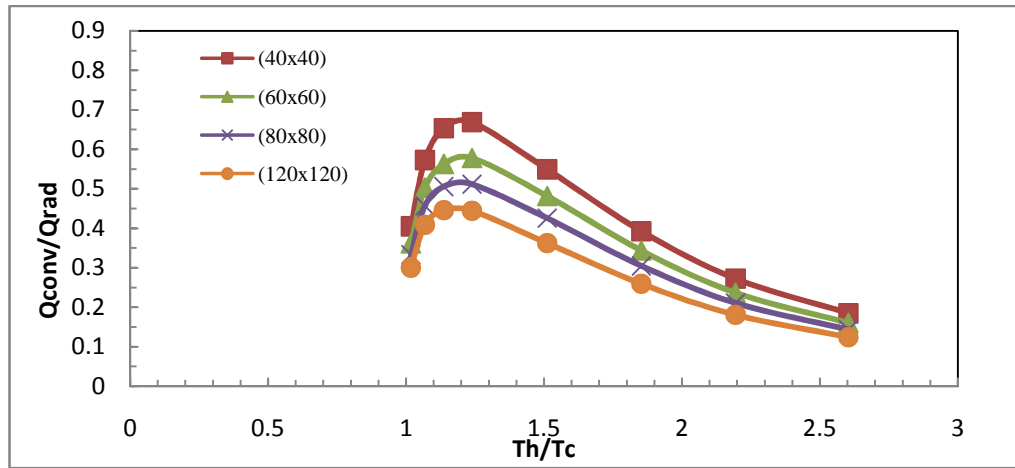


(c)

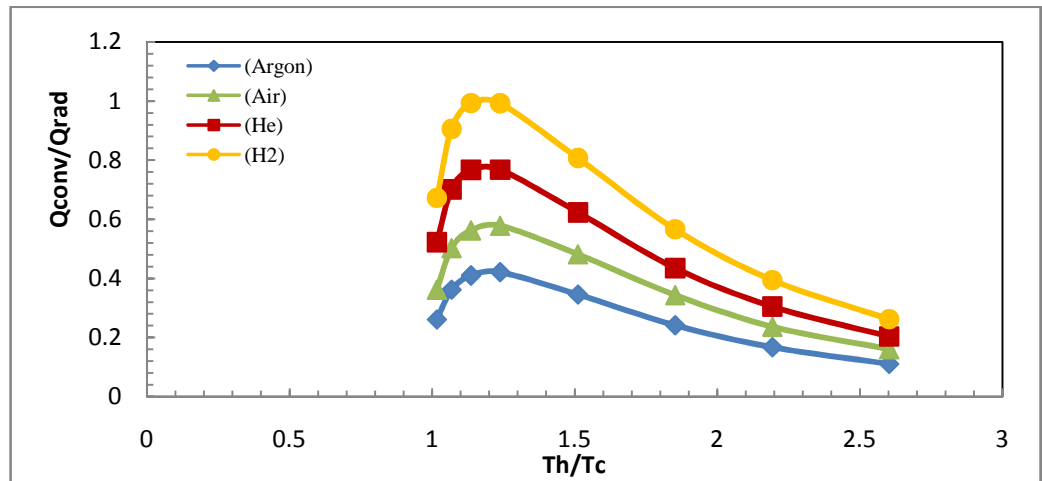
Figure 5.10 The average Nusselt number (for  $3 \times 10^7 \leq Ra \leq 9.3 \times 10^9$ ) and as a function of absolute temperature ratio for different (a) Fluids, (b) enclosure sizes and (c) Cold wall temperatures



(a)



(b)



(c)

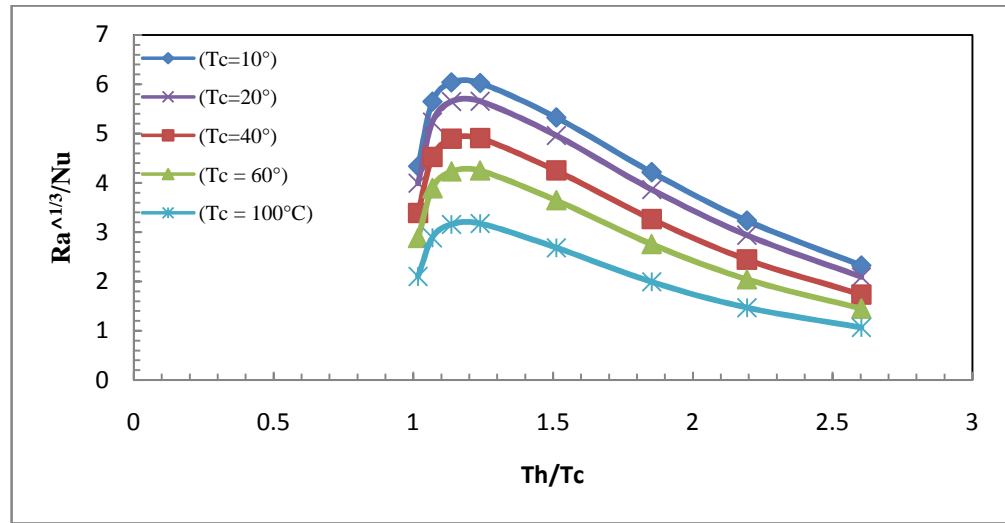
Figure 5.11 Relation between  $Q_c/Q_r$  with respect to  $Th/Tc$  (for  $3 \times 10^7 \leq Ra \leq 9.3 \times 10^9$ ) and for different (a) Cold wall temperatures, (b) Enclosure sizes and (c) Gases.

The relation between the ratio of  $(Ra^{1/3}/Nu)$  and the absolute temperature ratio  $Tr$  has the same trend as the relation between  $(Q_{conv}/Q_{rad})$  and  $Tr$ , as shown in Figure (5.12). This is because both of these two relations,  $[(Q_{conv}/Q_{rad})$  and  $(Ra^{1/3}/Nu)]$ , are increasing as a function of  $T$  and decreasing as a function of  $T^4$ . From Figure (5.12) it can be seen that, as the absolute temperature ratio increases, the ratio  $Ra^{1/3}/Nu$  increases until it reaches a value of  $Tr$  of 1.2 which is the same as before. After that, as  $Tr$  increases, the ratio of  $Ra^{1/3}/Nu$  decreases. This is because increasing the temperature will increase the dynamic viscosity and thermal conductivity linearly and decrease the density linearly; this causes the kinematic viscosity ( $\nu$ ) to increase quadratically (i.e. function of  $T^2$ ); because it is a function of dynamic viscosity and density, ( $\nu = \mu/\rho$ ). This results in a linear increase of the Nusselt number and a decrease of Rayleigh number as a function of  $1/\nu^2$ , which means that the Rayleigh number decreases as a function of  $T^4$ .

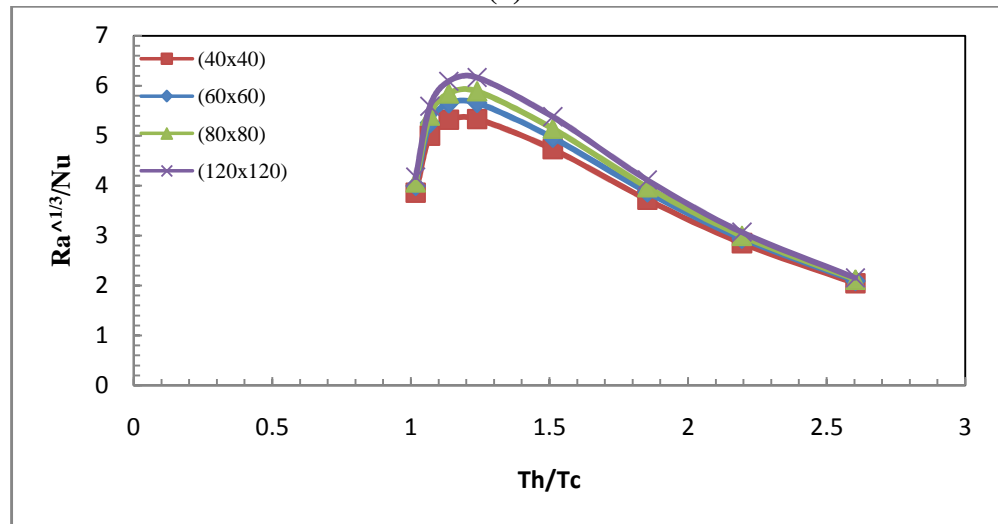
From Figure (5.12-a) it can be seen that increasing the cold wall temperature will decrease the overall trend of  $Ra^{1/3}/Nu$  with  $Tr$ . Also from Figures (5.12-b) and (5.12-c), increasing the enclosure size and the gas properties (such as thermal conductivity and kinematic viscosity), results in an increase of the overall trend of  $Ra^{1/3}/Nu$  with respect to  $Tr$ .

Also from figure (5.12) and as mentioned in chapter 4 section 4.3.1, the relation between Nusselt number in the natural convection heat transfer is not only function of Grashof and Prandtl numbers it is also function of temperature ratio. However, without using the temperature ratio it is impossible to collapse the results shown in figure 5.12.

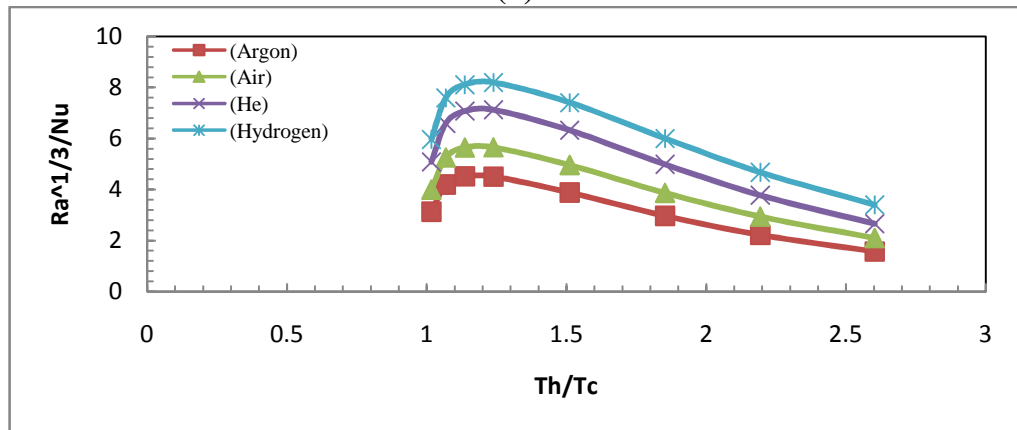
Each set of curves in figure 5.11 has collapsed into a single curve by using some exponents of the variables as conversion parameters. This can be seen by comparing Figure (5.11) and Figure (5.13). Where from Figures (5.11-a) to (5.13-a), the curves of the different cold wall temperature group collapsed into a single curve using only the cold wall temperature as a conversion factor. The same sort of results were obtained for the second and third groups by using different variables as conversion parameters, as shown in Figures (5.11-b) and (5.13-b) and Figures (5.11-c) and (5.13-c). From the similarity of the relationship of  $(Q_{conv}/Q_{rad})$  as a function of  $Tr$  it was possible to collapse these three groups into a single curve.



(a)



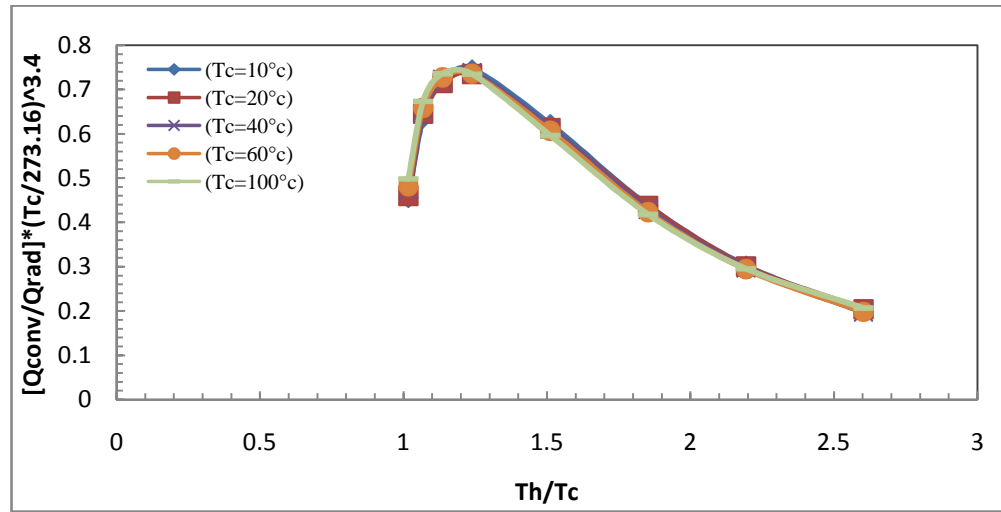
(b)



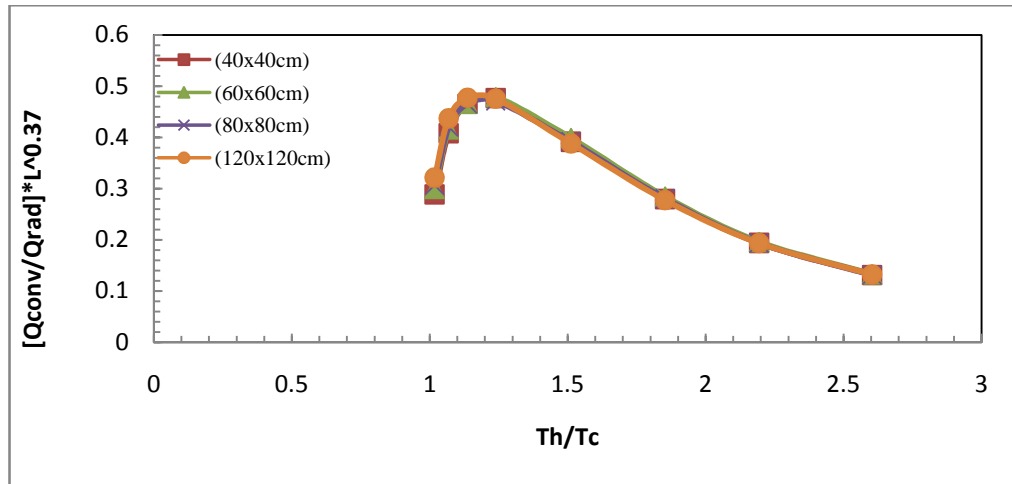
(c)

Figure 5.12 Relation between  $Ra^{1/3}/Nu$  with respect to  $Th/Tc$  (for  $3 \times 10^7 \leq Ra \leq 9.3 \times 10^9$ ) and for different (a) Cold wall temperatures, (b) Enclosure sizes and (c) Gases.

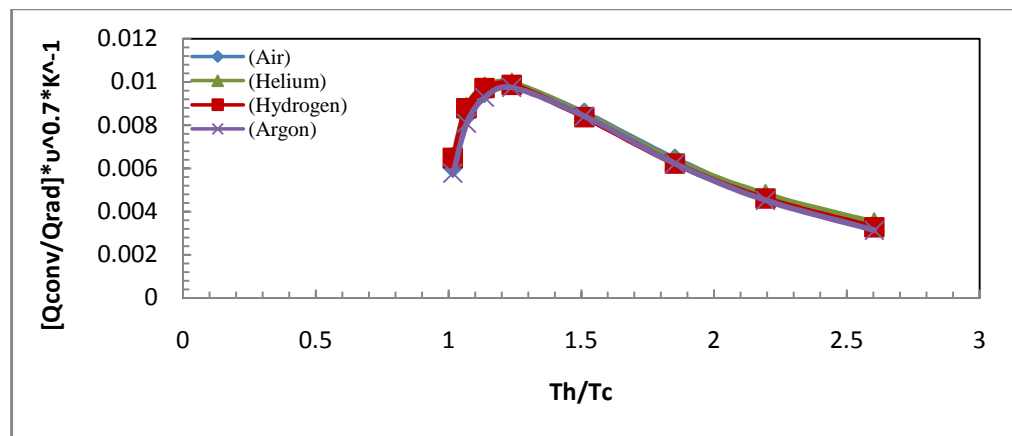




(a)



(b)



(c)

Figure 5.13 Resultant collapsed curves (for  $3 \times 10^7 \leq Ra \leq 9.3 \times 10^9$ ) and for different (a) Cold wall temperatures, (b) Enclosure sizes and (c) Gases.

### 5.5.2 Rectangular enclosure

The interaction effects of turbulent natural convection with and without surface thermal radiation on fluid flow in a rectangular enclosure are studied in detail.

The results include two cases of analysis; first for pure natural convection and second for natural convection with radiation.

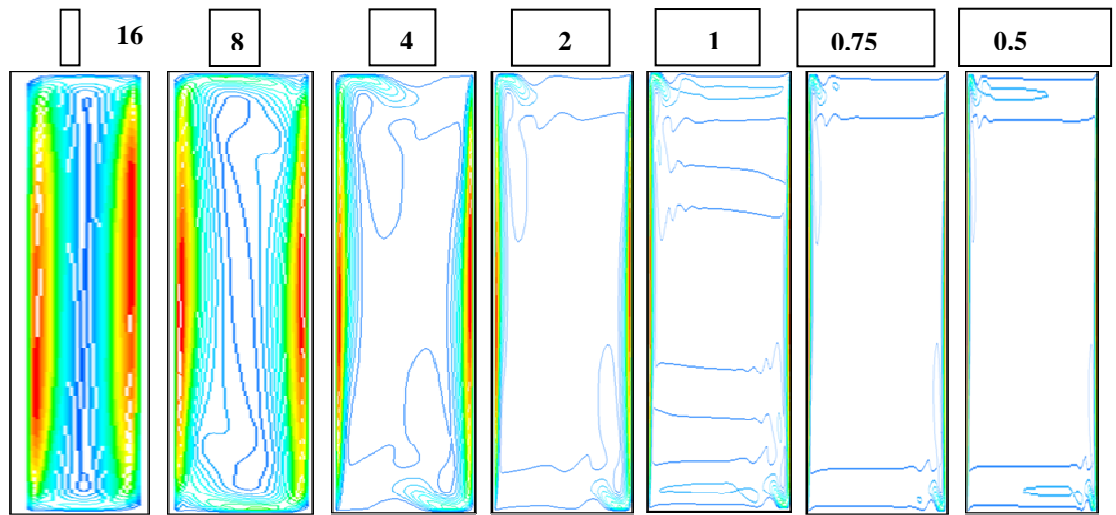
For the two cases the ratio between the hot and cold wall temperatures was in the range of ( $T_r = 1.02$  to  $2.61$ ) and the modelling was conducted with the fluid properties as a function of temperature.

For the case of natural convection with radiation interaction, shown in Figure 5.14-a, 5.14-b and 5.14-c the velocity contours, stream lines and isothermal lines for the aspect ratios 16, 8, 4, 2, 1.5, 1.0, 0.75 and 0.5; These have been scaled horizontally so that they are all the same width. It can be seen that there are three flow regimes:

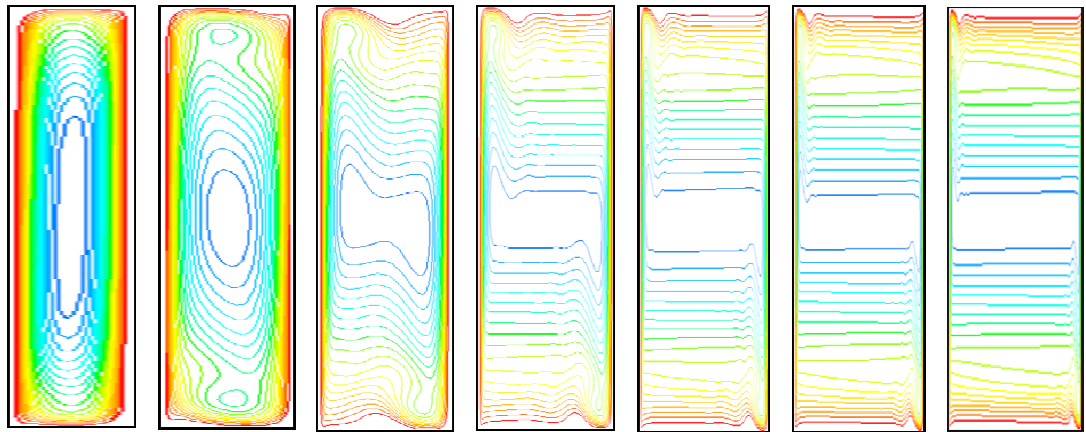
1. From an aspect ratio greater than 1.5 up to 16 (and probably beyond),
2. The second one (transitional) regime is between aspect ratios of 1.5 and 0.75 and
3. The third regime is from an aspect ratio less than 0.75 down to 0.0625 (and again probably beyond).

For the first regime it can be seen from Fig. 5.14-a that the unsteady eddies observed at the top of the hot wall and at the bottom of the cold wall increase in size as the aspect ratio increases and the flow on the two vertical walls tends to exert more force on the stratified core. The core shrinks as the aspect ratio increases and the stream lines, as well as the isothermal lines, vary from the horizontal until they disappear. By now, the two boundary layers of the hot and cold walls merge together and the conduction heat transfer become dominant.

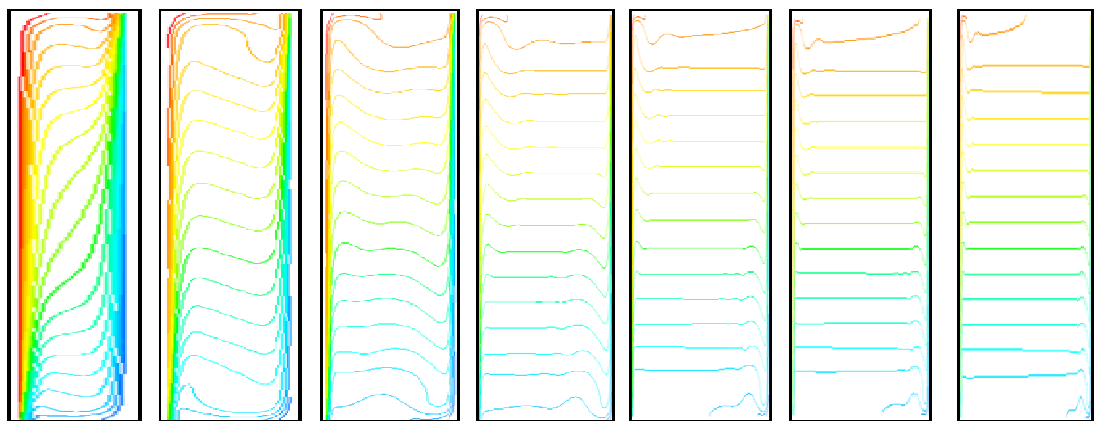
In the second flow regime the two hot and cold walls have balance effects on the core and show stratified transient flow in the core; this can be seen clearly from the stratified stream lines and isothermal lines as in Figures 5.14-b and 5.14-c. The core in the third flow regime can be seen in Figure 5.14 to be unaffected from the two hot and cold walls flow boundary layers and the convection heat transfer becomes dominant as the radiation dramatically decreases with the decrease of aspect ratio.



(a) Velocity contours



(b) Stream lines



(c) Isothermal lines

Figure 5.14 Flow profiles for aspect ratios 16, 8, 4, 2, 1.5, 1.0, 0.75 and 0.5 a) Velocity contours, b) Stream lines and c) Isothermal lines, the red colours means the maximum value for velocity or temperature and the blue colour is the minimum value.

According to the numerical results of the rectangular enclosure with different aspect ratios in this study, the flow could be divided into two regimes, where the second (transition) regime could be included into other two regimes:

1. Regime one starts from square to tall enclosures for aspect ratio ranging from 1 to 16,
2. Regime two starts from square to shallow enclosures for aspect ratio ranging from 1 to 0.0625.

#### **5.5.2.1 Pure natural convection inside rectangular enclosure**

The convection heat transfer decreases as the aspect ratio increases or decreases from the unity, Bejan[19] mentioned the same for laminar pure natural convection. This means that convection heat transfer decreases for both tall and shallow enclosures compared to the square enclosure.

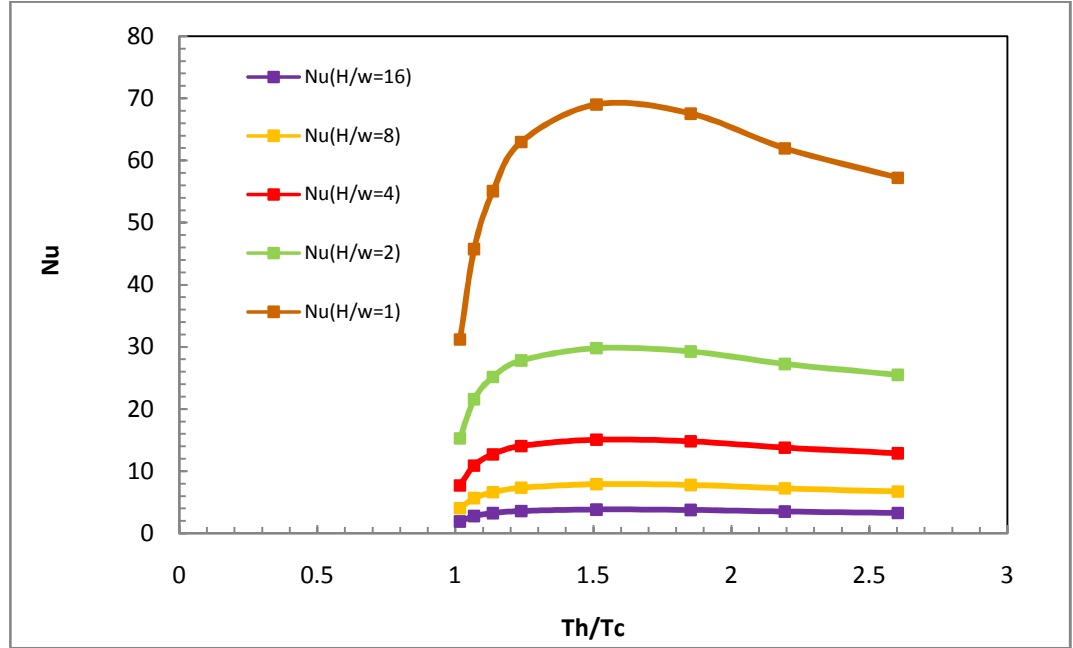
Figure 5.15 shows the relation between average Nusselt number of pure natural convection and absolute absolute temperature ratio  $T_r$  for the two regimes. It can be seen from the figure that; as  $T_r$  increases the average Nusselt number increases at the same time up to a certain value of  $T_r$  (which is around 1.2 for both regimes) then it start to slightly decrease. Also from the figure, the trend of the Nusselt number increasing as the aspect ratio decreases.

#### **5.5.2.2 Natural convection with radiation in a rectangular enclosure**

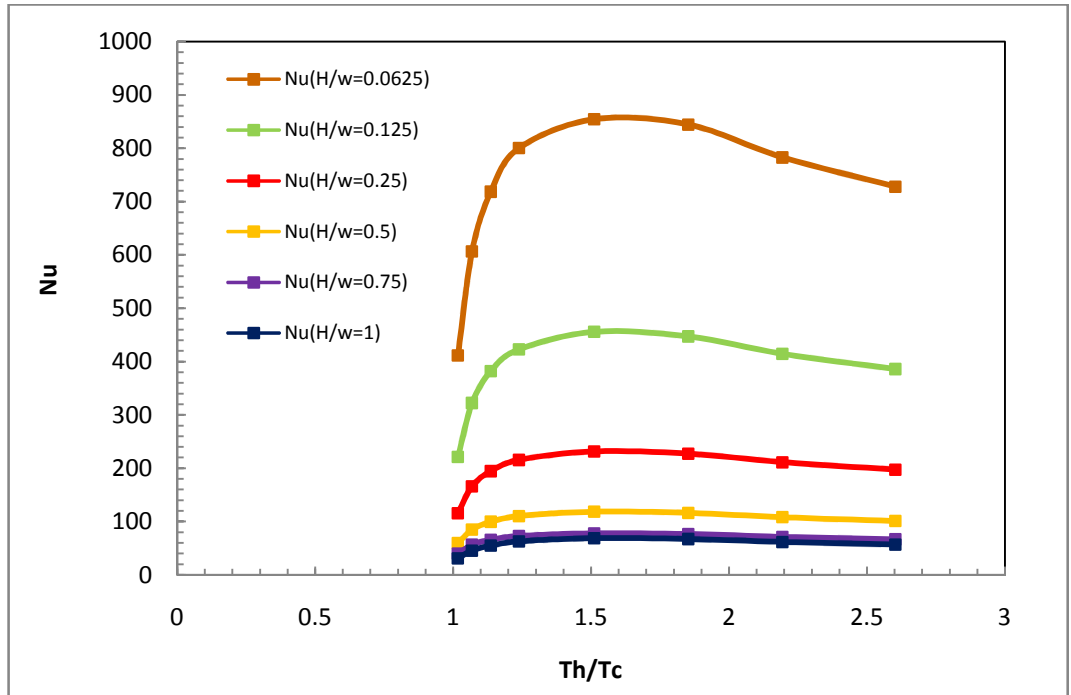
The numerical results for a natural convection with radiation in rectangular enclosure (for a fixed cavity height) shows that, radiation heat transfer is directly proportional to the aspect ratio, which means that radiation heat transfer increases with increasing aspect ratio.

Figure 5.16 shows the relation between  $(Q_{conv}/Q_{rad})$  and  $(T_r)$  for the two regimes. It can be seen from the Figures that; as  $T_r$  increases,  $(Q_{conv}/Q_{rad})$  increases at the same time up to a value of  $T_r$  which is around 1.2. Then for  $T_r > 1.2$ ,  $(Q_{conv}/Q_{rad})$  decreases as  $T_r$  continues to increase. This means that as  $T_r$  increases, convection increases more than radiation heat transfer up to a  $T_r$  of 1.2 for both regimes. At temperature ratios greater than 1.2, the radiation heat transfer becomes dominant, i.e. the radiation increases more rapidly than the convection and the ratio  $(Q_{conv}/Q_{rad})$  decreases. Also

from Figure 5.16-a it can be seen that for the first regime as the aspect ratio increases, the ratio  $(Q_{conv}/Q_{rad})$ , as a function of  $T_r$  has decreased slightly. On the other hand for the second regime, from Figure 5.16-b, as the aspect ratio decreases, the ratio  $(Q_{conv}/Q_{rad})$  as a function of  $T_r$ , increase dramatically.

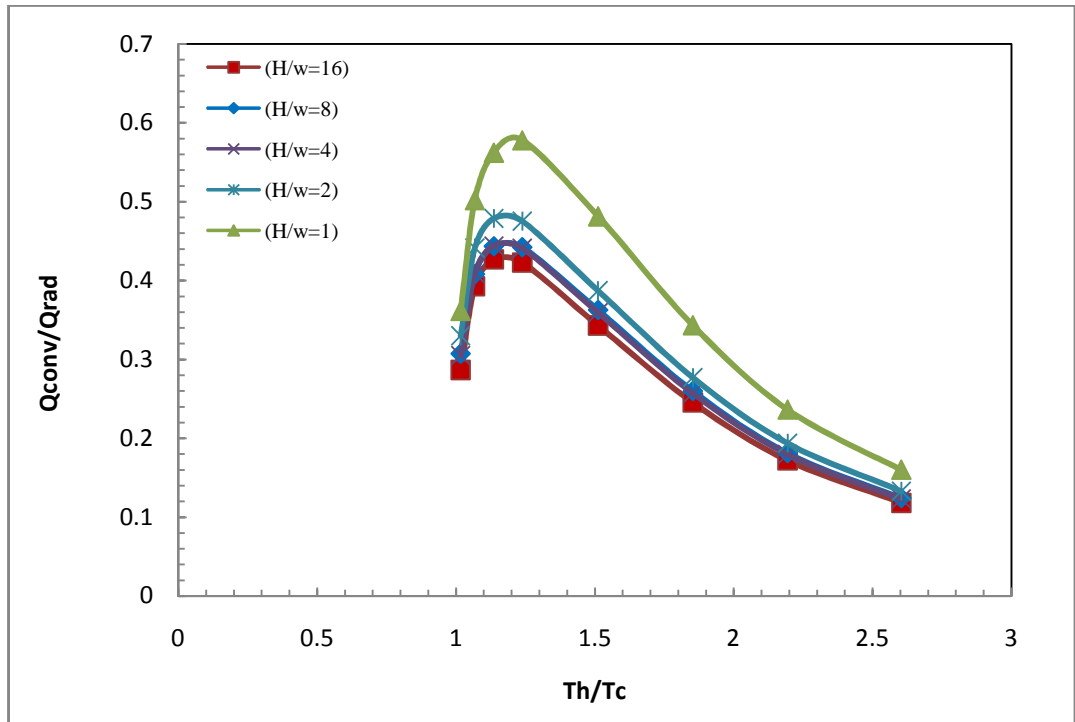


(a)

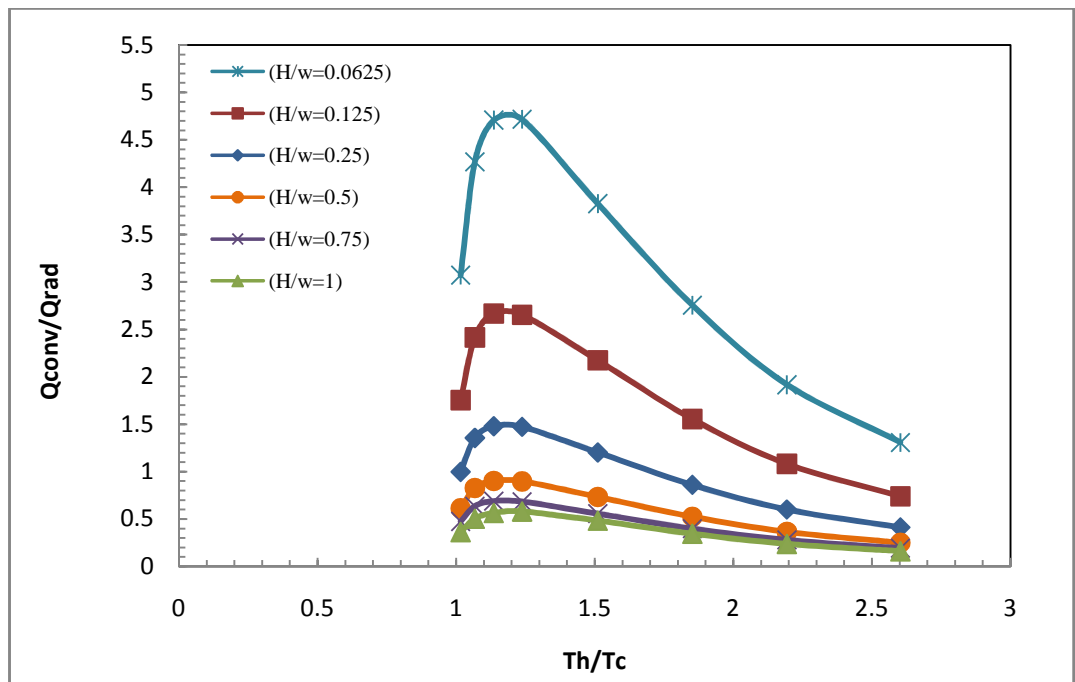


(b)

Figure 5.15 The average Nusselt number for rectangular enclosure as a function of absolute temperature ratio for a) first regime and b) second regime.



(a)



(b)

Figure 5.16 Relation between heat transfer ratio and absolute temperature ratio of: a) first regime (aspect ratios from 1 to 16), and b) second regime (aspect ratios from 0.0625 to 1).

By using certain exponents of the variables as conversion parameters, each set of curves for the two regimes can be collapsed into a single curve. Also from the similarity of the relationships of  $(Q_{conv}/Q_{rad})$  as a function of  $T_r$  it is possible to collapse these two regimes with different cold wall temperatures, enclosure sizes and with different fluid properties into a single curve.

### 5.5.3 The 3D numerical results

In order to ensure that the 2D numerical calculations described above are plausible, they should be compared with the experimental results. As the experimental results are 3D, the models that will be compared to the experimental ones must be run as 3D models. These calculations were performed for square and rectangular enclosures with three different aspect ratios 0.5, 1.0 and 2.0. Also the calculations were performed for different hot wall temperatures ranging from 50°C to 75°C with almost constant cold wall temperature at about 9°C. All the boundary conditions for the numerical simulation were selected to be almost the same as the experimental boundary conditions. The turbulent model used and its conditions were the same as that explained in detail earlier.

The numerical calculations were performed using the ANSYS 13 workbench software. The different enclosure shapes were designed using the design model in the ANSYS 13 work bench and then a non-uniform mesh was created for each enclosure aspect ratio using the ANSYS mesh; after that the numerical calculations performed using FLUENT 13 in the ANSYS workbench. The velocity and turbulent intensity profiles were extracted in each aspect ratio and for each hot wall temperature for different enclosure heights at  $y/h$  equal to 0.19, 0.3, 0.5, 0.65 and 0.85 to be compared with the experimental results.

In this section the 3D numerical results of the three aspect ratios and for the six hot wall temperatures were divided into two sections, first for thermal calculations and second for velocities and turbulent intensities profiles.

### 5.5.3.1 The 3D thermal results

The thermal calculations were established for both square and rectangular enclosures as can be seen in figure 5.17, with three different aspect ratios (0.5, 1.0 and 2.0) and for hot wall temperatures ranging from 50°C to 75°C while the cold wall temperature was kept fixed at about 9°C. The Rayleigh number for the three aspect ratios was in the range of  $9 \times 10^7 \leq Ra \leq 8 \times 10^9$ . The thermal results show that the total heat transfer as a function of absolute temperature ratio increases linearly for the three aspect ratios as the absolute temperature ratio increase this can be seen clearly in figure 5.18. Also from this figure it can be seen that, as the aspect ratio increases, the overall trend of the total heat transfer increases as a function of temperature ratio.

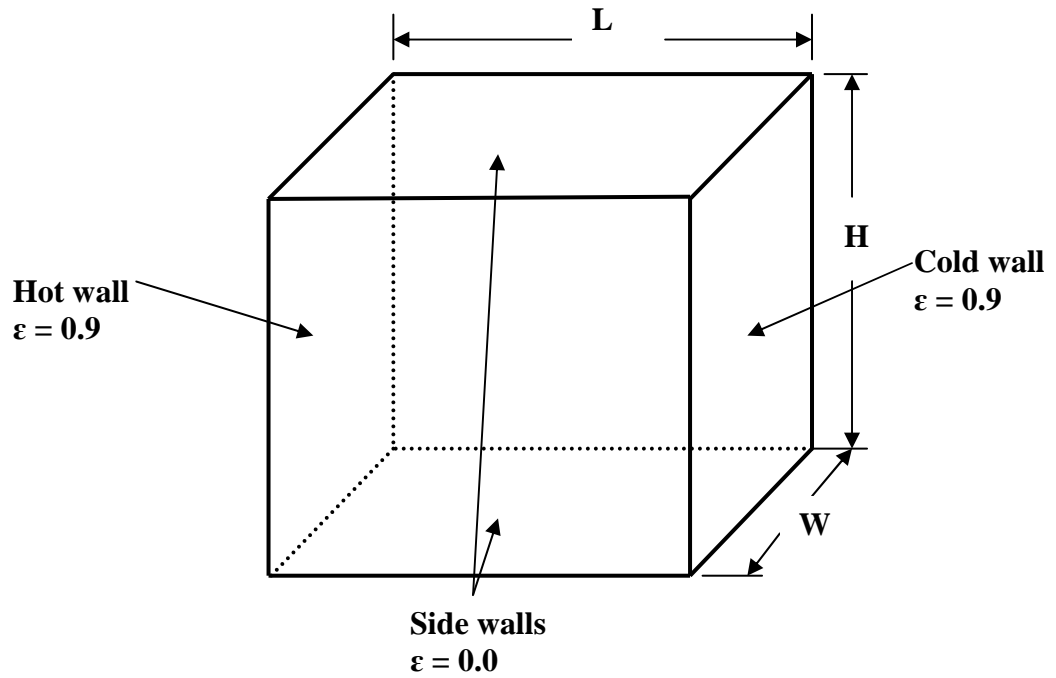


Figure 5.17 Schematic diagram for the three dimensional enclosure

### 5.5.3.2 The velocity and turbulent intensities results

The 3D numerical results provide velocity profiles for three aspect ratios at different enclosure heights. These velocity profiles will also be compared with the experimental results in the next chapters. To simplify the results the resultant velocity and turbulent intensity profiles are divided into two groups. The first group is for the velocity and turbulent intensity profiles for the two hot wall temperatures 60°C and 75°C which will



be shown and explained in this section for each aspect ratio. The other group includes the velocity and turbulent intensity profiles of the other hot wall temperatures 50°C, 55°C, 65°C and 70°C are in appendix A.

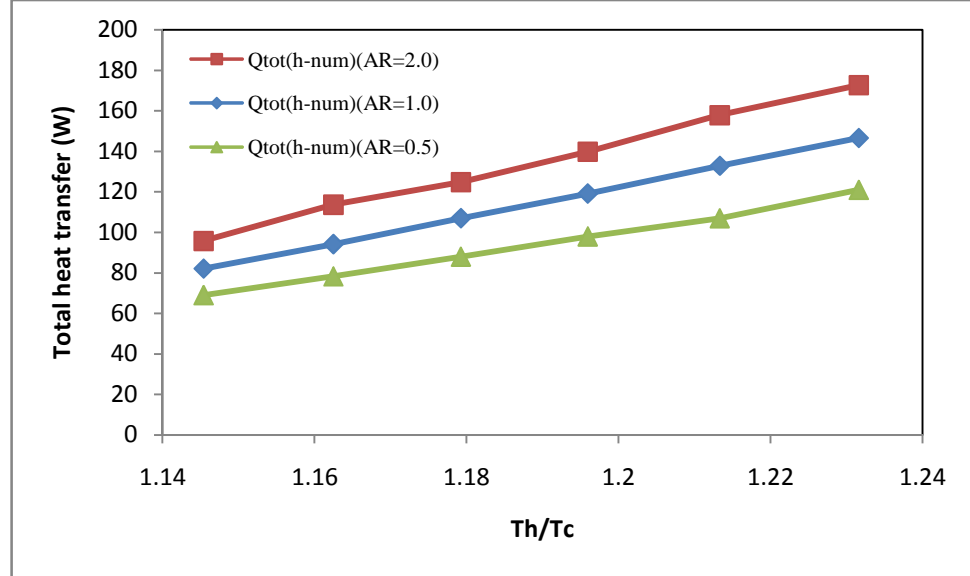
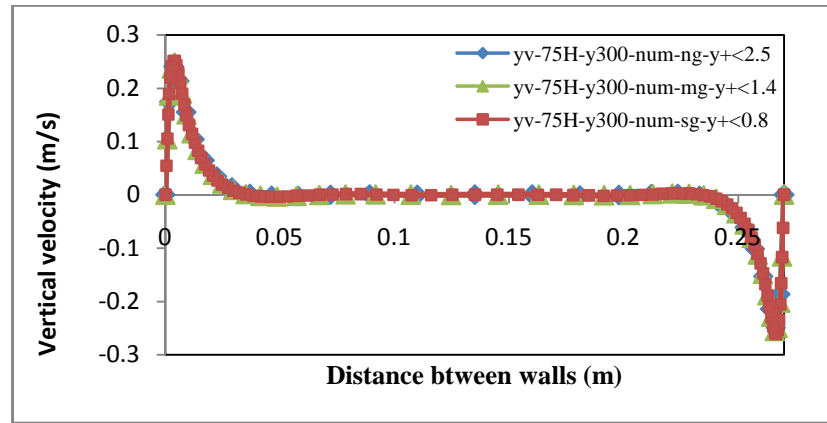


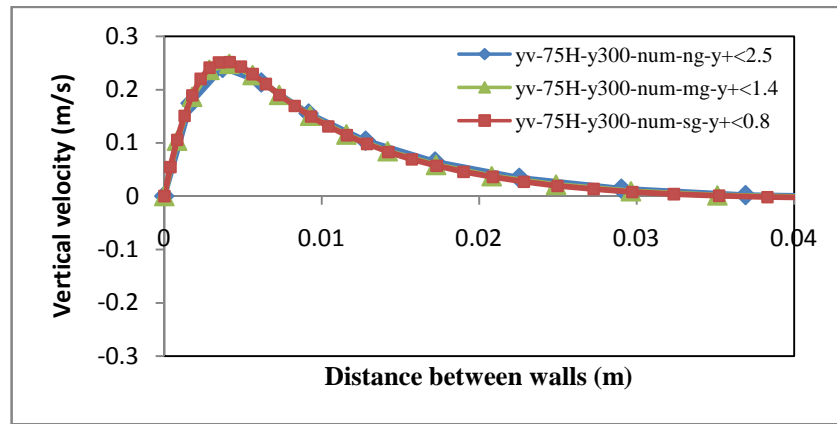
Figure 5.18 Total heat transfer inside the enclosure for aspect ratios 2, 1.0 and 0.5

The grid independence study for the velocity profiles was performed using three different grid sizes. The three grids have different number of cells and the first cell at the near wall region for each of them has certain distances from the wall according to the value of the  $y^+$ . The three grids have three values of  $y^+$  (<2.5, <1.4 and <0.8) respectively. The velocity profile at the mid-height was checked using the three different grids as it can be seen in figure 5.19. From the figure it can be seen that all the three grids have almost the same velocity profile. From the comparison of the three grids, the medium grid size was selected to be used in this study and compared with the experimental results because it has more velocity points near the wall than the first grid and less numerical cost than the third grid.

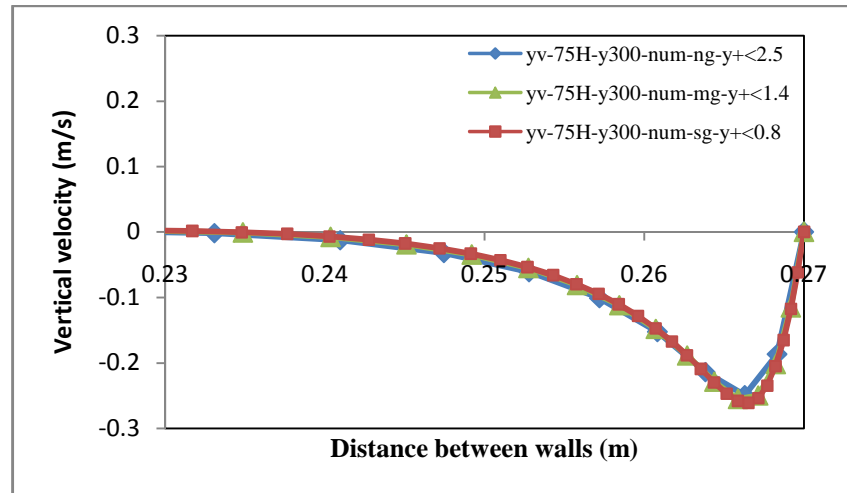
The velocity profiles for the three aspect ratios (AR=2.0, 1.0 and 0.5) at different enclosure heights for the hot wall temperatures of 60°C and 75°C, are shown in figures 5.20 to 5.25. From these figures it can be seen that at the hot wall side, the velocity value starts increase and reaches its maximum after a certain distance from the wall when it starts to decrease to its minimum; this is almost continuous for the whole enclosure core.



(a)

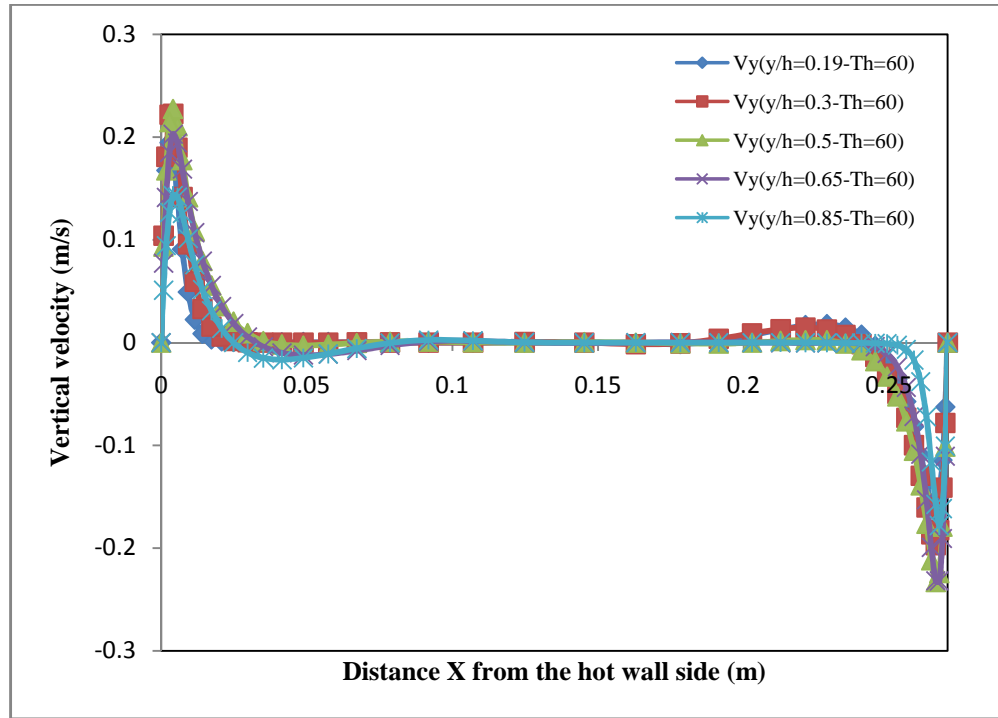


(b)

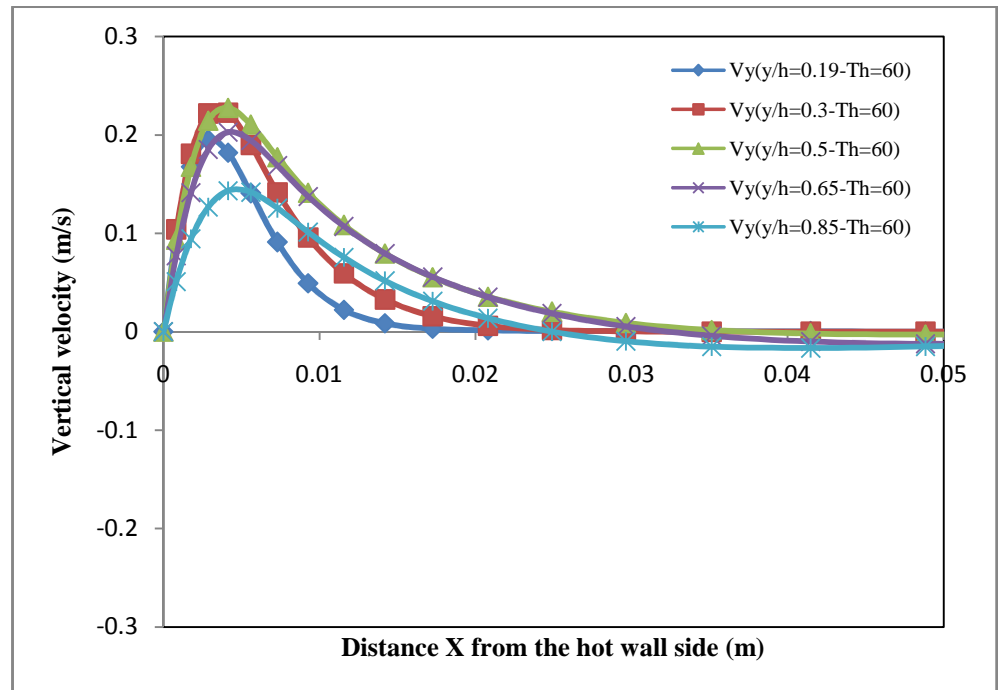


(c)

Figure 5.19 Velocity profiles at mid-height for aspect ratio 2.0 and 75°C hot wall temperature (a) between hot and cold walls, (b) near the hot wall and (c) near the cold wall

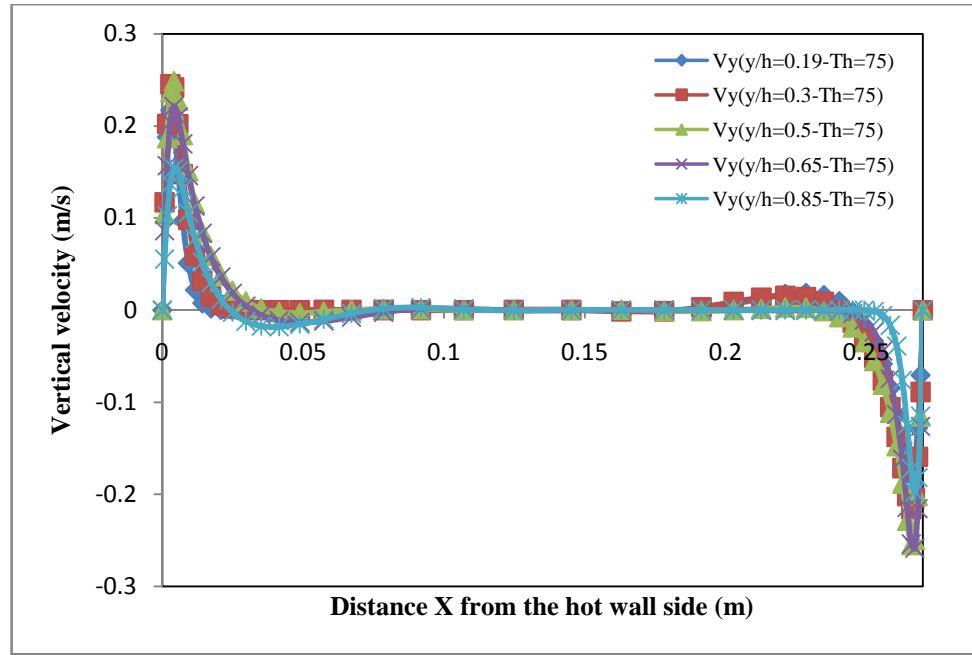


(a)

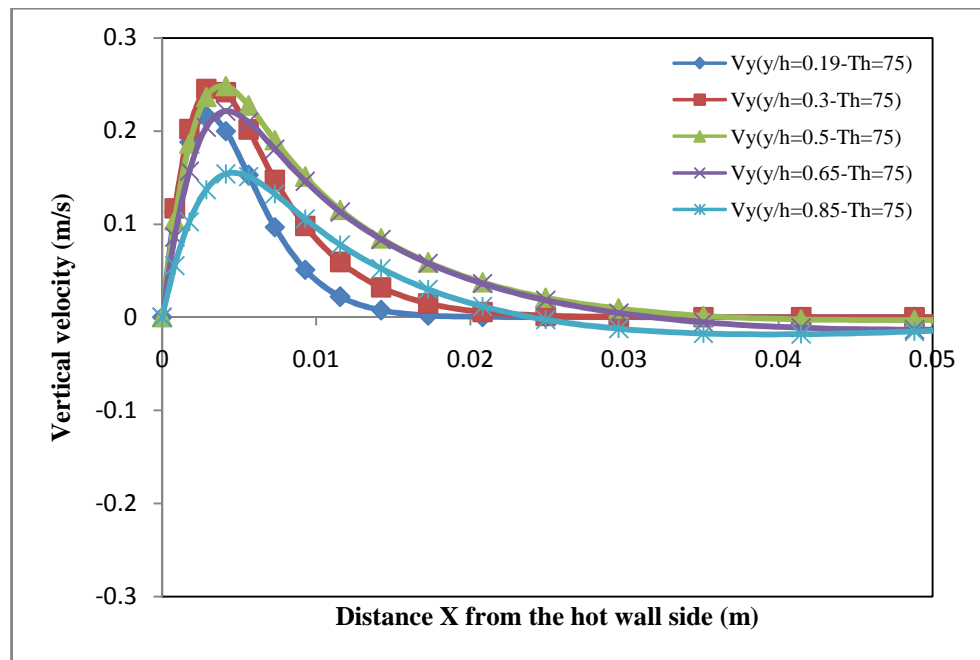


(b)

Figure 5.20 Velocity profiles for aspect ratio 2.0 and hot wall temperatures 60°C (a) between the two walls and (b) near the hot wall.

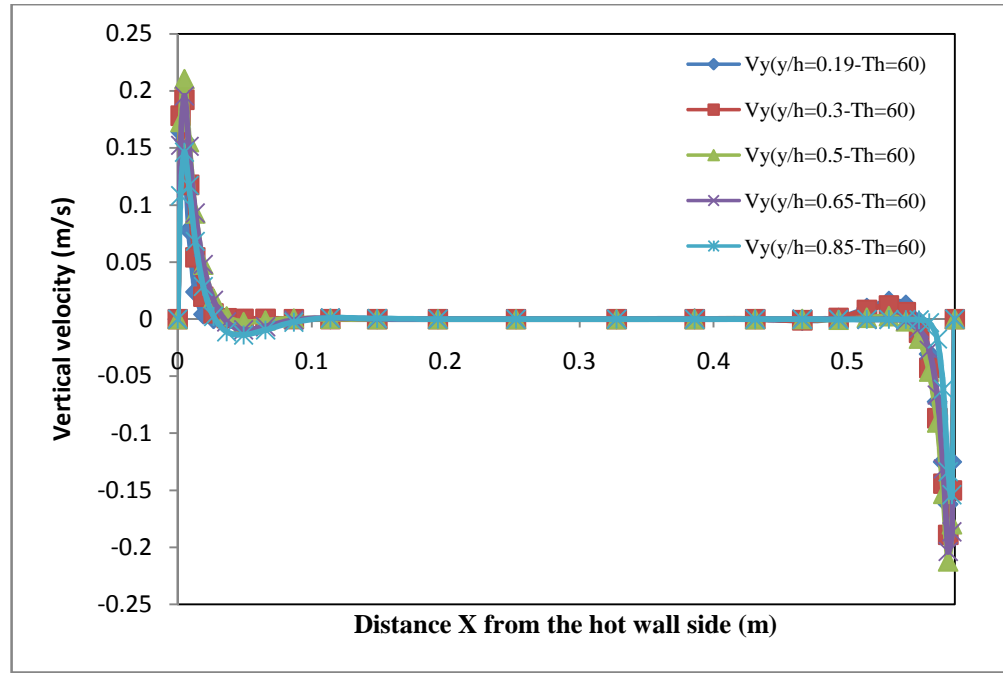


(a)

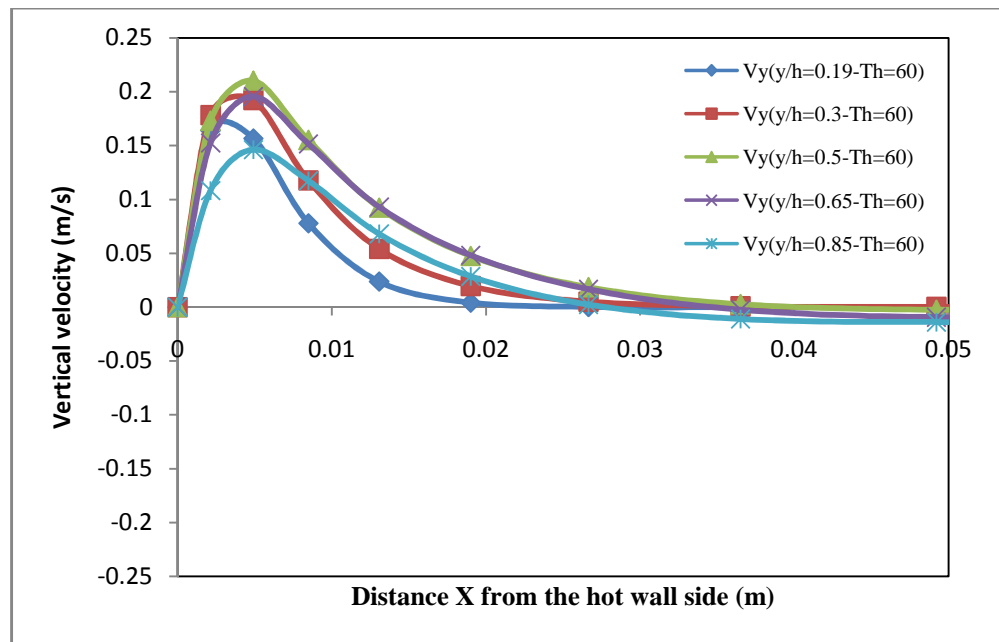


(b)

Figure 5.21 Velocity profiles for aspect ratio 2.0 and hot wall temperatures 75°C (a) between the two walls and (b) near the hot wall.

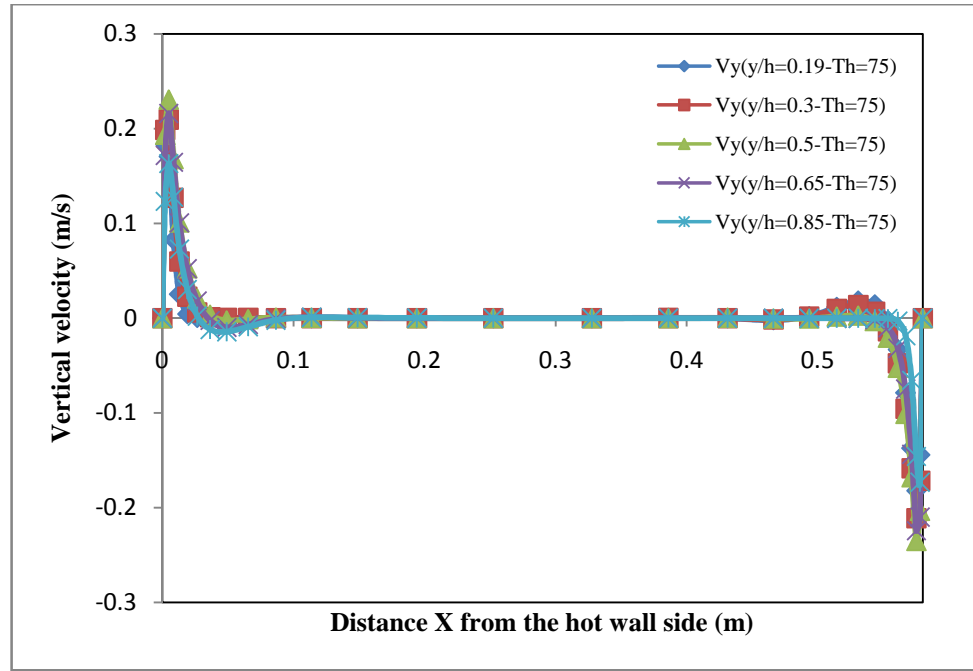


(a)

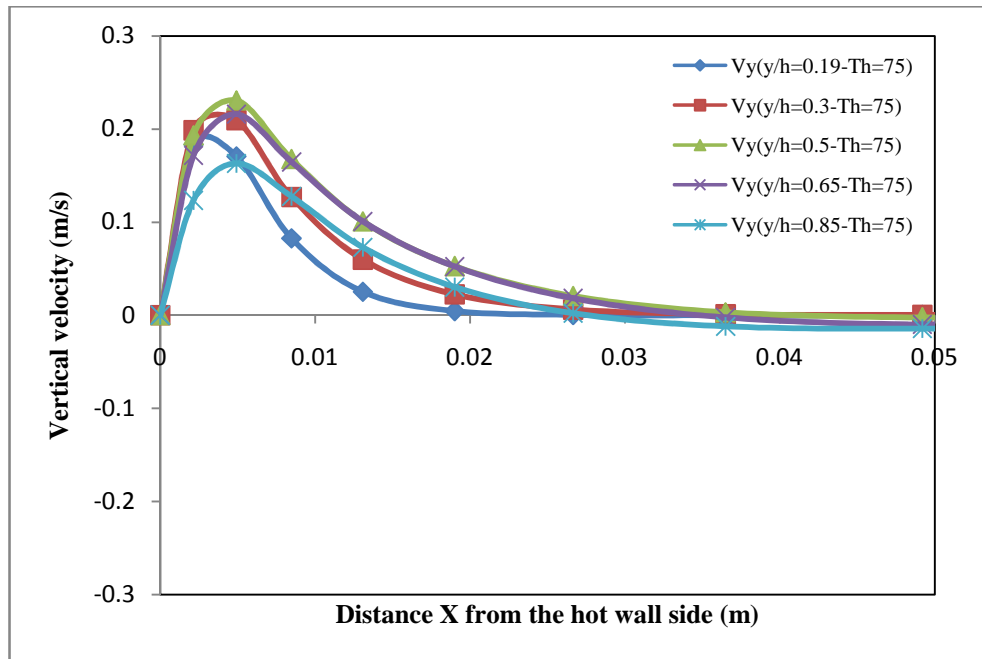


(b)

Figure 5.22 Velocity profiles for aspect ratio 1.0 and hot wall temperatures 60°C (a) between the two walls and (b) near the hot wall.

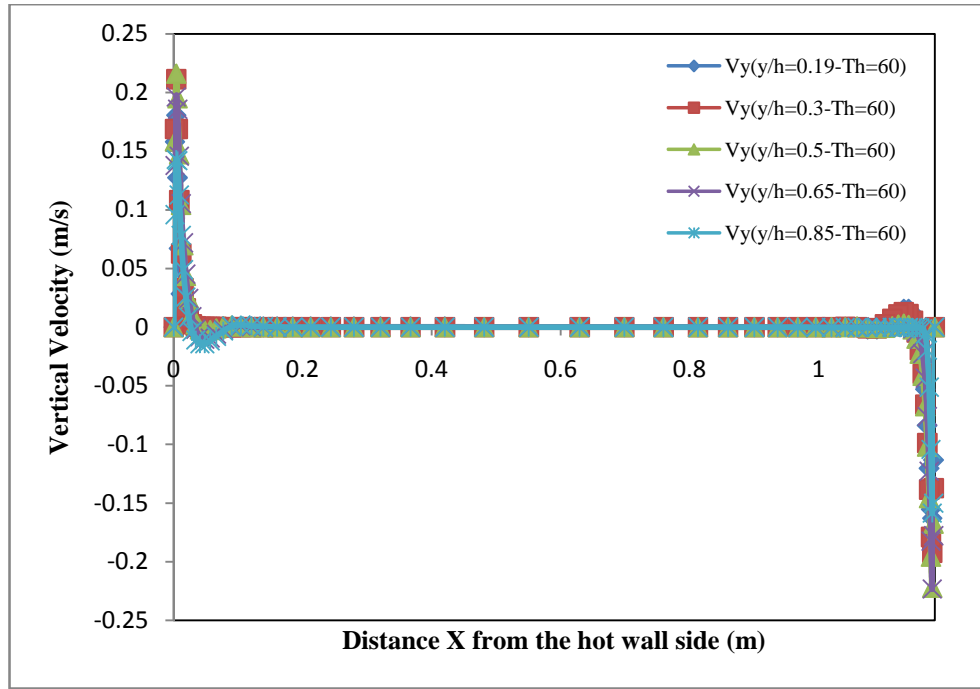


(a)

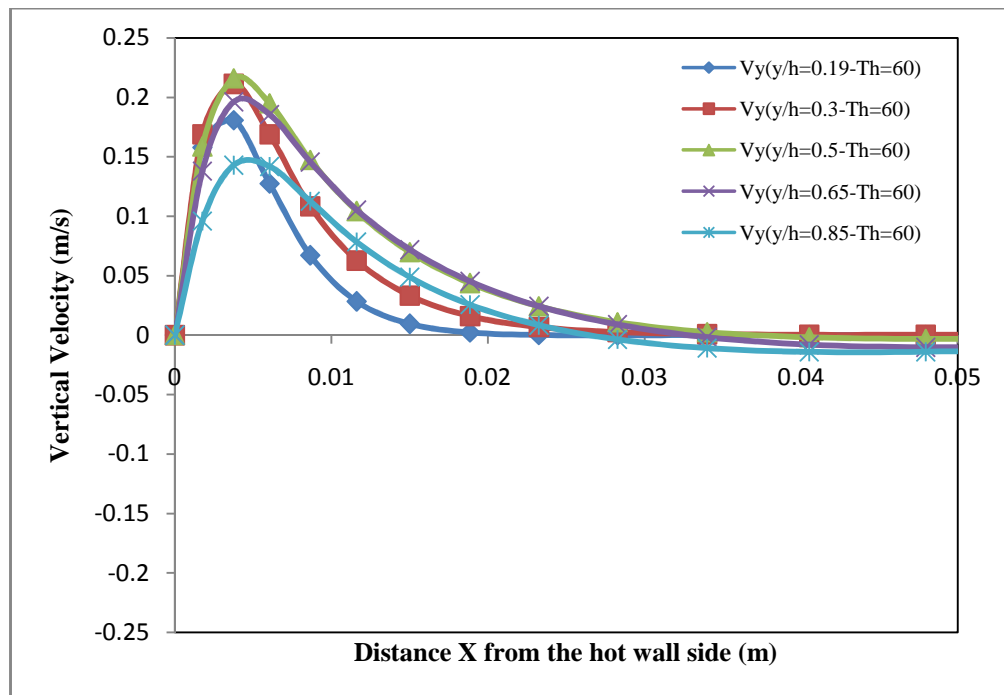


(b)

Figure 5.23 Velocity profiles for aspect ratio 1.0 and hot wall temperatures 75°C (a) between the two walls and (b) near the hot wall.

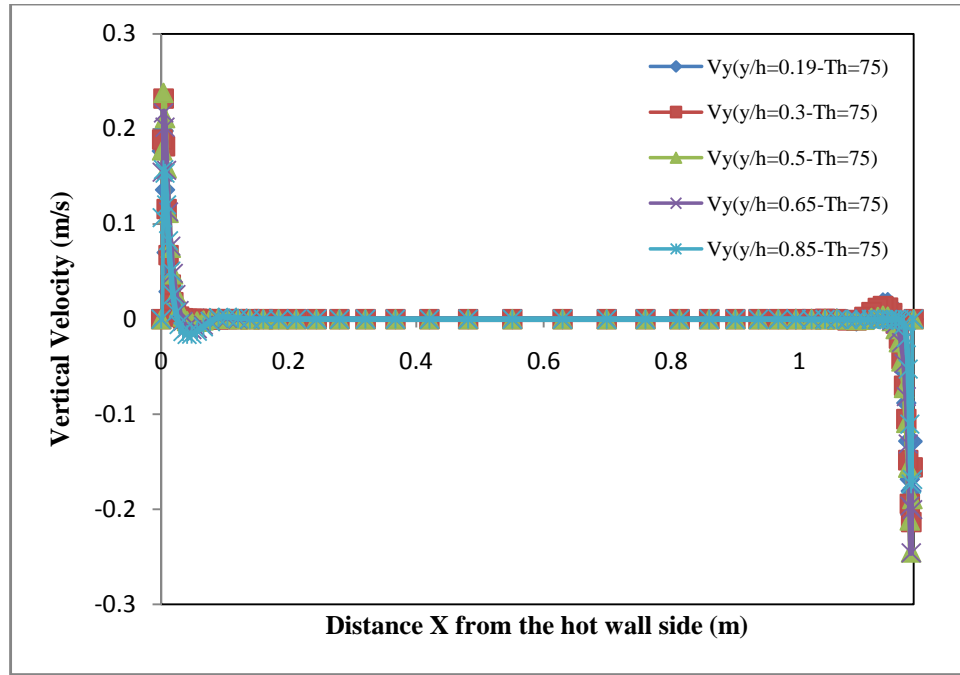


(a)

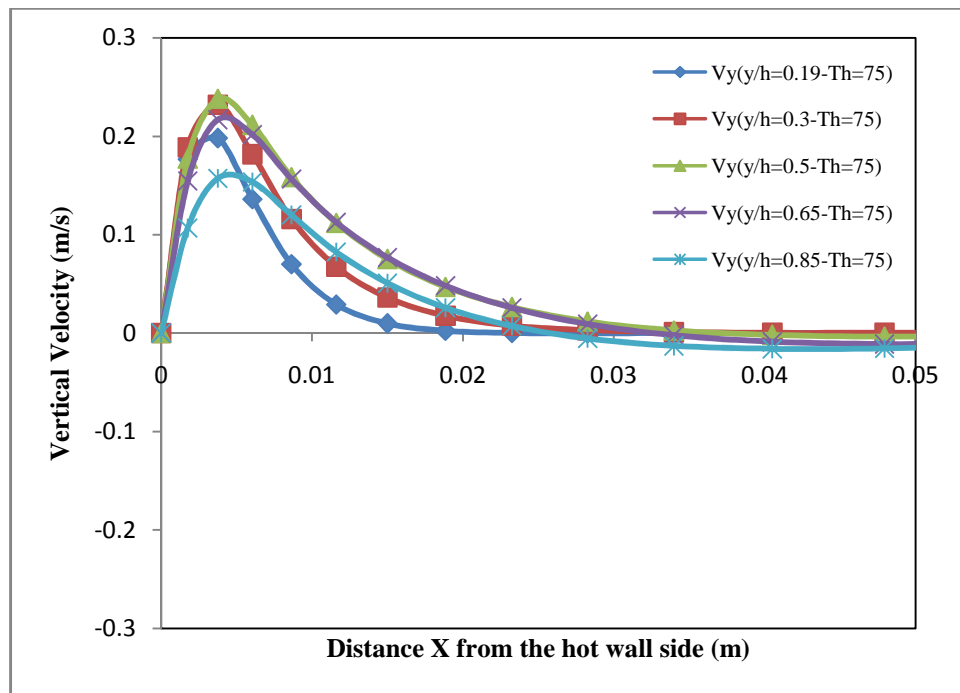


(b)

Figure 5.24 Velocity profiles for aspect ratio 0.5 and hot wall temperatures 60°C (a) between the two walls and (b) near the hot wall.



(a)



(b)

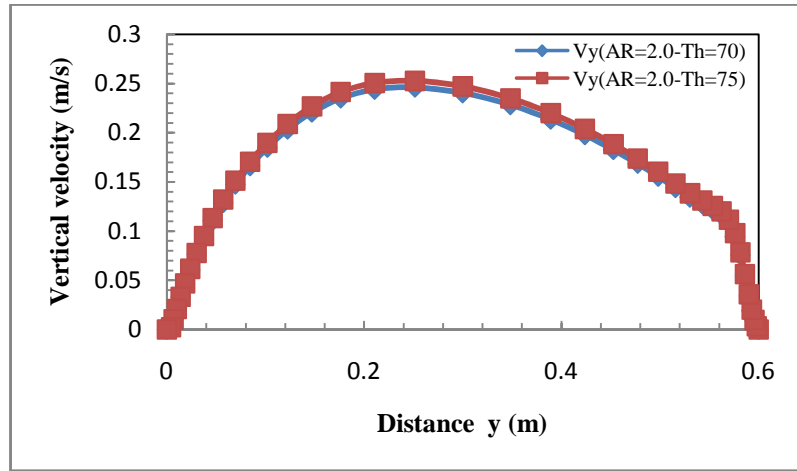
Figure 5.25 Velocity profiles for aspect ratio 0.5 and hot wall temperatures 75°C (a) between the two walls and (b) near the hot wall.



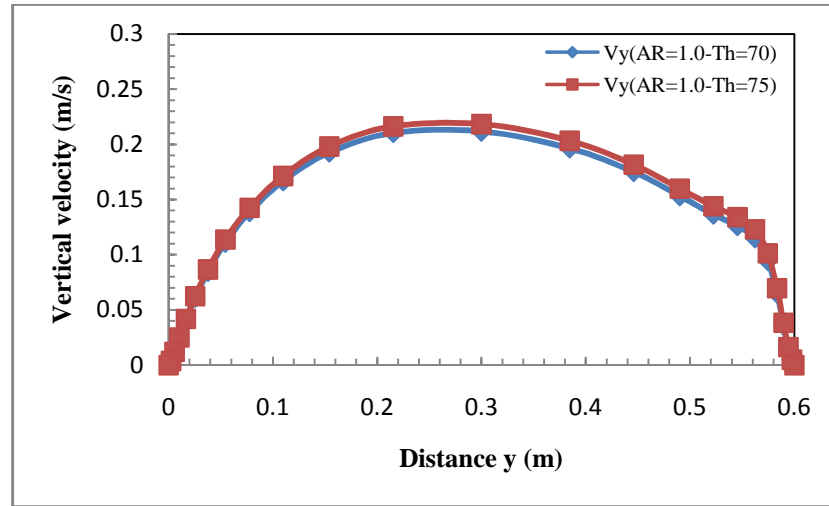
This velocity profile trend is the same for all enclosure heights and all aspect ratios. The same profile can be seen on the cold side where the velocity starts to increase to its maximum at a certain distance from the enclosure core; it then starts to decrease to a zero value at the wall. From the graphs it can be seen that the velocity values increase as the temperature increases for the same aspect ratio. Also from the figures, it can be seen that, at each aspect ratio the boundary layer thickness increases as the enclosure height increases until  $y/h$  becomes greater than 0.65 when the boundary layer thickness start to decrease. Moreover from the figures it can be seen that the velocity values increase as the enclosure height increases until  $y/h$  become greater than 0.5 when the velocity values start to decrease. Furthermore from the figures the velocity values increase as the aspect ratio increase. The maximum velocity for each aspect ratio occurs almost at or near the mid-height of the enclosure. The boundary layer thickness increases as the aspect ratio decrease.

The 3D numerical results data for the velocity and turbulent intensity profiles along the vertical axis and near the hot side are established at a position of a maximum velocity and for two hot wall temperatures 70°C and 75°C. The velocity profiles near the hot wall are shown in figure 5.26. From this graph, it can be seen that the maximum velocity occurs near or at the mid height of the enclosure. Here the velocity starts to increase from the lower edge of the enclosure until it reaches its maximum value near the enclosure mid height, when it starts to decrease again. Also from this figure, it can be seen that the velocity values at the lower part of the enclosure are smaller than that at the upper part for all aspect ratios. Moreover it can be seen from the figure the velocity profiles at the hot temperatures 70 and 75°C are quite similar for the three aspect ratios. The maximum velocity with an aspect ratio of 2.0 is greater than the other two aspect ratios.

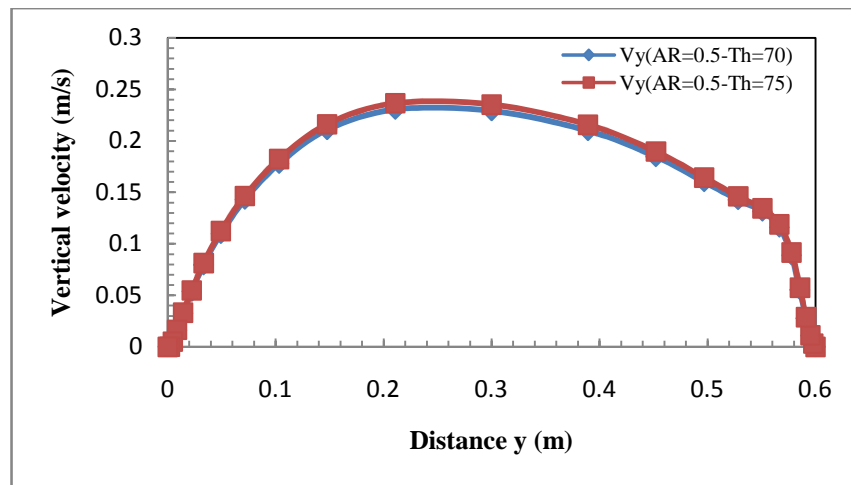
The 3D numerical results for the turbulence intensity for three aspect ratios and at different hot wall temperatures are again divided into the same two groups as the velocity profiles discussed above. The turbulence intensity profiles for the first group are shown in appendix A and that for the second group are shown in figures 5.27 to 5.29. From the figures it can be seen that the turbulent intensity values start to increase gradually from the wall side until they reach a maximum value after a certain distance from the wall, when it starts to decrease to its minimum value. Also from the figures, it can be seen that, at the same aspect ratio, the turbulence intensity increases as the temperature increase also increases as the aspect ratio increases.



(a)

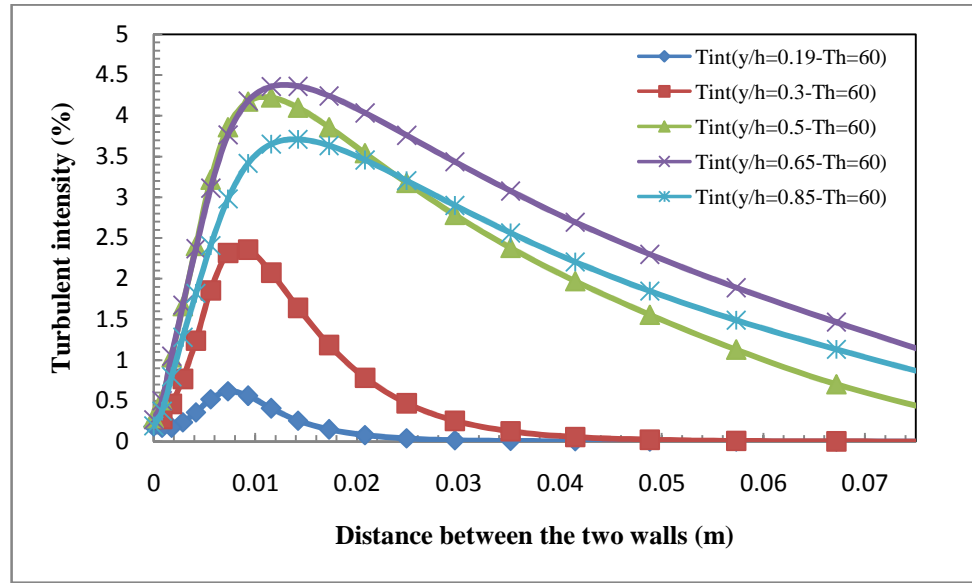


(b)

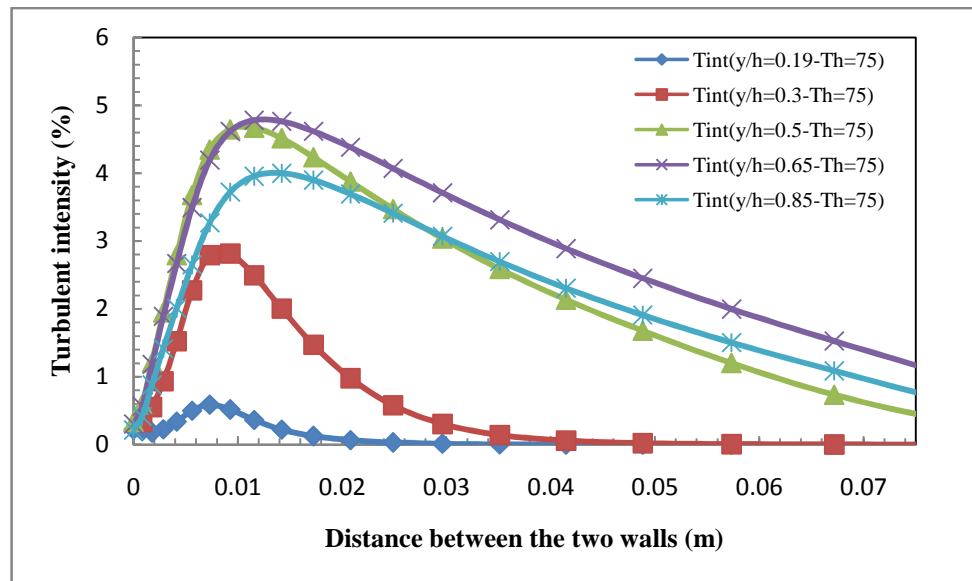


(c)

Figure 5.26 Velocity profiles near the hot wall for aspect ratios a) 2.0, b) 1.0 and c) 0.5

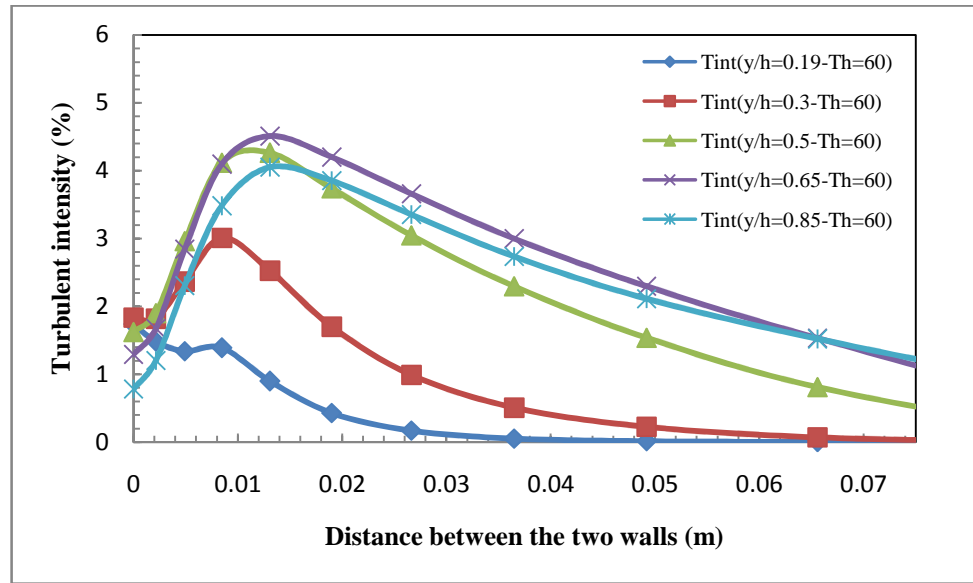


(a)

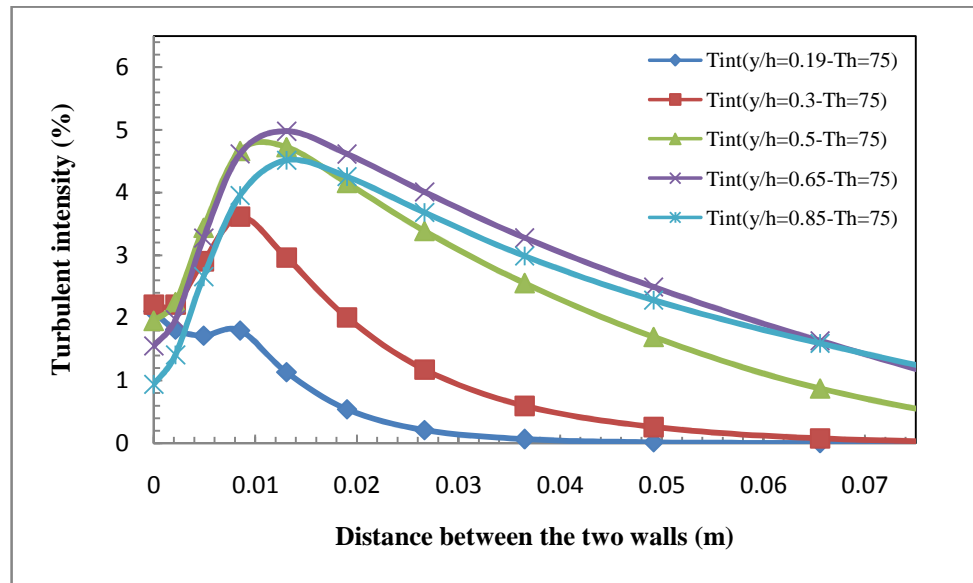


(b)

Figure 5.27 Turbulent intensity profiles for aspect ratio 2.0 and for hot wall temperature  
a) 60°C and b) 75°C

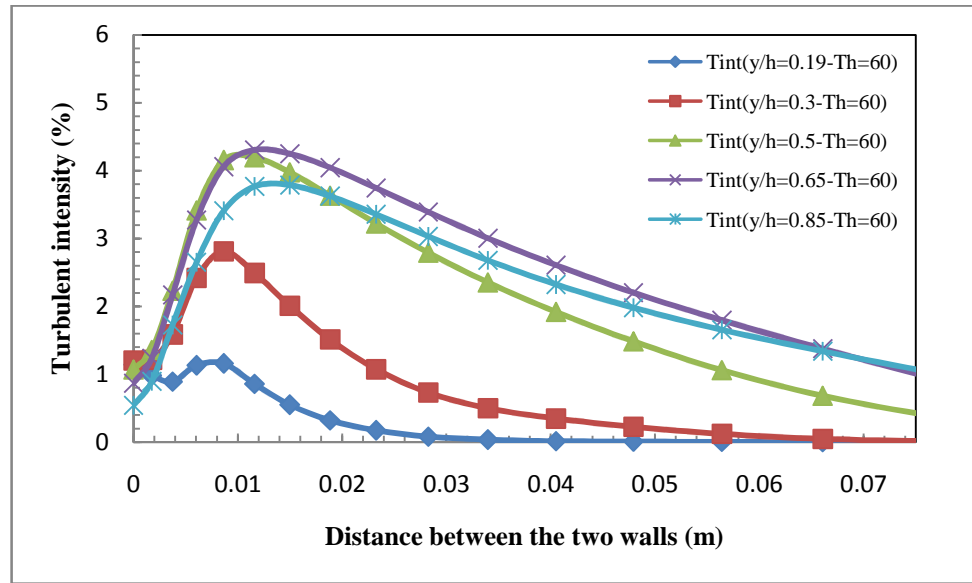


(a)

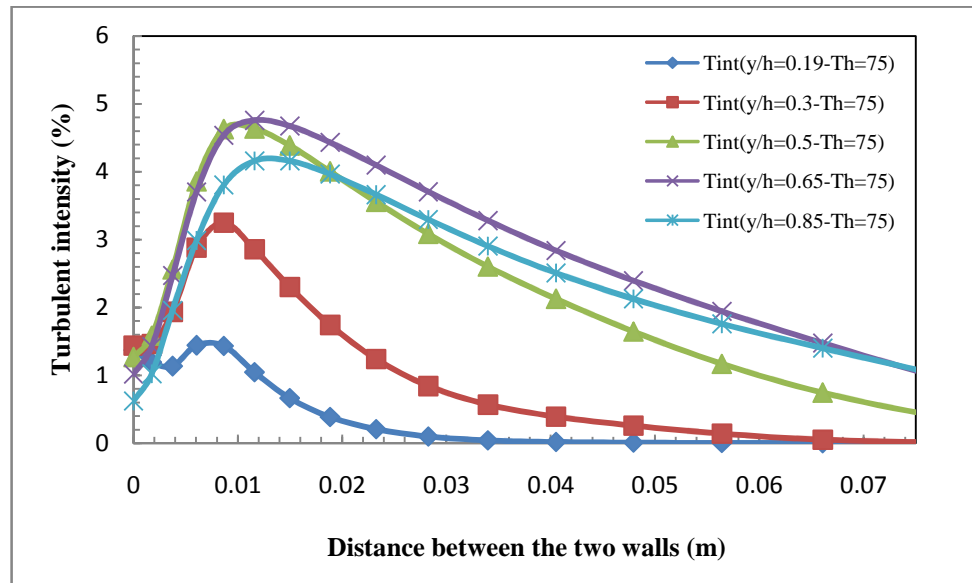


(b)

Figure 5.28 Turbulent intensity profiles for aspect ratio 1.0 and for hot wall temperature  
a)  $60^\circ\text{C}$  and b)  $75^\circ\text{C}$



(a)



(b)

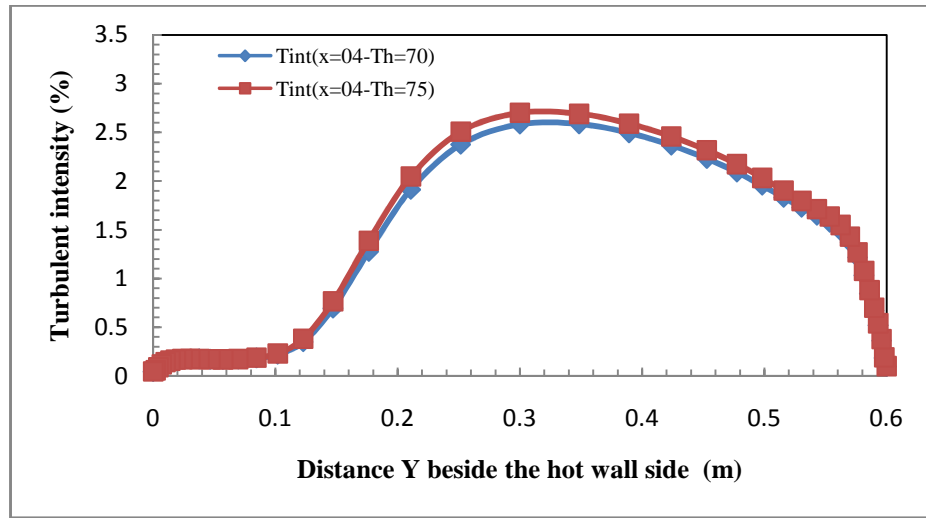
Figure 5.29 Turbulent intensity profiles for aspect ratio 0.5 and for hot wall temperature  
a) 60°C b) 75°C

The turbulent intensity along the vertical axis and near to the hot wall at the position of maximum velocity is shown in figure 5.30. From this graph it can be seen that the maximum turbulence intensity occurs near the mid height of the enclosure, where the turbulence intensity starts to decrease until it reaches its minimum value near the enclosure edges. Also from this figure it can be seen that the turbulence intensity values for all of the results decrease as the aspect ratio increases or decreases from unity. Moreover from the figure it can be seen that the turbulence intensity at the lower part of the enclosure is much smaller than at the upper part. It can be seen from figure 5.30a that the turbulence intensity of the aspect ratio of 2.0 at the lower part of the enclosure has a constant and small value for the first 100 mm compared to the other two aspect ratios.

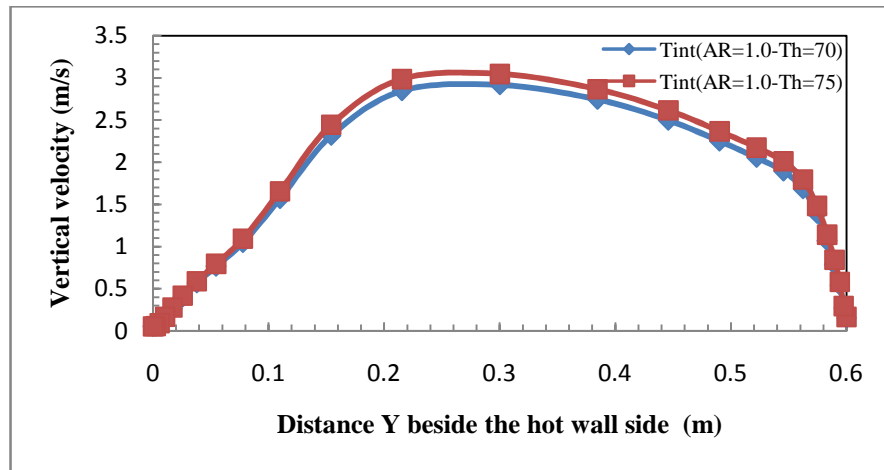
## **5.6 Summary and Conclusions**

The turbulent flow and turbulence properties are discussed and explained in this chapter. The turbulent flow is generated from laminar flow when the flow starts fluctuating and this instability develops as the Reynolds number increases. In natural convection heat transfer the flow inside cavities is dominated by the buoyancy forces which measured using the Raleigh number and by which the flow is known as laminar or turbulent. Turbulence models are used to solve the time averaged governing equations to obtain the unknown variables. The different turbulence models used for different classes of problems depend on the physics of the flow for that problem. The RNG k- $\epsilon$  model was chosen to be used and analyse the turbulent flow inside the enclosure in this study. This turbulence model is sufficiently accurate and reliable for a wider class of fully enclosed air flows and was recommended by many researchers to be used in such flows. The governing equations and boundary conditions of the RNG k- $\epsilon$  model were discussed in detail in this chapter. The grid independence has been studied. The model used has been validated by comparison with previous experimental and numerical results and shown to be adequate for the purposes that follow.

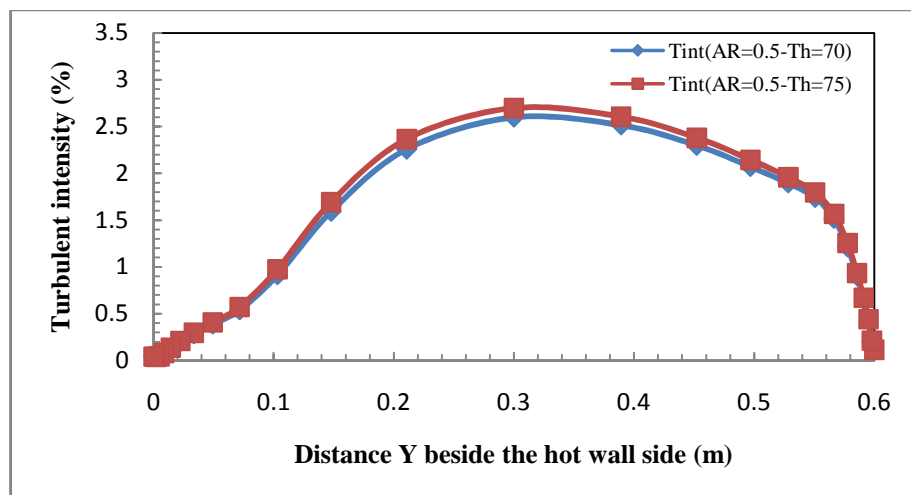
Also in this chapter, the numerical results of turbulent natural convection with and without the interaction of surface thermal radiation in square and rectangular enclosures have been analysed with different fluids, enclosure sizes, aspect ratios and cold and hot wall temperatures. The main conclusions from this section can be summarized as follows:



(a)



(b)



(c)

Figure 5.30 Turbulent intensity profiles near the hot wall for aspect ratios a) 2.0, b) 1.0 and c) 0.5

The Nusselt number as a function of absolute temperature ratio increases as the aspect ratio decreases. The average Nusselt number increases as the absolute temperature ratio increase up to a certain value of  $T_r$  (which is around 1.2 for both regimes) then it start to slightly decrease.

The new dimensional group as a function of absolute temperature ratio decreases slightly as the aspect ratio increases in the first regime and it increases dramatically as the aspect ratio decreases in the second regime.

The ratio between the convection and radiation heat transfer is increased by increasing the absolute temperature ratio up to a absolute temperature ratio of 1.2; then this ratio starts to decrease. It was shown that the ratio between Rayleigh number and Nusselt number follows a similar trend.

3D numerical calculations were conducted for square and rectangular enclosures with three different aspect ratios 0.5, 1.0 and 2.0 and for a hot wall temperatures ranging from 50°C to 75°. The results show that the total heat transfer increases as the temperature of the hot wall increase.

More clear conclusions will be extracted when these numerical results are compared with the derived correlation equations and the experimental results in the next chapters.



# CHAPTER 6

## Experimental Rig and Results

### 6.1 Introduction

In this chapter the description of the cavity, the thermocouples and data logger and the laser Doppler velocimetry will be discussed in detail. During the course of the experiments many modifications were made to the cavity to reduce the heat losses through the walls, to the hot and cold side loops to improve the control of the wall temperatures and in the laser Doppler velocimetry to improve the collected data by changing the controls and the seeder type and seeding time.

In this chapter the description of experimental test rig and the results are divided into four sections. The first section deals with the cavity design and the description of how three aspect ratios 2, 1 and 0.5 were created. Also this section will include the description of the design of the hot and cold loops and their temperature control.

The second section describes the thermal results which were collected using thermocouples mounted at the hot and cold sides. These results include the heat transfer calculations from the hot and cold sides and the heat losses through the walls for different temperatures and different aspect ratios.

The final section describes the specifications of the laser Doppler velocimetry (LDV) and its use in a series of experiments. Also this section includes data collected using the LDV. These results are for the velocity and turbulent intensities profiles. The last section will be a summary and the conclusions of this chapter.

### 6.2 Test cavity

The cavity or the enclosure consists of six walls, a hot side, a cold side and four side walls. The cavity has three configurations; these three configurations form three different aspect ratios, and in each of them the only change in the enclosure design will

be the length of the top and bottom walls (the hot and cold sides will be kept fixed in size). The enclosure is designed using a polystyrene board of a 120mm thickness and two layers of cavity wall double insulation, one from inside and another layer from outside. The temperatures of the hot and cold side walls were controlled using PID controllers.

### 6.2.1 Specifications and cavity design

The cavity is designed using polystyrene boards of thickness 120mm as shown in figure 6.1. These boards were cut to different sizes to form the cavity shapes for different aspect ratios.



Figure 6.1 Polystyrene board of thickness 120mm.

As an example, the design of the cavity of aspect ratio 0.5 will be explained in detail here. The polystyrene boards come in a standard size of 2400x1200x120mm and to form the cavity of inside dimensions 600x1200x600mm the board was cut to the following sizes; four walls being 600x1220x120mm and four pieces being 120x120x1220mm to form the four side walls. The base of the enclosure is connected and fixed to its size dimension using the steel frame with the hot and cold sides

connected to them and to the lab fixed steel base. All the other walls are mounted and connected initially to each other using the duct tape. This can be seen from figures 6.2 and 6.3 which show the cavity of aspect ratio 0.5 with the two hot and cold side walls.



Figure 6.2 The polystyrene four side walls for aspect ratio 0.5

The four side walls have aluminium foil stick on them from the inside to get a minimum emissivity on the inside surfaces of the enclosure. To fix tightly and remove the gaps between them the four side walls and the hot and cold walls, they were connected to each other using duct tape, and were gripped and connected to each other using a band clamp which can be seen in figure 6.4, this was to reduce the losses through the gaps between the walls to minimum. The heat losses are the heat transfer to the enclosure structure and then through the cavity walls or gaps to the surrounding air.

The losses through the gaps between the walls were quite high (in some cases reaching more than 50% of the total heat transfer of the hot side). Later two additional layers of cavity wall double insulation were added to the enclosure walls to reduce these losses. The first layer was connected from inside of the enclosure where it fitted to the four sides of the enclosure from inside and was connected and sealed to the four edges of the hot and cold side walls, as seen in the schematic diagram figure 6.5. The second layer of the cavity wall double insulation was fitted and connected from outside of the

enclosure where it was fitted and connected to the six sides of the enclosure and covered the whole enclosure; this also can be seen again in figure 6.5.



Figure 6.3 The cavity with aspect ratio 0.5 after assembling all the walls

Using these two layers of cavity wall double insulation reduced the heat losses dramatically. For example, the heat losses for the case of an aspect ratio 2.0 were around 50% of the total heat transfer of the hot side; after using the two additional layers of cavity wall double insulation, the heat losses through the walls were reduced to less than 12.5% with a minimum of 5.3%.

To this end these are promising results which giving a good thermal results with less heat losses compared to other researchers who struggled to get these low losses through the walls. King [57], report results from 7 experiments which show heat losses through the walls of between 22.8% and 48.0% with an average of 34.4%. In the present study the heat losses for 18 experiments were between 5.3% and 39.9% with an average of 17.3%.





(a)



(b)

Figure 6.4 Using the band clamp to connect the cavity walls together a)-  $AR=1$ . b)-  $AR=2.0$

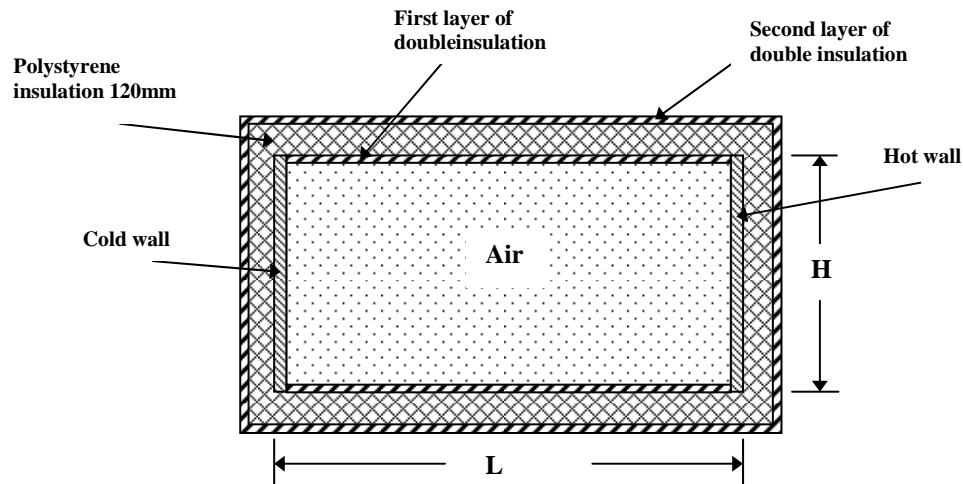


Figure 6.5 Schematic diagram of the enclosure with the hot and cold sides and all the insulation layers.

### 6.2.2 Hot side loop

The hot side of the cavity is a flat plate single panel radiator with standard dimensions, being 600mm high by 600mm wide arranged and supported by a steel frame as shown in figure 6.6. The radiator was insulated to a thickness of 120mm on the back side using polystyrene boards and the gap between the radiator and the polystyrene board was filled using expanding foam insulation.

A simplified hot water central heating system was constructed and connected to the radiator. A diagram of the hot side circuit setup is shown in figure 6.7. The heat input device was a 3kW immersion heater. To keep the temperature steady (to within  $\pm 0.1^\circ\text{C}$ ) in accordance with the European standard EN 442-2 [106], a PID temperature controller was fitted to the heater to match the energy input to the heater (and hence the water) with the heat being taken from the tank and removed in the hot radiator. This occurs by switching the heater on and off depending on the temperature inlet to the system. The PID controller provides proportional, integral and derivative control, and has been adjusted to automatically compensate for temperature changes in the system.



Figure 6.6 The steel frame used to fix and support the radiator.

The temperature at the inlet of the hot radiator side was measured using a T-type thermocouple which was connected to the PID controller and this temperature is compared to the setting point of the PID controller and from this difference the PID controller compensates and matches the energy input to the heater to get both temperatures the same to within  $\pm 0.1^{\circ}\text{C}$ . The flow rate was measured using a glass tube rotameter which was connected to the outlet of the radiator. The water was circulated by a standard central heating pump. The water flow rate was controlled through the use of a bypass and valves as shown in the schematic diagram figure 6.7. Using the bypass and the valves, the flow rate was adjusted and controlled for each inlet hot temperature. The water in the hot side enters the radiator from the top side and exits from the bottom side according to the British standard BS-3528-1977 [107].

The water temperature at each measuring point just before and after the radiator was measured using three T-type thermocouples attached to the surface of the pipes, which were insulated with 25mm thick foam as can be seen in figure 6.8. The pipes were assumed to be at the same temperature as the hot water. The six thermocouples were attached to a PC through a USB based data acquisition system, so it was possible to

monitor and record the temperatures at a suitable sampling rate, which was selected to be every five seconds.

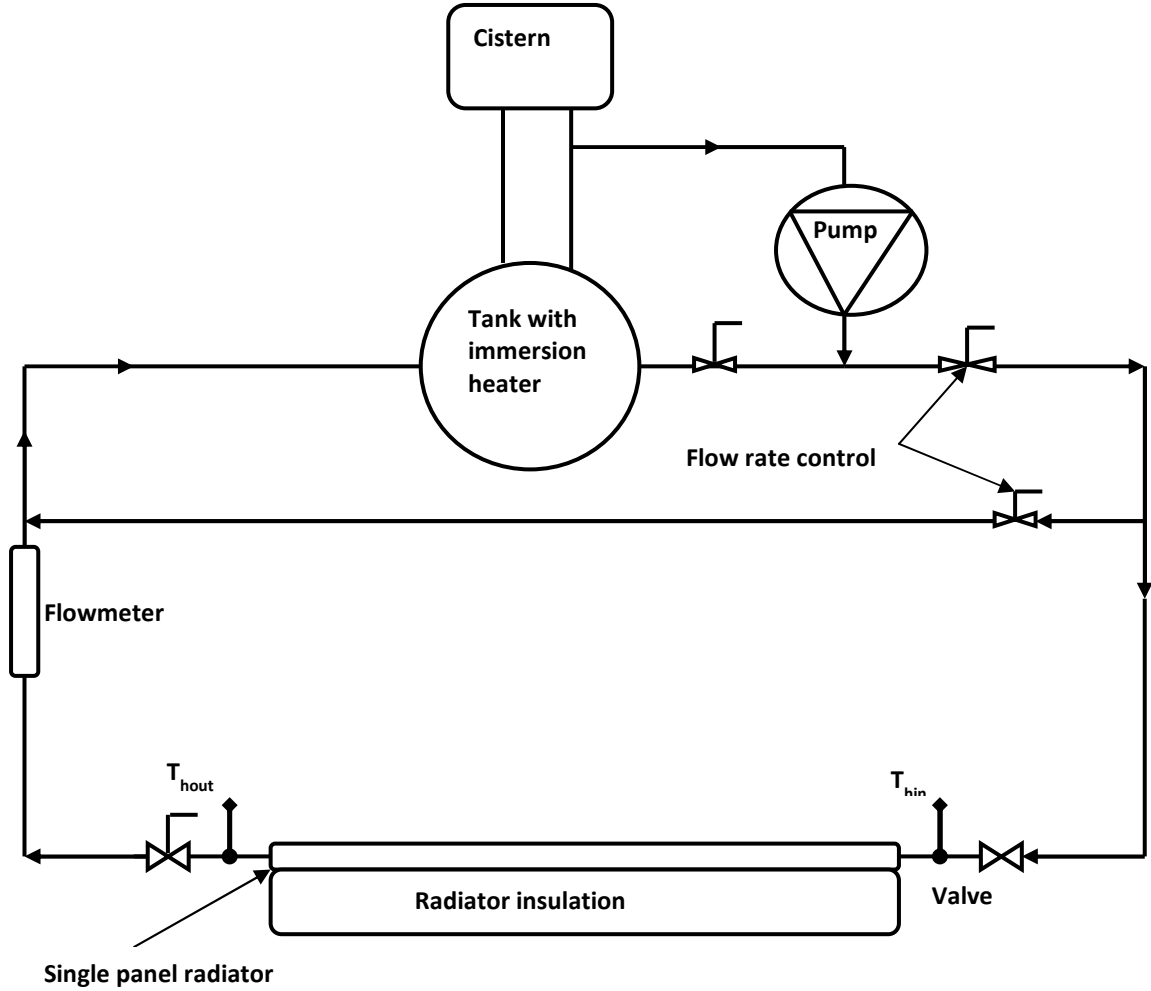


Figure 6.7 Schematic diagram of radiator hot water side.

In this study the PICO USB TC-8 data logger and Picolog data acquisition software were used to measure and save the collected data at each sampling rate [108, 109]. Each experiment starts by opening a new file for each inlet hot temperature, this file is used to monitor and collect the data for the hot side. The average temperature of the three inlet thermocouples and the three outlet thermocouples of the radiator were recorded as  $T_{hin}$  and  $T_{hout}$  respectively.



Tests were carried out for each aspect ratio and for each six inlet hot water temperatures to the radiator, these hot temperatures are from 50C° to 75C° in increments of 5C°, to measure and compare the total heat transfer from the hot side to that from the cold wall side inside the enclosure. The total heat transfer from the hot wall side of the cavity (radiator) can be calculated using the following equation:

$$\dot{Q}_{tot(h)} = \dot{m}_h C p_h (T_{hin} - T_{hout}) \quad (1)$$

Where  $\dot{Q}_{tot(h)}$  is the total heat transfer rate from the hot side of the enclosure.

$C p_h$  is the specific heat of the hot water side and it calculated using the following polynomial equation which based on the mean temperature  $T_{mean(h)}$  of the two hot side temperatures and the water properties from [1].

$$C p_h = -5.04 \times 10^{-8} T_{mean(h)}^5 + 1.65 \times 10^{-5} T_{mean(h)}^4 - 2.04 \times 10^{-3} T_{mean(h)}^3 + 0.128 T_{mean(h)}^2 - 3.84 T_{mean(h)} + 4221.3 \quad (2)$$

$$T_{mean(h)} = \frac{T_{hin} + T_{hout}}{2} \quad (3)$$

Where  $T_{hin}$  is the water inlet hot wall temperature and  $T_{hout}$  is the water outlet hot wall temperature.

$\dot{m}_h$  is the hot water mass flow rate which is calculated using the following equation

$$\dot{m}_h = Q_h \rho_h \quad (4)$$

Where  $Q_h$  is the volumetric flow rate of the hot water and calculated using the following polynomial equation:



Figure 6.8 The insulated thermocouples at the hot side exit.

$$Q_h = 1.628 \times 10^{-4} Q_o^2 + 2.738 \times 10^{-2} Q_o + 0.1448 \quad (5)$$

Where  $Q_o$  is the scale reading of the rotameter volumetric flow rate in cm, this rotameter is a glass tube graded from zero to 30cm, and these values are corresponding to a volumetric flow rates from zero to 1.2 L/min respectively as it can be seen in figure 6.9, where the polynomial equation (5) was provided based on the data from this figure. This figure is produced using the calibration of the rotameter by recording the time using stop watch and weighing the water using a digital scale for the whole rotameter measuring range.

$\rho_h$  is the water density for the hot wall side and it calculated using the polynomial equation shown below, where it also based on both the mean temperature of the inlet and outlet hot wall temperatures equation (3) and the water properties as a function of temperature from [1].

$$\begin{aligned} \rho_h = & -1.89 \times 10^{-7} T_{mean(h)}^4 + 5.39 \times 10^{-5} T_{mean(h)}^3 - 8.43 \times 10^{-3} T_{mean(h)}^2 \\ & + 0.075 T_{mean(h)} + 999.68 \end{aligned} \quad (6)$$

The calculation of  $\dot{Q}_{tot(h)}$  was done for a range of surface temperatures ranging from 50C° to 75C° with an increment of 5C° and for three aspect ratios 2.0, 1.0 and 0.5.

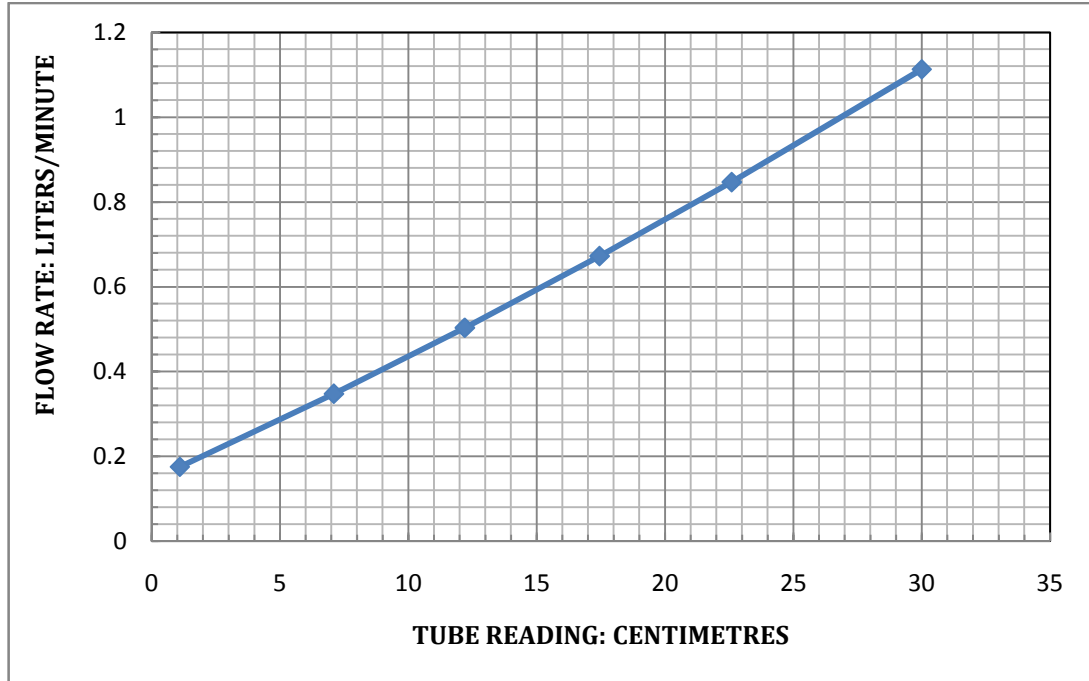


Figure 6.9 The rotameter chart 10 metric.

### 6.2.3 Cold side loop

The cold side of the cavity is also a flat plate single panel radiator with standard dimensions of 600mm high by 600mm wide, supported using a steel frame as shown in figure 6.6. The radiator was also insulated from the back to a thickness of 120mm using polystyrene boards and the gap between the radiator and the polystyrene board was filled using expanding foam insulation. The inlet and outlet of the radiator was connected to a recirculating chiller, (NESLAB CFC-FREE CFT-75) as shown in figure 6.10, to maintain the water inlet of the cold wall temperature fixed at about 8°C. The cooling unit has an air-cooled refrigeration system. Air is drawn in the front side of the unit and discharged through rear and side as seen in figure 6.11. For proper operation, the unit needs to pull substantial amount of air through a condenser. The plumbing connections are located on the rear of the unit and labelled as SUPPLY which will be connected to the radiator inlet and RETURN which will be connected to the radiator outlet.



Figure 6.10 The NESLAB CFT-75 recirculating chiller.

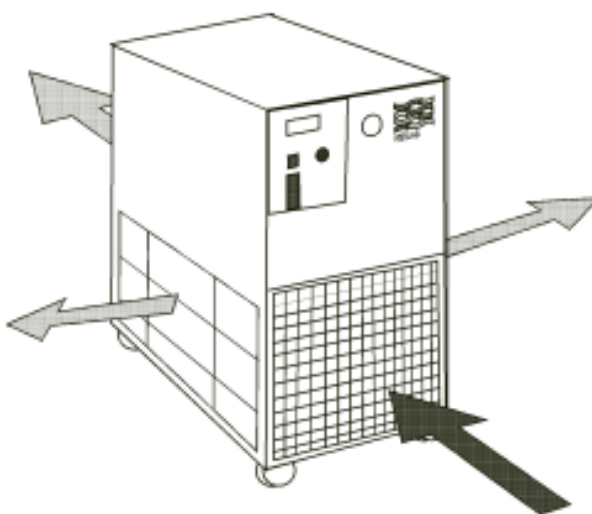


Figure 6.11 Draw and discharge the air in the cooling unit.

Before starting the unit the reservoir need to be filled with a clean cooling fluid, the tap water is the recommended fluid for operation. The tank has a vent which relieves pressure when it is built up and reaches 3-5psi. The CFT recirculating chiller is designed to provide a continuous supply of cooling fluid at a constant temperature and volume [110]. The unit consists of an air-cooled refrigeration system, a sealable reservoir, recirculating pump, and a temperature controller. The cooling capacity of the unit is 2500W with a temperature range of +5°C to +30°C. The temperature set-point is adjusted by pressing and holding the DISPLAY switch and then turning the ADJUST knob until the desired temperature set-point is indicated on the digital display [110].

The water temperature before and after the radiator was measured using three T-type thermocouples attached to the surface of the pipes, which were insulated with 25mm thick foam. The pipes were assumed to be at the same temperature as the water. The six thermocouples were attached to a PC through a USB based data acquisition system to monitor and record the temperatures at the selected sampling rate, which was every five seconds.

Tests were carried out for only one inlet cold temperature to the radiator which was around 8C°. The radiator connected to the lab fixed base using a steel frame by a way in which it can be simply moved towards or away from the wall to get a range of different aspect ratios. The total heat transfer from the cold wall side of the cavity can be calculated using the equations 1 to 4 and equation 6 by just replacing the hot side temperatures with the cold side temperatures.

The volumetric flow rate of the cold water side is calculated using the following polynomial equation.

$$Q_c = 4.975 \times 10^{-4} Q_o^2 + 3.297 \times 10^{-2} Q_o + 0.0916 \quad (7)$$

#### 6.2.4 Calculation of measurement uncertainty

All the thermocouples for the hot and cold sides were calibrated using an electronic reference thermometer which has a resolution of 0.01°C. This reference thermometer has been calibrated by the manufacturer using five reference points which produces an uncertainty of measurement equal to ±0.05°C, the calibration certificate of this reference thermometer is included in appendix B. All the twelve thermocouples used for this work were calibrated using this reference thermometer at three reference points:

0°C, ambient temperature which was around 23°C and 40°C, using a heater with a magnetic stirring device to keep the temperature constant. The calibration procedure and the results are included in appendix B. All the readings of the thermocouples had an error of  $\pm 0.2^\circ\text{C}$ .

The rotameter calibration test was performed by recording the time using stop watch and weighing the water using a digital scale for the whole rotameter measuring range. The detailed test and the results for both the rotameters for the hot and the cold sides are shown in appendix B. The resulting data is used to produce the polynomial equation as discussed above.

The uncertainty of this flow meter will be equal to the minimum scale reading divided by two, which will be equal to about  $\pm 0.02$  l/min.

The calculation of the uncertainty for the calculated heat transfer from the hot and cold sides will be according to equation (1) as below:

$$\frac{\delta Q}{Q} = \frac{\delta \dot{V}}{\dot{V}} + \frac{\delta(\Delta T)}{\Delta T} \quad (8)$$

Where  $\delta(\Delta T) = \delta T_{in} + \delta T_{out}$

From the calculated uncertainty of the thermocouples which is  $\pm 0.2^\circ\text{C}$ , then

$$\delta(\Delta T) = \pm 0.2 + \pm 0.2 = \pm 0.4$$

Therefore

$$\frac{\delta Q}{Q} = \frac{\delta \dot{V}}{\dot{V}} + \frac{\delta(\Delta T)}{\Delta T} = \frac{\pm 0.02}{1.0} + \frac{\pm 0.4}{2} = \pm 0.22$$

However, the calculated results involves the propagation of the uncertainty in the region, which is approximately  $\pm 22\%$  for  $\dot{Q}_{tot(h)}$  and  $\pm 22\%$  for  $\dot{Q}_{tot(c)}$ . The principle source of this error is due to the uncertainty in the thermocouples and flow rate readings as shown above.

### 6.3 Thermal calculations and results

The thermal calculations were performed for a range of hot wall temperatures ranging from  $50^\circ\text{C}$  to  $75^\circ\text{C}$  and for three enclosure sizes of aspect ratios 2.0, 1.0 and

0.5. The thermal calculations start with the collecting of the thermocouples readings for both the hot and cold sides and save them then taking the average values of each three thermocouples. The thermal calculations also include the calculation of the total heat transfer from the hot side as explained in section 6.2.2 and from the cold side as discussed in section 6.2.3. Moreover the thermal calculations include the calculation of the heat losses through the enclosure side walls which is the difference between the hot and cold heat transfer.

The thermal results are divided to two sub sections. One is for the different hot wall temperatures and the other one is for the different aspect ratios. Both of these will be discussed below.

### **6.3.1 Different aspect ratios**

The enclosure was designed to have three aspect ratios. Firstly an aspect ratio of 2.0 which has inside dimensions of  $600 \times 300 \times 600\text{mm}$ . The steps followed to construct and insulate this enclosure are the same as those explained in section 6.2.1. The enclosure is shown in figure 6.12a. The second enclosure had an aspect ratio of 1.0 (square) which is had inside dimensions of  $600 \times 600 \times 600\text{mm}$ . After attaching the second layer of the cavity wall double insulation the enclosure is shown in figure 6.12b. The last has an aspect ratio of 0.5, and has inside dimensions of  $600 \times 1200 \times 600\text{mm}$ . Its final shape is shown in figure 6.12c.

The preparation and steps of design procedure and the operational process of each of these cavities followed the same procedure and steps as that explained in section 6.2.

### **6.3.2 Different hot wall temperatures**

In the case of each of the three aspect ratios, the calculations were performed for different hot wall temperatures ranging from  $50\text{C}^\circ$  to  $75\text{C}^\circ$ . For each hot wall temperature, the experiment starts by checking the readings of the six thermocouples of the hot side and the six thermocouples of the cold side by monitoring their reading through the computer using the data acquisition system. Then the flow rates of the water to the hot and the cold sides were checked and adjusted using the bypass and valves by monitoring the reading of the glass tube rotameter.





(a)



(b)



(c)

Figure 6.12 Enclosure final shape for aspect ratios  $AR=$  a) 2.0, b) 1.0 and c) 0.5



To start collecting the data, the PID controller settings were adjusted to control the inlet hot side temperature to the setting point of the required temperature. A T-type thermocouple is connected between the inlet hot side temperature and the PID controller. As discussed in section 6.2.2 above this temperature is compared to the setting point of the PID controller and from the difference the PID controller compensates and matches the energy input of the heater to get both temperatures to within  $\pm 0.1^\circ\text{C}$  of each other.

Collecting the thermocouples readings starts just after checking the thermocouples, the flow rate readings and the adjustment of the temperature controllers for both hot and cold sides. To this end it was possible to monitor and record the temperatures every five seconds, and save them to files. Collecting the experimental data took from 24 hours to 48 hours depending on the stability of the data collected during the day. The repeatability of the data collected using the thermocouples are checked as it can be seen in figure 6.13 which show the stability of the thermocouple collected data for more than two days for both the hot and cold sides. The flow rate was monitored during the experimental time and the reading data of the glass tube rotameter is collected manually by taking the measuring scale level of the float. After getting enough collected data from the experiment for each hot wall temperature the experiment was deemed to be completed.

Then the average temperature of the three inlet thermocouples and the three outlet thermocouples were calculated for both hot and cold sides. From these four average temperatures the calculations of the mean temperatures at the hot and cold sides are calculated using equation (3) as explained in sections 6.2.2 and 6.2.3. From these two mean temperatures the water properties are calculated using equations (2) and (6).

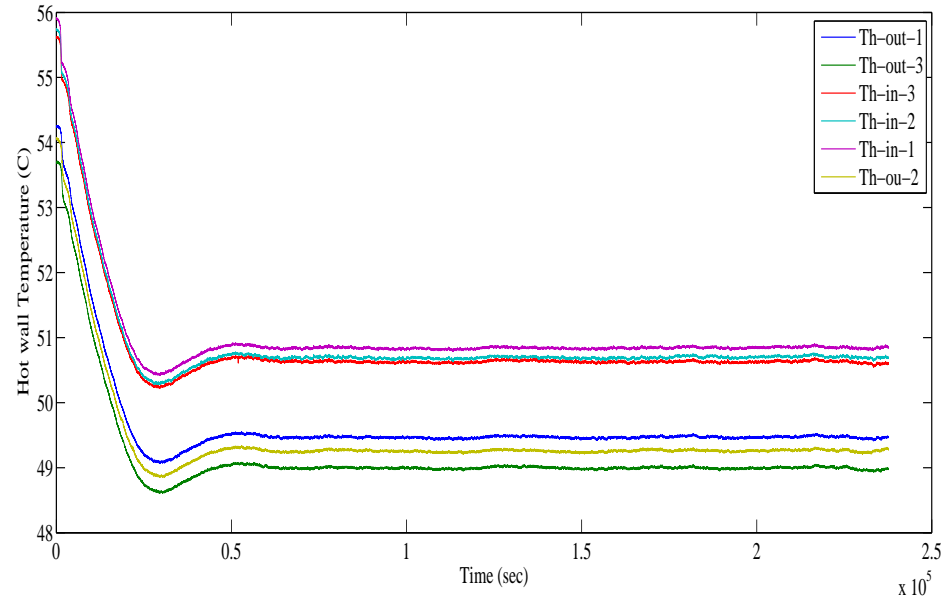
The volumetric flow rates for hot and cold sides are calculated using the collected readings of the glass tube rotameter at each side and by using equation (5).

Calculations of the thermal results for each hot wall temperature (which ranged from  $50^\circ\text{C}$  to  $75^\circ\text{C}$ ) were performed using equation (1) to calculate the total heat transfer for hot and cold walls. Then the heat losses were calculated using the following equation:

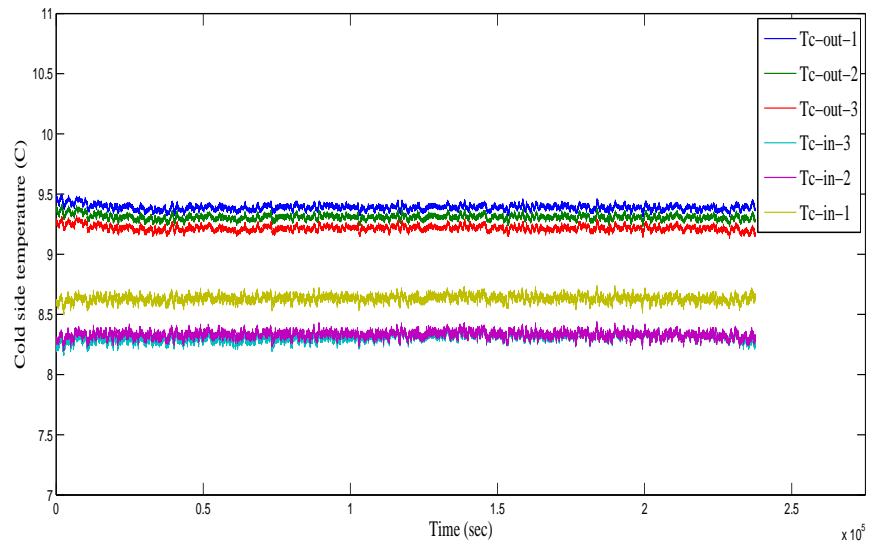
$$\dot{Q}_{loss} = \dot{Q}_{tot(h)} - \dot{Q}_{tot(c)} \quad (9)$$

Which is the heat transferred through the walls or the gaps in the walls then to the surrounding and it equal to the difference between the heat transferred to the medium

from the hot side and the heat removed by the cold side.



(a)



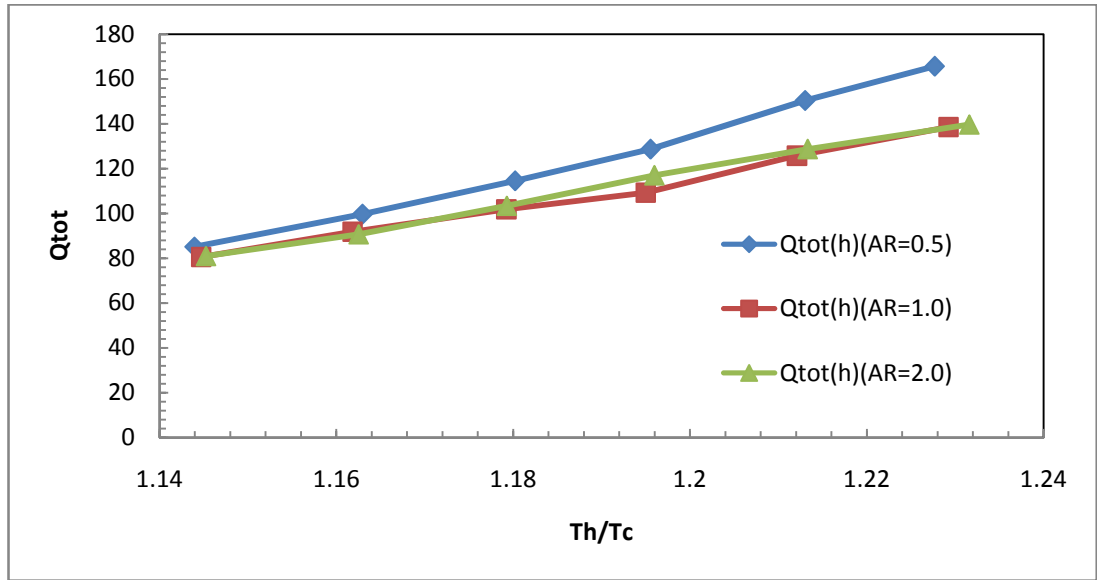
(b)

Figure 6.13 The thermocouples collected data of about two days for a) hot wall side and b) cold wall side

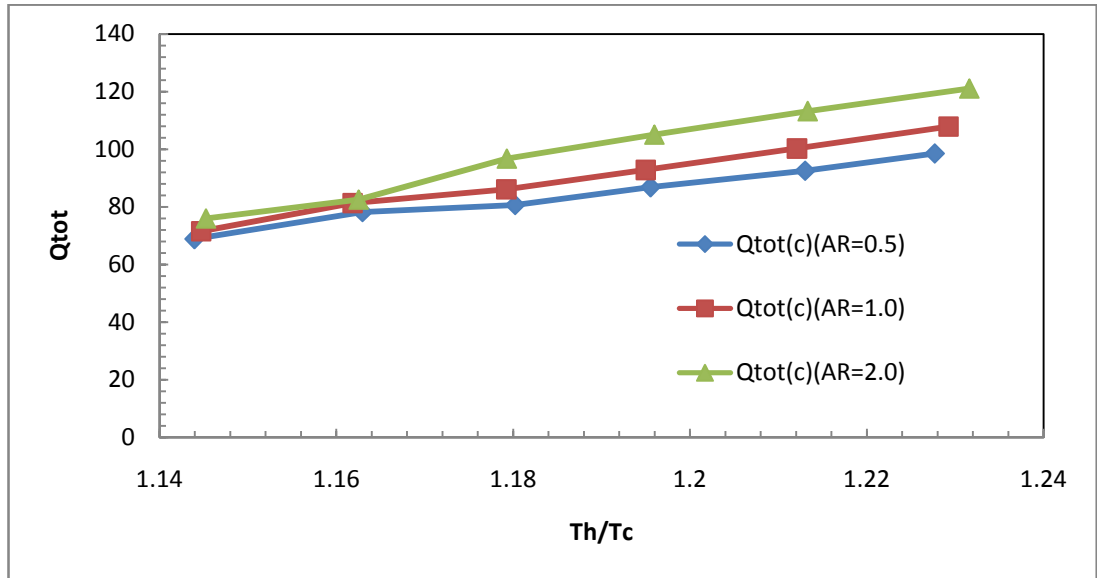
For each temperature the error of the heat losses were calculated

$$Error(\%) = \frac{\dot{Q}_{tot(h)} - \dot{Q}_{tot(c)}}{\dot{Q}_{tot(h)}} \times 100 \quad (10)$$

The final results for each aspect ratio and at each hot wall temperatures are shown in figure 6.14. The figure shows the relation between the heat transfer from the hot or the cold walls as a function of absolute temperature ratio between hot and cold walls. From this figure it can be seen that the total heat transfer increases as the absolute temperature ratio increases.



(a)



(b)

Figure 6.14 Thermal results of total heat transfer from three aspect ratios a) hot side and b) cold side.

Also from the figure it can be seen that the total heat transfer from the hot side increases as the aspect ratio decreases. Conversely the total heat transfer from the cold side increases as the aspect ratio increase which means that the heat losses increase as the aspect ratio decreases. Also the figure shows that the heat transfer for the aspect ratios 2.0 and 1.0 is very close to each other for both hot and cold sides. The difference between heat transfer for aspect ratio 0.5 and the other two aspect ratios increases as the absolute temperature ratio increases.

## **6.4 Laser Doppler Velocimetry specifications and principles**

### **6.4.1 Introduction**

Laser Doppler Velocimetry (LDV) is a widely accepted tool for fluid dynamic investigations in gases and liquids. It is a technique that has important characteristics which make it an ideal tool for dynamic flow measurement and turbulence characterization [111].

With the development of the helium-neon laser, it was shown that fluid flow measurement could be made from the Doppler effects on a He-Ne beam scattered by very small polystyrene spheres entrained in the fluid [112]. This phenomenon was used in developing the first laser Doppler flow-meter using heterodyne signal processing [113].

Its non-intrusive principle and directional sensitivity makes it very suitable for applications where physical sensors are difficult or impossible to use. It requires a tracer particles in the flow that can reflect the laser beams, e. g. liquids contain sufficient natural seeding on the other hand gases must be seeded in most cases.

### **6.4.2 Advantages**

The LDV has the following features [111, 114]:

1. Non intrusive.
2. No calibration required.
3. Velocity range negative to supersonic.

4. One, two or three velocity components.
5. Flow reversals can be measured
6. High spatial and temporal resolution
7. Instantaneous and time averaged

### **6.4.3 Components and Principles**

The basic configuration of an LDV as seen in figure 6.15 consists of [111, 114]:

1. A continuous wave laser
2. Transmitting optics, including a beam splitter and a focusing lens
3. Receiving optics, comprising a focusing lens, an interference filter and a photodetector
4. A signal processor and a data analysis system.

Advanced systems may include traverse systems (such as the one used in this study) and angular encoders.

A Bragg cell is often used as the beam splitter. It is a glass crystal with a vibrating piezo crystal attached, see figure 6.16.

The output of the Bragg cell is two beams of equal intensity with frequencies  $f_0$  and  $f$  shift. These are focused into optical fibres bringing them to a probe.

In the probe, the parallel exit beams from the fibres are focused by a lens to intersect in the measuring volume.

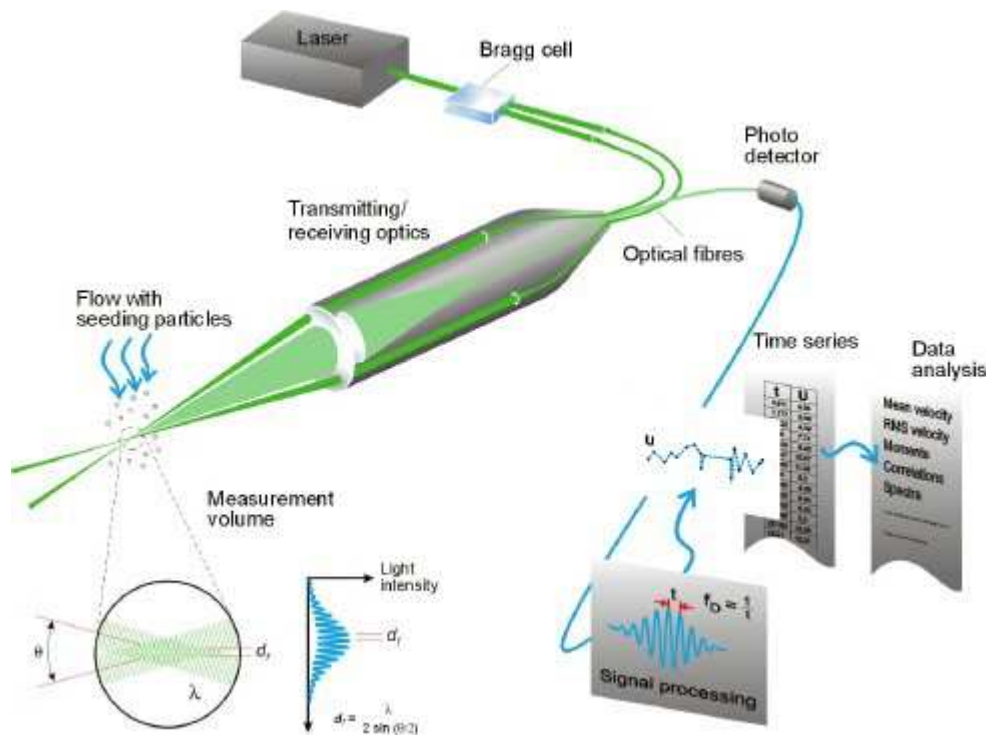


Figure 6.15 LDV principles[111]



Figure 6.16 The Bragg cell used as a beam splitter[111]

#### 6.4.4 The measuring volume

When two laser beams intersect, they interfere producing the measuring volume. The light intensity is modulated due to interference between the laser beams. This produces parallel planes of high light intensity, which are called fringes [111]. The fringe distance  $df$  is defined by the wavelength of the laser light and the angle between the beams as can be seen in figure 6.17:

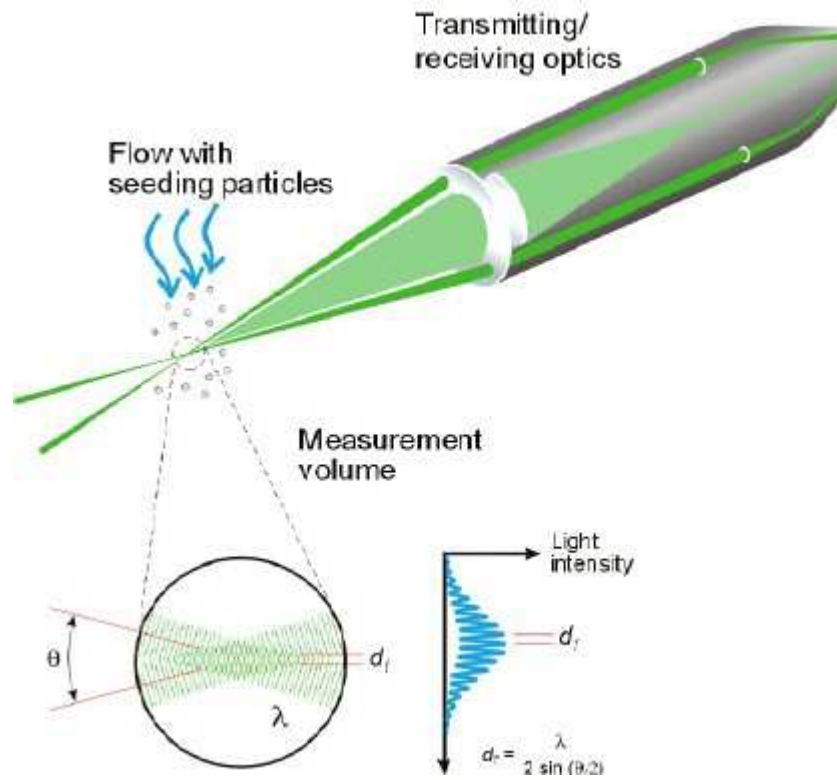


Figure 6.17 The probe and the measuring volume[111]

$$d_f = \frac{\lambda}{2 \sin\left(\frac{\theta}{2}\right)} \quad (11)$$

Each particle pass scatters light proportional to the local light intensity [111]. Flow velocity information comes from light scattered by seeding particles carried in the fluid as they move through the measuring volume. The scattered light contains a Doppler shift, the Doppler frequency  $f_D$ , which is proportional to the velocity component perpendicular to the bisector of the two laser beams.

The scattered light is collected by a receiver lens and focused onto a photo-detector. An interference high-pass and low-pass filters passes only the required wavelength from the photo-detector [114]. This removes both low frequency pedestal component and high frequency noise from the Doppler component.

### 6.4.5 Signal processing

The photo-detector converts the fluctuating light intensity to an electrical signal proportional to the light flux. The signal output from the photo-detector can be decomposed to low frequency (pedestal) output caused by the particle passing through the focused Gaussian-intensity laser beam, Doppler frequency,  $fD$ , has a regular sinusoidal pattern and a high frequency noise [114].

The Doppler frequencies are filtered and amplified in the signal processor, which determines  $fD$  for each particle, often by frequency analysis. The fringe spacing,  $df$  provides information about the distance travelled by the particle. The Doppler frequency  $fD$  provides information about the time:  $t = 1/fD$ . The velocity equals distance divided by time: Velocity  $V = df * fD$ .

### 6.4.6 Determination the sign of the flow direction

The frequency shift obtained by the Bragg cell added to the diffracted beam, which then results in a measured frequency of a moving particle and allows measurement of negative velocities down to  $V > 57.6m/s$  and maximum positive velocities up to supersonic [111, 115]. Particles which are not moving will generate a signal of the shift frequency  $f$ -shift which corresponding to zero velocity. The velocities  $V_{pos}$  and  $V_{neg}$  will generate signal frequencies  $f_{pos}$  and  $f_{neg}$  respectively as shown in figure 6.18.

LDV systems without frequency shift cannot distinguish between positive and negative flow direction or measure 0 velocity.

LDV systems with frequency shift can distinguish the flow direction and also measure zero velocities.

### 6.4.7 Two and three component measurements

To measure two velocity components, two extra beams can be added to the optics in a plane perpendicular to the first beams.

All three velocity components can be measured by two separate probes measuring two and one components, respectively with all the beams intersecting in a common volume as shown in figure 6.19 [111]. Different wavelengths are used to separate the



measured components. Three photo-detectors with appropriate interference filters are used to detect scattered light of the three wavelengths.

Modern LDV systems employ a compact transmitter unit comprising the Bragg cell and colour beam splitters to generate up to 6 beams: un-shifted and frequency shifted beams of three different colours. These beams are passed to the probes via optical fibres.

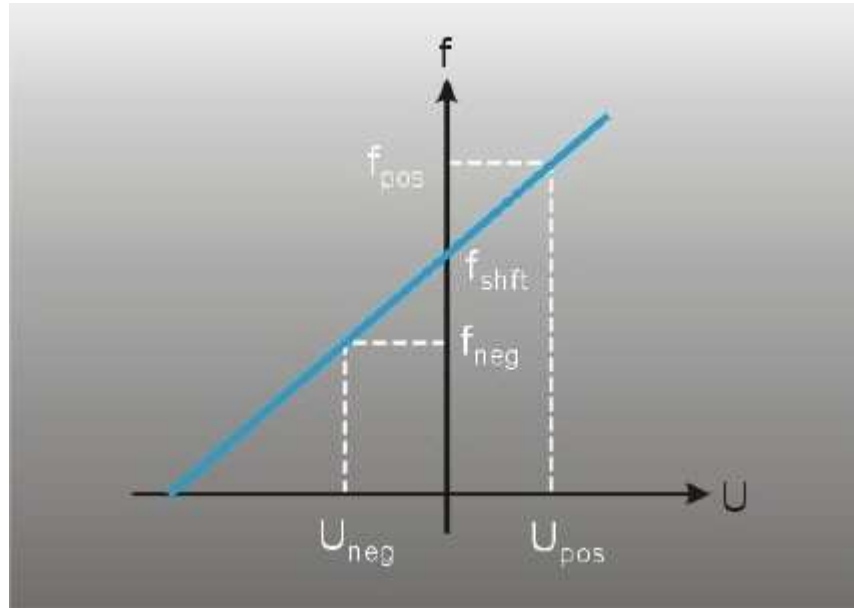


Figure 6.18 Doppler frequency to velocity for a frequency shifted LDV system [111]

#### 6.4.8 Seeding particles

Liquids usually contain sufficient natural seeding, whereas gases must be seeded in almost all cases. In the ideal cases, the particles should be small enough to follow the flow and also large enough to scatter sufficient light. The seeding particle material can be solid powder or liquid droplets depending on the practice case. In most of the gas flow cases seeding particles are needed hence, an atomizer is used to produce these seeding particles. In the present study the Six-Jet atomizer is used to produce the seeding particle which is olive oil. The Six-Jet atomizer principle and operation is discussed in the next section.

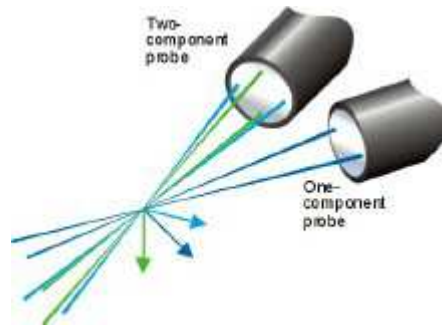


Figure 6.19 LDV optics for measuring three velocity components [111]

#### 6.4.8.1 The Six-Jet atomizer principle

The Six-Jet atomizer as seen in figure 6.20 has many features that make it a widely used instrument for providing seeding particles. The atomizer has a built-in pressure regulator and a pressure gage to control the pressure. It has a self-dilution system that controls the output concentration and six particle-generator atomizer jets, have an orifice diameter of 0.015 inch, where one to six atomizer jets can be selected.

The atomizer can produce liquid particles from liquids; in this study the olive oil used to produce the seeding particles. It can also produce solid particles from solutions or suspensions such as spheres from uniform polystyrene latex [116].

#### 6.4.8.2 Operating the Six-Jet atomizer

The atomizer reservoir is half filled with the liquid to be atomized which in this case is the fruity olive oil. The liquid level in the reservoir should be less than half to be sure that the atomizer jets are not submerged [116]. The regulator valve and the dilution air valve should be closed before connecting the compressed air. The atomizer outlet is connected to the top of the enclosure using a flexible tube. The regulator pressure was set to 25 pounds per square inch, as this level is recommended to work well [116], and connected to a continuous source of compressed air using an air compressor. In this study one atomizer jet is used which gives 6.6 l/min aerosol flow-rate [116] and the seeding time depended on the size of the enclosure, at about 10 to 15 seconds for an aspect ratio of 2.0, to 20 to 25 seconds for an aspect ratio of 1.0 and 35 to 40 seconds for an aspect ratio of 0.5. It was noticed that the fruity extra virgin olive oil used lasted better in the enclosure than an extra virgin olive oil.



Figure 6.20 The Six-Jet atomizer.

## 6.5 LDV experiments and results

The velocity profiles and turbulent intensities were acquired for the different enclosure sizes with aspect ratios of 2.0, 1.0 and 0.5 and for different hot wall temperatures ranging from 50°C to 75°C.

In each experiment, preparation to use the LDV system is needed such as the LDV controls settings and traverse system positions. These and the LDV operation steps will be explained in the next sections.

### 6.5.1 LDV experiments preparation

For each aspect ratio after collecting the thermal results (as explained in section 6.3) the side wall was removed and exchanged for a Perspex surface as can be seen in figure 6.21.

The same steps are followed as in section 6.3 to start collecting the thermal results. Collecting the data using the LDV system starts after the reading of the thermocouples become stable. Before collecting the velocity and turbulent intensities inside the enclosure, the FLOWSIZER software package must be installed and a new main project folder created to monitor and save the data collected. Each project folder contains various experiment folders and each of them contains many runs. For example in this study a main project folder is opened that contains three experimental folders for each aspect ratio. Each experimental folder contains another six experimental folders for each hot wall temperature which ranging from 50°C to 75°C. Each hot wall temperature experiment folder contains six runs calculated at different enclosure heights for  $y/h$  equal to 0.19, 0.3, 0.5, 0.65 and 0.85 and one run at  $x$  equal to 4mm, which is very close to the hot wall.

The LDV controls require the adjusting of the Run setup settings which for example includes the maximum particle measurement attempts, wavelength, focal length and some other parameters. These settings need to be set correctly in order to take accurate velocity data. The other most important input settings are the LDV controls which is on the main software window. The settings of these parameters are often slightly iterative among the various parameters to get good velocity measurements [114]. The graphing capabilities of the FLOWSIZER data acquisition and analysis software has a wide flexibility to create histogram plots, scatter plots, smoothed line plots, etc. [114]. A velocity histogram, instantaneous velocity plot, and the velocity and turbulence statistics are created, monitored and saved during each run.

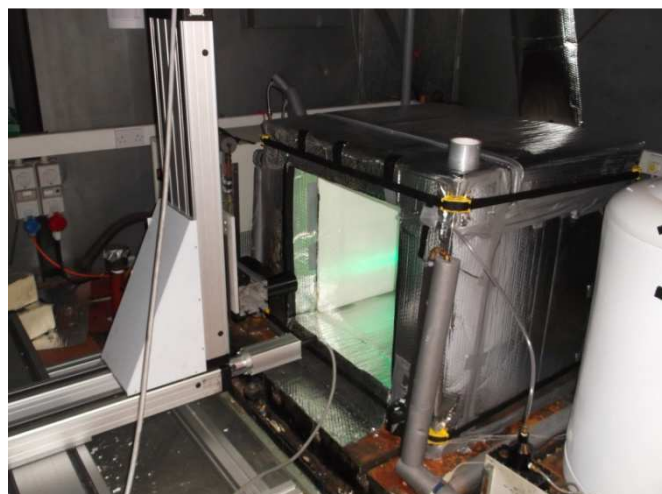
The traverse menu options are selected to start setting the parameters and moving the laser probe to the start point where data need to be start collected. There are two modes to operate the traverse system, manually by setting the moving positions each time or automatically based on the matrix of positions and filenames selected. The matrix of positions can be created manually or automatically. In this study the automatically selected matrix positions are used in each run.



(a)



(b)



(c)

Figure 6.21 Exchanging the side wall by a Perspex surface.

### **6.5.2 Collecting the data using the LDV**

Before starting to collect the data, the laser probe needs to be moved and adjusted to the starting point. The matrix of the collecting data positions inside the enclosure is created automatically and has all the position points that the traverse system will follow during the experiment to capture the data. By pressing the “scan capture” button, the LDV system is started and data collection commences. The laser probe is moved automatically to the next point after the maximum particle measurement attempts of the first point is reached.

For example collecting the data for the aspect ratio 2.0 and hot wall temperature 50°C starts by moving the laser probe using the traverse system to the position at  $y/h$  equal 0.19 and at the closest point to the hot wall. After pressing the “scan capture” button the LDV system starts collecting the data for each position point, which in this experiment was at every 1.0 mm near the hot and cold walls for about 100 mm from the wall edge and at every 10 mm for the whole enclosure core distance. Collecting the data continues at each point until the maximum particle measurement attempts reached, which in this experiment was 10,000. Then the traverse system moves to the next point. This is the case for each measuring point until finishing all the measuring points across the enclosure width. The collected data for each measuring point is saved to the named file and then after finishing the experiment the saved data can be exported to an excel sheet for analysis. The same steps were repeated for each aspect ratio and each experimental run. The only difference between aspect ratios is the measuring positions inside the matrix at the core are increased as the enclosure width increase where it was at each 100mm for the aspect ratio 1.0 and 200mm for the aspect ratio 0.5.

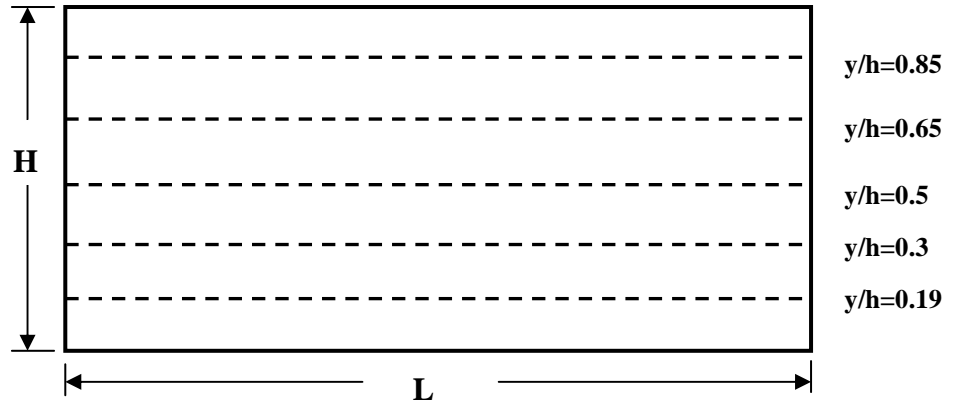
### **6.5.3 Velocity and turbulent intensities profiles for different aspect ratios**

As was mentioned in chapter two the velocity boundary layer is considered to be the region of velocity values which extends from the wall to the first zero or near to zero velocity value and does not include the region of reversed flow. Also the core of the enclosure is defined based on the velocity boundary layers and as King [57], defines the core as that region which exists beyond the velocity boundary layer which ends at the first position of zero velocity.

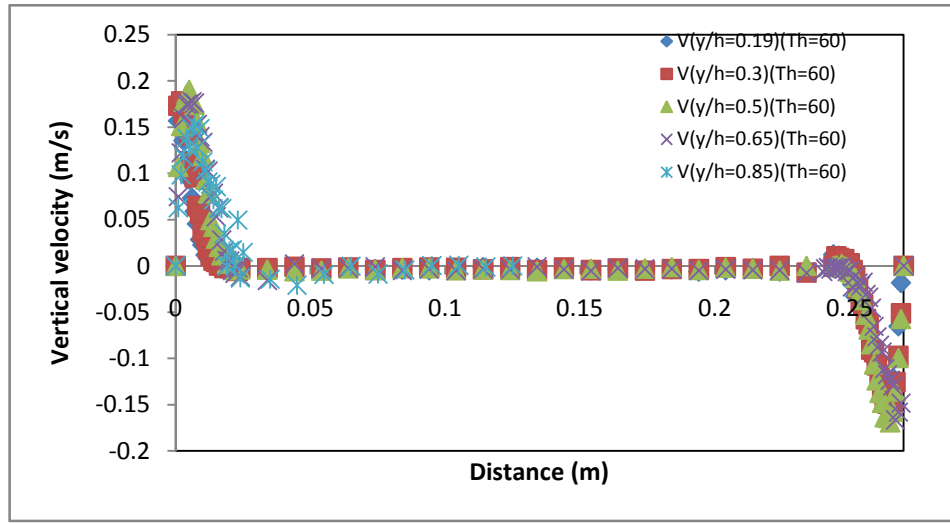
In this study and for each experimental run, the velocity and turbulent intensities for each aspect ratio and at each  $y/h$  for different hot wall temperatures are plotted and shown in different figures. To simplify the results, the velocity result graphs are divided into two groups. One of which will be included in appendix B and the other one will be explained and shown in this section. The velocity profiles of the first group, which includes three hot wall temperatures of 55, 65 and 70°C at different enclosure heights are shown in appendix B. The second group (which will be explained here) is for the three aspect ratios and containing the velocity profiles at different enclosure height for two hot wall temperatures, these are 60°C and 75°C. The velocity profiles for this group are shown in figures 6.22 to 6.27. The repeatability of the collected data using the LDA was checked using the velocity profile as shown in figure 6.28. This plot show that the velocity profiles collected at mid-height of aspect ratio 2.0 and two hot temperatures 50°C and 75°C of collecting data for two different days are repeatable.

From the figures 6.22 to 6.27 it can be seen that at the hot wall side the velocity starts at zero and increases to reach to its maximum after a certain distance and then it starts to decrease to its minimum value. This velocity is almost constant for the whole enclosure core. This velocity profile trend is the same for the velocity profiles at all enclosure heights and all aspect ratios. The same profile can be seen on the cold side where the velocity starts to increase to its maximum at a certain distance from the enclosure core and then decreases to zero at the wall. Also from the figures, the boundary layer thickness near the hot wall side increases as the enclosure height increases and vice versa. It is noticed as mentioned by King [57] that the peak of the mean velocity were at its minimum at the bottom of the heated wall then it starts to increase up to the mid-height when it starts to decrease again. Moreover, it can be seen from the figures that as the temperature increases, the velocity values and the boundary layer thickness increase at the same time. Furthermore from these figures it can be seen that as the aspect ratio increases, the velocity values and the boundary layer thickness decrease.

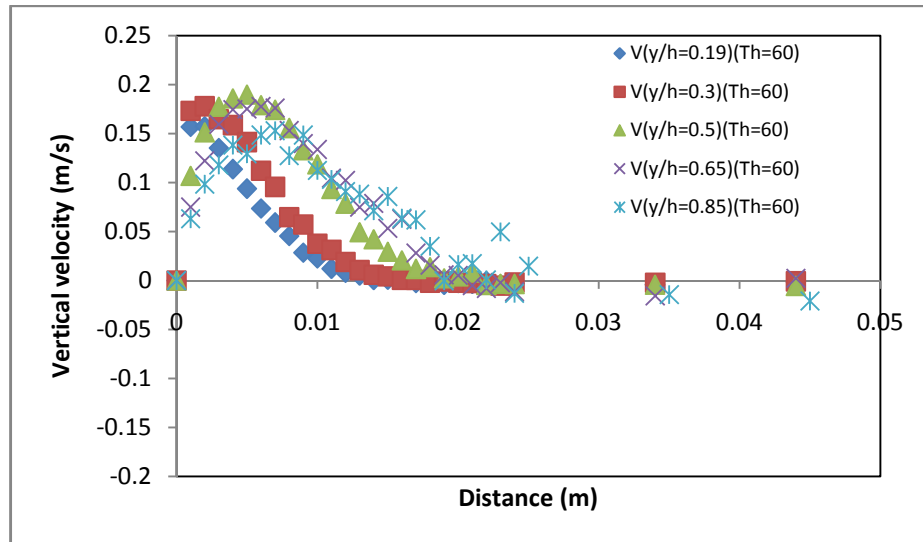
The maximum velocity for each aspect ratio occurs almost at or near the mid-height of the enclosure. Also it can be noticed here, and is also as mentioned by Kutaleladze et al [65] and Lankhorst et al [12] that the lateral position of the peak mean velocity is increased as the height of the enclosure increases. Also it was noticed again as mentioned by Kutaleladze et al [65] that increasing the cavity width will also increase the boundary layer thickness.



(a)



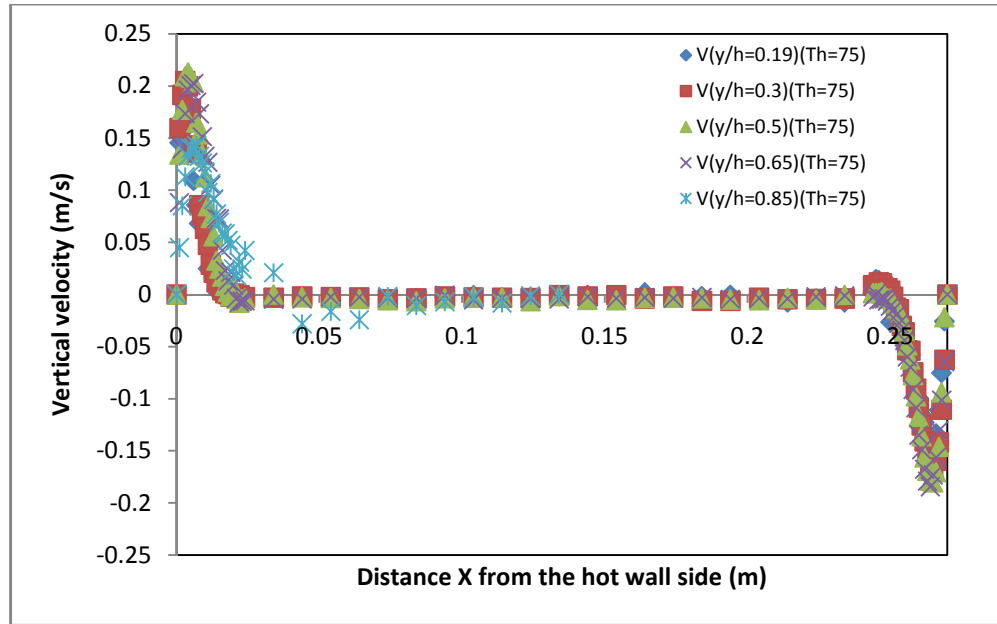
(b)



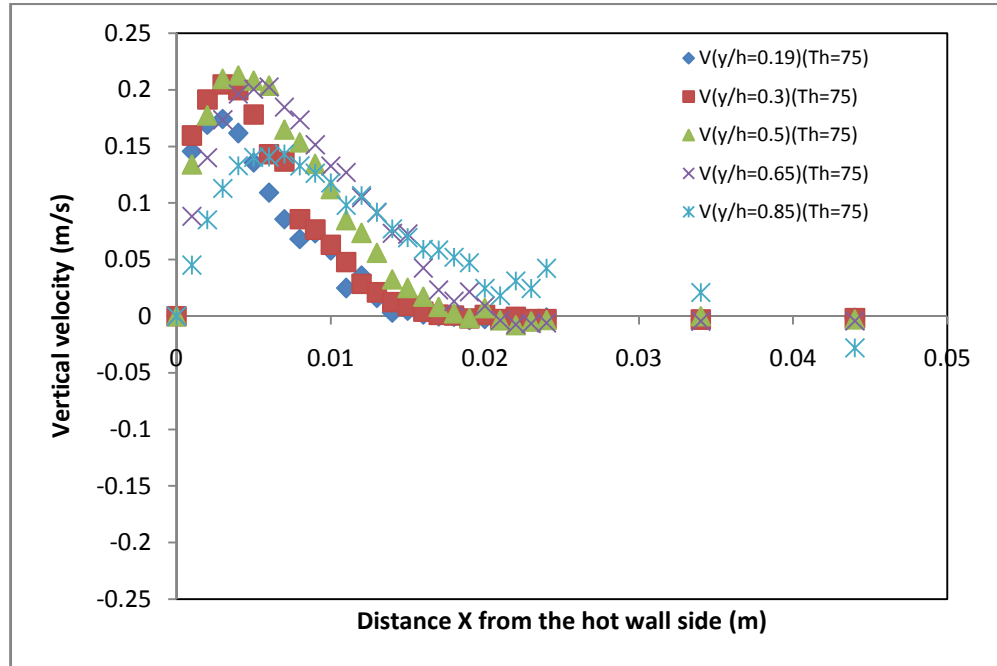
(c)

Figure 6.22 Velocity profiles for aspect ratio 2.0 and hot wall temperatures  $60^{\circ}\text{C}$  and  $Ra = 8 \times 10^7$  a) Traverse lines diagram b) between hot and cold walls b) near the hot wall





(a)

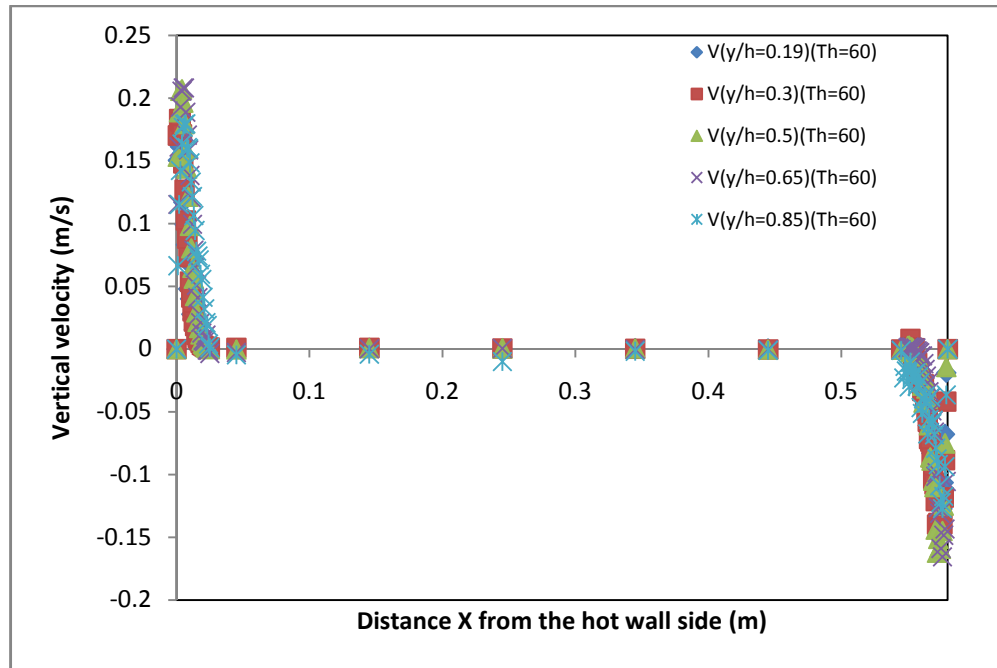


(b)

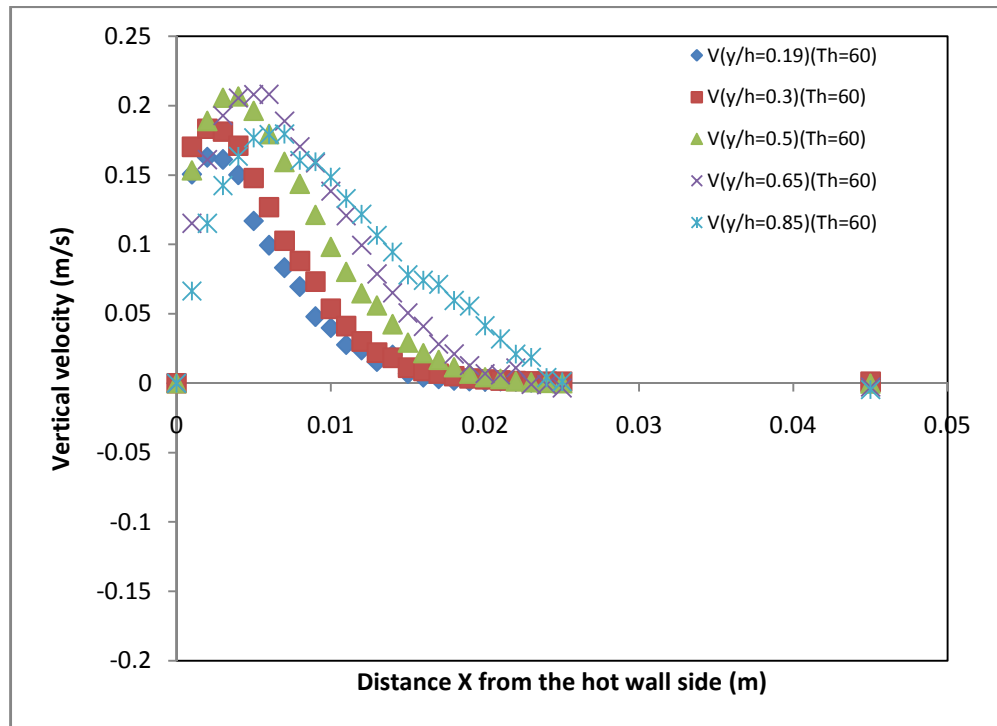
Figure 6.23 Velocity profiles for aspect ratio 2.0 and hot wall temperatures 75°C and  $Ra = 9.3 \times 10^7$  a) between hot and cold walls b) near the hot wall

The collected data for the velocity and turbulence intensity profiles along the vertical axis and near to the hot side were collected at a position of the maximum velocity and at 5mm intervals. The velocity profiles for this case are shown in figure 6.29. From the figure, it can be seen that the maximum velocity occurs near the mid height of the enclosure. Here the velocity starts to increase from the lower edge of the enclosure until

reaches its maximum value near the enclosure mid height where it upon starts to decrease again.

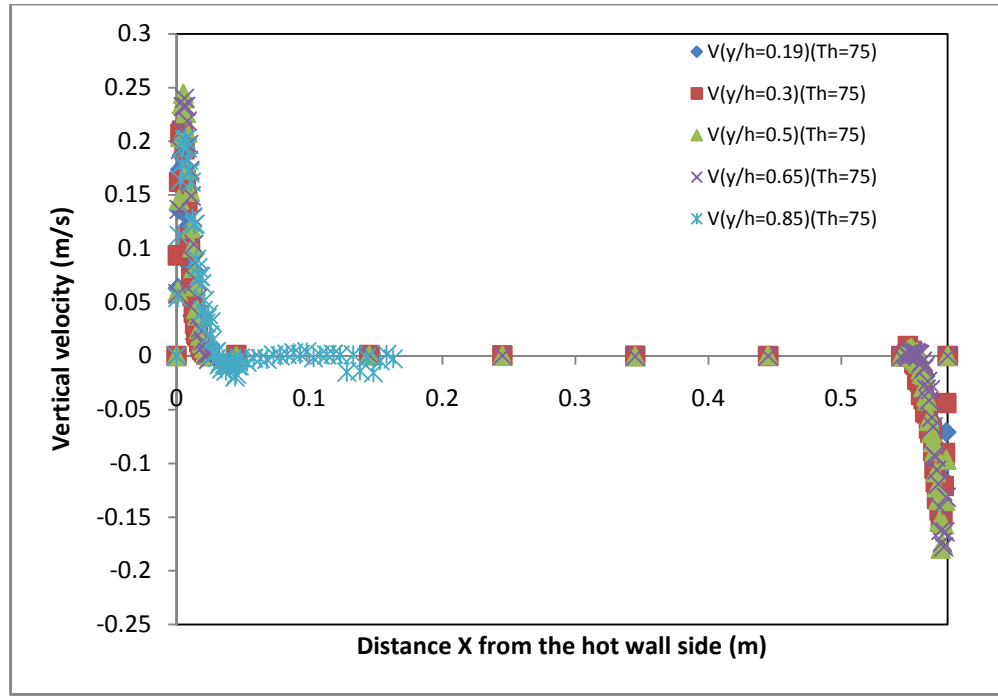


(a)

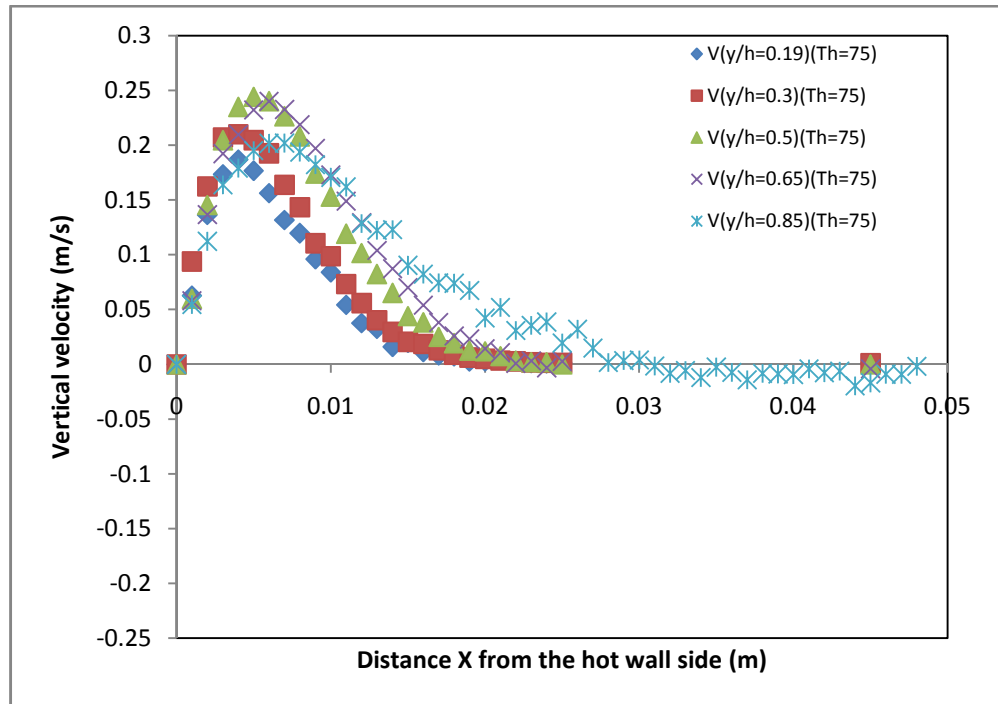


(b)

Figure 6.24 Velocity profiles for aspect ratio 1.0 and hot wall temperatures 60°C and  $Ra = 8.8 \times 10^8$  a) between hot and cold walls b) near the hot wall



(a)

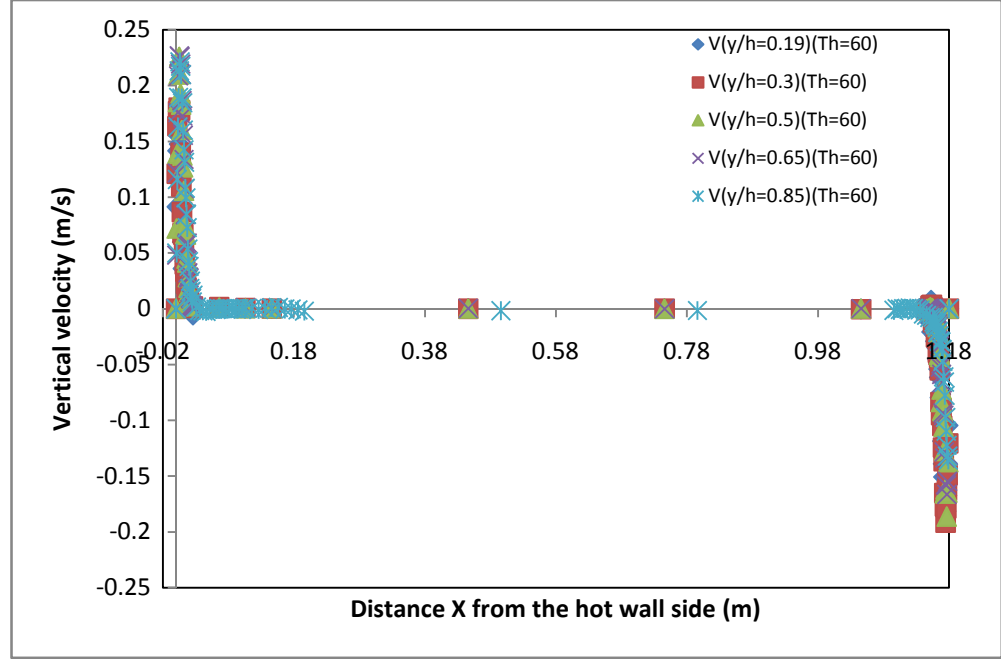


(b)

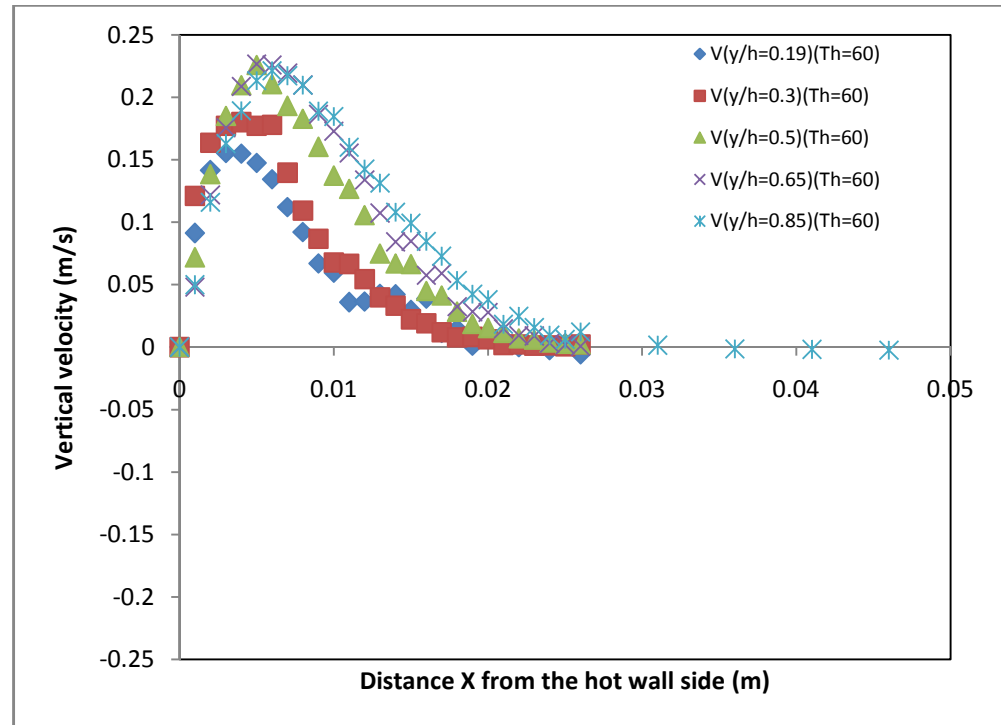
Figure 6.25 Velocity profiles for aspect ratio 1.0 and hot wall temperatures 75°C and  $Ra = 1 \times 10^9$  a) between hot and cold walls b) near the hot wall

Also from this figure it can be seen that the velocity values at the lower part of the enclosure are smaller than that at the upper part for a aspect ratio of 2.0 and its value looks quite similar for both parts for an aspect ratio 1.0. On the other hand the upper

part of the enclosure for an aspect ratio of 0.5 has larger velocity values than the lower part. Moreover it can be seen from the figure that the velocity profiles at the hotter temperatures of 70° and 75°C are quite similar for all three aspect ratios.

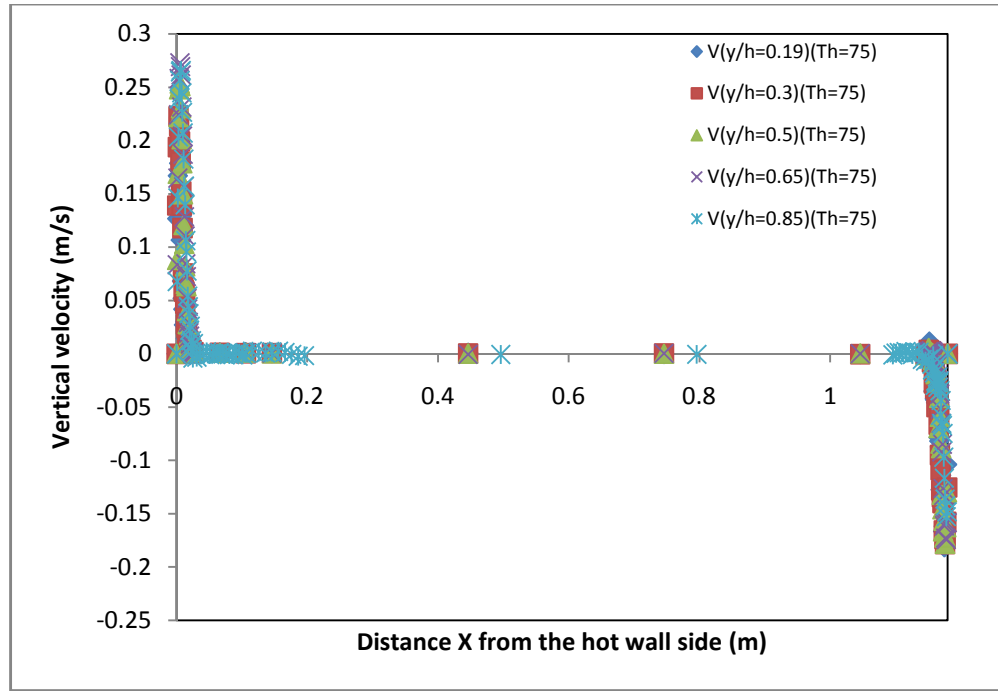


(a)

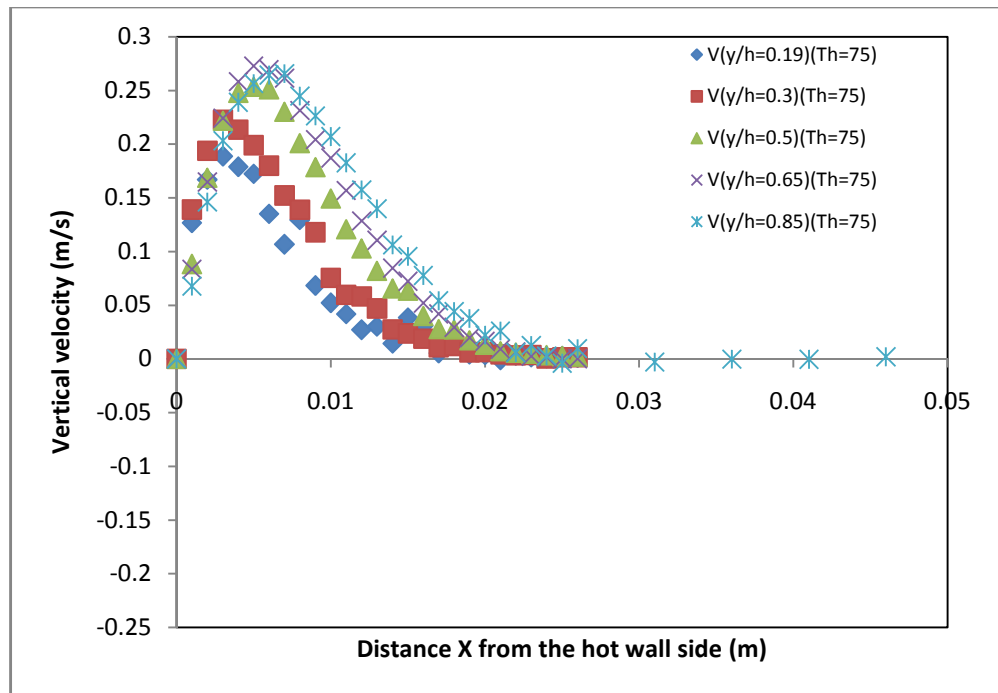


(b)

Figure 6.26 Velocity profiles for aspect ratio 0.5 and hot wall temperatures 60°C and  $Ra = 7.1 \times 10^9$  a) between hot and cold walls b) near the hot wall



(a)

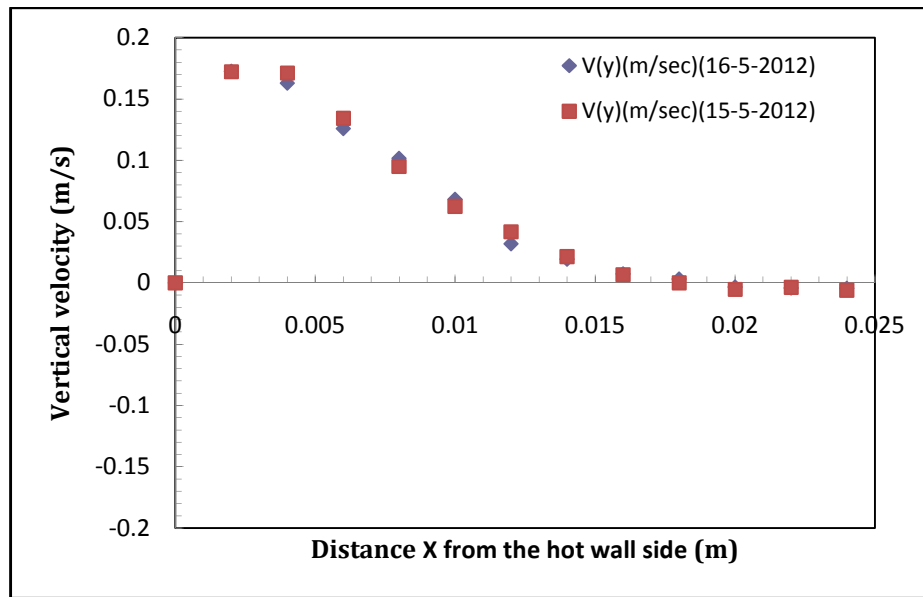


(b)

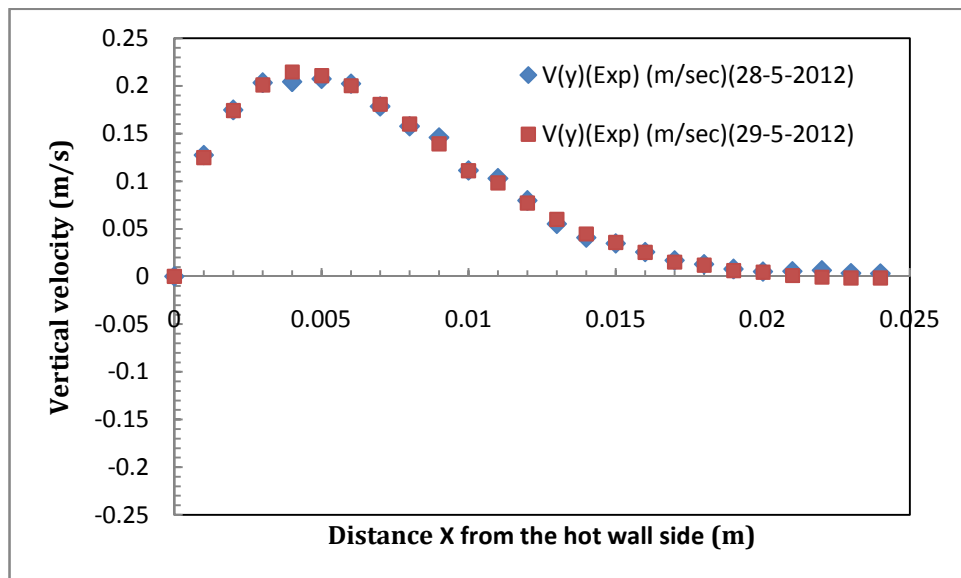
Figure 6.27 Velocity profiles for aspect ratio 0.5 and hot wall temperatures 75°C and  $Ra = 8.1 \times 10^9$  a) between hot and cold walls b) near the hot wall

The data was also collected for the turbulence intensity (which is the ratio between the RMS velocity and the average velocity) following the same steps as that for the velocity profiles and was exported at the same time with the collected velocity values to

the spreadsheet. The turbulence intensity profiles are again divided into two groups like the velocity profiles. The final profiles for the second group are shown in figures 6.30 to 6.32. From these graphs it can be seen that very close to the wall for about 3 to 4mm from the wall edge the turbulence intensity values are small and constant. As it moves away from the wall their values start to increase gradually until a distance of 100mm from the wall whereupon it starts to increase dramatically. Also from the figures it can be seen that the turbulence intensity increases as the aspect ratio increases and decrease slightly as the temperature increase.

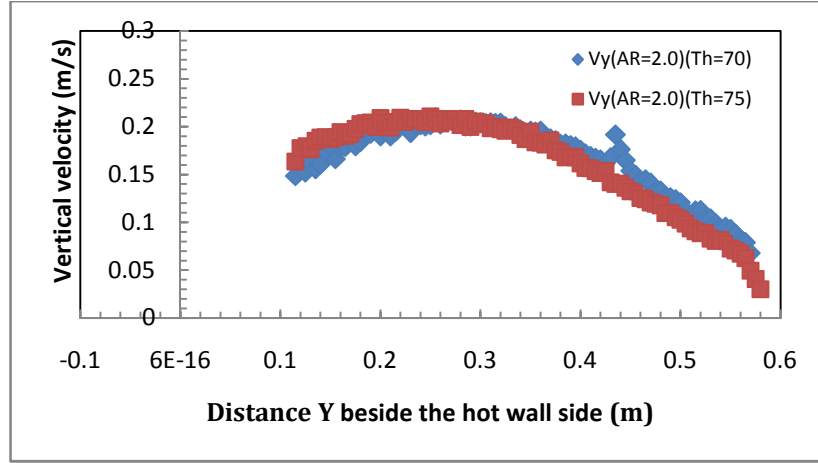


(a)

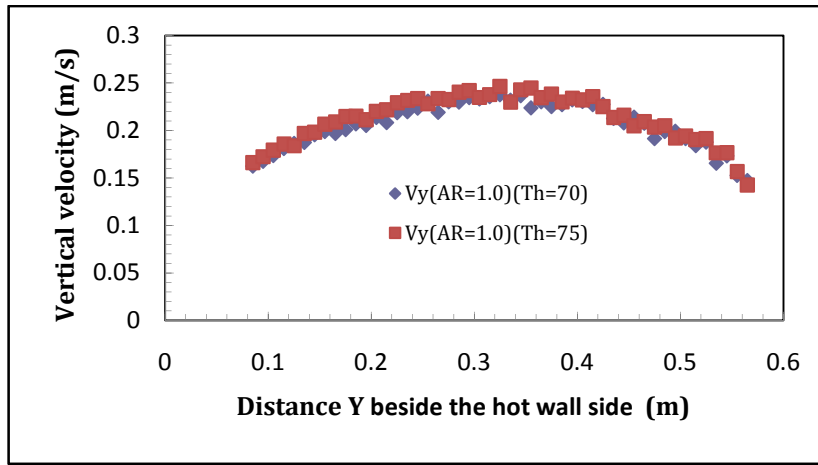


(b)

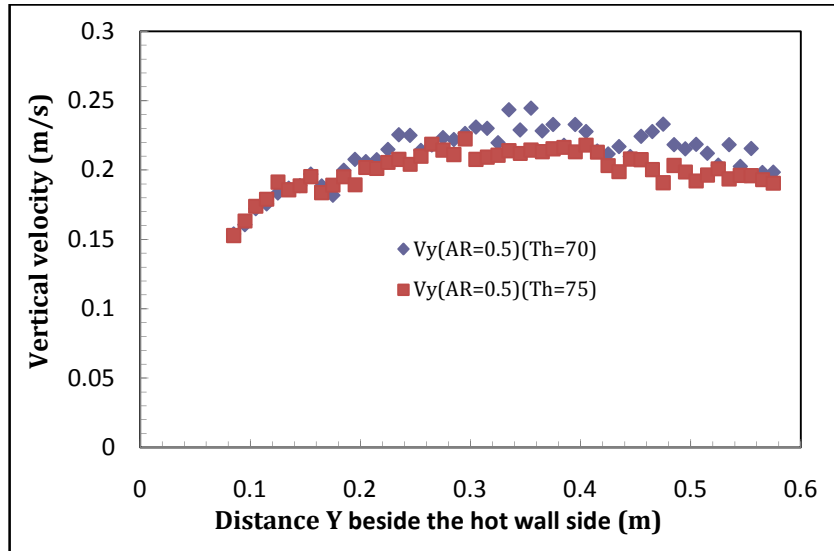
Figure 6.28 The repeatability of the LDA measurement for aspect ratio 2.0 and hot wall temperature a) 50°C and b) 75°C.



(a)

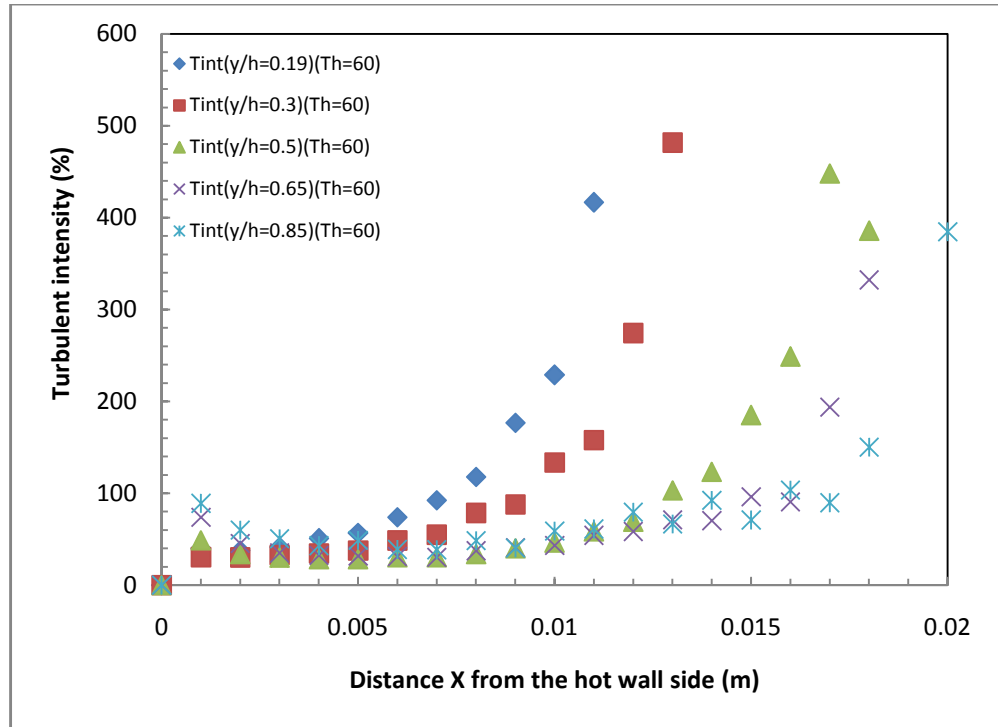


(b)

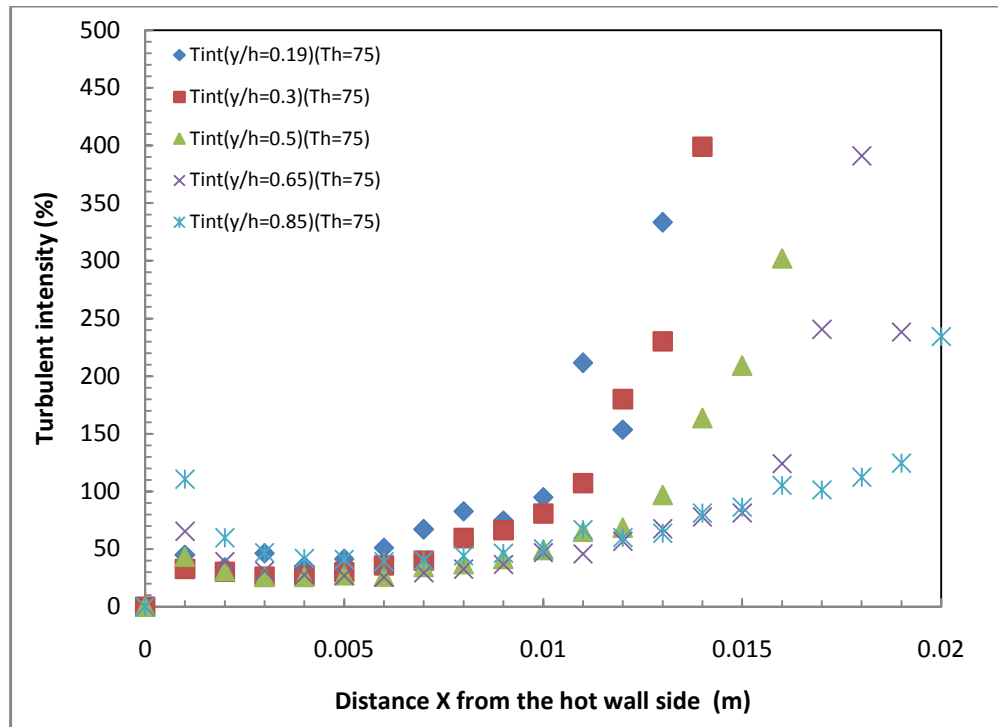


(c)

Figure 6.29 Velocity profiles near the hot wall at ( $x=4\text{mm}$  from the hot side) for aspect ratios a) 2.0 for  $Ra = 8.9 \times 10^7$  &  $9.3 \times 10^7$ , b) 1.0 for  $Ra = 9.7 \times 10^8$  &  $1 \times 10^9$  and c) 0.5 for  $Ra = 7.8 \times 10^9$  &  $8.1 \times 10^9$



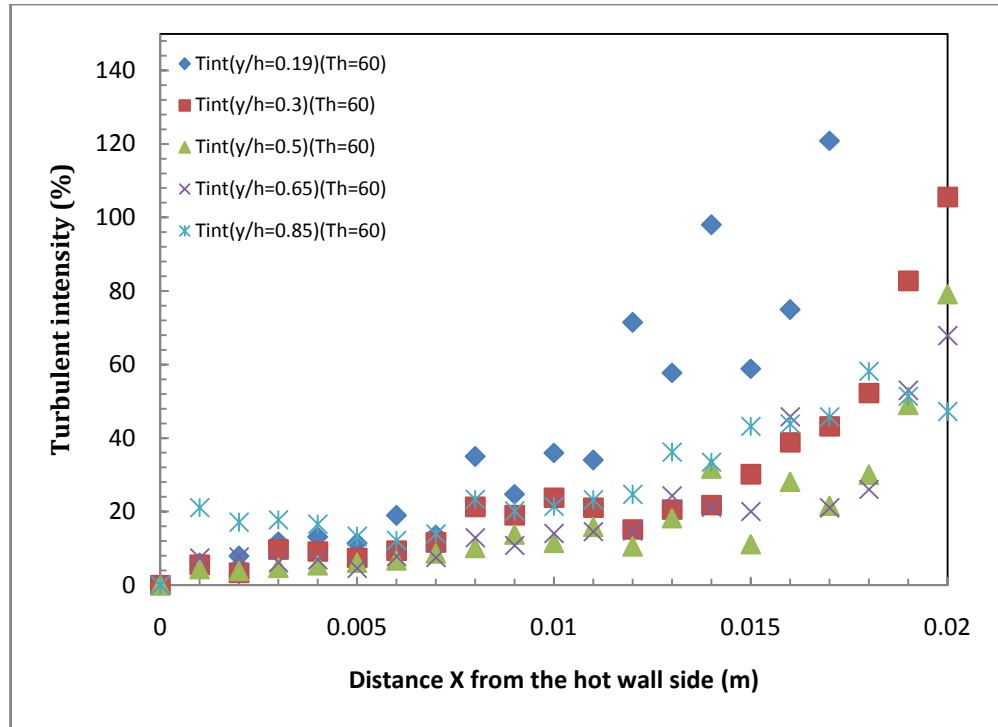
(a)



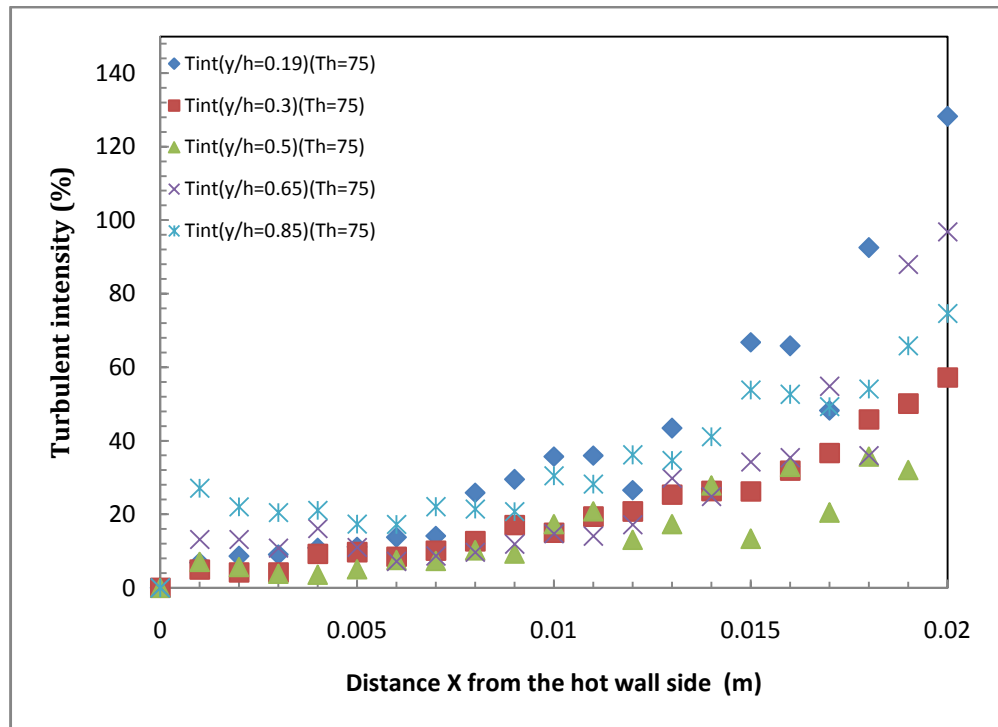
(b)

Figure 6.30 Turbulence intensity profiles for aspect ratio 2.0 and for hot wall temperature a) 60°C for  $Ra = 8 \times 10^7$  b) 75°C for  $Ra = 9.3 \times 10^7$ .



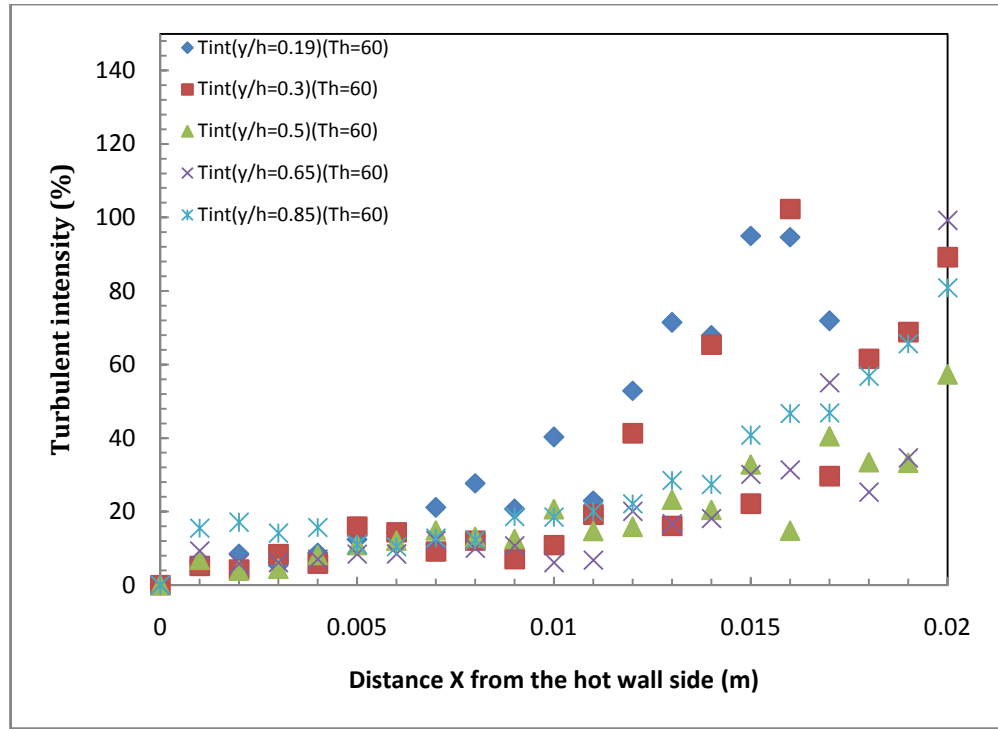


(a)

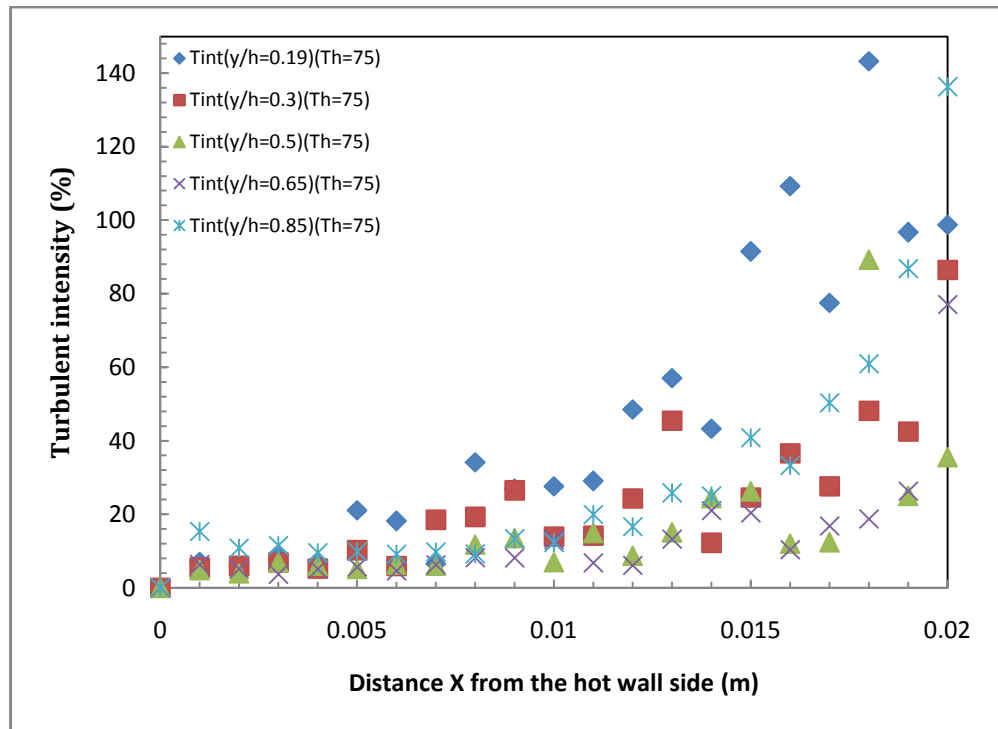


(b)

Figure 6.31 Turbulence intensity profiles for aspect ratio 1.0 and for hot wall temperature a) 60°C for  $Ra = 8.8 \times 10^8$  b) 75°C for  $Ra = 1 \times 10^9$ .



(a)



(b)

Figure 6.32 Turbulence intensity profiles for aspect ratio 0.5 and for hot wall temperature a) 60°C for  $Ra = 7.1 \times 10^9$  b) 75°C for  $Ra = 8.1 \times 10^9$ .

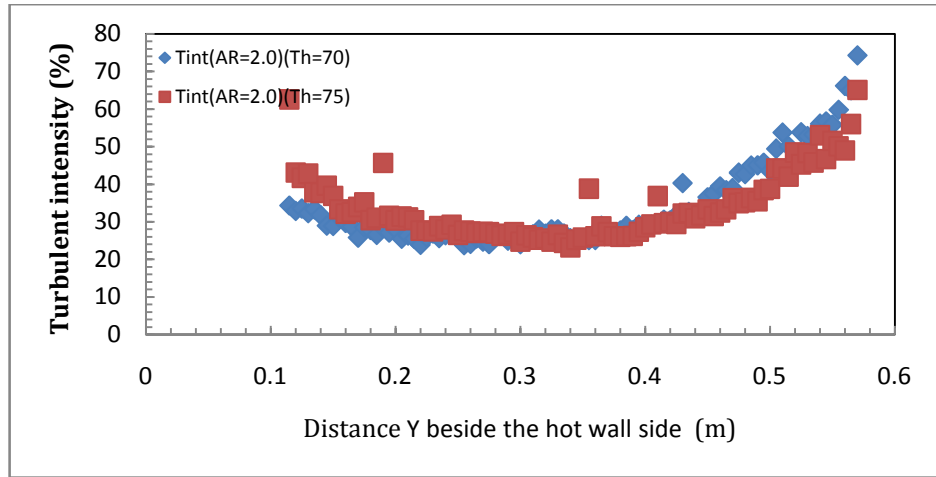
The turbulence intensity along the vertical axis and near to the hot side wall is collected at a position of a maximum velocity for each 5mm increment distance. The turbulent profile is shown in figure 6.33. From this figure it can be seen that the maximum turbulence intensity occurs near the two corners of the enclosure, where the turbulence intensity starts to decrease from the two edges of the enclosure until it reaches its minimum value near the enclosure mid height. Also from this figure it can be seen that the turbulence intensity values increase overall as the aspect ratio increases. Moreover from this graph it can be seen that the turbulence intensity at the lower part of the enclosure tends to decrease more than the upper part as the aspect ratio decreases. It can also be seen from figure 6.33c that the turbulence intensity at the lower part of the enclosure has quite similar values to that at the mid height of the enclosure for aspect ratio 0.5.

## **6.6 Summary and Conclusions**

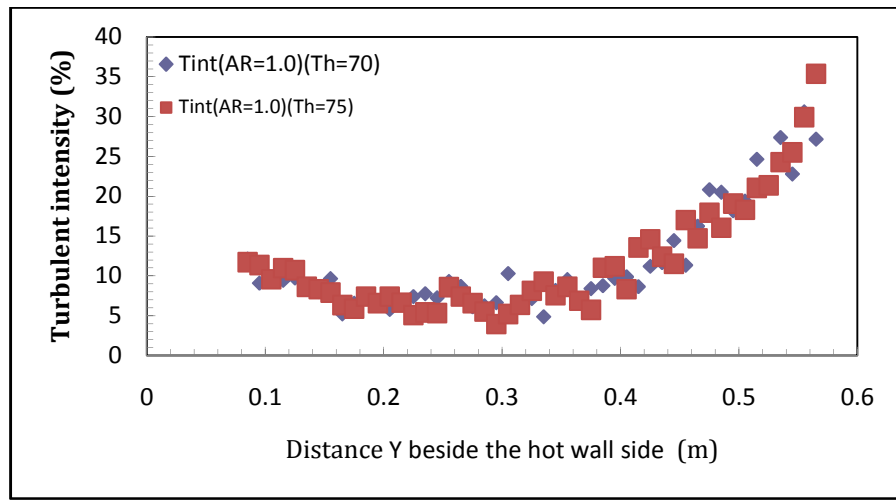
In this chapter the design of the experimental test rig and the process of collecting the data are explained in detail. The design of the test rig in this study includes the design of the enclosure with both hot and cold sides and with different aspect ratios. Also in this chapter the calibration of the thermocouples and how to use them with the data acquisition system to collect the thermal data were explained. This chapter also includes the specifications and the use of the laser Doppler velocimetry to collect the velocity profiles. The thermal calculations were discussed in this chapter for a range of hot wall temperatures ranging from 50C° to 75C° and for three enclosure sizes of different aspect ratios 2.0, 1.0 and 0.5.

The thermal results show that the total heat transfer increases as the absolute temperature ratio increases. Also the total heat transfer from the hot side increases as the aspect ratio decreases and on the other hand the total heat transfer from the cold side increases as the aspect ratio increases which means the heat losses also increase as the aspect ratio decreases.

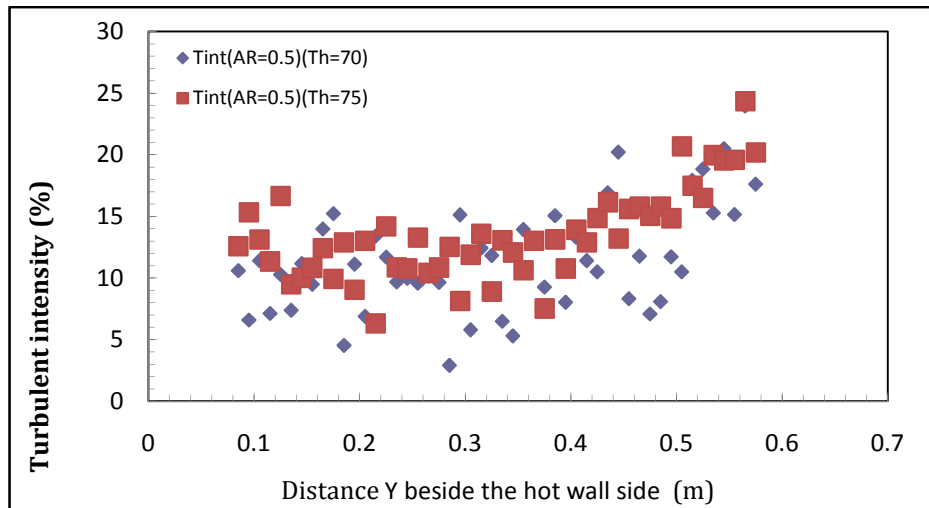
The collected results using the LDV system show that the velocity starts to increase to its maximum value after a certain distance from the wall then it starts to decrease to its minimum. The boundary layer thickness increases as the enclosure height or the temperature increase in all aspect ratios. The velocity values and the boundary layer thickness will decrease as the aspect ratio increase.



(a)



(b)



(c)

Figure 6.33 Turbulence intensity profiles near the hot wall at ( $x=4\text{mm}$  from the hot side) for aspect ratios a) 2.0 for  $Ra = 8.9 \times 10^7$  &  $9.3 \times 10^7$ , b) 1.0 for  $Ra = 9.7 \times 10^8$  &  $1 \times 10^9$  and c) 0.5 for  $Ra = 7.8 \times 10^9$  &  $8.1 \times 10^9$ .

The velocity near the hot and cold sides starts to increase and reaches a maximum value. Then it starts to decrease to its minimum (near to zero) for the whole enclosure core. The boundary layer near the hot wall side increases as the enclosure height increases. As the temperature increases, the velocity values and the boundary layer thickness will increase at the same time. On the other hand, as the aspect ratio increases the velocity values and the boundary layer thickness will decrease.

The collected data for the velocity along the vertical axis show that the maximum velocity always occurs near the mid height of the enclosure.

The turbulence intensity value increases gradually across the enclosure until the velocity values decrease to less than 0.05m/s near the end of the boundary layer then it starts to increase dramatically. The turbulence intensity increases as the aspect ratio increases and it decreases slightly as the temperature increases.

The maximum turbulence intensity along the vertical axis and at the maximum velocity values occurs near the two corners of the enclosure, where the turbulence intensity start to decrease until it reach its minimum value near the enclosure mid height. The turbulence intensity values increases as the aspect ratio increase.

These experimental results will be compared with the numerical results in the next chapters.

# CHAPTER 7

## CORRELATION EQUATIONS FOR HEAT TRANSFER IN CAVITIES

### 7.1 Producing the correlation equations for pure natural convection in square and rectangular enclosures

The correlation equations for both square and rectangular enclosures will be produced in this chapter using the provided dimensionless relations in chapter 4 and the numerical results provided in chapter 5. The analysis method will produce the correlation equations for the two cases pure natural convection and natural convection with radiation in square and rectangular enclosures.

#### 7.1.1 Providing the correlation equation for square enclosures

As explained in chapter 4 and from equation (1) below, the correlation equation for natural convection without radiation interaction in a square enclosure is formed, equation 2.

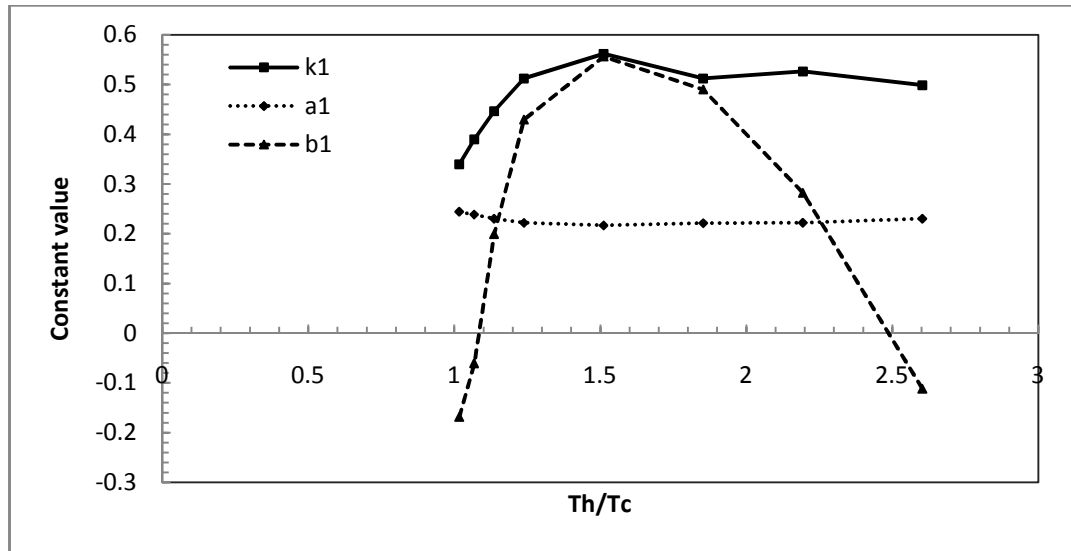
$$Nu_c = \emptyset(Gr, Pr, T_r) \quad (1)$$

This forms a relationship between the average convection Nusselt, Grashof and Prandtl numbers in a square enclosure:

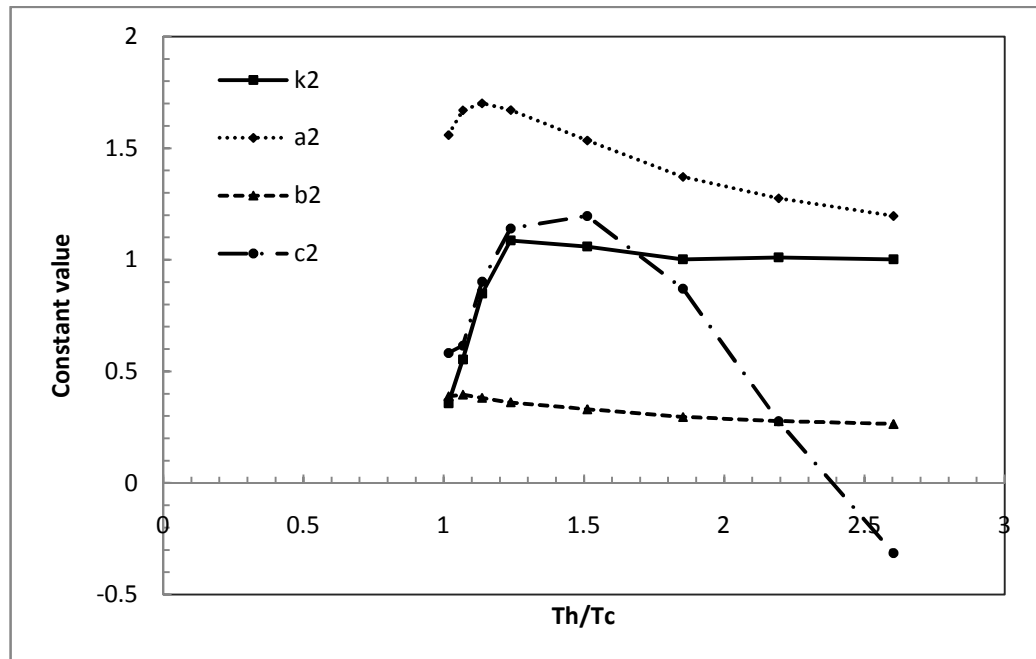
$$Nu_c = \frac{k_1 Gr^{a_1}}{Pr^{b_1}} \quad (2)$$

Where  $k_1$ ,  $a_1$  and  $b_1$  are constants and are a function of the absolute temperature ratio  $T_r$  of the hot and cold walls of the enclosure. These constants are found by using all the numerical results for the three different groups then fitting them to get the average convection Nusselt number. The fitting and optimization of the numerical results was

done using the solver in the Microsoft office excel software package (office 2007), which uses the generalized reduced gradient (GRG2) nonlinear optimization code, which was developed by Leon et.al [117, 118]. The values of these resultant constants as a function of absolute temperature ratio which fit equation 2 are shown in figure 7.1a.



(a)



(b)

Figure 7.1 - Constants values as a function of  $T_h/T_c$  for (a) Natural convection without radiation equation (2), (b) Natural convection with interaction of surface thermal radiation equation (8).

### 7.1.2 Providing the correlation equation for rectangular enclosures

According to the numerical results of the heat transfer in the rectangular enclosure with different aspect ratios examined in this study (which discussed in detail in chapter 5), the flow could be divided into two regimes, where the second (transition) regime could be included into the other two regimes:

1. Regime one starts from square to tall enclosures for aspect ratio ranging from 1 to 16,
2. Regime two starts from square to shallow enclosures for aspect ratio ranging from 1 to 0.0625.

From equation 3 below (provided in section 4.3.2 in chapter 4), the following correlation equation for natural convection without radiation interaction in a rectangular enclosure is formed, equation 4.

$$Nu_c = \emptyset(Gr, Pr, T_r, AR) \quad (3)$$

This forms a relationship between the average convection Nusselt, Grashof, Prandtl numbers and aspect ratio in rectangular enclosures:

$$Nu_c = \frac{k_1 Gr^{a_1}}{Pr^{b_1}} * f(AR) \quad (4)$$

Where  $k_1, a_1$  and  $b_1$  are constants and are a function of the absolute temperature ratio  $T_r$  of the hot and cold walls of the rectangular enclosure and their values are shown in figure 7.1a.

And  $f(AR)$  is the aspect ratio conversion equation which has two forms for each regime:

For the first regime (aspect ratio from 1 to 16)

$$f(AR) = AR^{ka1} + ka2e^{AR^{ka3}} + ka4 \quad (5)$$

For the second regime (aspect ratio from 1 to 0.0625)

$$f(AR) = kb1 \left( AR^{kb2} + kb3e^{AR^{kb4}} + kb5 \right) \quad (6)$$



Where  $ka_1$ ,  $ka_2$ ,  $ka_3$  and  $ka_4$  and  $kb_1$ ,  $kb_2$ ,  $kb_3$ ,  $kb_4$  and  $kb_5$  are constants and are a function of the absolute temperature ratio  $T_r$  of the hot and cold walls of the rectangular enclosure. These constants are also found by using all the numerical results for the rectangular enclosure with different aspect ratios then fitting them to get the average convection Nusselt number. The fitting and optimization of the numerical results was done using the solver in the Microsoft office excel software package (office 2007), as explained before. The values of these constants as a function of absolute temperature ratio which fit equations 5 and 6 are shown in figure 7.2.

## **7.2 Providing the correlation equations for natural convection with radiation interaction in square and rectangular enclosures**

### **7.2.1 The correlation equations for square enclosures**

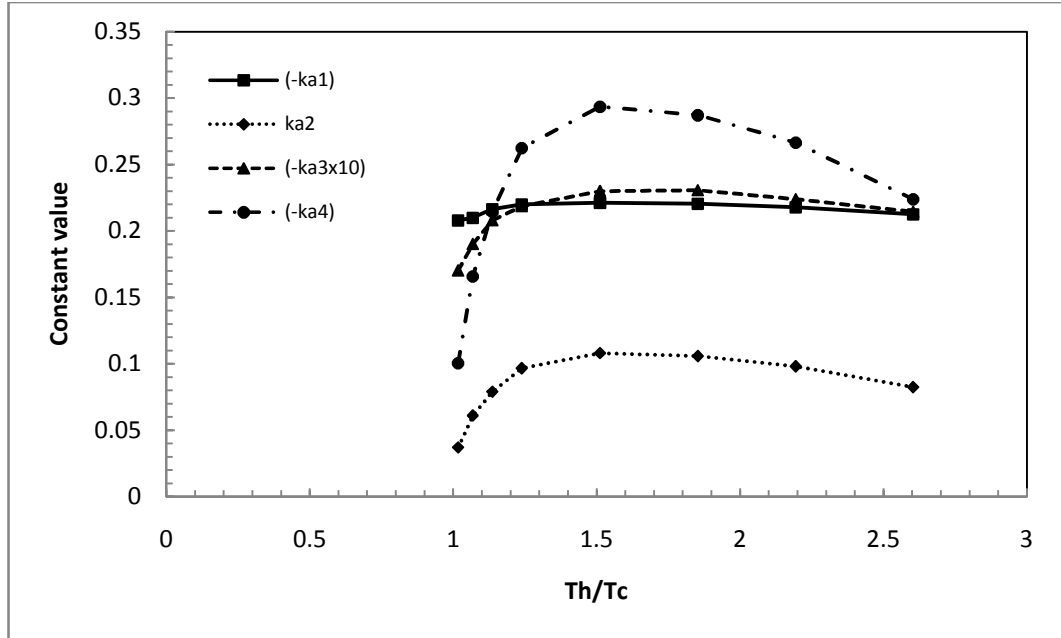
As given in section 4.3.1 in chapter 4 and using equation 7 below, the following correlation equation for the natural convection with the interaction of thermal surface radiation has been provided which shows the relation between the new dimensionless group (natural convection to radiation heat transfer) and the total Nusselt number, Grashof number and Prandtl number in the square enclosure equation8:

$$RC_n = \varphi(Nu_t, Gr, Pr, T_r) \quad (7)$$

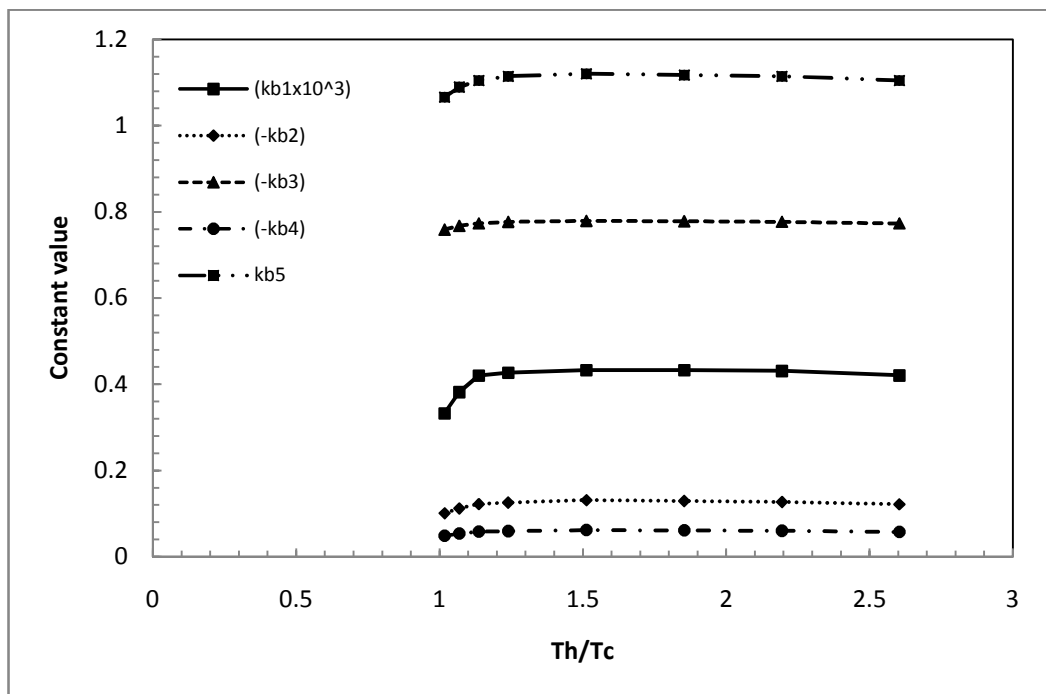
$$\frac{Q_{conv}}{Q_{rad}} = Nu_c Pl = \frac{k_2 Gr^{b_2}}{Nu_t^{a_2} Pr^{c_2}} \quad (8)$$

Where  $k_2$ ,  $a_2$ ,  $b_2$  and  $c_2$  are constants and are a function of the absolute temperature ratio  $T_r$  of the hot and cold walls of the enclosure. These constants are also found by using all the numerical results for the square enclosure and for the case of natural convection with radiation interaction then fitting these constants to get the dimensionless group. The fitting and optimization of the numerical results was done again using the solver in

the Microsoft office excel software package (office 2007), as explained before. The values of these constants as a function of the absolute temperature ratio which fit equation 8 are shown in figure 7.1b.



(a)



(b)

Figure 7.2 Constants as a function of absolute temperature ratio for a) Equation (5) and b) Equation (6).

Also from equation 9 below (which discussed in chapter 4) and the numerical results in the square enclosure (which explained in chapter 5), the following dimensionless correlation equation for the total Nusselt number as a function of Grashof, Prandtl and Planck numbers can be derived equation 10:

$$Nu_t = \Phi(Gr, Pr, Pl, T_r) \quad (9)$$

$$Nu_t = a \frac{Gr^b}{Pr^c Pl^d} \quad (10)$$

Where  $a$ ,  $b$ ,  $c$  and  $d$  are constants and are a function of the absolute temperature ratio  $T_r$  of the hot and cold walls of the square enclosure. These constants are found by using all the numerical results for the square enclosure for the case of natural convection with radiation interaction then these constants was fitted to get the total average Nusselt number. The fitting and optimization of the numerical results was done also using the solver in the Microsoft office excel software package (office 2007), as explained before; the values of these constants are shown in figure 7.3.

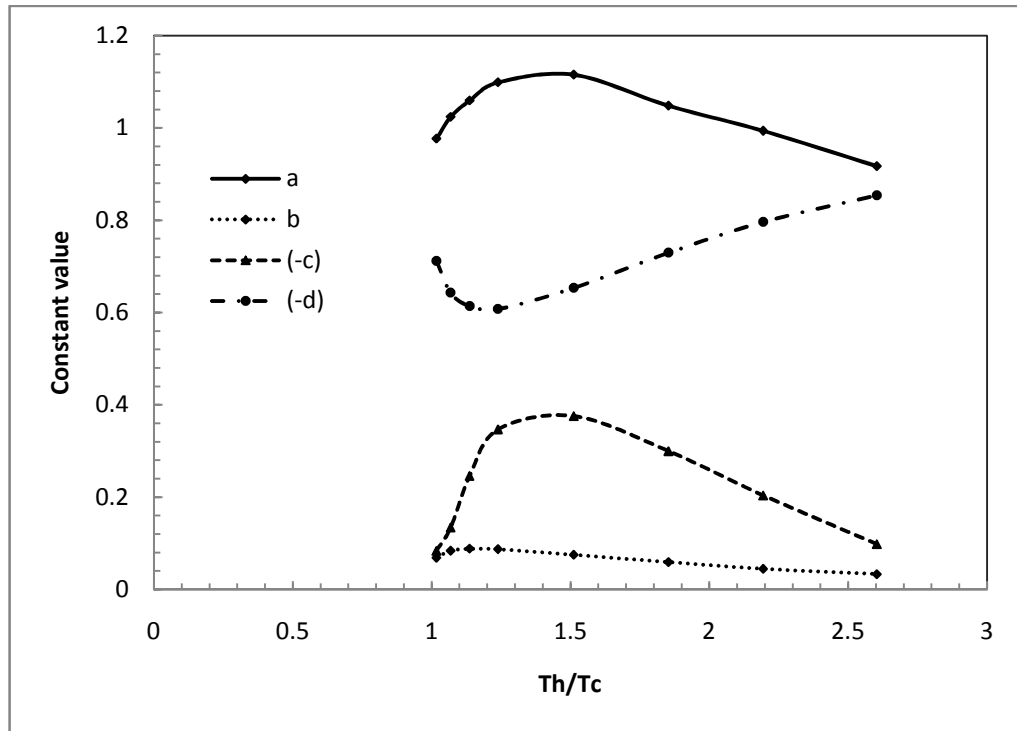


Figure 7.3 Constants as a function of absolute temperature ratio Equation (10).

## 7.2.2 The correlation equations for rectangular enclosures

Using equation 11 below (which given in section 4.3.2 chapter 4) and the numerical results in chapter 5, the following correlation equation (equation 12) for the case of natural convection with the interaction of thermal surface radiation has been provided which matches the relationship between the new dimensionless group and the total Nusselt number, Grashof number, Prandtl number and the aspect ratio in the rectangular enclosure

$$RC_n = \varphi(Nu_t, Gr, Pr, T_r, AR) \quad (11)$$

$$RCn = \frac{Q_{conv}}{Q_{rad}} = \frac{k_2 Gr^{b_2}}{Nu_t^{a_2} Pr^{c_2}} * f(AR) \quad (12)$$

Where  $k_2$ ,  $a_2$ ,  $b_2$  and  $c_2$  are again a function of the absolute temperature ratio  $T_r$  of the hot and cold walls of the rectangular enclosure and their values are again as explained before and are shown in figure 7.1b.

Here  $f(AR)$  is the aspect ratio conversion equation and it also has two forms for each regime:

For the first regime (aspect ratio from 1 to 16)

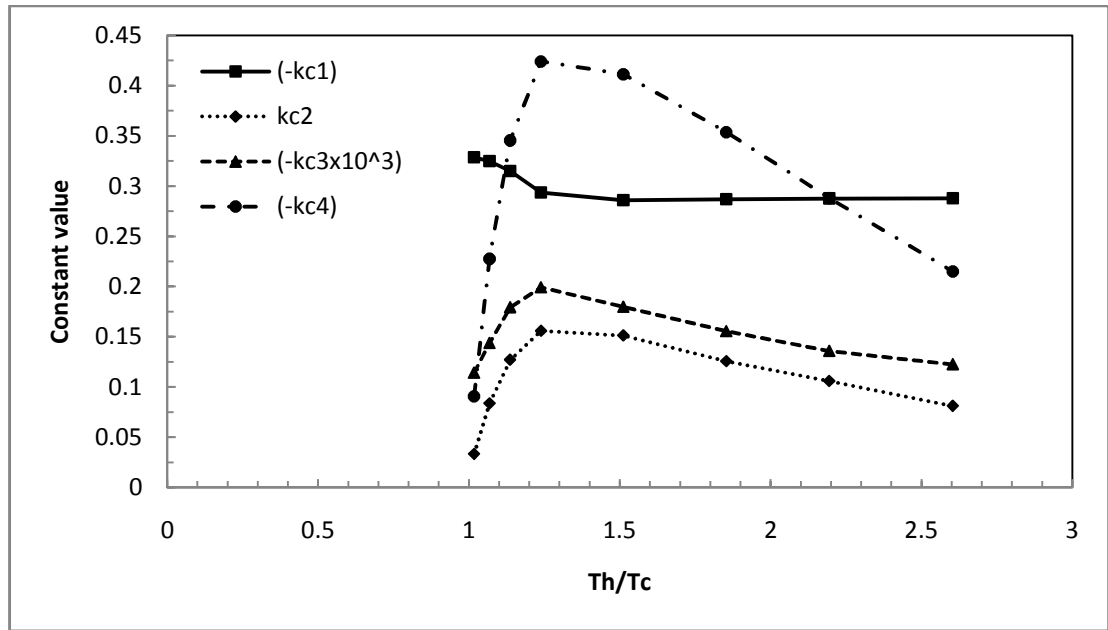
$$f(AR) = AR^{kc1} + kc2e^{AR^{kc3}} + kc4 \quad (13)$$

For the second regime (aspect ratio from 1 to 0.0625)

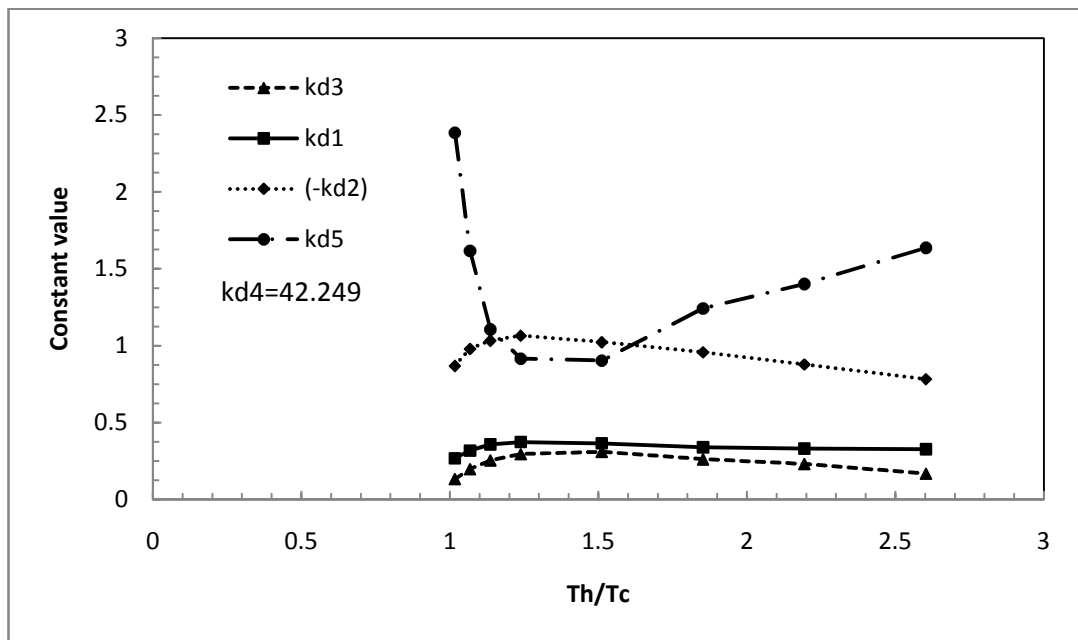
$$f(AR) = kd1 \left( AR^{kd2} + kd3e^{AR^{kd4}} + kd5 \right) \quad (14)$$

Where  $kc_1$ ,  $kc_2$ ,  $kc_3$  and  $kc_4$  and  $kd_1$ ,  $kd_2$ ,  $kd_3$ ,  $kd_4$  and  $kd_5$  are constants and are a function of the absolute temperature ratio  $T_r$  of the hot and cold walls of the rectangular enclosure. These constants are also found by using all the numerical results for the rectangular enclosure with different aspect ratios for the case of natural convection with radiation interaction then fitting these constants to get the new dimensionless group. The fitting and optimization of the numerical results was again conducted using the solver in the Microsoft office excel software package (office 2007), as explained above.

The values of these constants as a function of absolute temperature ratio which fit equations 13 and 14 are given in figure 7.4.



(a)



(b)

Figure 7.4 - Constants as a function of absolute temperature ratio for a) Equation (13) and b) Equation (14).

Also from equation 15 below(as explained in chapter 4) and the numerical results, the following dimensionless correlation equation for the total Nusselt number can be derived equation 16:

$$Nu_t = \Phi(Gr, Pr, Pl, T_r, AR) \quad (15)$$

$$Nu_t = a \frac{Gr^b}{Pr^c Pl^d} * f(AR) \quad (16)$$

Where  $a$ ,  $b$ ,  $c$  and  $d$  are constants and are a function of the absolute temperature ratio  $T_r$  of the hot and cold walls of the square enclosure; their values are shown in figure 7.3.  $f(AR)$  is the aspect ratio conversion equation. For the case of rectangular enclosure, the aspect ratio conversion equation has two equations for the two regimes; these are described above in section 7.1.2.

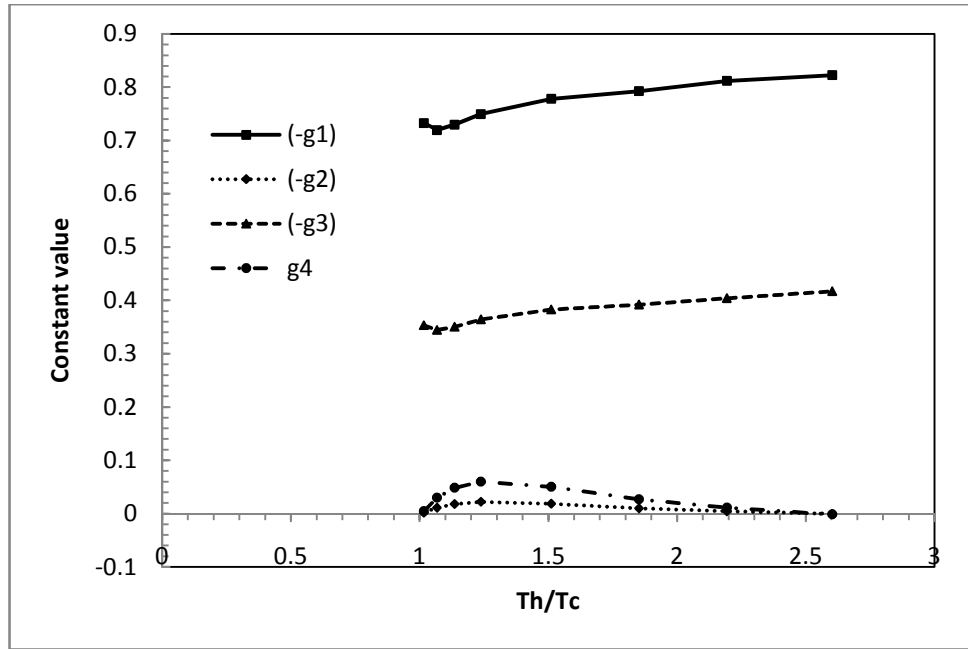
For the first regime (aspect ratio from 1 to 16)

$$f(AR) = AR^{g1} + g2e^{AR^{g3}} + g4 \quad (17)$$

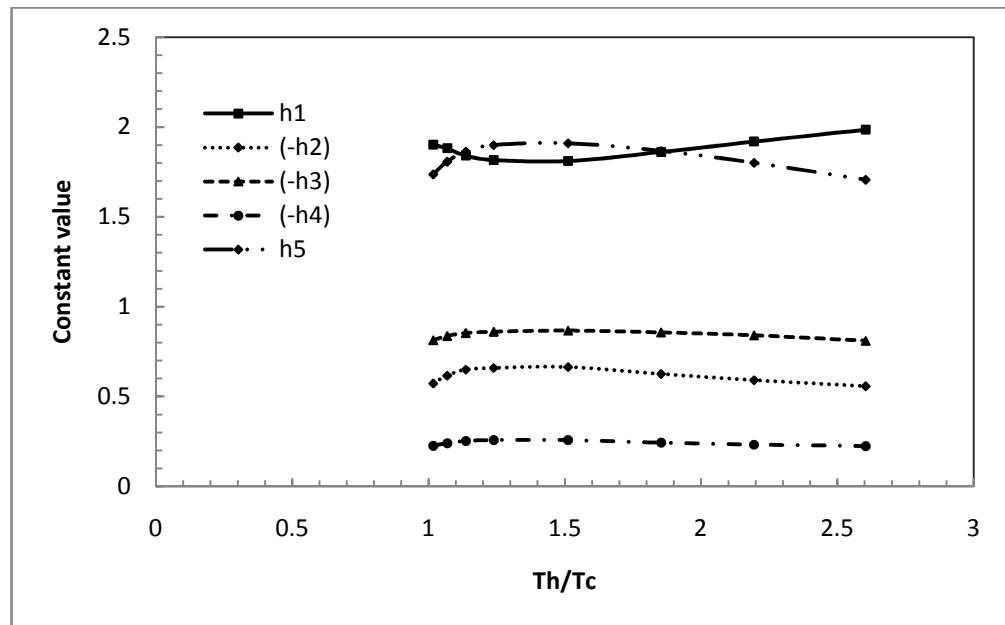
For the second regime (aspect ratio from 1 to 0.0625)

$$f(AR) = h1 \left( AR^{h2} + h3e^{AR^{h4}} + h5 \right) \quad (18)$$

Where  $g1$ ,  $g4$  and  $h1$ ,  $h5$  are constants and are shown to be a function of the absolute temperature ratio  $T_r$  of the hot and cold walls of the rectangular enclosure. These constants are also found by using all the numerical results for the rectangular enclosure with different aspect ratios for the case of natural convection with radiation interaction then fitting these constants to get the total average Nusselt number. The fitting and optimization of the numerical results was done again using the solver in the Microsoft office excel software package (office 2007), as explained before. The values of these constants as a function of absolute temperature ratio which fit equations 17 and 18 are shown in figure 7.5.



(a)



(b)

Figure 7.5 Constants as a function of absolute temperature ratio a) Equation (17) and b) Equation (18).

### 7.3 Producing polynomial equations

To simplify using these correlation equations for both square and rectangular enclosures with and without radiation the constants of each equation are correlated and

a polynomial equation for each of them has been produced. The polynomial equations have been produced using the constants values given in figures 7.1 to 7.5.

These polynomial equations are correlated and provided according to three absolute temperature ratio ranges:

- Temperature range  $1.017 \leq T_r \leq 1.238$
- ,temperature range  $1.238 \leq T_r \leq 1.852$
- and temperature range  $1.852 \leq T_r \leq 2.603$ .

The constants of each polynomial equation are given along with the equations in tables 7.1 to 7.6.

From equation 2 above, the constants  $k_l, a_l$  and  $b_l$  which are shown in figure 7.1a were obtained and polynomial equations for each constant as a function of absolute temperature ratio for the square enclosure are provided. These polynomial equations as a function of temperature range with their constants values are given in table 7.1.

Table 7.1 the values of constants  $p_1, p_2, p_3$  and  $p_4$  for the polynomial equations of  $k_l, a_l$  and  $b_l$  for the case of pure natural convection in square enclosure, equation 2.

$k_l, a_l, b_l = p_1 T_r^3 + p_2 T_r^2 + p_3 T_r + p_4$ for $1.017 \leq T_r \leq 1.238$							
	$p_1$	$p_2$	$p_3$	$p_4$			
$k_l$	0.253	-2.015	4.356	-2.273			
$a_l$	1.703	-5.608	6.03	-1.8795			
$b_l$	105.5	-354.4	392.575	-143.5			
$k_l, a_l, b_l = p_1 T_r^2 + p_2 T_r + p_3$ for $1.238 \leq T_r \leq 1.852$				$k_l, a_l, b_l = p_1 T_r^2 + p_2 T_r + p_3$ for $1.852 \leq T_r \leq 2.603$			
	$p_1$	$p_2$	$p_3$		$p_1$	$p_2$	$p_3$
$k_l$	-0.5316	1.644	-0.7084	$k_l$	-0.1436	0.6217	-0.1467
$a_l$	0.05332	-0.1657	0.3452	$a_l$	0.02365	-0.09368	0.3136
$b_l$	1.074	-3.418	2.157	$b_l$	0.4694	-1.29	0.2895

For the case of pure natural convection in rectangular enclosures shown in equation 4, the polynomial equations of the constants  $k_l, a_l$  and  $b_l$  are same as in square enclosure, equation 2, and their constants values again given in table 7.1.

And  $f(AR)$  in equation 4 is the aspect ratio conversion equation and it has two forms for each aspect ratio regime as given in equations 5 and 6 above.



Where  $ka_1$ ,  $ka_2$ ,  $ka_3$  and  $ka_4$  and  $kb_1$ ,  $kb_2$ ,  $kb_3$ ,  $kb_4$  and  $kb_5$  which are shown in figure 7.2 for the rectangular enclosure are correlated, a polynomial equation for each constant as a function of absolute temperature ratio is provided. These polynomial equations as a function of temperature range with their constants values are given in table 7.2.

Table 7.2 The values of constants  $p_1$ ,  $p_2$ ,  $p_3$  and  $p_4$  for the polynomial equations of  $k_{a1}$ ,  $k_{a2}$ ,  $k_{a3}$ ,  $k_{a4}$  and  $k_{b1}$ ,  $k_{b2}$ ,  $k_{b3}$ ,  $k_{b4}$ ,  $k_{b5}$  for the case of pure natural convection in a rectangular enclosure, equations 5 and 6.

$k_{ai}, k_{bi} = p_1 T_r^3 + p_2 T_r^2 + p_3 T_r + p_4$ for $1.017 \leq T_r \leq 1.238$							
	$p_1$	$p_2$	$p_3$	$p_4$			
$k_{a1}$	3.762	- 12.61	13.98	- 5.34			
$k_{a2}$	5.428	- 19.22	22.84116	- 9.023			
$k_{a3}$	-5.781	29.21	- 45.941	20.89			
$k_{a4}$	-14.75	52.24	- 62.0813	24.52			
$k_{b1}$	2273	-10700	15859.85	-7121			
$k_{b2}$	0.4816	-0.9766	0.24745	0.1508			
$k_{b3}$	-2.033	7.288	-8.7376	2.728			
$k_{b4}$	0.3051	-0.74	0.4527	-0.0647			
$k_{b5}$	5.453	-19.54	23.4175	-8.276			
$k_{ai}, k_{bi} = p_1 T_r^2 + p_2 T_r + p_3$ for $1.238 \leq T_r \leq 1.852$				$k_{ai}, k_{bi} = p_1 T_r^2 + p_2 T_r + p_3$ for $1.852 \leq T_r \leq 2.603$			
	$p_1$	$p_2$	$p_3$		$p_1$	$p_2$	$p_3$
$k_{a1}$	0.0103	-0.03241	-0.1957	$k_{a1}$	0.007575	-0.02328	-0.2033
$k_{a2}$	-0.07873	0.2584	-0.1027	$k_{a2}$	-0.021	0.06244	0.06212
$k_{a3}$	0.6494	-2.204	-0.4523	$k_{a3}$	0.04228	0.02775	-2.502
$k_{a4}$	0.2153	-0.7059	0.2816	$k_{a4}$	0.05813	-0.1748	-0.1628
$k_{b1}$	-33.05	111.3	339.9	$k_{b1}$	-26.57	102.2	334.5
$k_{b2}$	0.04261	-0.1377	-0.0206	$k_{b2}$	0.009094	-0.03031	-0.1045
$k_{b3}$	0.02088	-0.06585	-0.7272	$k_{b3}$	0.009093	-0.03477	-0.7443
$k_{b4}$	0.01874	-0.06069	-0.01308	$k_{b4}$	0.003697	-0.01201	-0.05163
$k_{b5}$	-0.05657	0.1784	0.9795	$k_{b5}$	-0.02457	0.09393	1.026

For the case of natural convection with radiation interaction in square enclosures from equation 8,  $k_2$ ,  $a_2$ ,  $b_2$  and  $c_2$  which are shown in figure 7.1b are constants and are a function of the absolute temperature ratio  $T_r$  of the hot and cold walls of the enclosure. These constants are correlated and polynomial equations for each constant as a function

of absolute temperature ratio are provided. These polynomial equations as a function of temperature range with the values of their constants are given in table 7.3.

For the case of natural convection with radiation interaction in rectangular enclosure from equation 12  $k_2$ ,  $a_2$ ,  $b_2$  and  $c_2$  are again the same as the square enclosure equation 8 and their values are given in table 7.3.

Table 7.3 The values of constants  $p_1$ ,  $p_2$ ,  $p_3$  and  $p_4$  for the polynomial equations of  $k_2$ ,  $a_2$ ,  $b_2$  and  $c_2$  for the case of natural convection with radiation interaction in square enclosure equation 8.

$k_2, a_2, b_2, c_2 = p_1 T_r^3 + p_2 T_r^2 + p_3 T_r + p_4$ for $1.06 \leq T_r \leq 1.238$							
	$p_1$	$p_2$	$p_3$	$p_4$			
$k_2$	-70.04	229.5676	- 246.4	87.18			
$a_2$	-44.82	158.743	- 187	71.58			
$b_2$	13.96	- 48	54.7	- 20.28			
$c_2$	184.1	- 623.1	698.1	- 259.73			
$k_2, a_2, b_2, c_2 = p_1 T_r^2 + p_2 T_r + p_3$ for $1.238 \leq T_r \leq 1.852$				$k_2, a_2, b_2, c_2 = p_1 T_r^2 + p_2 T_r + p_3$ for $1.852 \leq T_r \leq 2.603$			
	$p_1$	$p_2$	$p_3$		$p_1$	$p_2$	$p_3$
$k_2$	-0.1103	0.2022	1.005	$k_2$	-0.06594	0.295	0.6811
$a_2$	-0.03596	0.5983	-2.357	$a_2$	-0.1174	0.7571	-2.371
$b_2$	0.02185	-0.1751	0.545	$b_2$	0.02855	-0.1684	0.5095
$c_2$	1.887	-5.396	2.647	$c_2$	-0.3966	3.346	-5.708

Here  $f(AR)$  in equation 12 is the aspect ratio conversion equation and it also has two forms for each regime as given in the two equations 13 and 14 above.

Where  $kc_1$ ,  $kc_2$ ,  $kc_3$  and  $kc_4$  and  $kd_1$ ,  $kd_2$ ,  $kd_3$ ,  $kd_4$  and  $kd_5$ , shown in figure 7.4 for the rectangular enclosure are correlated, polynomial equations for each constant as a function of absolute temperature ratio are provided. These polynomial equations as a function of temperature range with their constants values are given in table 7.4.

For the case of natural convection with radiation interaction in square enclosure from equation 10 the constants  $a$ ,  $b$ ,  $c$  and  $d$  as shown in figure 7.3, are correlated and correlation equations for each constant as a function of absolute temperature ratio are provided. The polynomial equations with their constants are given in table 7.5.

Table 7.4 The values of constants  $p_1$ ,  $p_2$ ,  $p_3$  and  $p_4$  for the equations of  $k_{c1}$ ,  $k_{c2}$ ,  $k_{c3}$ ,  $k_{c4}$  and  $k_{d1}$ ,  $k_{d2}$ ,  $k_{d3}$ ,  $k_{d4}$ ,  $k_{d5}$  for the case of natural convection with radiation interaction in rectangular enclosure, equations 13 and 14.

$k_{ci}, k_{di} = p_1 T_r^3 + p_2 T_r^2 + p_3 T_r + p_4$ for $1.06 \leq T_r \leq 1.238$							
	$p_1$	$p_2$	$p_3$	$p_4$			
$k_{c1}$	-1.211	4.52	-5.40294	1.765			
$k_{c2}$	3.819	-15.22	20.26562	-8.852			
$k_{c3}$	6491	-20440	20872.1	-7028			
$k_{c4}$	-10.38	41.37	-55.08434	24.06			
$k_{d1}$	3.05	-13.1	18.3559	-8.06			
$k_{d2}$	-38.83	136.6	-160.2863	61.7			
$k_{d3}$	3.949	-16.18	22.11	-9.77288			
$k_{d4}$	0	0	0	42.249			
$k_{d5}$	-134.6	496.3	-610.96	252			
$k_{c1}$	-1.211	4.52	-5.40294	1.765			
$k_{ci}, k_{di} = p_1 T_r^2 + p_2 T_r + p_3$ for $1.238 \leq T_r \leq 1.852$				$k_{ci}, k_{di} = p_1 T_r^2 + p_2 T_r + p_3$ for $1.852 \leq T_r \leq 2.603$			
	$p_1$	$p_2$	$p_3$		$p_1$	$p_2$	$p_3$
$k_{c1}$	-0.05007	0.166	-0.4225	$k_{c1}$	0.002626	-0.01319	-0.27138
$k_{c2}$	-0.0945	0.2429	0.00003806	$k_{c2}$	-0.002993	-0.04584	0.220927
$k_{c3}$	-0.8903	73.79	-289.3	$k_{c3}$	-33.19	191.7	-396.822
$k_{c4}$	0.2003	-0.5048	-0.106	$k_{c4}$	-0.01861	0.2675	-0.7853
$k_{d1}$	-0.07203	0.1676	0.2759	$k_{d1}$	0.02003	-0.1065	0.4678
$k_{d2}$	0.05988	-0.009579	-1.145	$k_{d2}$	0.001066	0.2279	-1.383
$k_{d3}$	-0.3193	0.9312	-0.369	$k_{d3}$	-0.08931	0.2733	0.06044
$k_{d4}$	0	0	42.249	$k_{d4}$	0	0	42.249
$k_{d5}$	1.688	-4.686	4.128	$k_{d5}$	0.1436	-0.1146	0.9605

For the case of natural convection with radiation interaction in rectangular enclosure from equation 16 the constants  $a$ ,  $b$ ,  $c$  and  $d$  are again same as in square enclosure equation 10 and their values are given in table 7.5.

The conversion equation for aspect ratio  $f(AR)$  in equation 16 has two forms for each regime as given in the two equations 17 and 18 above.

Where  $g_1$  to  $g_4$  and  $h_1$  to  $h_5$  which shown in figure 7.5 for the rectangular enclosure are correlated, a polynomial equations for each constant as a function of absolute temperature ratio are provided. These polynomial equations with their constants values are given in table 7.6.

Table 7.5 The values of constants  $p_1$ ,  $p_2$  and  $p_3$  for the polynomial equations of a, b, c and d for the case of natural convection with radiation interaction in square enclosure equation 49.

$a, b, c, d = p_1 T_r^2 + p_2 T_r + p_3 \text{ for } 1.06 \leq T_r \leq 1.238$							
	$p_1$	$p_2$	$p_3$				
$a$	-3.3949	8.0018	- 2.3285				
$b$	-1.9309	4.3209	- 2.3285				
$c$	-5.4553	10.388	- 5.0057				
$d$	-7.7874	17.59	-10.546				
$a, b, c, d = p_1 T_r^2 + p_2 T_r + p_3$ for $1.238 \leq T_r \leq 1.852$				$a, b, c, d = p_1 T_r^2 + p_2 T_r + p_3$ for $1.852 \leq T_r \leq 2.603$			
	$p_1$	$p_2$	$p_3$		$p_1$	$p_2$	$p_3$
$a$	-0.8651	2.4403	-0.597	$a$	0.0041	-0.1966	1.4017
$b$	-0.09	0.2034	-0.0267	$b$	0.013	-0.0923	0.1849
$c$	2.3423	-6.548	4.1703	$c$	0.0213	0.1695	-0.6821
$d$	-0.6163	-1.5264	-1.5527	$d$	0.0579	-0.4227	-0.1465

## 7.4 Comparison between numerical results and the derived correlation equations

The comparison between the numerical result and the calculated results using the derived correlation equations are explained in this section and it used just to show how these correlation equations accurate and can fit the numerical results.

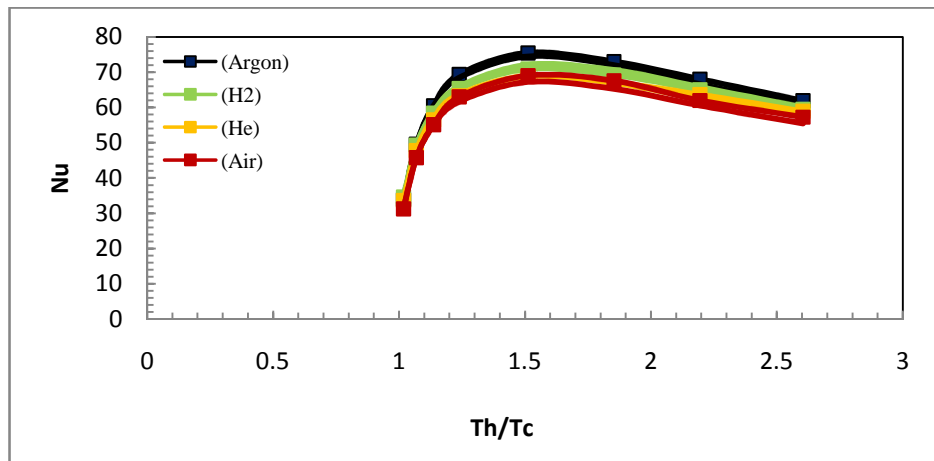
### 7.4.1 Pure natural convection inside a square enclosure

The comparison between the numerical results of the average Nusselt number as a function of absolute temperature ratio  $T_r$  and the calculated results using equation 2 and the provided polynomial equations, given in table 7.1 and discussed above for the square enclosure, are shown in Figure 7.6. From this Figure it can be seen that the numerical and the calculated curves using equation 1 with the provided polynomial correlation equations collapse on the top of each other.

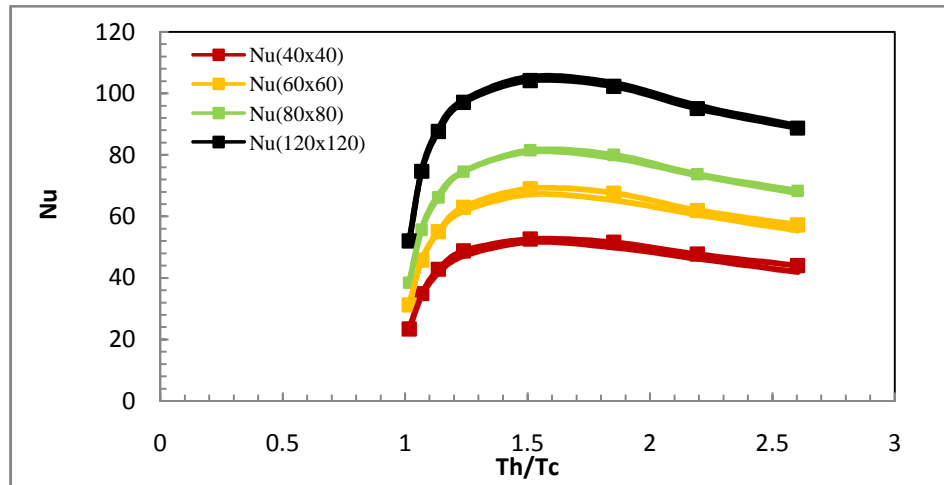
Table 7.6 The values of constants  $p_1$ ,  $p_2$  and  $p_3$  for the equations of  $g_1$ ,  $g_2$ ,  $g_3$ ,  $g_4$  and  $h_1$ ,  $h_2$ ,  $h_3$ ,  $h_4$ ,  $h_5$  for the case of natural convection with radiation interaction in rectangular enclosure, equations 17 and 18.

$g_i, h_i = p_1 T_r^2 + p_2 T_r + p_3$ for $1.06 \leq T_r \leq 1.238$							
	$p_1$	$p_2$	$p_3$				
$g_1$	-3.4219	7.3961	-4.7153				
$g_2$	0.6825	-1.6051	0.9247				
$g_3$	-2.1627	4.6805	-2.8764				
$g_4$	-1.8549	4.3623	-2.5131				
$h_1$	-1.5538	2.8279	0.6332				
$h_2$	2.9773	-7.0566	3.524				
$h_3$	1.8796	-4.3844	1.7011				
$h_4$	1.1286	-2.66	1.3123				
$h_5$	-4.6402	11.053	-4.7052				
$g_i, h_i = p_1 T_r^2 + p_2 T_r + p_3$ for $1.238 \leq T_r \leq 1.852$				$g_i, h_i = p_1 T_r^2 + p_2 T_r + p_3$ for $1.852 \leq T_r \leq 2.603$			
	$p_1$	$p_2$	$p_3$		$p_1$	$p_2$	$p_3$
$g_1$	0.236	-0.7546	-0.1768	$g_1$	0.0132	-0.0964	-0.6618
$g_2$	0.1423	-0.3784	0.2283	$g_2$	-0.0097	0.0573	-0.0828
$g_3$	0.1809	-0.5659	0.059	$g_3$	-0.0026	-0.0212	-0.3447
$g_4$	-0.3866	1.0281	-0.6204	$g_4$	0.0264	-0.1556	0.225
$h_1$	0.3261	-0.9411	2.4859	$h_1$	0.0082	0.127	1.5992
$h_2$	0.2103	-0.5952	-0.2452	$h_2$	-0.0217	0.1874	-0.8985
$h_3$	0.094	-0.2854	-0.6515	$h_3$	0.031	-0.0758	-0.8241
$h_4$	0.0839	-0.2364	-0.0935	$h_4$	-0.0166	0.0995	-0.371
$h_5$	-0.3616	1.0771	1.1112	$h_5$	-0.0722	0.1106	1.9075

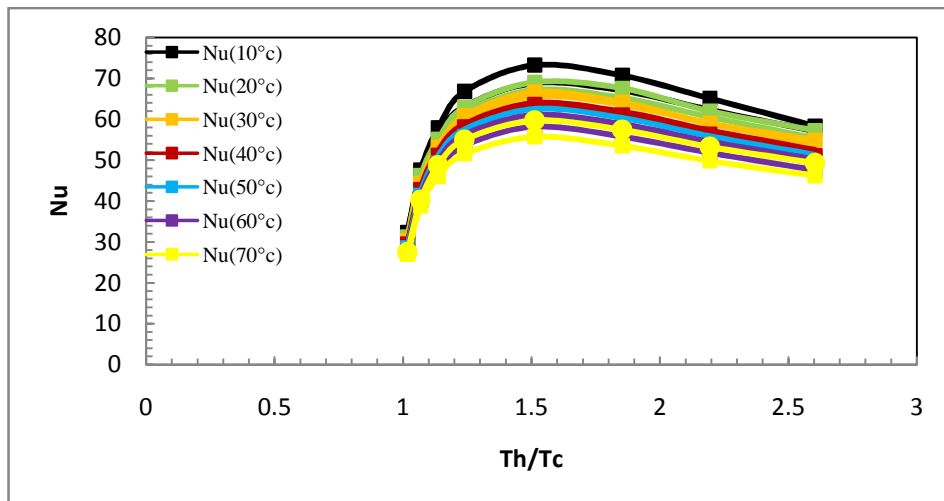
The calculated results of the average Nusselt number of pure natural convection in square enclosures using the derived correlation equation, equation 2, and its constants which shown in figure 7.1a and table 7.1 are found to be within an average deviation of 2.9% and a maximum deviation of less than 7.2% compared to the numerical predicted results for the three different groups.



(a)



(b)



(c)

Figure 7.6 Comparison between numerical (—■—) and calculated (—) results for the average Nusselt number in square enclosure.

### 7.4.2 Natural convection with radiation in square enclosure

The identification of the parameters describing the values that define the new dimensionless group ( $Q_{conv}/Q_{rad}$ ) has arisen by fitting the numerical results produced in chapter 5 section 5.5. The dimensionless groups controlling this system are shown in equation 8 and their derivation is explained in detail in sections 4.3 and 7.2 above.

The comparison between the numerical results of the new dimensionless group ( $Q_{conv}/Q_{rad}$ ) as a function of absolute temperature ratio  $T_r$  and the calculated results using equation 8 and the provided polynomial equations, (which discussed above for the square enclosure), are shown in Figure 7.7. From this Figure it can be seen that the numerical and the calculated curves using equation 8 with the provided polynomial correlation equations again are seen to collapse on the top of each other.

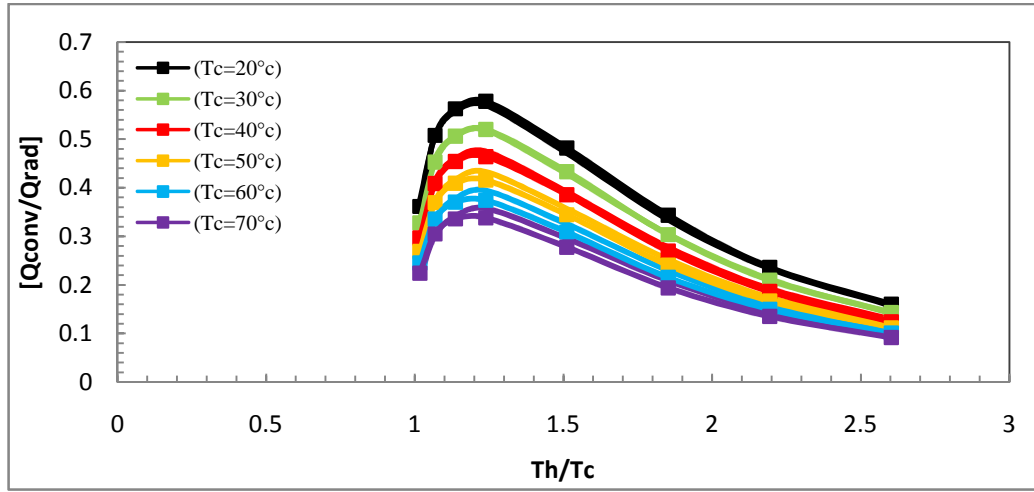
The calculated results of the new dimensionless group ( $Q_{conv}/Q_{rad}$ ) using the correlation equation 8, and its constants which shown in figure 7.1b and table 7.3 for the three different groups were within an average deviation of 2.8% and a maximum deviation of 7.3%; compared to the numerical results. When using equation (8) to calculate ( $Q_{conv}/Q_{rad}$ ) for other two sets of parameter, (different sizes and different properties) give an average deviation of less than 1.4% and a maximum deviation of less than 2.7%; compared to the numerical results.

Also in this section (of natural convection with radiation interaction in square enclosure), the calculated results for the total average Nusselt number, using the derived correlation equations (equation 10 and the constants shown in figure 7.3 and table 7.5), are found to be within a maximum deviation of less than 2.8% compared to the numerical results.

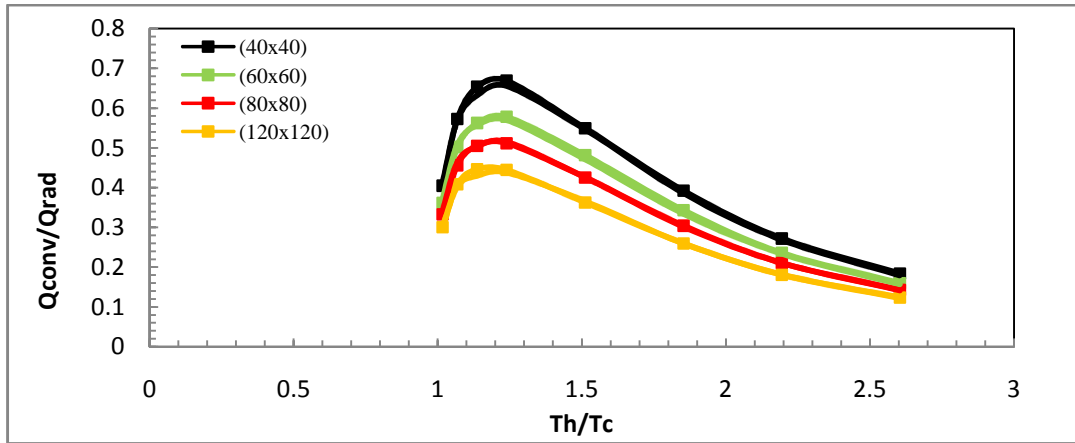
### 7.4.3 Pure natural convection inside rectangular enclosure

The comparison between the numerical results of the average Nusselt number for each aspect ratio and the calculated results using the empirical correlation equation 4 for the two regimes of aspect ratio, using equations 5 and 6, are shown in figure 7.8-a and 7.8-b. From the figure the numerical and the calculated curves collapsed together and the Nusselt number as a function of absolute temperature ratio is increases for all aspect ratios to a certain value of  $T_r$  then it starts to decrease. Also from this figure it can be seen that, the trend of the Nusselt number increasing as the aspect ratio decreases. This

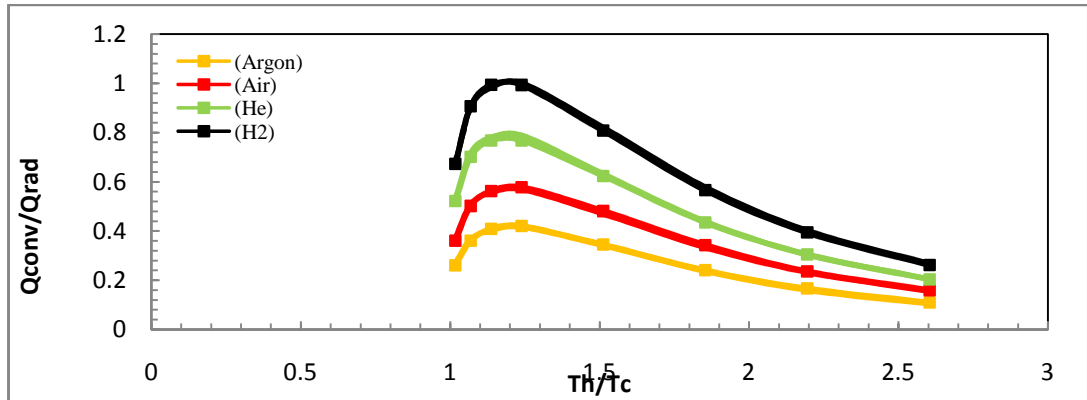
is because the Nusselt number is directly proportional to the enclosure width and as the aspect ratio decreases which means that the enclosure width will increase this which in turn causes the Nusselt number to increase.



(a)



(b)



(c)

Figure 7.7 Comparison between numerical (—■—) and calculated (—) results of the new dimensionless group for different (a) Cold wall temperatures, (b) Enclosure sizes and (c) Gases.



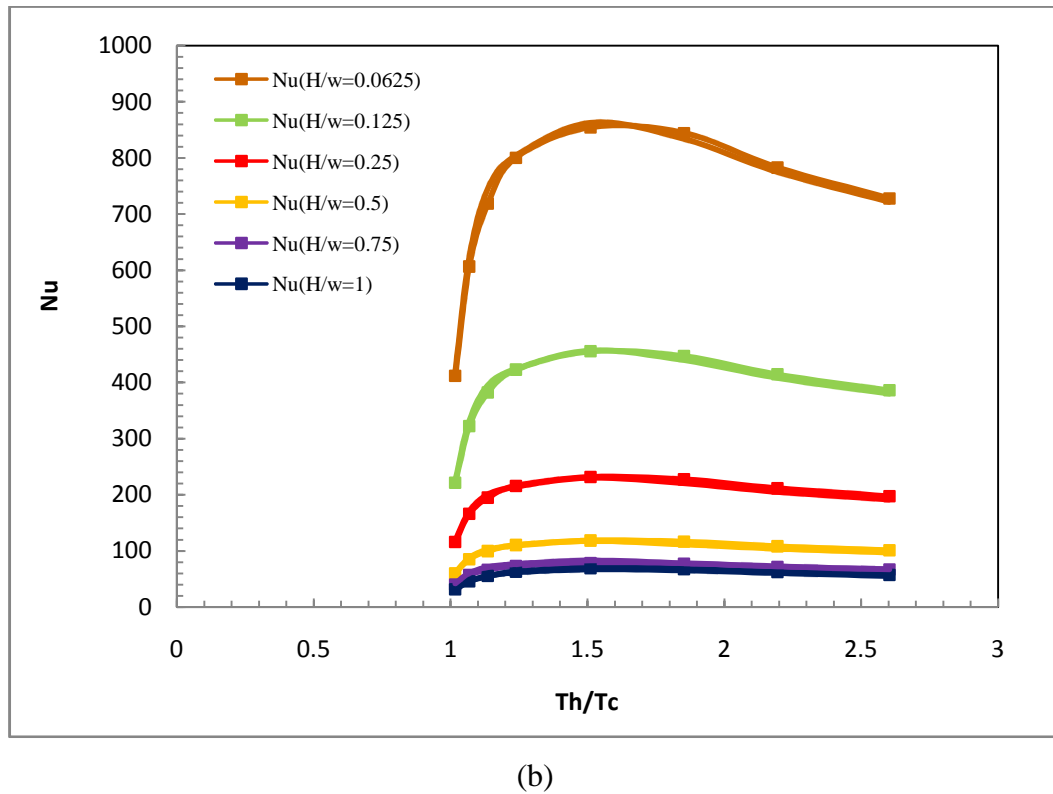
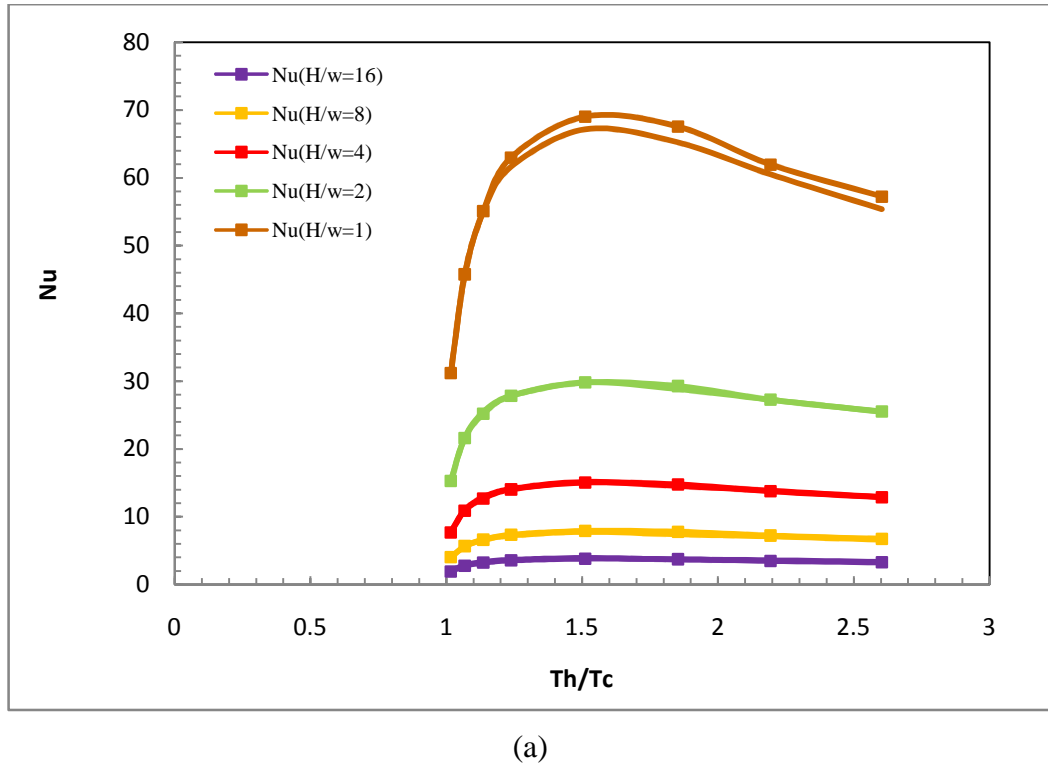


Figure 7.8 Comparison between numerical (—■—) and empirical calculated (—) average Nusselt number of pure natural convection for a) first regime and b) second regime.

The calculated results of the average Nusselt number from equations 4, 5 and 6, (and its constants shown in figures 7.1a and 7.2 and tables 7.1 and 7.2), for the first regime

are found to be within an average deviation of 2.7% and a maximum deviation of less than 7.3% compared to the numerical predicted results. Also for the second regime with the three different groups the results were within an average deviation of 3.2% and a maximum deviation of 6.6%; compared to the numerical results.

#### **7.4.4 Natural convection with radiation in a rectangular enclosure**

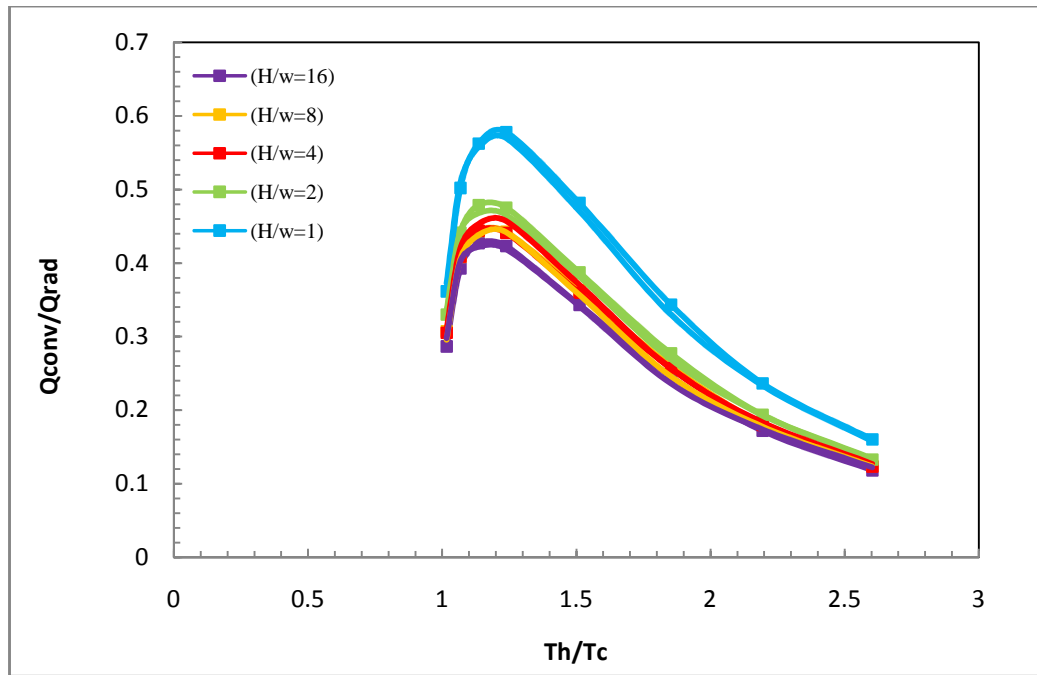
The comparison between numerical results of the new dimensionless group for each aspect ratio and the calculated empirical results using Equation (12) for the two regime of aspect ratio and using aspect ratio conversion Equations (13) and (14) are shown in Figures 7.9-a and 7.9-b. From these graphs it can be seen that the numerical and the calculated curves using equation 12 with the derived correlation equations agreed with each other.

The calculated results of the new dimensionless group ( $Q_{conv}/Q_{rad}$ ) using Equations 12 to 14, and their constants shown in figures 7.1b and 7.4 and tables 7.3 and 7.4 are given these results. For the first regime with the three different groups, compared to the numerical results these scales results were within an average deviation of 3.1% and a maximum deviation of 7.2%. Also for the second regime with the three different groups, compared to the numerical results, these results were within an average deviation of 2.9% and a maximum deviation of 7.3%.

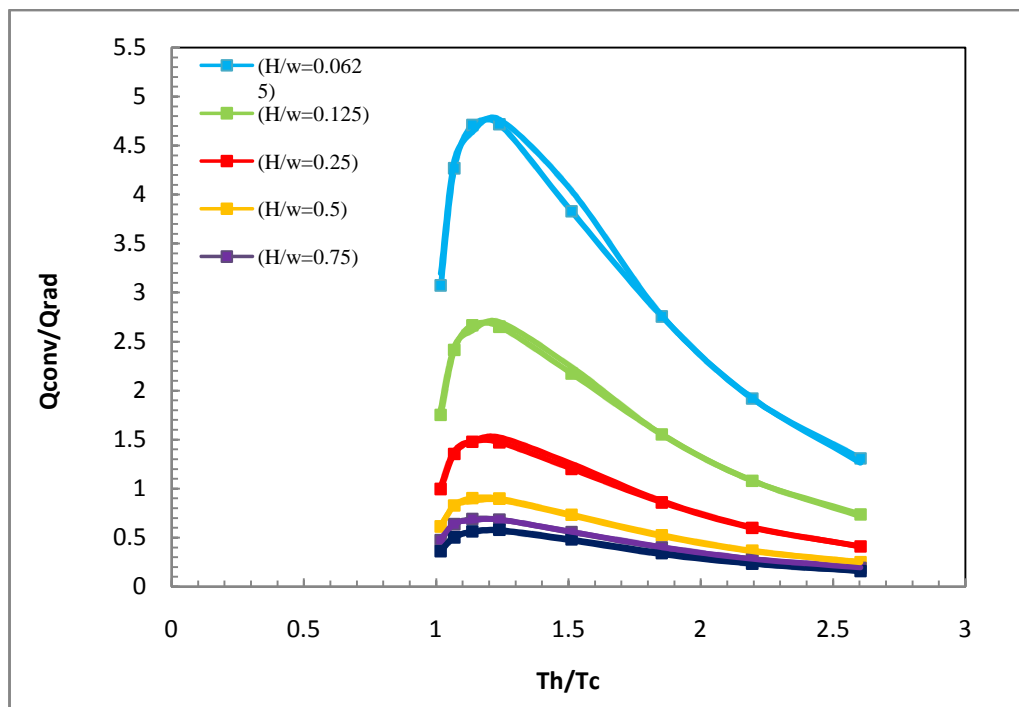
Additionally, the calculated results of the total Nusselt number for the rectangular enclosure using Equation (16) with the two aspect ratio conversion equations (17) and (18) for the two flow regimes , withtheir constants shown in figures 7.3 and 7.5 and tables 7.5 and 7.6, were within a maximum deviation of less than 7.7%, compared to the numerical results.

### **7.5 Using the provided polynomial correlation equations**

The empirical solution was established using all the results for both square and rectangular enclosures and for the two cases of pure natural convection and natural convection with radiation interaction. This is combined with the results found for the total Nusselt number for square and rectangular enclosures. All these results were used to produce the polynomial equations for the constants of the derived correlation equations.



(a)



(b)

Figure 7.9 Comparison between numerical (—■—) and empirical calculated results (—) of natural convection with radiation interaction for a) the first regime and b) the second regime.

The production of these correlation equations is explained in detail in earlier sections. Also the produced polynomial equations for the correlation equations constants are discussed in detail in the above sections. In this section the use of the provided polynomial and correlation equations together to find out the flow parameters will be discussed.

There are two methods to determine the flow parameters in the square and rectangular enclosures for the two cases of study, pure natural convection and natural convection with radiation interaction, which are described below:

1. The direct solution when the hot and cold wall temperatures are given. This is able to ascertain the heat transfer rate by looking up the parameters and producing a result.
2. The indirect (iterative) solution when only one wall temperature given along with the heat transfer rate. This will allow the temperature of the other wall to be found.

For the first method, when the hot and cold wall temperatures are given, all the other parameters can be found directly using the figures and the equations given for both square and rectangular enclosures. To show how this method is implemented, twelve examples are given for square and rectangular enclosures. The first six examples are for cases of pure natural convection and the other six examples are for natural convection with radiation interaction.

The first example for pure natural convection in square enclosure is solved in detail below and the solutions for the other eleven examples follow the same steps. The final results for all of the six examples are summarized in tables 7.7 (pure natural convection) and 7.8 (natural convection with radiation interaction).

**Example 1:** For the case of pure natural convection in square enclosure,

Given: Argon as the working fluid,  $T_c = 20^\circ\text{C}$ ,  $T_h = 60^\circ\text{C}$ ,  $AR = \frac{60\text{cm}}{60\text{cm}} = 1$

Calculated:  $T_r = 1.136$ ,  $G_r = 1.241 \times 10^9$  and  $P_r = 0.666$

Then from table 7.1 at  $T_r = 1.136$ , the constants  $k_1 = 0.446$ ,  $a_1 = 0.23$  and  $b_1 = -0.223$

From these, and using Equation 2, the Nusselt number will be 60.3 with an error of less than 0.2% compared to the numerical results. This will give a heat transfer rate due to convection of 40.21W.

The other five examples are for the case of pure natural convection in square and rectangular enclosures and they follow the same steps as example 1 and the calculated results of these examples are shown in table 7.7. The results of the other six examples which are for the case of natural convection with radiation interaction are shown in table 7.8. These all show errors of less than 5% and the answers can be extracted with ease.

Table 7.7 Results for examples 1 to 6 for pure natural convection using the explicit method.

Given				Calculated			Error (%) to numerical
Gas	$T_c$	$T_h$	$AR \left( \frac{\text{cm}}{\text{cm}} \right)$	$T_r$	$G_r$	$Pr$	$Nu_c$
Argon	20°C	60°C	1.0	1.136	$1.241 \times 10^9$	0.666	0.2
Air	20°C	90°C	8.0	1.238	$2.492 \times 10^6$	0.72	1.5
Air	20°C	370°C	0.125	2.19	$6.318 \times 10^{11}$	0.7	1.49
H2	20°C	170°C	1.0	1.511	$2.279 \times 10^9$	0.713	1.6
He	20°C	490°C	1.0	2.603	$1.085 \times 10^9$	0.725	0.2
Air	60°C	105°C	1.0	1.136	$5.791 \times 10^8$	0.714	4.8

For the second method when only one wall temperature is given along with the total heat transfer between the hot and cold walls, not all the parameters can be found explicitly as they are all a function of temperature ratio. Therefore an iterative approach is needed. In this case:

1. An initial absolute temperature ratio is selected. Generally, the value of 1.238 is a good choice as this is where the ratio of convection to radiation is a maximum.

2. The absolute temperature ratio will allow the unknown temperature to be calculated. Hence the other parameters and the associated Nusselt number can be calculated.
3. This Nusselt number can be used with the given total heat transfer rate to calculate the new temperature value from either:
  - If the cold wall temperature is given

$$T_{h_{i+1}} = \frac{Q_{(given)}}{Nu_{(i)} \times H/L \times k} + T_c \quad (19)$$

- If the hot wall temperature is given

$$T_{c_{i+1}} = T_h - \frac{Q_{(given)}}{Nu_{(i)} \times H/L \times k} \quad (20)$$

4. This new temperature value can be used to work out the new absolute temperature ratio and Nusselt number. Processes 3 and 4 can then be repeated until the error in the calculated heat transfer rate is small enough.

$$\text{Error} = \frac{Q_{(given)} - Q_{(i)}}{Q_{(given)}} \quad (21)$$

Table 7.8 Results for examples 7 to 12 for natural convection with radiation interaction using the explicit method.

Given				Calculated			Error (%) to numerical	
Gas	$T_c$	$T_h$	$AR \left( \frac{\text{cm}}{\text{cm}} \right)$	$T_r$	$G_r$	$Pr$	$Nu_t$	$\frac{Q_{conv}}{Q_{rad}}$
Argon	20°C	90°C	1.0	1.238	$1.754 \times 10^9$	0.666	0.17	0.8
Air	20°C	40°C	8.0	1.068	$9.988 \times 10^5$	0.727	1.34	0.73
Air	20°C	270°C	0.125	1.852	$7.742 \times 10^{11}$	0.704	1.49	0.01
H2	20°C	60°C	1.0	1.136	$1.189 \times 10^9$	0.722	1.44	1.02
He	20°C	170°C	1.0	1.511	$1.986 \times 10^9$	0.731	0.12	1.17
Air	50°C	127°C	1.0	1.238	$9.135 \times 10^8$	0.713	0.55	4.0

This method was initially seen to be somewhat unstable when the cold wall temperature given, showing a notable overshoot on each result, so an under relaxation factor of 0.7 was applied to the temperature difference calculated in step 3 above, that means equation 19 should be replaced by equation 22 below. This tends to halve the number of iterations needed to achieve an acceptable solution.

$$T_{hi+1} = \left( \left( \left( \frac{Q_{(given)}}{Nu_{(i)} \times H/L \times k} + T_c \right) - T_{hi} \right) \times 0.7 \right) + T_{hi} \quad (22)$$

To show how this method can be used, eleven examples are given for square and rectangular enclosures, one for the case of pure natural convection and ten for the case of natural convection with radiation interaction. The first six examples are for the case when the cold wall temperature given, equations 19 and 22 and the other five examples are for the case when the hot wall temperature given, using equation 20. The first example, for the case of natural convection with radiation interaction in a square enclosure, is solved in detail below:

**Example 13:** For the case of natural convection with radiation interaction in square enclosure,

Given: Air as working fluid,  $T_c = 20^\circ C$ ,  $Q_t = 600W$ ,  $AR = \frac{60cm}{60cm} = 1$

Calculated:

First by assuming,  $T_{h1} = 90^\circ C = 363.1K$ ,  $T_{r1} = 1.238$

Then using equation 10 and also using table 7.5,  $N_{t1} = 172.7$ ,  $Error(Q_t\%) = 42.0\%$

#### Iteration 1

From the previous results and using equation 22, the new hot wall temperature can be found,  $T_{h2} = 398.6K$ ,  $T_{r2} = 1.359K$ ,  $\Delta T_{h1} = 35.49$

So from,  $T_{r2} = 1.359K$ , and using equation 10,  $N_{t2} = 191.3$ ,  $Error(Q_t) = -1.3\%$

Then the process continued as below until an acceptable error is achieved

#### Iteration 2

From equation 22  $T_{h3} = 397.6K$ ,  $T_{r3} = 1.356K$ ,  $\Delta T_{h2} = -0.98$

From  $T_{r3} = 1.356$ , and using equation 10,  $N_{t3} = 190.8$ ,  $Error(Q_t) = -0.02\%$

### Iteration 3

From equation  $22T_{h4} = 397.7K$ ,  $T_{r4} = 1.356$ ,  $\Delta T_3 = -0.016$

From  $T_{r4} = 1.356$ , and using equation 10,  $N_{t4} = 190.75$ ,  $Error(Q_t) = 0.00027\%$

Here the difference in  $T_r$  occurs after the third digit.

The other ten examples follow the same steps as in example 19 and these results are summarized in tables 7.9, to 7.19. Figure 7.10 shows the graphical solution of example 18 and iteration number and process. It will be seen that in all cases, two iterations are sufficient to provide a heat transfer rate whose error is less than the derived equations. Indeed in most cases, a single iteration will provide a reasonable answer.

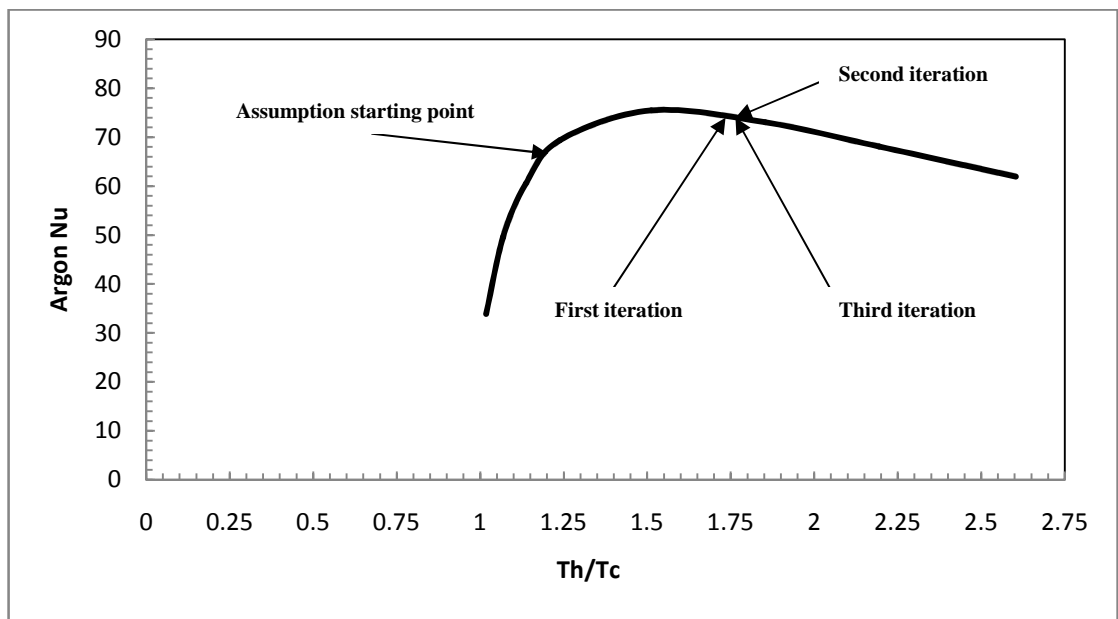


Figure 7.10 Graphical solution for example 18 showing the iteration number.

Table 7.9 Results for example 13: a square enclosure for natural convection with radiation interaction, cold wall temperature supplied and using the iterative method.

	Given: Air, $T_c = 20^\circ\text{C}$ , $AR = \frac{60}{60} = 1$ , $Q_{\text{tot}} = 600\text{W}$				
Iteration	$T_h$	$T_r$	$\Delta T_h$	Error (%) of $T_h$	Error (%) of $Q_t$
	363.16	1.238			42.0
1	398.657	1.359	35.49	8.9	-1.3
2	397.675	1.356	-0.98	-0.24	-0.02
3	397.658	1.3564	-0.016	-0.004	0.0003



Table 7.10 Results for example 14: a square enclosure for natural convection with radiation interaction, cold wall temperature supplied and using the iterative method.

	Given: Helium, $T_c = 20^\circ\text{C}$ , $AR = \frac{60}{60} = 1$ , $Q_{\text{tot}} = 1000\text{W}$				
Iteration	$T_h$	$T_r$	$\Delta T_h$	Error (%) of $T_h$	Error (%) of $Q_t$
	363.16	1.238			-57.13
1	345.34	1.178	-17.81	8.9	-7.71
2	342.73	1.169	-2.61	-0.76	-0.93
3	342.4	1.168	-0.323	-0.094	-0.11

Table 7.11 Results for example 15: a square enclosure for natural convection with radiation interaction, cold wall temperature supplied and using the iterative method.

	Given: Hydrogen, $T_c = 20^\circ\text{C}$ , $AR = 1.0$ , $Q_{\text{tot}} = 2000\text{W}$				
Iteration	$T_h$	$T_r$	$\Delta T_h$	Error (%) of $T_h$	Error (%) of $Q_t$
	363.16	1.238			12.76
1	370.33	1.263	7.17	1.9	0.77
2	370.75	1.264	0.422	0.11	0.053

Table 7.12 Results for example 16: a rectangular enclosure with aspect ratio equal to 8 for natural convection with radiation interaction, cold wall temperature supplied.

	Given: Air, $T_c = 20^\circ\text{C}$ , $AR = \frac{60}{7.5} = 8$ , $Q_{\text{tot}} = 600\text{W}$				
Iteration	$T_h$	$T_r$	$\Delta T_h$	Error (%) of $T_h$	Error (%) of $Q_t$
	363.16	1.238			36.64
1	391.5	1.335	28.34	7.23	-0.14
2	391.398	1.335	-0.101	0.026	-0.0035

Table 7.13 Results for example 17: a rectangular enclosure with aspect ratio equal to 0.125 for natural convection with radiation interaction, cold wall temperature supplied and using the iterative method.

	Given: Air, $T_c = 20^\circ\text{C}$ , $AR = \frac{60}{480} = 0.125$ , $Q_{\text{tot}} = 600\text{W}$				
Iteration	$T_h$	$T_r$	$\Delta T_h$	Error (%) of $T_h$	Error (%) of $Q_t$
	363.16	1.238			75.42
1	513.52	1.751	150.36	29.28	-11.57
2	497.518	1.697	-16.0	-3.2	-0.3
3	497.0	1.695	-0.5	-0.1	-0.003

Table 7.14 Results for example 18: a square enclosure for pure natural convection, cold wall temperature supplied and using the iterative method.

	Given: Argon, $T_c = 20^\circ\text{C}$ , $AR = \frac{60}{60} = 1$ , $Q_c = 300\text{W}$				
Iteration	$T_h$	$T_r$	$\Delta T_h$	Error (%) of $T_h$	Error (%) of $Q_c$
	363.16	1.238			69.6
1	475.37	1.621	160.3	0.23	1.05
2	476.72	1.626	1.93	0.28	0.25
3	477.05	1.627	0.47	0.06	0.06

Table 7.15 Results for example 19: a square enclosure for natural convection with radiation interaction, hot wall temperature supplied and using the iterative method.

	Given: Air, $T_h = 200^\circ\text{C}$ , $AR = \frac{60}{60} = 1$ , $Q_t = 600\text{W}$				
Iteration	$T_c$	$T_r$	$\Delta T_c$	Error (%) of $T_c$	Error (%) of $Q_t$
	382.19	1.238			-24.0
1	399.8	1.183	17.64	4.41	-0.7
2	400.32	1.181	0.52	0.13	-0.02
3	400.337	1.181	0.017	0.004	-0.0006

Table 7.16 Results for example 20: a square enclosure for natural convection with radiation interaction, hot wall temperature supplied and using the iterative method.

	Given: Helium, $T_h = 120^\circ\text{C}$ , $AR = 1.0$ , $Q_t = 1000\text{W}$				
Iteration	$T_c$	$T_r$	$\Delta T_c$	Error (%) of $T_c$	Error (%) of $Q_t$
	317.57	1.238			-96.0
1	354.6	1.108	37.03	10.44	-0.48
2	354.79	1.108	0.18	0.052	0.011

Table 7.17 Results for example 21: a square enclosure for natural convection with radiation interaction, hot wall temperature supplied and using the iterative method.

	Given: Hydrogen, $T_h = 150^\circ\text{C}$ , $AR = 1.0$ , $Q_t = 2500\text{W}$				
Iteration	$T_c$	$T_r$	$\Delta T_c$	Error (%) of $T_c$	Error (%) of $Q_t$
	341.81	1.238			-7.87
1	347.74	1.217	5.93	1.7	-0.32
2	347.98	1.216	0.245	0.07	-0.017

Table 7.18 Results for example 22: a rectangular enclosure with aspect ratio equal to 8 for natural convection with radiation interaction, hot wall temperature supplied and using the iterative method.

	Given: Air, $T_h = 300^\circ\text{C}$ , $AR = \frac{60}{7.5} = 8$ , $Q_t = 600\text{W}$				
Iteration	$T_c$	$T_r$	$\Delta T_c$	Error (%) of $T_c$	Error (%) of $Q_t$
	462.97	1.238			-133.7
1	526.025	1.09	63.05	11.9	-3.0
2	527.406	1.08	1.38	0.26	-0.2
3	527.52	1.086	0.11	0.02	-0.02

Table 7.19 Results for example 23: a rectangular enclosure with aspect ratio equal to 0.125 for natural convection with radiation interaction, hot wall temperature supplied and using the iterative method.

	Given: Air, $T_h = 300^\circ\text{C}$ , $AR = \frac{60}{480} = 0.125$ , $Q_t = 600\text{W}$				
Iteration	$T_c$	$T_r$	$\Delta T_c$	Error (%) of $T_c$	Error (%) of $Q_t$
	462.97	1.238			9.2
1	451.672	1.268	-11.29	-2.5	0.97
2	450.473	1.272	-1.19	-0.26	0.11
3	450.334	1.272	-0.13	-0.03	0.012

## 7.6 Summary and discussion

The analysis method to produce the correlation equations for square and rectangular enclosures is provided in this chapter. Using these correlation equations the new dimensionless group, which is the ratio between natural convection to radiation heat transfer, is provided for both square and rectangular enclosures. Also using the correlation equations from the dimensional analysis the correlation equations for pure natural convection, which is the average Nusselt number, is provided for square and rectangular enclosures. For the case of natural convection with radiation interaction, the correlation equations for the total Nusselt number are provided for both square and rectangular enclosure. The constants, as a function of temperature ratio, of all the derived correlation equations are given along with these equations. These constants are correlated and a polynomial equations for each constant as a function of absolute temperature ratio is given.

This chapter provides correlation equations for the average convection Nusselt number, the total Nusselt number and the new dimensionless equation for square and rectangular enclosures. All these equations are valid for different temperature ratios, different enclosure sizes, different aspect ratios and different fluid properties.

Using these provide equations for a such conditions and for all the previous cases will give a results that has an average deviation error of less than 8% compared to the numerical results, this will be explained in more detail in the next chapter.

The main conclusions from this section can be summarized as follows:

Correlation equations are provided to calculate the average Nusselt number as a function of Grashof and Prandtl numbers for the turbulent natural convection in square enclosure without radiation interaction. The calculated results using the correlation equations had an average deviation of 2.9% and a maximum deviation of less than 7.2% for the three different groups for the square enclosure, compared to the numerical results.

The calculated results of the total Nusselt number in a square enclosure using the derived correlation equation were within a maximum deviation of less than 2.8% compared to the numerical results.

The calculated results of the average Nusselt number in rectangular enclosures using the correlation equations for the first regime (which is for aspect ratio ranging from 1 to 16) had an average deviation of 2.7% and a maximum deviation of less than 7.3% and for the second regime had an average deviation of 3.2% and a maximum deviation of 6.6%.

The correlation equation for the new dimensionless group to predict the relation between convection and radiation in the square enclosure had a maximum error of 2.7% when it used for different fluid properties and enclosure sizes and a maximum error of 7.3% when the effect of cold wall temperature was included.

The derived correlation equation for the new dimensionless group to predict the relation between convection and radiation heat transfer as a function of absolute temperature ratio in the rectangular enclosure had an average deviation of 3.1% and a maximum deviation of 7.2% for the first regime and an average deviation of 2.9% and a maximum deviation of 7.3% for the second regime.

The calculated results of the total Nusselt number in the rectangular enclosure using the derived correlation equations for the two flow regimes were within a maximum deviation of less than 7.7%; compared to the numerical results.

The use of the provided polynomial and correlation equations to find out the flow parameters was discussed in this chapter. There were two methods to find out the flow parameters in the square and rectangular enclosures for the two cases of study, pure natural convection and natural convection with radiation interaction, first the direct solution when the hot and cold wall temperatures are given and second the indirect (iterative) solution when only one wall temperature given along with the heat transfer rate.

More clear conclusions will be extracted when these results are compared with the experimental results in the next chapters.

# **CHAPTER 8**

## **RESULTS COMPARISON AND DISCUSSION**

### **8.1 Introduction**

The discussion of the individual results is included at the end of each of the relevant chapters. What follows is a comparison of the various experiments models and analytical results.

In this chapter the numerical results (which are explained in chapter 5) and experimental results (which are explained in chapter 6) will be compared and discussed. This will include the comparison between numerical calculations and experimental data of the temperature and heat transfer results and also the velocity and turbulence intensity profiles. The results using the correlation equations for the dimensionless groups, explained in chapter 7, will also be compared with previous derived correlation equations and with the experimental results.

### **8.2 Comparison between numerical and experimental results**

The numerical results include the calculations of the Nusselt number for the pure natural convection, the total Nusselt number and the relationship between heat transfer by convection and radiation (the new dimensionless group) in square and rectangular enclosures. From these results a correlation equation for convection Nusselt number and the new dimensionless group along with the total Nusselt number has been provided. These results have been explained in detail in chapter 7. The results using these provided equations will be compared with the previous derived correlation equations, the present experimental results and with the previous experimental results [57]. As the experimental results are 3D, a 3D numerical calculations as explained in chapter 5, were performed so that they could be compared better with the experimental results. These 3D results include the thermal results (total heat transfer from hot and cold sides) and

the velocity and turbulence intensity profiles inside the enclosure. These results will be compared in this chapter using different aspect ratios, enclosure heights and hot wall temperatures.

### **8.2.1 Comparison between the present and the previous correlation equations**

The provided correlation equation (equation (29) in chapter 2 section 2.4.3) of Catton[36] to calculate the convection Nusselt number in rectangular enclosure has been compared with the present derived correlation equation for the range of Rayleigh number between  $1.6 \times 10^6 \leq Ra \leq 1.8 \times 10^7$  the maximum deviation was less than 4.5%. Also the same equation of Catton [36] and the present derived correlation equation for the convection Nusselt number have been compared for a Rayleigh number ranging from  $1.3 \times 10^7 \leq Ra \leq 1.4 \times 10^8$  the maximum deviation was less than 7%. Also the provided correlation equation (equation (38) in chapter 2 section 2.4.3) of Trias et al.[46] to calculate the convection Nusselt number for a rectangular enclosure of aspect ratio 4 has been compared with the present derived correlation equation for a Rayleigh number range  $1.6 \times 10^6 \leq Ra \leq 1.8 \times 10^7$  the maximum deviation was less than 20%.

More over for the case of natural convection with radiation interaction, the provided correlation equations (equations (40 and 41) also in chapter 2 section 2.6) of Balaji and Venkateshan[48] for square enclosure have been compared with the present derived correlation equation to calculate the total Nusselt number for a Grashof number range  $5 \times 10^8 \leq Gr \leq 1.2 \times 10^9$  the maximum deviation was less than 7% even the Grashof number range for comparison was out of Balaji and Venkateshan equation range.

The comparison between the present derived correlation equation for the case of natural convection with radiation interaction in square enclosure with the provided correlation equation (equation (42) again in chapter 2 section 2.6) of Akiyama and Chong [50] for a temperature ratio 1.033 and at Rayleigh number  $Ra = 3 \times 10^7$  the maximum deviation was less than 13%.

Also the comparison between the provided correlation equations (equations (43 and 44) chapter 2 section 2.6) of Velusamy et al. [51] for the case of natural convection with radiation interaction in rectangular enclosure at Rayleigh number  $Ra = 1.5 \times 10^9$



with the present derived correlation equation, the maximum deviation was less than 6.5%.

Finally the comparison between the present derived correlation equation (equation (21) in chapter 2 section 2.4.2) for the case of natural convection with radiation interaction in square enclosure has been compared with the derived correlation equation of Sharma et al. [4] at temperature ratio 1.14 and Rayleigh number  $Ra = 7.3 \times 10^8$  the maximum deviation was less than 14% and for Rayleigh number  $Ra = 5.2 \times 10^9$  the maximum deviation was less than 13.5%.

## **8.2.2 Comparison between the derived correlation equations and the experimental results**

The 2D numerical results are explained and discussed in detail in chapter 5. From these results correlation equations were provided for both pure natural convection and natural convection with radiation in square and rectangular enclosures for a wide range of parameters. From these equations, the average Nusselt number can be calculated for both pure natural convection and natural convection with radiation and from these results the total heat transfer can be extracted (as explained in chapter 7). In this section the results using the correlation equations will be compared with the present and previous [57] experimental results.

### **8.2.2.1 Comparison between the derived correlation equations and the previous experimental results**

The experimental results of King [57] for a rectangular enclosure of aspect ratio 5 and four temperature ratios are compared with the present numerical results using the derived correlation equation. The comparison was performed using the total heat transfer which was calculated using the total Nusselt number. The comparison between these results is shown in figure 8.1 below. From this graph, it can be seen that the thermal results of the derived correlation equations are in fairly good agreement with the previous experimental results.

The calculated results show that the maximum deviation between these results using the derived correlation equations and the previous experimental results was less than 16%.

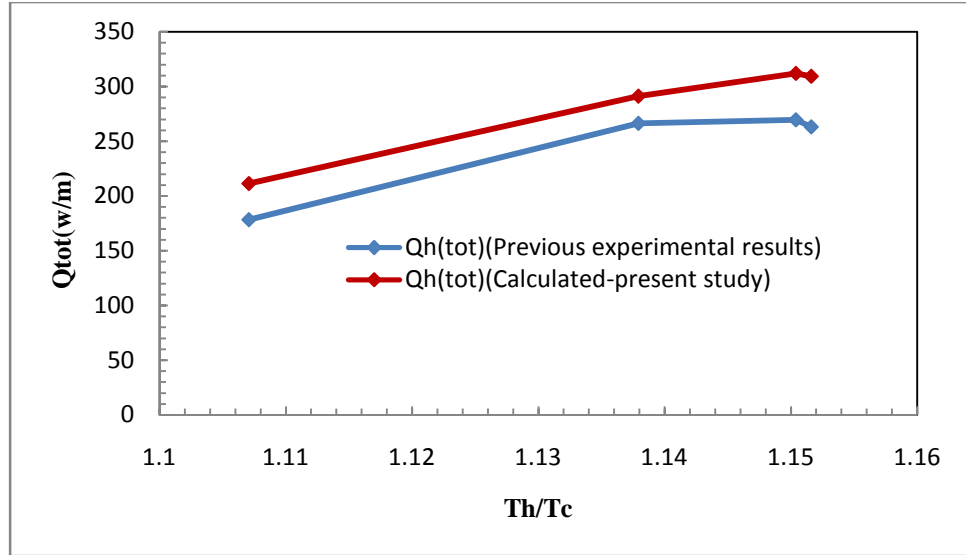
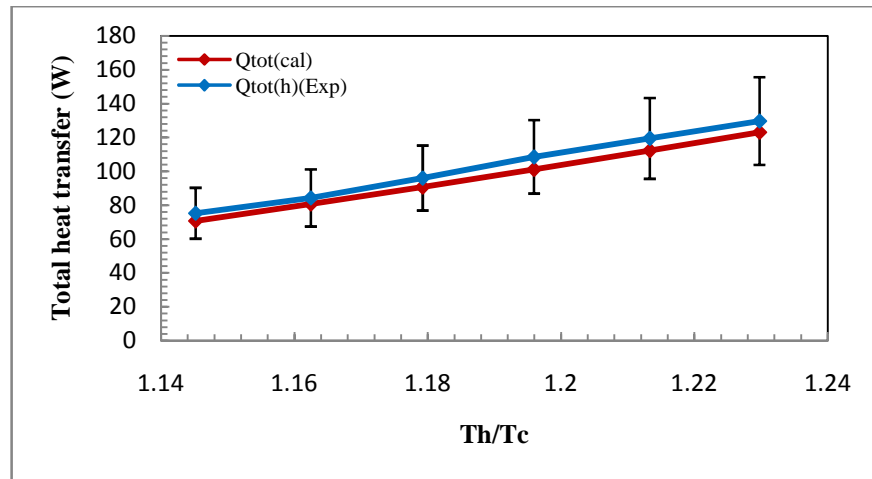


Figure 8.1 Comparison between the derived correlation equations and previous experimental results

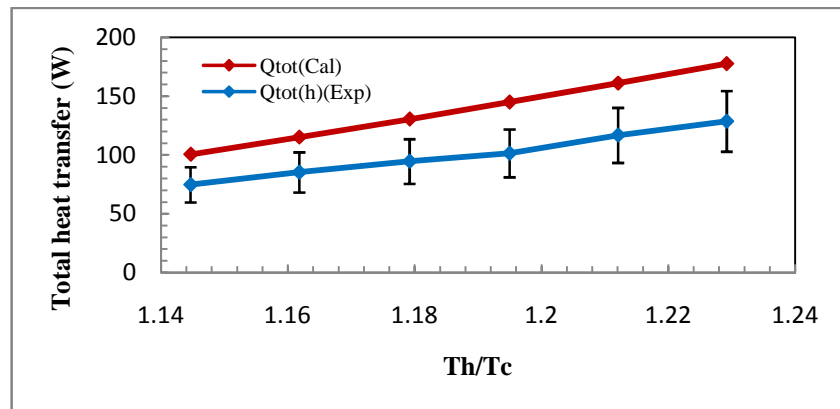
#### 8.2.2.2 Comparison between the derived correlation equations and the present experimental results

The comparison between the correlation equation results and the author's experimental results were performed for three different aspect ratios 0.5, 1.0 and 2.0 and for a hot temperature ranging between 50°C to 75°C. The comparison between these results was established by calculating the total heat transfer using the correlation equations to find the total average Nusselt number as was explained in detail in chapter 6. The compared results are shown in figure 8.2. From this figure it can be seen that as the aspect ratio increases from unity both the calculated and the experimental results become much closer to each other. Also from the figure it can be seen that for the three aspect ratios the total heat transfer increases linearly as the absolute temperature ratio increase.

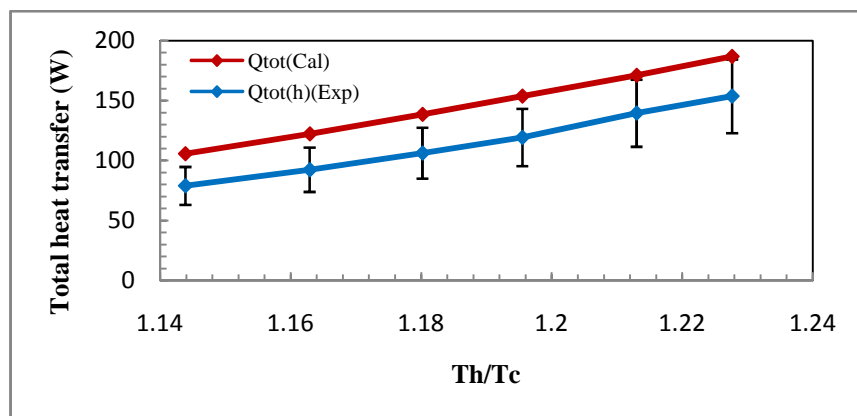
The calculated results using the derived correlation equations were within an average deviation of less than 15% for the three aspect ratios compared to the experimental results.



(a)



(b)



(c)

Figure 8.2 Comparison between calculated heat transfer and experimental results for aspect ratio a) 2.0, b) 1.0 and c) 0.5

### **8.2.3 Comparison between the 3D numerical calculations and the experimental results**

The 3D numerical calculations, as explained in chapter 5, were provided so that they could be compared with the experimental results for three aspect ratios and for a hot temperature ranging from 50°C to 75°C. The 3D numerical calculations performed using the same boundary conditions as the experiments. The 3D numerical results include the thermal results and the velocity and turbulence intensity profiles inside the enclosure. These results will be compared with the experimental results at different aspect ratios, different enclosure heights and different hot wall temperatures.

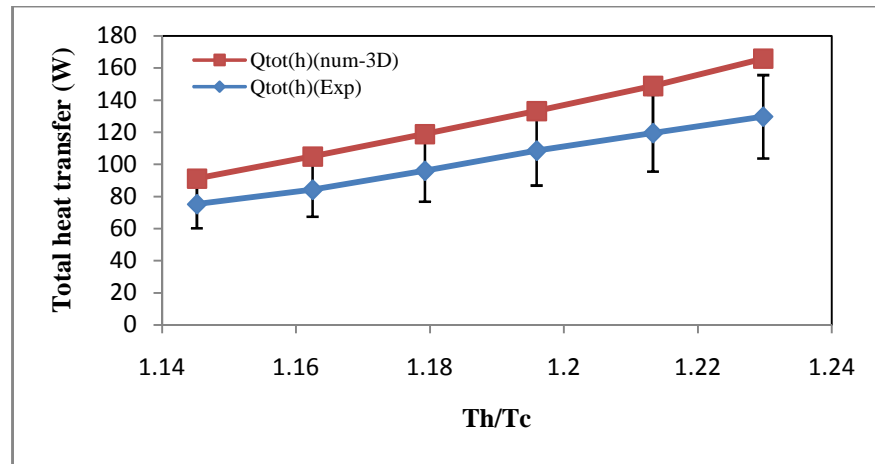
#### **8.2.3.1 Thermal results**

The thermal result comparison between the 3D numerical and experimental results includes the comparison of the total heat transfer from the hot side between both of these results. Figure 8.3 shows the comparison between these results for different aspect ratios and different hot wall temperatures. From this figure it can be seen that the 3D numerical results become closer to the experimental results as the aspect ratio approaches unity. Also from the figure it can be seen that the heat transfer increases as the aspect ratio decreases.

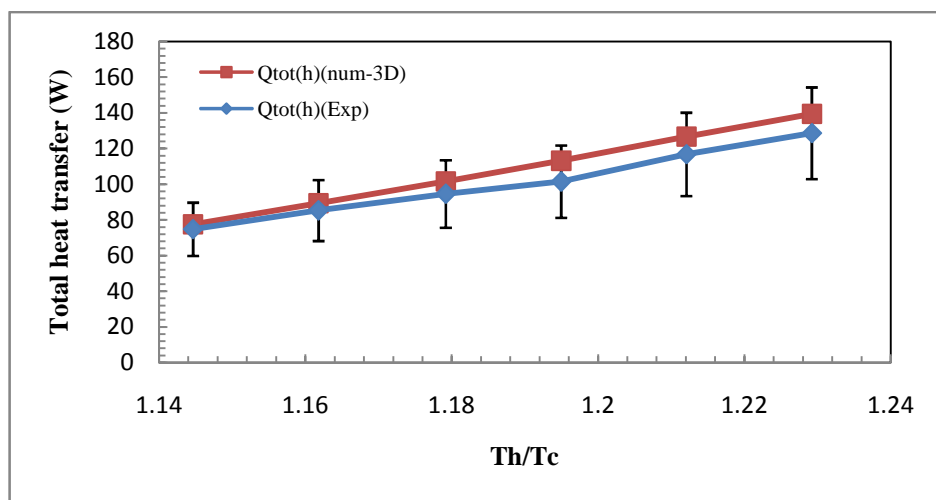
Compared to the experimental results, the 3D numerical results were within an average deviation of less than 13% for the three aspect ratios.

#### **8.2.3.2 Velocity and turbulence intensity profiles**

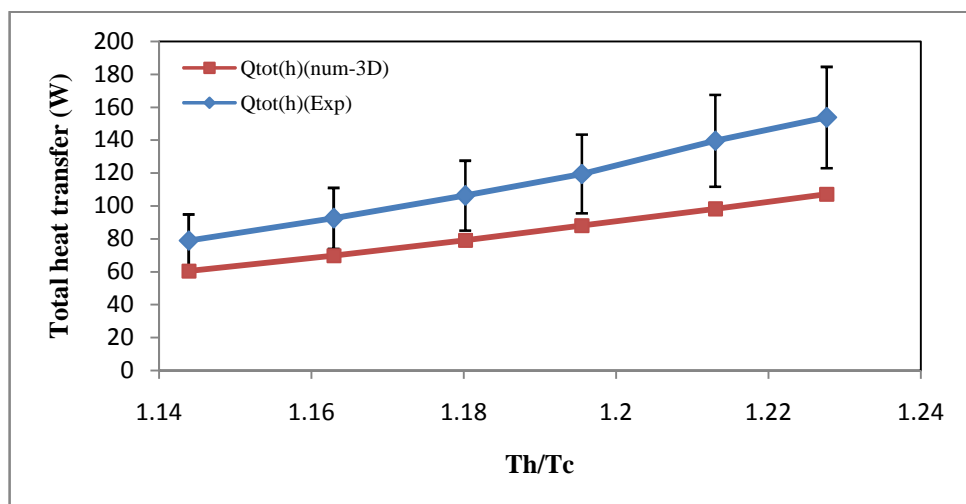
The velocity and turbulence intensity profiles for numerical and experimental results are compared for different aspect ratios and different hot wall temperatures. The velocity profiles at the mid-height of the enclosure for the three aspect ratios and for two hot wall temperatures of 60°C and 75°C are shown in figures 8.4 to 8.9. The comparisons of the results of the velocity profiles for the other hot wall temperatures (50°C, 55°C, 65°C and 70°C) are shown in appendix C. From the figures 8.4 to 8.9 it can be seen that, at the hot side, the velocity profiles for numerical and experimental results are in good agreement with each other. This agreement becomes better as the aspect ratio decreases or the temperature of the hot wall increases.



(a)

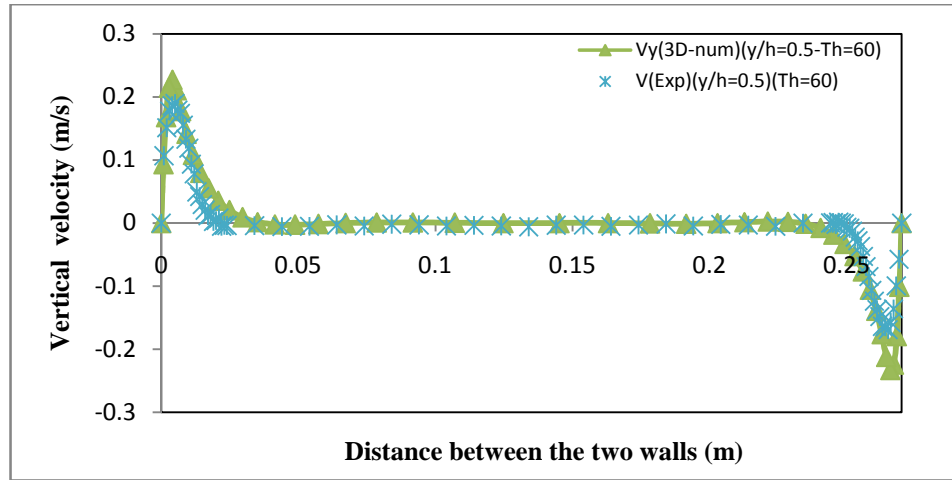


(b)

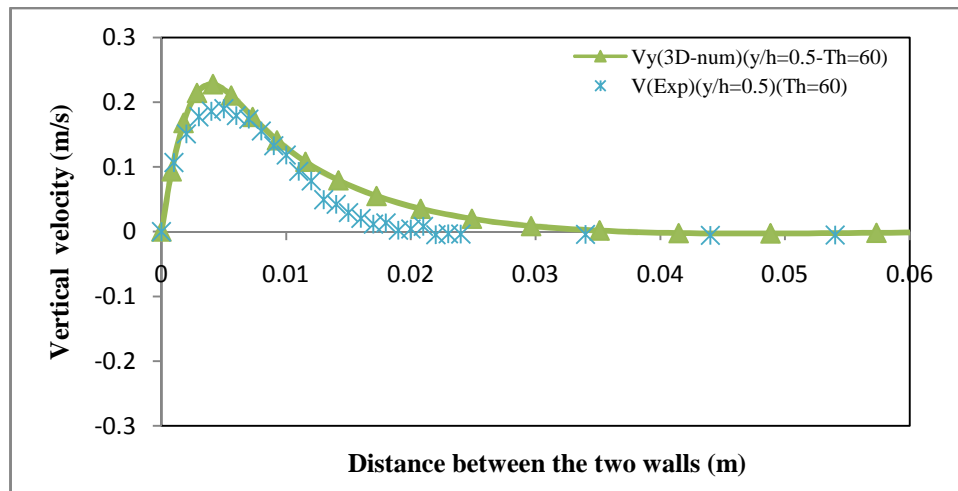


(c)

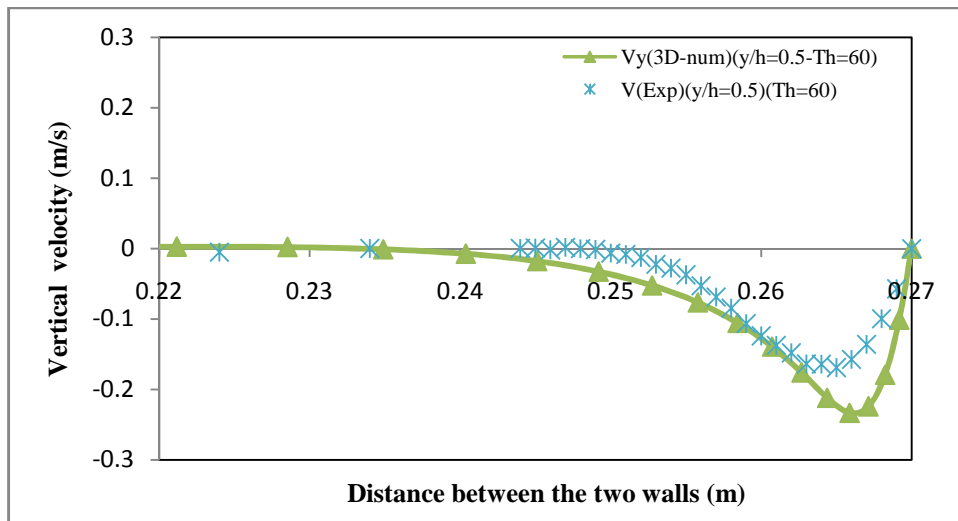
Figure 8.3 Comparison between 3D thermal results and experimental results for aspect ratio a) 2.0, b) 1.0 and c) 0.5



(a)

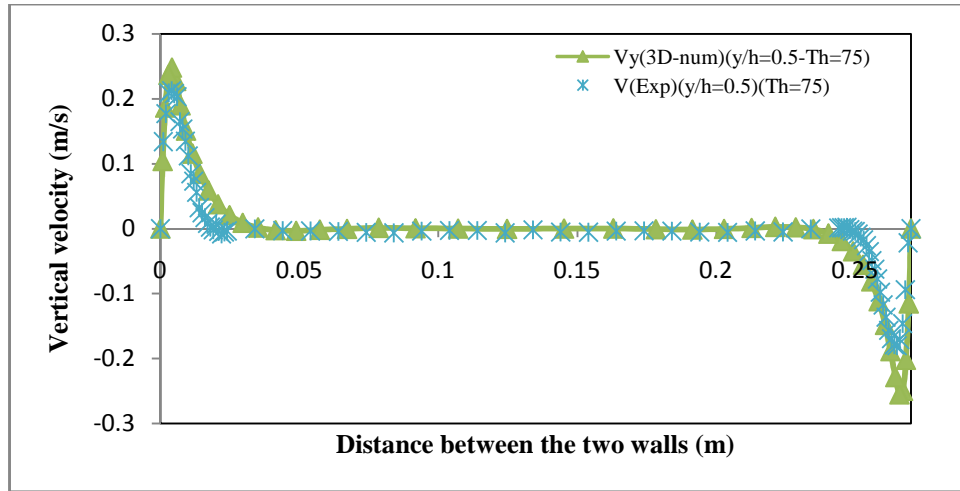


(b)

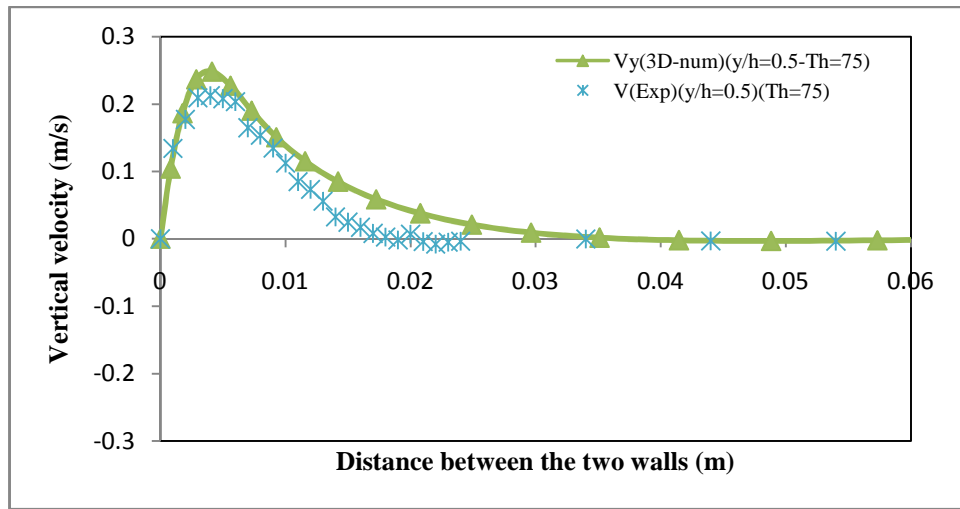


(c)

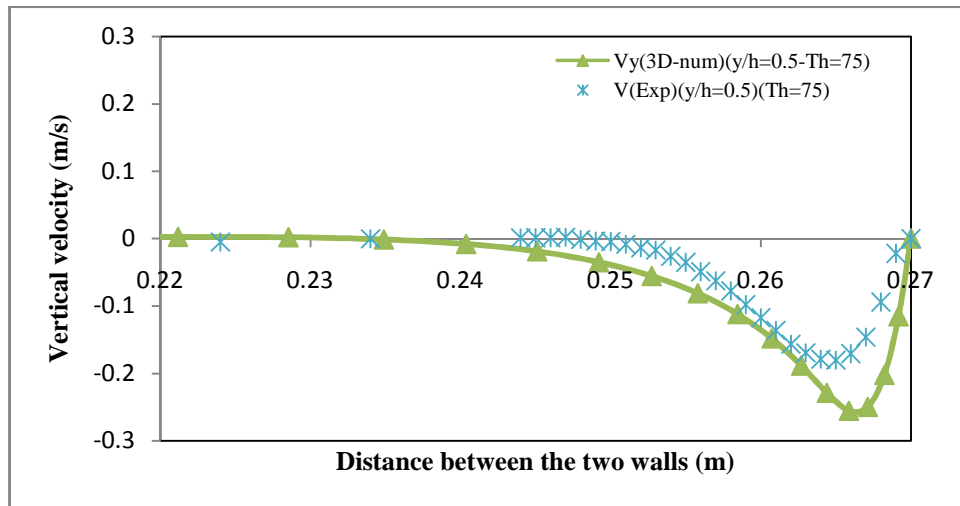
Figure 8.4 Comparison of velocity profiles between experimental and numerical results for aspect ratio 2.0 and hot wall temperature 60 °C a) between the two walls b) near the hot side c) near the cold side.



(a)

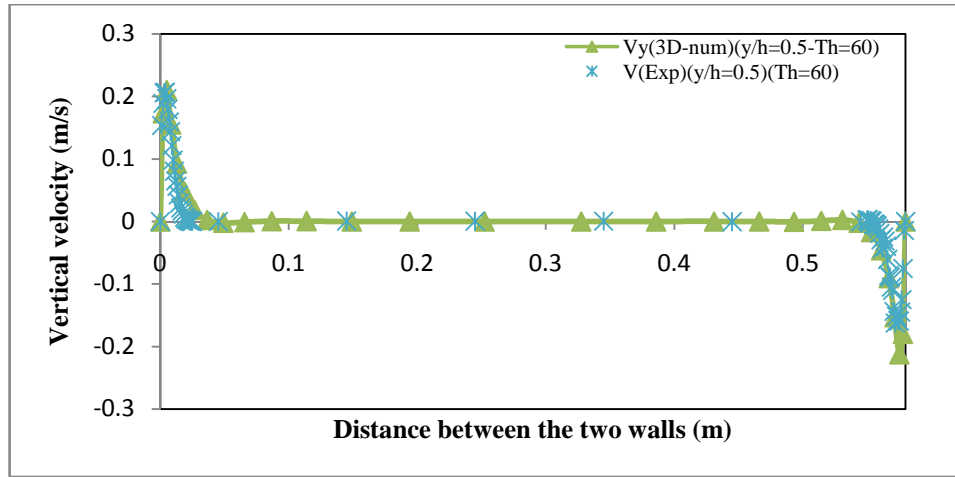


(b)

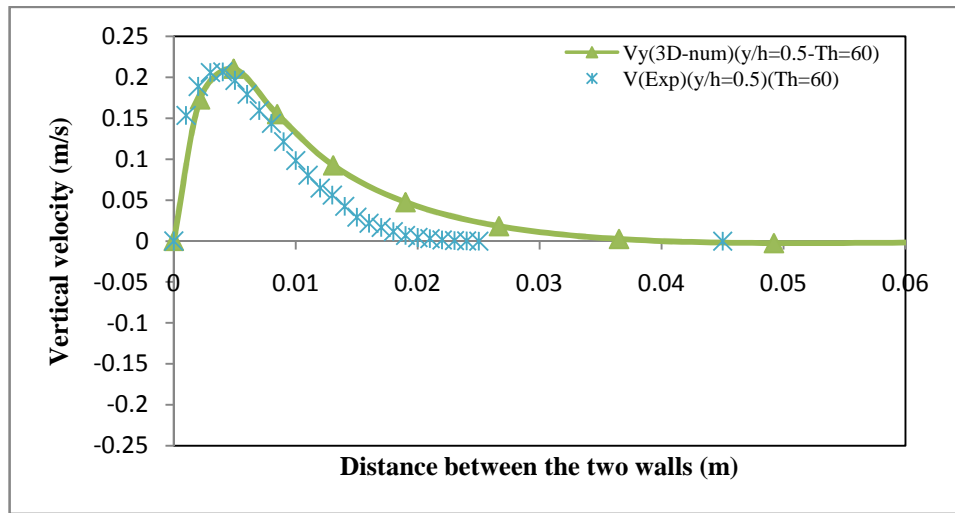


(c)

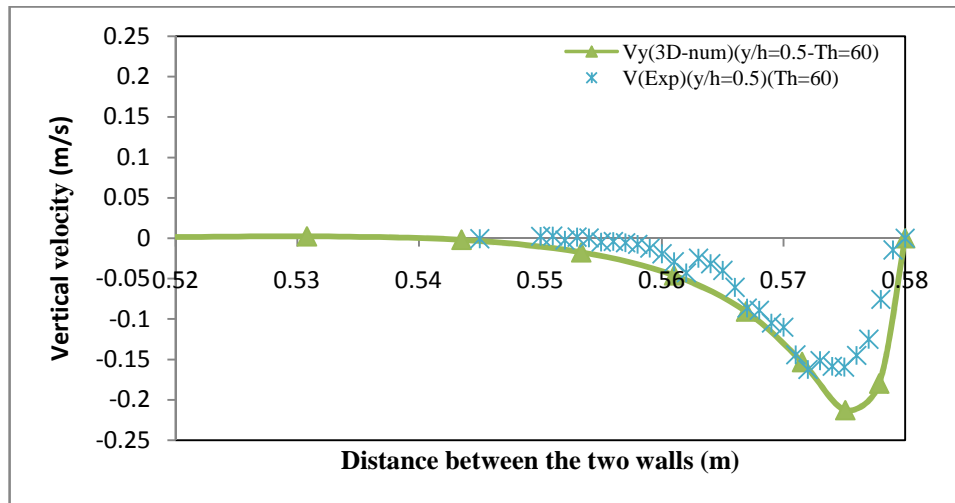
Figure 8.5 Comparison of velocity profiles between experimental and numerical results for aspect ratio 2.0 and hot wall temperature 75 °C a) between the two walls b) near the hot side c) near the cold side



(a)



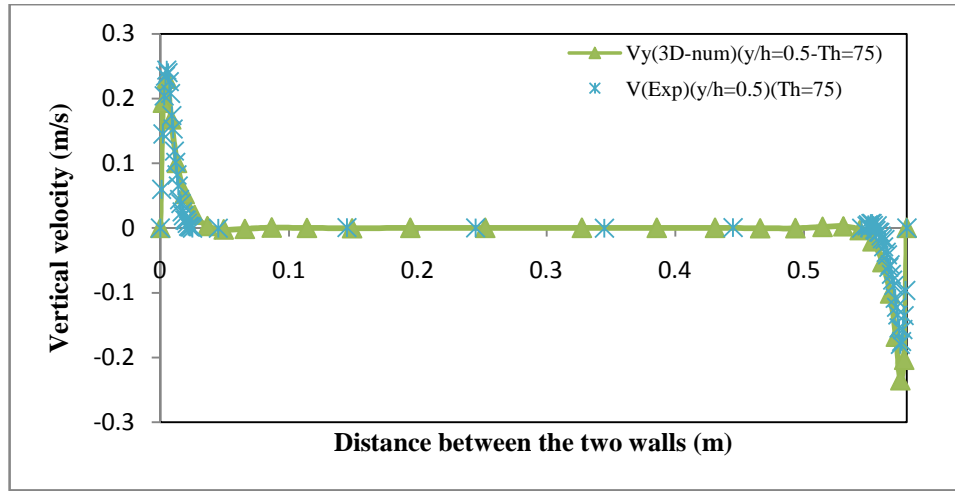
(b)



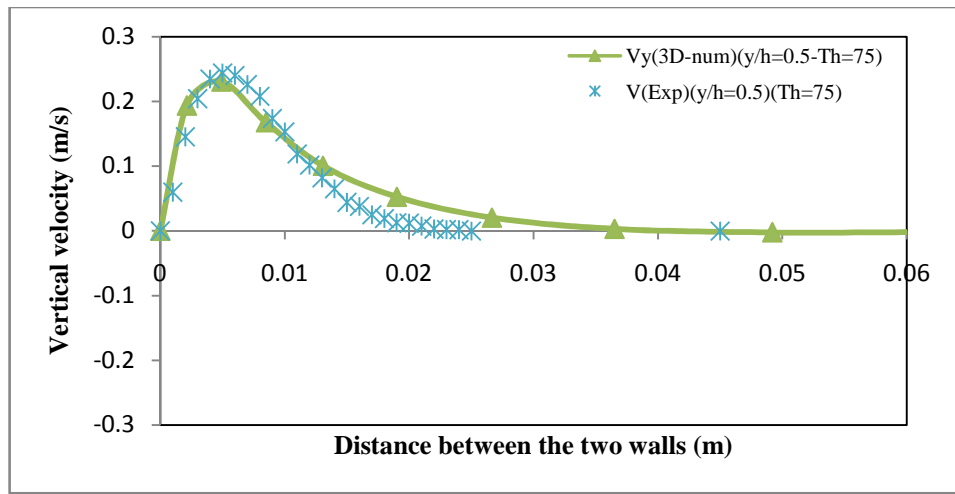
(c)

Figure 8.6 Comparison of velocity profiles between experimental and numerical results for aspect ratio 1.0 and hot wall temperature 60 °C a) between the two walls b) near the hot side c) near the cold side

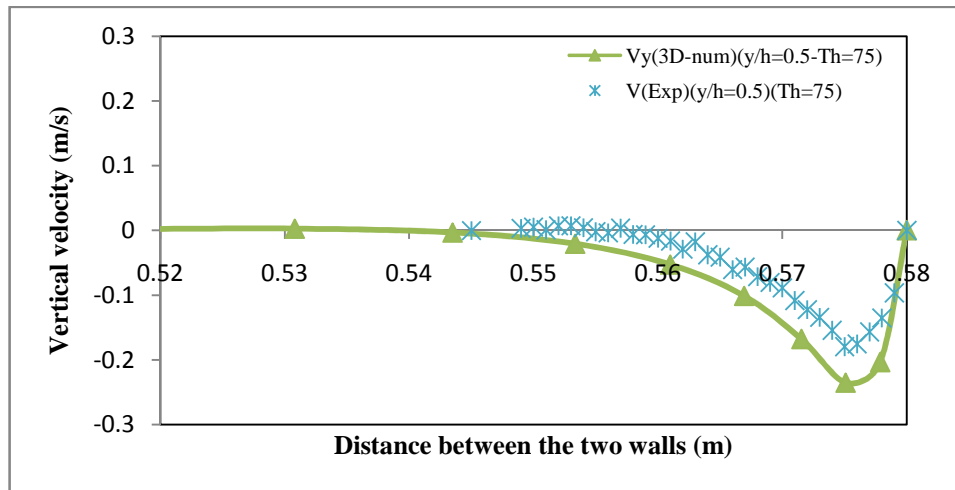




(a)

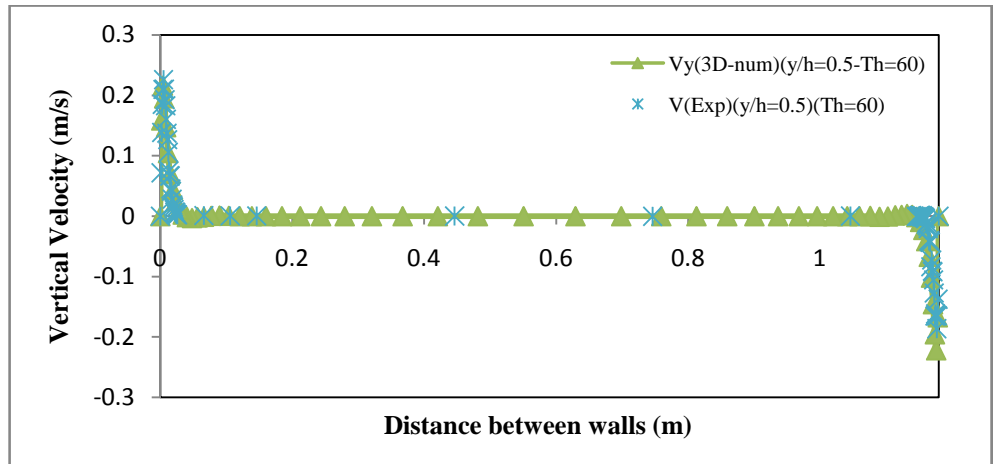


(b)

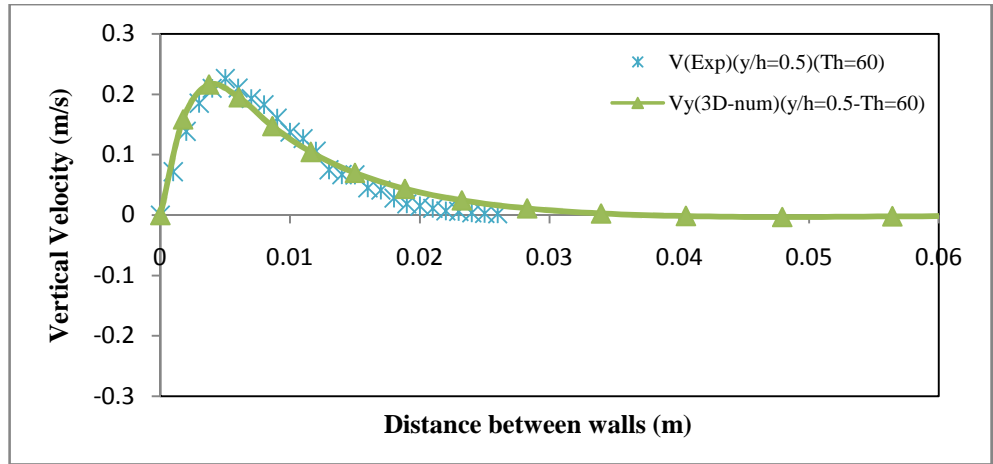


(c)

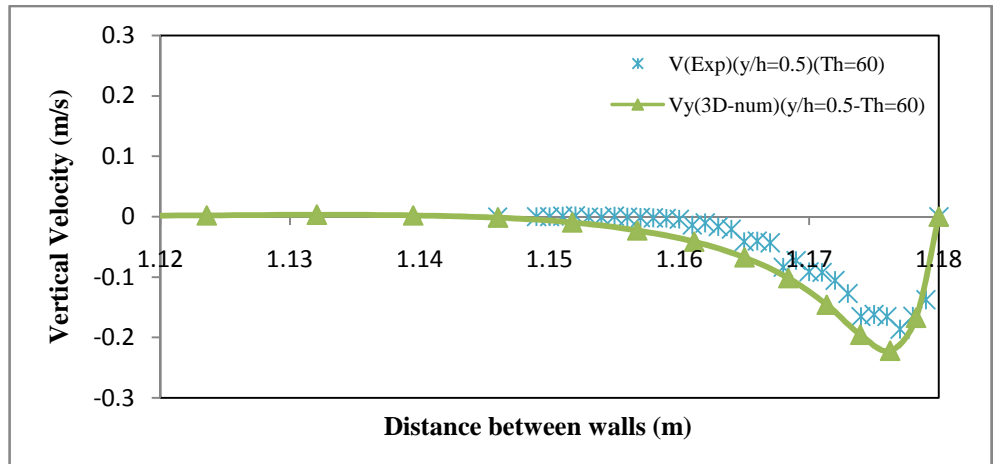
Figure 8.7 Comparison of velocity profiles between experimental and numerical results for aspect ratio 1.0 and hot wall temperature 75 °C a) between the two walls b) near the hot side c) near the cold side



(a)

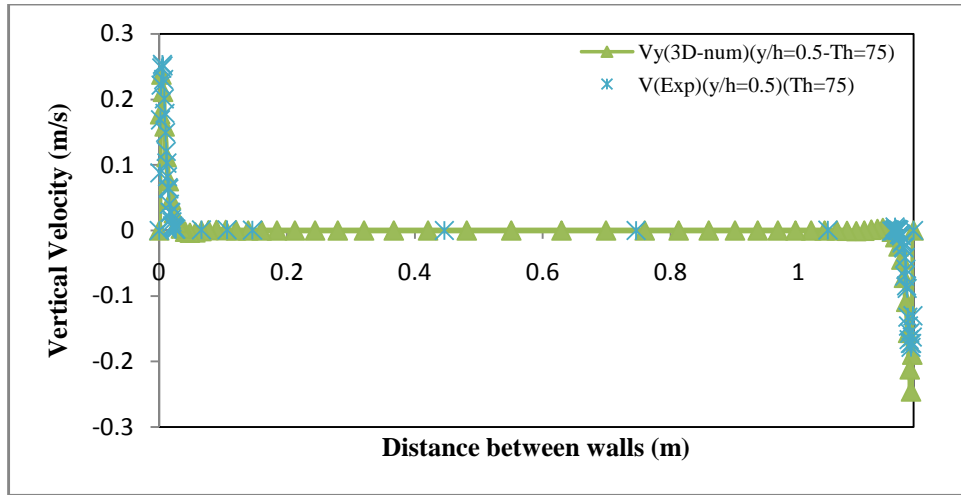


(b)

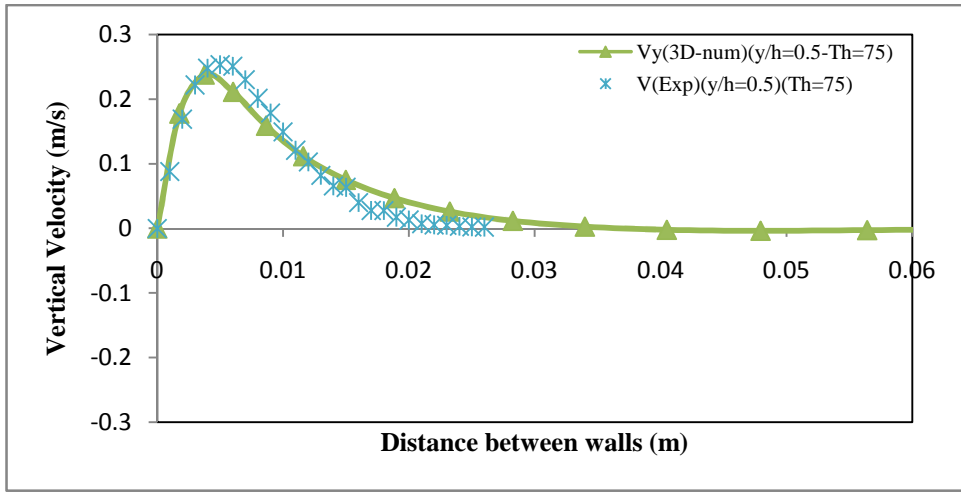


(c)

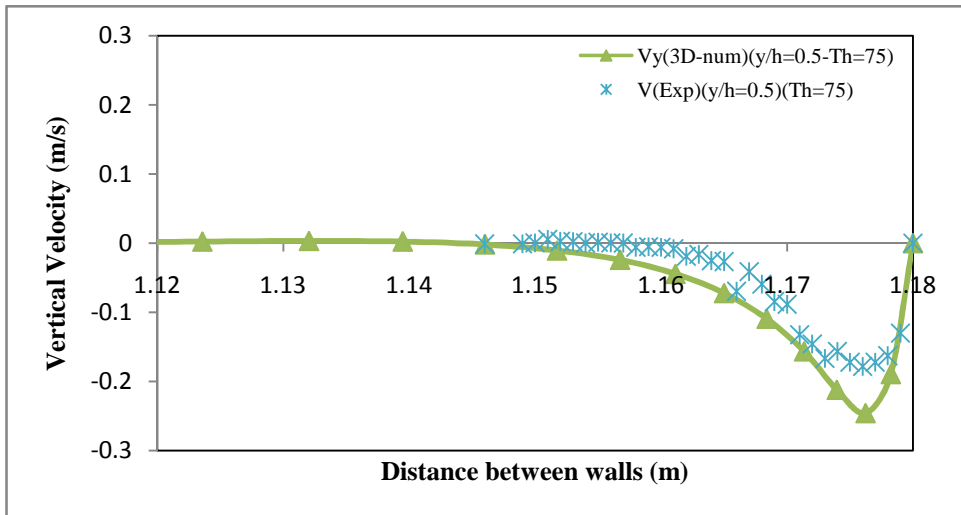
Figure 8.8 Comparison of velocity profiles between experimental and numerical results for aspect ratio 0.5 and hot wall temperature 60 °C a) between the two walls b) near the hot side c) near the cold side



(a)



(b)



(c)

Figure 8.9 Comparison of velocity profiles between experimental and numerical results for aspect ratio 0.5 and hot wall temperature 75 °C a) between the two walls b) near the hot side c) near the cold side

Also from the graphs it can be seen that the velocity profiles at the enclosure core for the three aspect ratios are in good agreement between the numerical and experimental results. Moreover, from these figures, the boundary layer thickness of the experimental results on the hot side is smaller than the boundary layer of the numerical results and this difference decreases as the aspect ratio decreases.

These figures show that the velocity profiles and the boundary layer thickness on the cold side for the numerical results are different to that from the experimental results. The velocity values of the experimental results on the cold side are less than the numerical results. Also the boundary layer thickness of the experimental results can be seen to be less than that of the numerical results. Also from the graphs, it can be seen that, as the aspect ratio decreases the velocity profiles on the cold side start fluctuating.

This fluctuation can be seen in figures 8.6 to 8.9 where it started at the aspect ratio of 1.0 and increases as the aspect ratio decreases.

The velocity reversals were noticed at about 65% of the enclosure height and upward, this is compared to Schmidt and Wang [66] who observed the same type of reversed flow at about 60% from the upstream flow of the wall and also the reversed flow was seen at 70% by Giel and Schmidt [67]. The trend of the velocity profiles were similar to that of King [57] and Ziai[44], where the velocity starts to increase from minimum at the hot wall until reach its peak value then it decreases to zero at the cavity core.

The velocity profiles along the vertical axis and near to the hot side of the experimental results are compared with the numerical results at a position of the maximum velocity. The comparison of the velocity profiles between numerical and experimental results for the three aspect ratios and for two hot wall temperatures 70°C and 75°C are shown in figures 8.10 and 8.11. From these figures it can be seen that the maximum velocity occurs near the mid-height of the enclosure, where the velocity starts to increase from the lower edge of the enclosure until reaches its maximum value near the enclosure mid-height where it starts to decrease again. Also from these figures it can be seen that the velocity values at the lower part of the enclosure are smaller than that at the upper part for experimental and numerical results. The experimental velocity profiles for aspect ratio 2.0 results display the same trends as the numerical results and their values become closer to each other as the flows approach the top edge of the enclosure. This can be seen by comparing figures 8.10a and 8.11a. Moreover from these plots it can be seen that the velocity values for the experimental results increases more

than the numerical results with the decrease of the aspect ratio. Furthermore the velocity profile, at the top edge of the enclosure, for the experimental results (compared to the numerical results) becomes almost flat (and have similar values to that at the mid-height) as the aspect ratio decreases. This is due to the fact that decreasing the aspect ratio will increase both the Rayleigh number and the enclosure width, where the former will increase the velocity values and the later will decrease the effects coming from the core and the other side on the velocity.

The comparison of the turbulence intensity profiles between numerical and experimental results and for the three aspect ratios and for the hot wall temperatures  $60^{\circ}\text{C}$  and  $75^{\circ}\text{C}$  are shown in figures 8.12 and 8.13. The comparison between the numerical and experimental results for the other hot wall temperatures ( $50^{\circ}\text{C}$ ,  $55^{\circ}\text{C}$ ,  $65^{\circ}\text{C}$  and  $70^{\circ}\text{C}$ ) will again be shown in appendix C. From the figures it can be seen that the experimental turbulence intensities for the three aspect ratios are in a fairly agreement with the numerical ones.

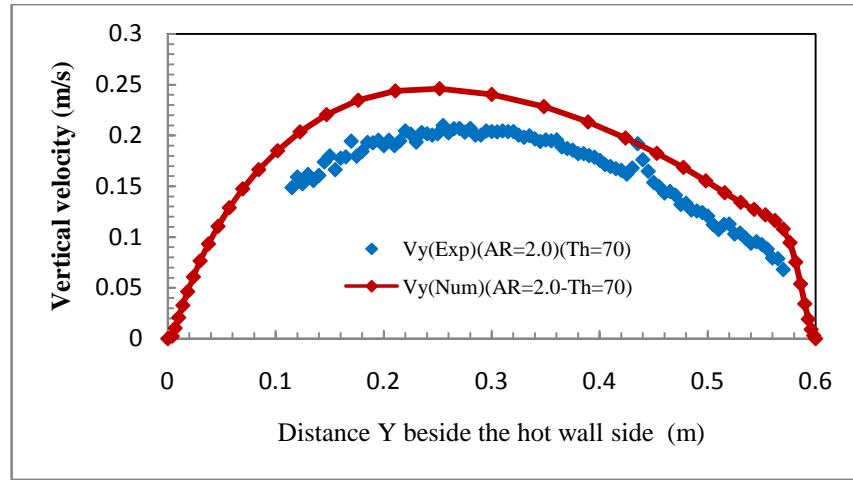
The turbulent intensity of the experimental results for the aspect ratio 2.0 is seen to have big difference comparing to the numerical results very close to the wall, then this difference reduces as is get away from the wall, this can be seen clearly in both figures 8.12a and 8.13a. On the other hand the turbulent intensity of the experimental results for both aspect ratios 1.0 and 0.5 is seen to be very close to the numerical turbulent intensity near the wall and this difference increases as it get away from the wall, this can be seen from both figures 8.12 and 8.13.

### **8.3 Summary and Conclusions**

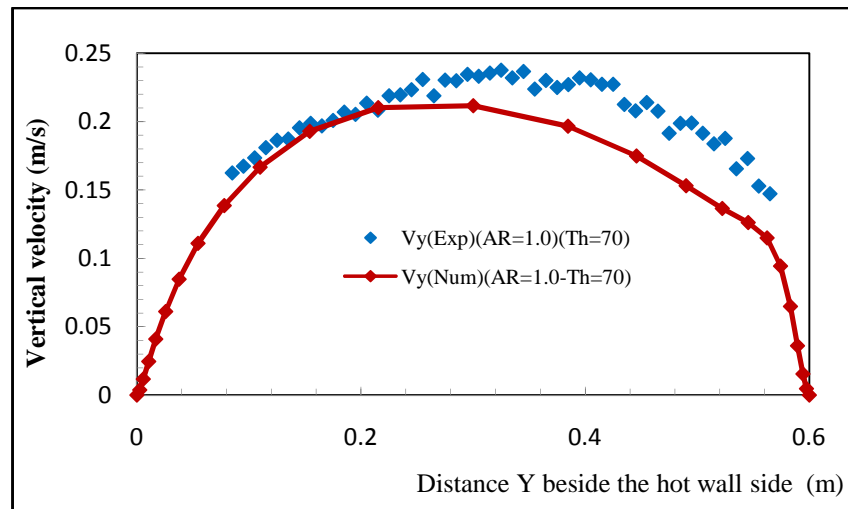
The numerical and experimental results are compared in this chapter. This comparison includes the thermal results and the velocity and turbulence intensity profiles. The main conclusions from this chapter can be summarized as follows:

The comparison between the present derived correlation equations and the previous correlation equations for natural convection with and without radiation interaction were in a good agreement.

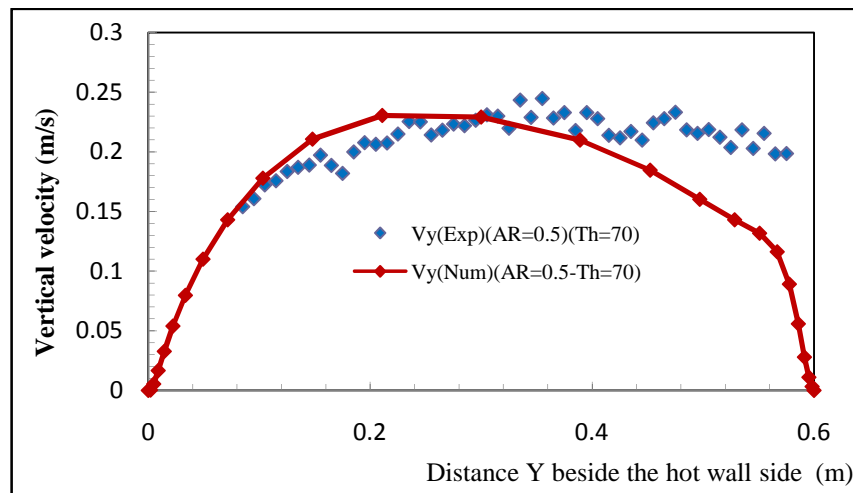
The thermal results of the derived correlation equations are in a good agreement with the previous experimental results. The calculated results show that the maximum deviation between these two results was less than 16%.



(a)

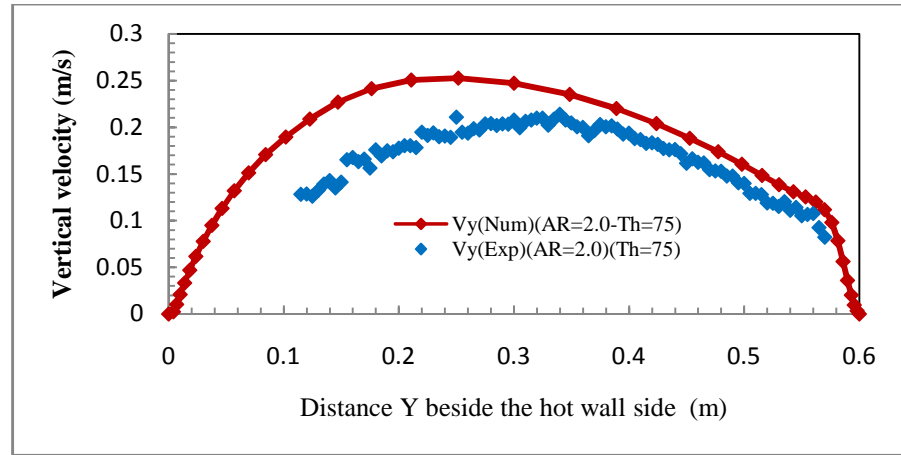


(b)

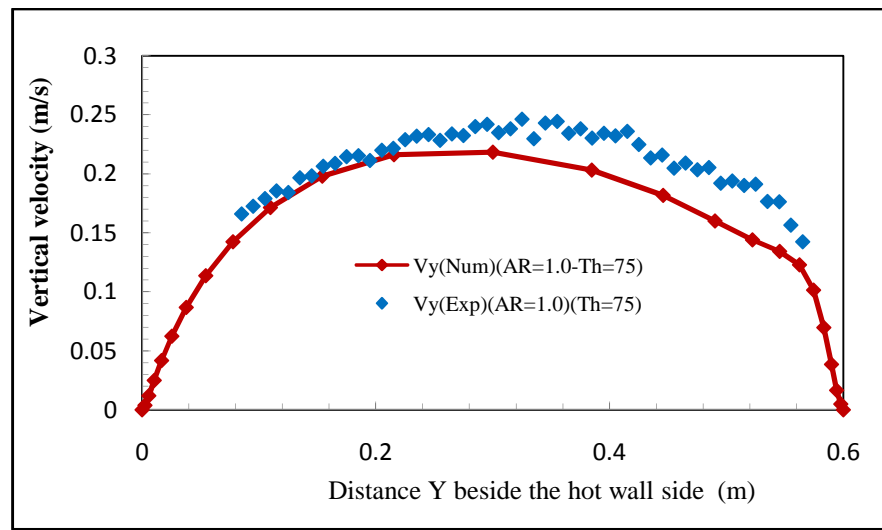


(c)

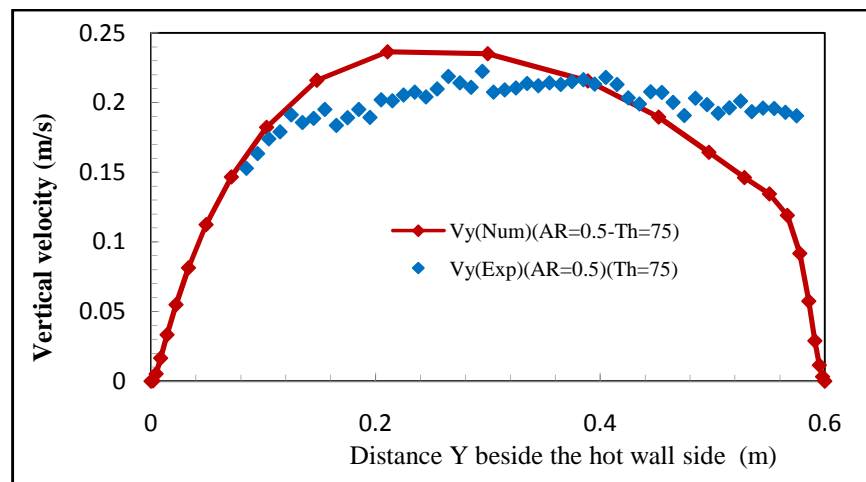
Figure 8.10 Velocity profiles at  $x = 4\text{mm}$  near the hot wall side at  $70^\circ\text{C}$  and for aspect ratio a) 2.0, b) 1.0 and c) 0.5



(a)

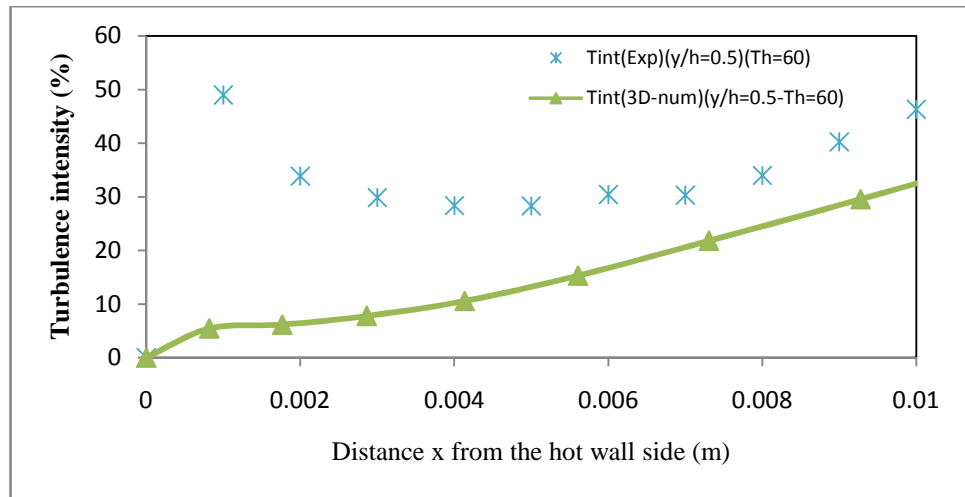


(b)

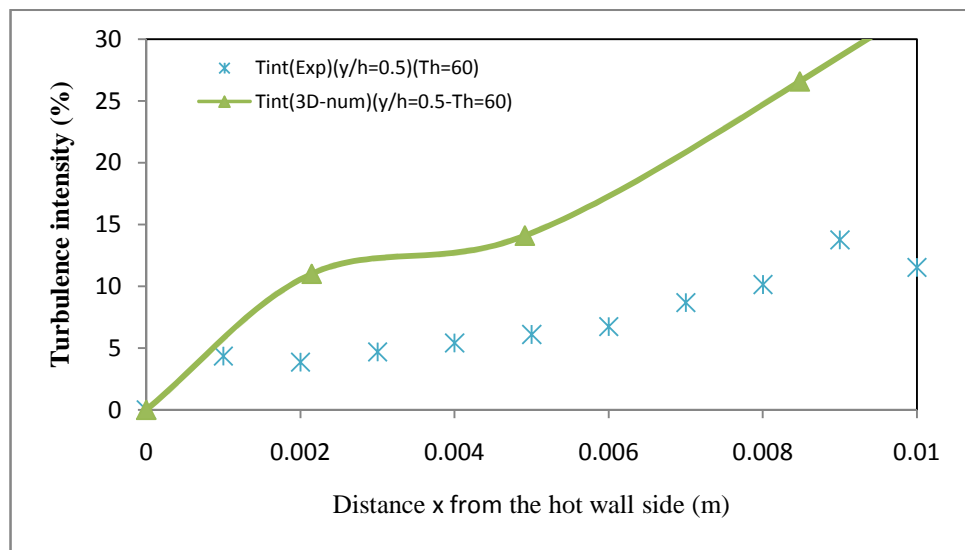


(c)

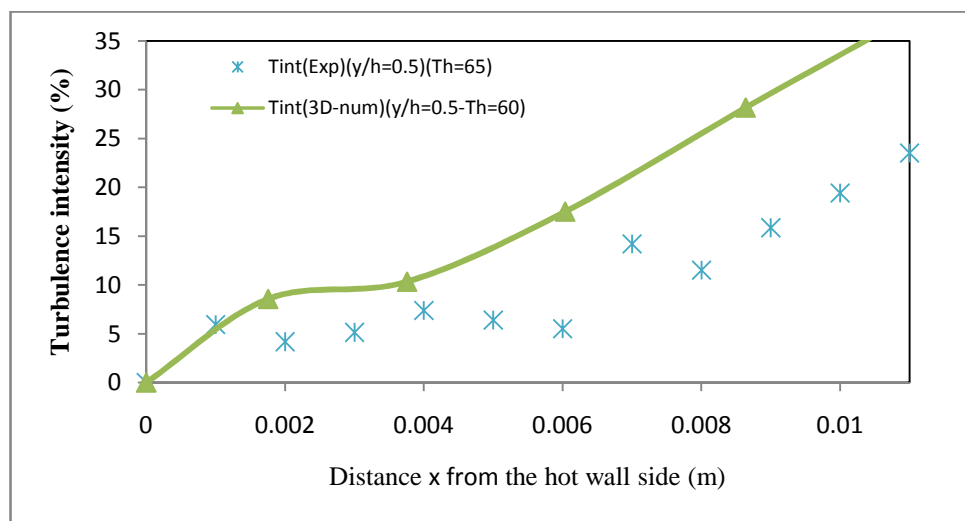
Figure 8.11 Velocity profiles at  $x = 4\text{mm}$  near the hot wall side at  $75^\circ\text{C}$  and for aspect ratio a) 2.0, b) 1.0 and c) 0.5



(a)



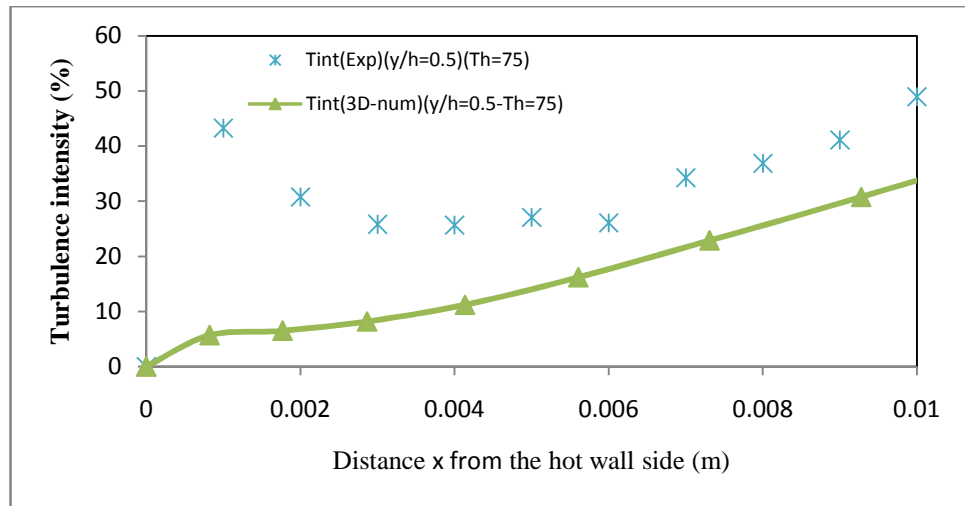
(b)



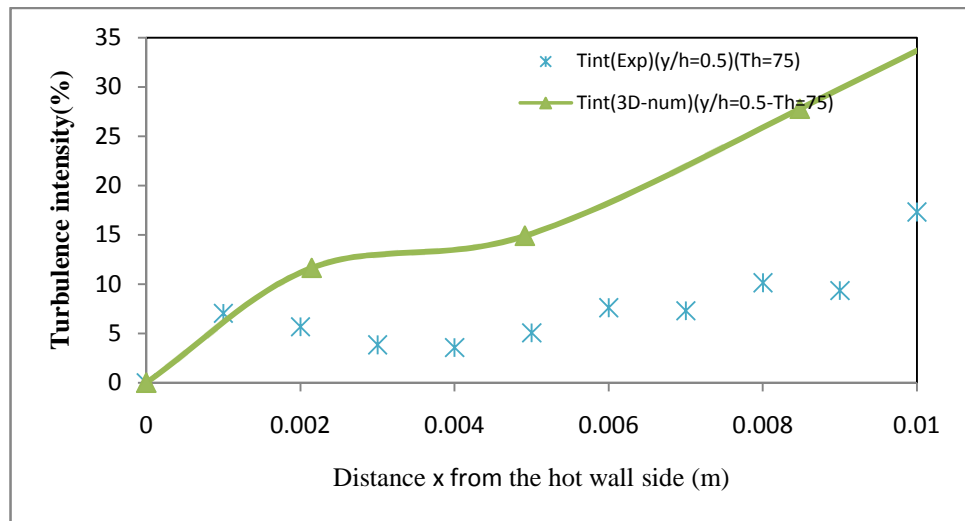
(c)

Figure 8.12 Turbulence profiles near the hot wall side for 60°C and aspect ratio a) 2.0, b) 1.0 and c) 0.5

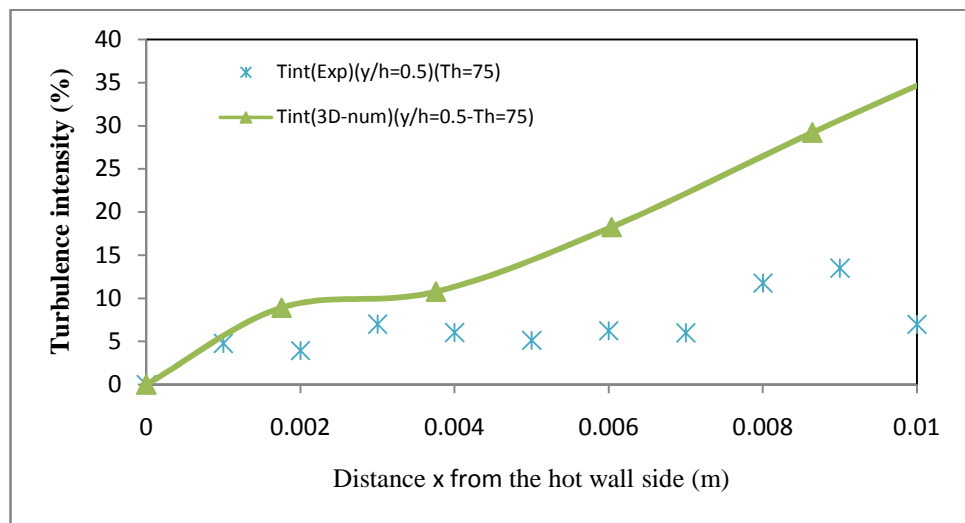




(a)



(b)



(c)

Figure 8.13 Turbulence profiles near the hot wall side for 75°C and aspect ratio a) 2.0, b) 1.0 and c) 0.5

The calculated results using the derived correlation equations and the experimental results become closer to each other as the aspect ratio increases. Also the total heat transfer increases linearly as the absolute temperature ratio increases. The calculated results using the derived correlation equations were within an average deviation of less than 15% for the three aspect ratios compared to the experimental results.

The 3D numerical results become closer to the experimental results as the aspect ratio getting closer to unity. Also the total heat transfer increases as the aspect ratio decreases. The comparison between the experimental results and the 3D numerical results were within an average deviation of less than 13% for the three aspect ratios.

The velocity profiles at the hot wall side for numerical and experimental results are in good agreement with each other. This agreement becomes clearer as the aspect ratio decreases or the temperature of the hot wall increases. The velocity profiles at the enclosure core for the three aspect ratios shown a good agreement between the numerical and experimental results. The boundary layer thickness of the experimental results on the hot side is smaller than the boundary layer of the numerical results and this difference decreases as the aspect ratio decrease.

The velocity values and the boundary layer thickness of the experimental results on the cold side is less than that of the numerical results. Also as the aspect ratio decreases the velocity profiles on the cold side start fluctuating.

The velocity reversals were noticed for about 65% of the enclosure height and above. Comparing the velocity profiles along the vertical axis and near the hot side of the experimental and numerical results show that the maximum velocity occurring near the mid-height of the enclosure. The velocity values for the experimental results increases more than the numerical results as the aspect ratio decreases.

The experimental turbulence intensities for the three aspect ratios are in a fairly agreement with the numerical ones especially for the aspect ratio of 2.0 a bit far from the wall and for aspect ratios 1.0 and 0.5 very close to the wall.

# CHAPTER 9

## FINAL FINDINGS AND FUTURE WORK

### 9.1 Final conclusions

The problem of natural convection with and without the interaction of surface radiation in square and rectangular enclosures has been studied, numerically and theoretically. The analyses were carried out over a wide range of parameters.

A dimensional analysis was established to produce correlation equations controlling the flow inside square and rectangular enclosures for pure natural convection and natural convection with radiation. All these equations are valid for a different temperature ratio, different enclosure size, different aspect ratio and different fluid properties.

Experimental study was performed for square and rectangular enclosures. The testing process involves the use of the laser Doppler velocimetry to collect the velocity and turbulent profiles.

The main conclusions from this study can be summarized as follows:

The ratio between convection to radiation heat transfer as a function of absolute temperature ratio decreases slightly as the aspect ratio increases from unity and it increases dramatically as the aspect ratio decreases from unity.

The ratio between the convection and radiation heat transfer is increased by increasing the absolute temperature ratio up to a absolute temperature ratio of 1.2; then this ratio starts to decrease. It was shown that the ratio between Rayleigh number and Nusselt number follows a similar trend.

The 3D numerical calculations show that the total heat transfer increases as the temperature of the hot wall increase. The thermal results show that the total heat transfer increases as the absolute temperature ratio increases.

The collected results using the LDV system show that the velocity starts to increase to its maximum value after a certain distance from the wall then it starts to decrease to minimum. The boundary layer thickness increases as the enclosure height or the temperature increase in all aspect ratios. The velocity values and the boundary layer thickness decreases as the aspect ratio increase. The boundary layer thickness near the hot wall side increases as the enclosure height increase. The velocity values and the boundary layer thickness increases as the temperature increases. The collected data for the velocity along the vertical axis show that the maximum velocity occurs near the mid height of the enclosure. The turbulence intensity across the enclosure increases as the aspect ratio increase and it decreases slightly as the temperature increase. The maximum turbulence intensity along the vertical axis and at the maximum velocity values occurs near the two corners of the enclosure. The turbulence intensity values increases as the aspect ratio increase.

Correlation equations have been provided for the case of natural convection with and without radiation in square and rectangular enclosures. These correlation equations are as follows:

- The Nusselt number for pure natural convection in square enclosure

$$Nu_c = \frac{k_1 Gr^{a_1}}{Pr^{b_1}}$$

- The Nusselt number for pure natural convection in rectangular enclosure

$$Nu_c = \frac{k_1 Gr^{a_1}}{Pr^{b_1}} * f(AR)$$

- For the first regime (aspect ratio from 1 to 16)

$$f(AR) = AR^{ka1} + ka2e^{AR^{ka3}} + ka4$$

- For the second regime (aspect ratio from 1 to 0.0625)

$$f(AR) = kb1 \left( AR^{kb2} + kb3e^{AR^{kb4}} + kb5 \right)$$

- The new dimensionless group for natural convection with radiation in square enclosure

$$\frac{Q_{conv}}{Q_{rad}} = \frac{k_2 Gr^{b_2}}{Nu_t^{a_2} Pr^{c_2}}$$

- The total Nusselt number for natural convection with radiation in square enclosure

$$Nu_t = a \frac{Gr^b}{Pr^c Pl^d}$$

- The new dimensionless group for natural convection with radiation in rectangular enclosure

$$RCn = \frac{Q_{conv}}{Q_{rad}} = \frac{k_2 Gr^{b_2}}{Nu_t^{a_2} Pr^{c_2}} * f(AR)$$

- For the first regime (aspect ratio from 1 to 16)

$$f(AR) = AR^{kc1} + kc2e^{AR^{kc3}} + kc4$$

- For the second regime (aspect ratio from 1 to 0.0625)

$$f(AR) = kd1 \left( AR^{kd2} + kd3e^{AR^{kd4}} + kd5 \right)$$

- The total Nusselt number for natural convection with radiation in rectangular enclosure

$$Nu_t = a \frac{Gr^b}{Pr^c Pl^d} * f(AR)$$

- For the first regime (aspect ratio from 1 to 16)

$$f(AR) = AR^{g1} + g2e^{AR^{g3}} + g4$$

- For the second regime (aspect ratio from 1 to 0.0625)

$$f(AR) = h1 \left( AR^{h2} + h3e^{AR^{h4}} + h5 \right)$$

The calculated results using the correlation equations for pure natural convection had an average deviation of 2.9% and a maximum deviation of less than 7.2% for the square enclosure, compared to the numerical results.

The calculated results of the total Nusselt number in a square enclosure using the derived correlation equation were within a maximum deviation of less than 2.8% compared to the numerical results.

The calculated results of the average convection Nusselt number in rectangular enclosures using the correlation equations for the first regime (which is for aspect ratio ranging from 1 to 16) had an average deviation of 2.7% and a maximum deviation of less than 7.3% and for the second regime had an average deviation of 3.2% and a maximum deviation of 6.6%.

The correlation equation for the new dimensionless group to predict the relation between convection and radiation in the square enclosure had a maximum error of 2.7% when it used for different fluid properties and enclosure sizes and a maximum error of 7.3% when the effect of cold wall temperature was included.

The derived correlation equation for the new dimensionless group as a function of absolute temperature ratio in the rectangular enclosure had an average deviation of 3.1% and a maximum deviation of 7.2% for the first regime and an average deviation of 2.9% and a maximum deviation of 7.3% for the second regime.

The calculated results of the total Nusselt number in the rectangular enclosure using the derived correlation equations for the two flow regimes were within a maximum deviation of less than 7.7%; compared to the numerical results.

There were two methods to find out the flow parameters in the square and rectangular enclosures for the two cases of study, pure natural convection and natural convection with radiation interaction, first the direct solution when the hot and cold wall temperatures are given and second the indirect (iterative) solution when only one wall temperature given along with the heat transfer rate.

The thermal results of the derived correlation equations are in a good agreement with the previous experimental results. The calculated results show that the maximum deviation between these two results was less than 16%.

The calculated results using the derived correlation equations were within an average deviation of less than 15% for the three aspect ratios compared to the experimental results.

The comparison between the thermal experimental results and the 3D numerical results were within an average deviation of less than 13% for the three aspect ratios.

The velocity profiles at the hot wall side for numerical and experimental results are in well agreement with each other. This agreement becomes clearer as the aspect ratio decrease or the temperature of the hot wall increase.

The velocity profiles for the 3D numerical results and at the enclosure core for the three aspect ratios are in a well agreement between the numerical and experimental results.

The velocity values and the boundary layer thickness of the experimental results on the cold side is less than that of the numerical results. Also as the aspect ratio decreases the velocity profiles for the experimental results on the cold side start fluctuating.

The velocity reversals were noticed for about 65% of the enclosure height and upward. The velocity profiles along the vertical axis and near the hot side of the experimental and numerical results show that the maximum velocity occurring near the mid-height of the enclosure.

The experimental turbulence intensities for the three aspect ratios are in a fairly agreement with the numerical ones especially for the aspect ratio of 2.0 a bit far from the wall and for aspect ratios 1.0 and 0.5 very close to the wall.

It is hoped that the results of this study will usefully contribute to the literature in this field and enhance the understanding of the natural convection with radiation interaction in rectangular enclosures. Also this will be a useful technique, as, by using the results it is possible to generalise the heat transfer in square and rectangular cavities filled with ideal gases.

## **9.2 Future work**

The current study has produced some correlation equations including the new dimensionless group based on the dimensional analysis inside cavities. These correlation equations are used to find the heat transfer parameters of the natural convection with and without radiation inside rectangular enclosures.

In order to extend the use of these derived correlation equations and understand the flow inside enclosures, there are some other parameters need to be studied. Following is a list of recommendations to extend this study:

- Study the effect of the other parameters on these correlations, such as the effect of surface emissivity and roughness.
- Experimentally study more deeply the turbulence parameters using the LDV and compare them with the numerical results.
- Study the effect of the enclosure edge and width on the flow inside the cavity.
- Study the effect of natural convection with radiation interaction for the enclosures heated from below. Produce correlation equations for the enclosures heated from below.
- Study the effect of natural convection with radiation interaction for inclined enclosures. Produce correlation equations for the inclined enclosures.

# References

1. Incropera, F.P., *Introduction to heat transfer*. 3rd ed. 1985, New York: John Willey & Sons.
2. Holman, J.P., *Heat transfer*. eight ed. 1997, International Edition: McGraw-Hill.
3. Cengel, Y.A., *Heat transfer*. 2003, International Edition: McGraw-Hill.
4. Sharma, A.K., K. Velusamy, and C. Balaji, *Interaction of turbulent natural convection and surface thermal radiation in inclined square enclosures*. Heat Mass Transfer, 2008. **44**: p. 1153-1170.
5. Lankhorst, A.M., *Laminar and turbulent natural convection in cavities*. 1991, Delft University of Technology: the Netherlands.
6. Markatos, N.C. and K.A. Pericleous, *Laminar and Turbulent Natural-Convection in an Enclosed Cavity*. International Journal of Heat and Mass Transfer, 1984. **27**(5): p. 755-772.
7. Elsherbiny, S.M., G.D. Raithby, and K.G.T. Hollands, *Heat transfer by natural convection across vertical and inclined air layers*. ASME J. Heat Transfer 1982. **104**: p. 96-102.
8. Davis, G.D.V., *Natural convection of air in a square cavity a bench mark numerical solution*. International Journal for Numerical Methods in Fluids, 1983. **3**: p. 249-264.
9. Davis, G.D.V., *Natural convection in a square cavity: a comparison exercise*. Int. J. for numerical methods in Fluids, 1983. **3**: p. 227-248.
10. Barletta, A., et al., *Natural convection in a 2D-cavity with vertical isothermal walls: cross-validation of two numerical solutions*. International Journal of Thermal Sciences 2006. **45**: p. 917-922.
11. Ramesh, N. and S.P. Venkateshan, *Experimental study of natural convection in a square enclosure using differential interferometer*. International Journal of Heat and Mass Transfer, 2001. **44**: p. 1107-1117.
12. Lankhorst, A.M., D. Angirasa, and C.J. Hoogendoorn, *Ldv Measurements of Buoyancy-Induced Flows in an Enclosure at High Rayleigh Numbers*. Experimental Thermal and fluid Science, 1993. **6**(1): p. 74-79.
13. Schmidt, F.W., et al., *A comparison of experimental and predicted results for laminar natural convection in an enclosure*. Int. J. Heat & Fluid Flow, 1986. **7**: p. 183-190.
14. Henkes, R.A.W.M., F.F.V.D. Vlugt, and C.J. Hoogendoorn, *Natural-convection flow in a square cavity calculated with low-Reynolds number turbulence models*. Int. J. Heat Mass Transfer 1991. **34**: p. 377-388.
15. Henkes, R.A.W.M. and C.J. Hoogendoorn, *Comparison exercise for computations of turbulent natural convection in enclosures*. Numerical Heat Transfer, 1995. **28**(Part B): p. 59-78.
16. Henkes, R.A.W.M. and C.J. Hoogendoorn. *Turbulent natural convection in enclosures; a computational and experimental benchmark study*. in *Proc. Eurotherm Sem.* 1993. Paris: EETI.
17. Patterson, J. and J. Imberger, *Unsteady natural convection in rectangular cavity*. Journal of Fluid Mechanics, 1980. **100**: p. 65-86.
18. Bejan, A., A. Al-Homoud, and J. Imberger, *Experimental study of high Rayleigh number convection in a horizontal cavity with different end temperatures*. Journal of Fluid Mechanics, 1981. **109**: p. 283-299.



19. Bejan, A., *Convection heat transfer*. 2nd ed. 1995, New York: John Wiley & Sons Inc.
20. Zhong, Z.Y., K.T. Yang, and J.R. Lloyd, *Variable Property Effects in Laminar Natural Convection in a Square Enclosure*. Journal of Heat Transfer, 1985. **107**: p. 133-138.
21. Fusegi, T. and J.M. Hyun, *Laminar and Transitional Natural Convection in an Enclosure With Complex and Realistic Conditions*. Int. J. Heat and Fluid Flow, 1994. **15**: p. 258-268.
22. Nithyadevi, N., P. Kandaswamy, and J. Lee, *Natural convection in a rectangular cavity with partially active side walls*. International Journal of Heat and Mass Transfer, 2007. **50**(23-24): p. 4688-4697.
23. Kato, H., N. Nishiwaki, and M. Hirata, *On the turbulent Heat Transfer By Free Convection From a Vertical Plate*. int. J. heat and mass transfer, 1968. **11**.
24. Vliet, G.C. and C.K. Liu, *An Experimental Study of Turbulent Natural Convection Boundary Layers*. Journal of Heat Transfer, 1969. **91**(4): p. 517-&.
25. Churchill, S.W. and H.H.S. Chu, *Correlation equations for laminar and turbulent free convection from a vertical plate*. Int. J. Heat Mass Transfer, 1975. **18**.
26. Holman, J.P., *Heat transfer*. 7th ed ed. 1992, International (UK): McGraw-Hill.
27. Incropera, F.P. and D.P. DeWitt, *Introduction to Heat transfer*. THIRD ed. 1985, New York: JOHN WILEY & SONS.
28. Siebers, D.L., R.F. Moffatt, and R.G. Schwind, *Experimental, Variable Properties Natural-Convection from a Large, Vertical, Flat Surface*. Journal of Heat Transfer-Transactions of the Asme, 1985. **107**(1): p. 124-132.
29. Elenbaas, W., *Heat dissipation of parallel plates by free convection*. Physica, 1942. **9**.
30. Bar-Cohen, A. and W.M. Rohsenow, *Thermally optimum spacing of vertical natural convection cooled, parallel plates*. J. Heat Transfer, 1984. **106**.
31. Azevedo, L.F.A. and E.M. Sparrow, *Natural convection in open ended inclined channels*. J. Heat Transfer, 1985. **107**.
32. Jakob, M., *Heat transfer*. 1949, New York: Wiley.
33. Globe, S. and D. Dropkin, *Natural convection heat transfer in liquids confined between two horizontal plates*. J. Heat Transfer, 1959. **81C**.
34. Hollands, K.G.T., et al., *Free convection heat transfer across inclined air layers*. J. Heat Transfer, 1976. **98**: p. 189-193.
35. Graaf, G.A.D. and E.F.M.V.D. Held, *The relation between the heat transfer and the convection phenomena in enclosed plane air layers*. Appl. Sci. Res., 1953. **3**: p. 393-409.
36. Catton, I. *Natural convection in enclosures*. in *Proc. 6th Int. Heat Transfer conf.* 1978. Toronto, Canada.
37. Ayyaswamy, P.S. and I. Catton, *The boundary layer regime for natural convection in a differentially heated, tilted rectangular cavity*. J. Heat Transfer, 1973. **95**.
38. Arnold, J.N., I. Catton, and D.K. Edwards, *Experimental investigation of natural convection in inclined rectangular regions of differing aspect ratios*. J. Heat Transfer, 1976. **98**(1): p. 67-72.
39. Eckertf, E.R.G. and W.O. Carlson, *Natural convection in an air layer enclosed between two vertical plates with different temperatures*. International Journal of Heat and Mass Transfer, 1961. **2**(1-2): p. 106-110, IN3, 111-120.

40. Macgregor, R.K. and A.F. Emery, *Prandtl Number Effects on Natural Convection in an Enclosed Vertical Layer*. Journal of Heat Transfer, 1971. **93**(2): p. 253-&.
41. Seki, N., S. Fukusako, and H. Inaba, *Heat-Transfer of Natural-Convection in a Rectangular Cavity with Vertical Walls of Different Temperatures*. Bulletin of the Jsme-Japan Society of Mechanical Engineers, 1978. **21**(152): p. 246-253.
42. Cowan, G.H., P.C. Lovegrove, and G.L. Quarini. *Turbulent Natural Convection Heat Transfer in Vertical Single Water Filled Cavities*. in *Proc. 7th Int. Heat Transfer Conf.* 1982.
43. Macgregor, R.K. and A.P. Emery, *Free convection through vertical plane layers: moderate and high Prandtl number fluids*. J. Heat Transfer, 1969. **91**.
44. Ziai, S., *Turbulent Natural Convection in a Large Rectangular Air Cavity*, in *Mech. Eng. Dept.* 1983, Queen Mary College: London.
45. Trias, F.X., et al., *Direct numerical simulation of a differentially heated cavity of aspect ratio 4 with Rayleigh numbers up to 1011 - Part I: numerical methods and time averaged flow*. int. J. Heat Mass Transfer, 2010. **53**(4): p. 665-673.
46. Trias, F.X., et al., *Direct numerical simulation of a differentially heated cavity of aspect ratio 4 with Rayleigh numbers up to 10(11) - Part II: Heat transfer and flow dynamics*. International Journal of Heat and Mass Transfer, 2010. **53**(4): p. 674-683.
47. Balaji, C. and S.P. Venkateshan, *Interaction of Surface Radiation with Free-Convection in a Square Cavity*. International Journal of Heat and Fluid Flow, 1993. **14**(3): p. 260-267.
48. Balaji, C. and S.P. Venkateshan, *Correlations for Free-Convection and Surface Radiation in a Square Cavity*. International Journal of Heat and Fluid Flow, 1994. **15**(3): p. 249-251.
49. Sen, S. and A. Sarkar, *Effects of Variable Property and Surface Radiation on Laminar Natural Convection in a Square Enclosure*. Int. J. Num. Meth. Heat Fluid Flow, 1995. **5**: p. 615-627.
50. Akiyama, M. and Q.P. Chong, *Numerical analysis of natural convection with surface radiation in a square enclosures*. ASME J. Heat Transfer 1997. **104**: p. 96-102.
51. Velusamy, K., T. Sundararajan, and K.N. Seetharamu, *Interaction effects between surface radiation and turbulent natural convection in square and rectangular enclosures*. ASME Journal of Heat Transfer 2001. **123**: p. 1062-1070.
52. Colomer, G., et al., *Three-dimensional numerical simulation of convection and radiation in a differentially heated cavity using the discrete ordinates method*. International Journal of Heat and Mass Transfer 2004. **47**: p. 257-269.
53. Ridouane, E.H. and M. Hasnaoui, *Effect of surface radiation on multiple natural convection solutions in a square cavity partially heated from below*. Journal of Heat Transfer-Transactions of the Asme, 2006. **128**(10): p. 1012-1021.
54. Sharma, A.K., et al., *Conjugate turbulent natural convection with surface radiation in air filled rectangular enclosures*. International Journal of Heat and Mass Transfer, 2007. **50**(3-4): p. 625-639.
55. FLUENT, I., *FLUENT 6 User's Guide*. 2001, Lebanon: NH.
56. Zhang, T., et al., *Comparison of turbulence models for natural convection in enclosures: applications to crystal growth processes*. American Society of Mechanical Engineers, Heat Transfer Division, 1996. **323**: p. 17-26.
57. King, K.J., *Turbulent natural convection in rectangular air cavities*. 1989, Queen Mary College: London, UK.

58. Cheesewright, R., K.J. King, and S. Ziai, *Experimental data for the validation of computer codes for the prediction of two-dimensional buoyant cavity flows*. Proc. ASME Meeting HTD, 1986. **60**: p. 75-81.
59. Gan, G., *Prediction of turbulent buoyant flow using an RNG  $k-\epsilon$  model*. Numerical Heat Transfer, Part A: Applications 1998. **33**: p. 169-189.
60. Zhang, Z., et al., *Evaluation of various turbulence models in predicting airflow and turbulence in enclosed environments by CFD: Part 2-comparison with experimental data from literature*. Hvac&R Research, 2007. **13**(6): p. 871-886.
61. Coussirat, M., et al., *Performance and influence of numerical sub-models on the CFD simulation of free and forced convection in double-glazed ventilated facades*. Energy and Buildings, 2008. **40**(10): p. 1781-1789.
62. Omri, M., N. Galanis, and R. Abid, *Turbulent Natural Convection in Non-Partitioned and Partitioned Cavities: Cfd Predictions with Different Two-Equation Models*. Engineering Applications of Computational Fluid Mechanics, 2008. **2**(4): p. 393-403.
63. Ampofo, F. and T.G. Karayiannis, *Experimental benchmark data for turbulent natural convection in an air filled square cavity*. International Journal of Heat and Mass Transfer, 2003. **46**(19): p. 3551-3572.
64. Johnstone, R.E. and M.W. Thring, *Pilot plants, models, and scale-up methods in chemical engineering*. 1957, New York: McGraw-Hill.
65. Kutatela.Ss, Kirdyash.Ag, and V.P. Ivakin, *Turbulent Natural-Convection on a Vertical Plate and in a Vertical Layer*. International Journal of Heat and Mass Transfer, 1972. **15**(2): p. 193-&.
66. Schmidt, F.W. and D.F. Wang, *Experimental Study of Turbulent Natural Convection in an Enclosure*. A.S.M.E., 1982. **82-WA/HT-72**.
67. Giel, P.W. and F.W. Schmidt. *An Experimental Study of High Rayleigh Number Natural Convection in an Enclosure*. in *Int. Hest Trans. Conf.* 1986. San Francisco.
68. Ayinde, T.F., S.A.M. Said, and M.A. Habib, *Experimental investigation of turbulent natural convection flow in a channel*. Heat and Mass Transfer, 2006. **42**(3): p. 169-177.
69. Jiji, L.M., *Heat convection*. 2006, Berlin ; New York: Springer. xv, 434 p.
70. Jiji, L.M., *Heat Convection*. Second ed. 2009, Berlin Heidelberg: Springer.
71. White, F.M., *Heat transfer*. 1984, Printed in USA: Addison-Wesley Inc.
72. Bejan, A. and A.D. Kraus, *Heat transfer handbook*. 2003, Hoboken, New Jersey: JOHN WILEY & SONS, INC.
73. Modest, M.F., *Radiative heat transfer*. McGraw-Hill series in mechanical engineering. 1993, New York: McGraw-Hill. xxv, 832 p.
74. Pankhurst, R.C., *Dimensional analysis and scale factors*. 1964, London, New York,: Published on behalf of the Institute of Physics and the Physical Society by Chapman and Hall;Reinhold. 151 p.
75. Taylor, E.S., *Dimensional Analysis For Engineering*. 1974, Oxford: Oxford University Press.
76. Palmer, A.C., *Dimensional analysis and intelligent experimentation*. 2008, Singapore ; Hackensack, NJ: World Scientific. x, 154 p.
77. Ipsen, D.C., *Units, dimensions, and dimensionless numbers*. 1960, New York,: McGraw-Hill. 236 p.
78. Szirtes, T. and P. Rózsa, *Applied dimensional analysis and modeling*. 2nd ed. 2007, Amsterdam ; New York: Elsevier/Butterworth-Heinemann. xxxi, 820 p.

79. Douglas, J.F., *An introduction to dimensional analysis for engineers*. 1969, London,: Pitman. vii, 134 p.
80. Versteeg, H.K. and W. Malalasekera, *An introduction to computational fluid dynamics : the finite volume method*. 2nd ed. 2007, Harlow, England ; New York: Pearson Education Ltd. xii, 503 p.
81. Douglas, J.F., *Solving problems in fluid mechanics*. 1986, Harlow, Essex, England: Longman Scientific & Technical.
82. Fox, R.W. and A.T. McDonald, *Introduction to fluid mechanics*. 2d ed. 1978, New York: Wiley. xvi, 684 p.
83. Henke, R.W., *Introduction to fluid mechanics*. 1966, Reading, Mass.: Addison-Wesley Pub. Co. vii, 232 p.
84. Lydersen, A., *Fluid flow and heat transfer*. 1979, Chichester Eng. ; New York: Wiley. x, 357 p.
85. White, F.M., *Fluid mechanics*. 4th ed. McGraw-Hill series in mechanical engineering. 1999, Boston, Mass.: WCB/McGraw-Hill. xiv, 826 p.
86. Schlichting, H., *Boundary-layer theory*. 7th ed. McGraw-Hill series in mechanical engineering. 1979, New York: McGraw-Hill. xxii, 817 p.
87. White, F.M., *Viscous fluid flow*. 2nd ed. McGraw-Hill series in mechanical engineering. 1991, New York: McGraw-Hill. xxi, 614 p.
88. John, V., *Large eddy simulation of turbulent incompressible flows : analytical and numerical results for a class of LES models*. Lecture notes in computational science and engineering,. 2004, Berlin ; New York: Springer. xii, 261 p.
89. Versteeg, H.K. and W. Malalasekera, *An introduction to computational fluid dynamics : the finite volume method*. 1995, Harlow, Essex, England Longman Scientific & Technical :: New York : Wiley. x, 257 p.
90. Berselli, L.C., *Mathematics of large eddy simulation of turbulent flows*. Scientific computation. 2006, Berlin ; New York: Springer. xvii, 348 p.
91. Pope, S.B., *Turbulent flows*. 2000, Cambridge ; New York: Cambridge University Press. xxxiv, 771 p.
92. Schiestel, R., *Modeling and simulation of turbulent flows*. 2008, Hoboken, NJ, USA: Wiley : ISTE.
93. Lesieur, M., *Turbulence in fluids*. 2008, New York: Springer.
94. Durbin, P.A. and B.A.P. Reif, *Statistical theory and modeling for turbulent flows*. 2nd ed. 2011, Chichester, West Sussex: Wiley. xiii, 357 p.
95. Markatos, N.C. and K.A. Pericleous, *Laminar and turbulent natural convection in an enclosed cavity*. Int. J. Heat Mass Transfer 1984. **27**: p. 755-772.
96. Hirsch, C., *Numerical computation of internal and external flows*. Wiley series in numerical methods in engineering. 1988, Chichester England ; New York: Wiley.
97. Abbott, M.B. and D.R. Basco, *Computational fluid dynamics : an introduction for engineers*. 1989, Harlow, Essex, EnglandNew York: Longman Scientific & Technical ;Wiley. xiv, 425 p.
98. Tannehill, J.C., D.A. Anderson, and R.H. Pletcher, *Computational fluid mechanics and heat transfer*. 2nd ed. Series in computational and physical processes in mechanics and thermal sciences. 1997, Washington, DC: Taylor & Francis. xiii, 792 p.
99. Bradshaw, P., T. Cebeci, and J.H. Whitelaw, *Engineering calculation methods for turbulent flow*. 1981, London ; New York: Academic Press. xii, 331 p.

100. Cebeci, T., *Turbulence models and their application : efficient numerical methods with computer programs*. 2004, Long Beach, Calif.: Horizons Pub. ix, 118 p.
101. Versteeg, H.K. and W. Malalasekera, *An introduction to computational fluid dynamics*. First ed. 1995, Malaysia: PEARSON Prentice Hall.
102. Launder, B.E. and D.B. Spalding, *The numerical computation of turbulent flows*. Computer methods in applied mechanics and engineering, 1974. **3**: p. 269-289.
103. Kim, S.E. and D. Choudhury, *A near-wall treatment using wall functions sensitized to pressure gradient*. ASME FED Separated and Complex flows, 1995. **217**.
104. Wolfstein, M., *The velocity and temperature distribution in one-dimensional flow with turbulence augmentation and pressure gradient*. Int. J. Heat Mass Transfer, 1969. **12**: p. 301-318.
105. Chen, H.C. and V.C. Patel, *Near-Wall Turbulence Models for Complex Flows Including Separation*. Aiaa Journal, 1988. **26**(6): p. 641-648.
106. EN-442, *Radiators and Convectors*. 1997. **Part 2. BSI**.
107. British-standard, *Specification for Convection type space heaters operating with steam or hot water*. 1977. **BS-3528**.
108. PICO-Technology, *USB TC-08, Temperature logger Programmer's Guide*. 2005-2012.
109. PICO-Technology, *USB TC-08, Temperature logger user's Guide*. 2005-2012.
110. NESLAB, *CFT-75 Recirculating Chiller Instruction and operation manual*. 1997.
111. Jensen, A.D., *Flow Measurements*. Soc. of Mch. Sci. and Eng., 2004.
112. Yea, *localized fluid flow measurement*. Appl. Phys. Letters, 1964(4): p. 176-178.
113. Foreman, *Measurement of localized*. Appl. Phys., 1965. **7**: p. 77-78.
114. (TSI), T.S.I., *Laser Doppler Velocimeter/ Phase Doppler Particle analyzer (PDPA) - Operations Manual*. July 2011.
115. Zhang, Z., *LDV application methods*. 2010.
116. (TSI), T.S.I., *Partical Instruments Six-Jet Atomizer Instruction Manual*. February 2003.
117. Beck, P., L.S. Lasdon, and M. Engquist, *A reduced gradient algorithm for nonlinear network problems*. Working paper / College of Business Administration, The University of Texas at Austin. 1981, Austin, Tex.: College of Business Administration Distributed by Bureau of Business Research, University of Texas at Austin. 23 p.
118. Lasdon, L.S. and A.D. Waren, *Large-Scale Non-Linear Programming*. Computers & Chemical Engineering, 1983. **7**(5): p. 595-604.

## Appendix-A

### A.1. Using the Pi theorem for the case of natural convection heat transfer.

$$Qc = f(L, \rho, \mu, k, Cp, \beta g, \Delta T, T, H)$$

The parameters units will be as below:

$Qc$	$L$	$\rho$	$\mu$	$k$	$Cp$	$\Delta T$	$T$	$H$	$\beta g$
$HT^{-1}$	$L$	$ML^{-3}$	$ML^{-1}T^{-1}$	$HL^{-1}T^{-1}\theta^{-1}$	$HM^{-1}\theta^{-1}$	$\theta$	$\theta$	$L$	$LT^{-2}\theta^{-1}$

The number of parameter,  $n = 10$ , and the number of dimensions are five, therefore  $J \leq 5$ . From this the number of dimensionless groups will be  $K = n - J = 10 - 5 = 5$

The number of  $\pi_i$ 's which are the dimensionless groups will be  $(Qc, Cp, H, T, \beta g)$

$$\pi_1 = \Delta T^a L^b \rho^c \mu^d k^e Qc$$

From this equation and the table above then:

$$\text{For } [H]e + 1 = 0 \text{ therefore } e = -1$$

$$\text{For } [\theta]a - e = 0 \text{ therefore } a = e = -1$$

$$\text{For } [L]b - 3c - d - e = 0$$

$$\text{For } [M]c + d = 0 \text{ therefore } c = -d$$

$$\text{For } [T] - d - e - 1 = 0 \text{ therefore } d = 0 \text{ and } c = 0 \text{ and } b = e = -1$$

Therefore

$$\pi_1 = \frac{Qc}{kL\Delta T} = Nuc$$

The second dimensionless group

$$\pi_2 = \Delta T^a L^b \rho^c \mu^d k^e Cp$$

From this equation and the table above then:

$$\text{For } [H]e + 1 = 0 \text{ therefore } e = -1$$

$$\text{For } [\theta]a - e - 1 = 0 \text{ therefore } a = 0$$

$$\text{For } [L]b - 3c - d - e = 0$$

$$\text{For } [M]c + d - 1 = 0$$

$$\text{For } [T] - d - e = 0 \text{ therefore } d = 1 \text{ and } c = 0 \text{ and } b = 0$$

Therefore

$$\pi_2 = \frac{Cp\mu}{k} = Pr$$

The third dimensionless group

$$\pi_3 = \Delta T^a L^b \rho^c \mu^d k^e \beta g$$

From this equation and the table above then:

For  $[H]e = 0$

For  $[\theta]a - e - 1 = 0$  therefore  $a = 1$

For  $[L]b - 3c - d - e + 1 = 0$

For  $[M]c + d = 0$

For  $[T]-d - e - 2 = 0$  therefore  $d = -2$  and  $c = 2$  and  $b = 3$

Therefore

$$\pi_3 = \frac{\beta g \Delta T L^3 \rho^2}{\mu^2} = Gr$$

The forth dimensionless group

$$\pi_4 = \Delta T^a L^b \rho^c \mu^d k^e H$$

From this equation and the table above then:

For  $[H]e = 0$

For  $[\theta]a - e = 0$  therefore  $a = 0$

For  $[L]b - 3c - d - e + 1 = 0$

For  $[M]c + d = 0$

For  $[T]-d - e = 0$  therefore  $d = 0$  and  $c = 0$  and  $b = -1$

Therefore

$$\pi_4 = \frac{H}{L} = AR$$

The fifth dimensionless group

$$\pi_5 = \Delta T^a L^b \rho^c \mu^d k^e T$$

From this equation and the table above then:

For  $[H]e = 0$

For  $[\theta]a - e + 1 = 0$  therefore  $a = -1$

For  $[L]b - 3c - d - e = 0$

For  $[M]c + d = 0$

For  $[T]-d - e = 0$  therefore  $d = 0$  and  $c = 0$  and  $b = 0$

Therefore

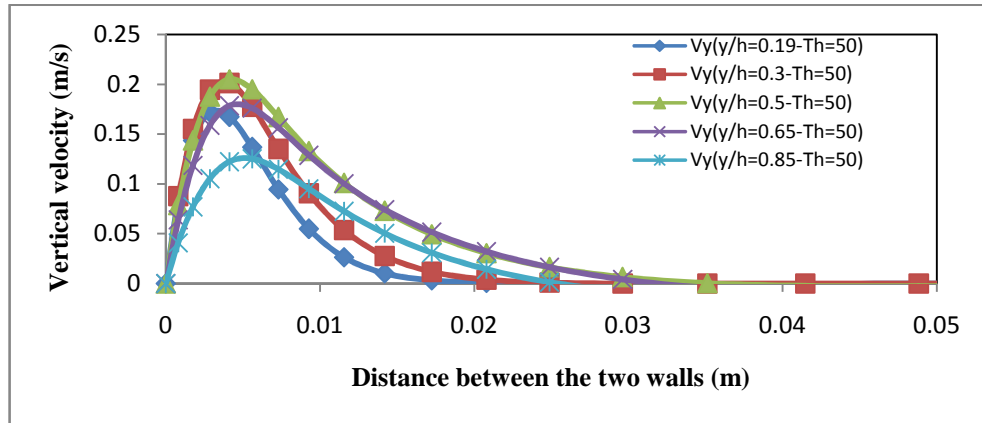
$$\pi_5 = \frac{T}{\Delta T} = Tr$$

Note: if the  $T_1$  and  $T_2$  added instead of  $T$  to the table of parameters, then the fifth dimensionless group will be:

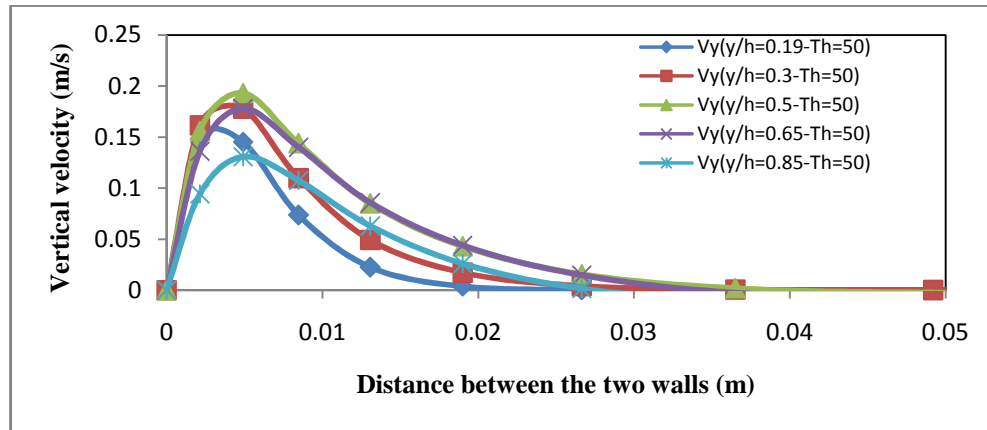
$$\pi_5 = \frac{T_1}{T_2} = Tr$$



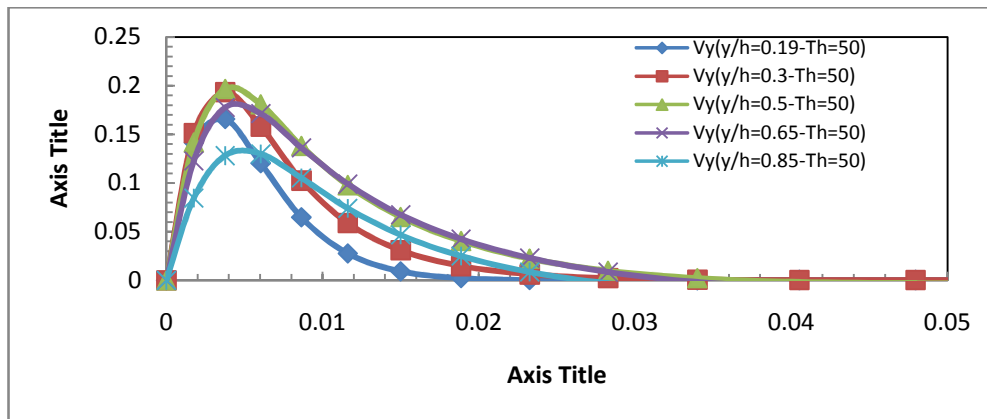
## A.2. Velocity profiles for numerical results at hot wall temperatures 50°C, 55°C, 65°C and 70°C.



(a)

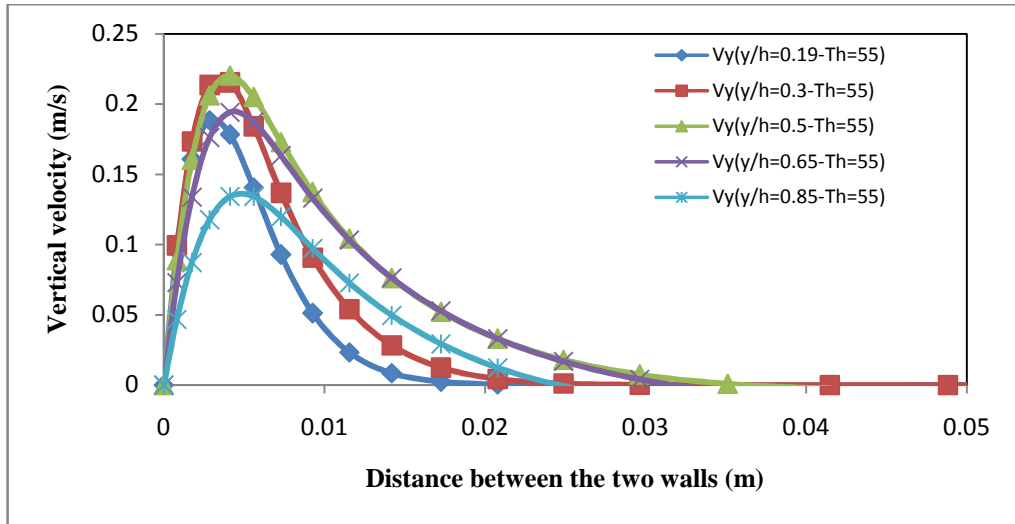


(b)

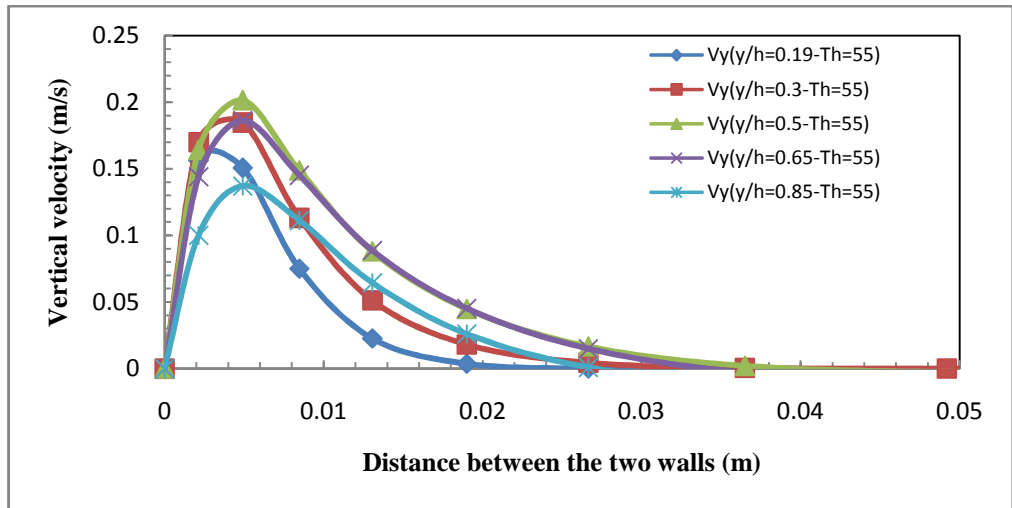


(c)

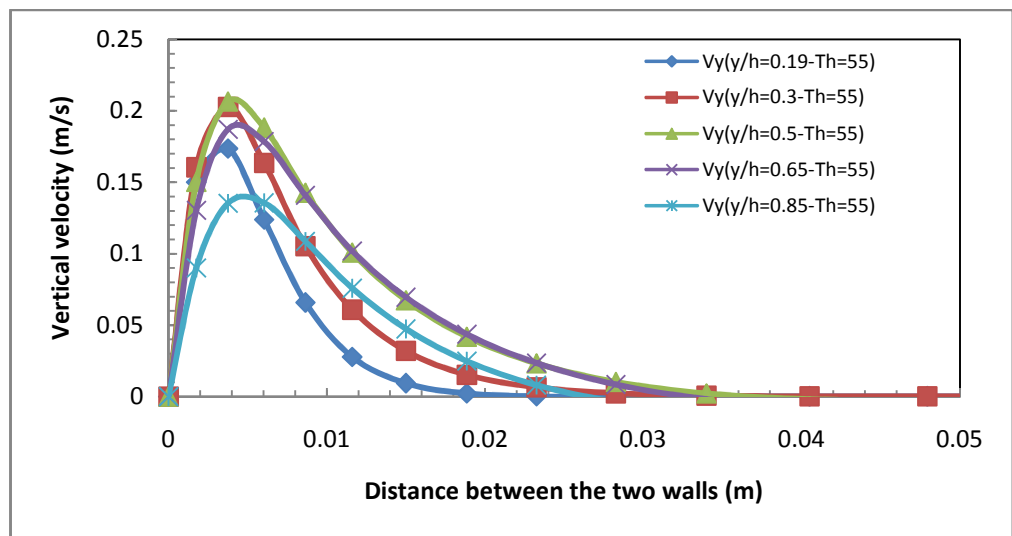
Figure A-1 Velocity profiles for aspect ratios a) 2.0, b) 1.0 and b) 0.5.



(a)

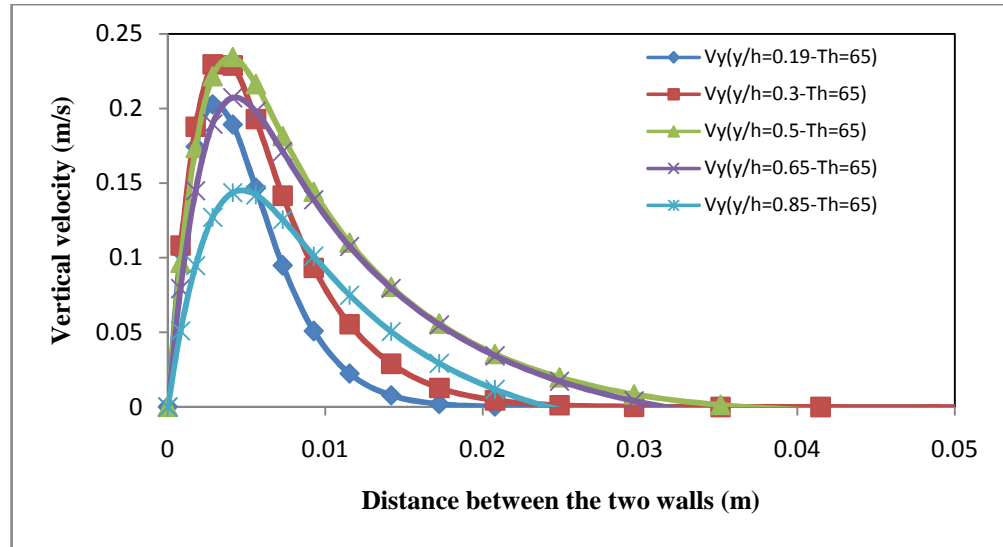


(b)

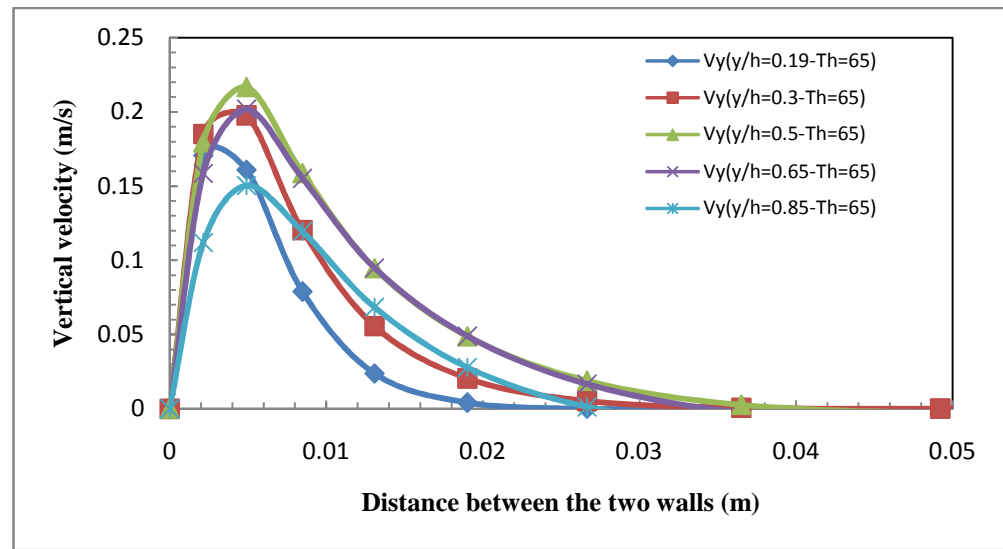


(c)

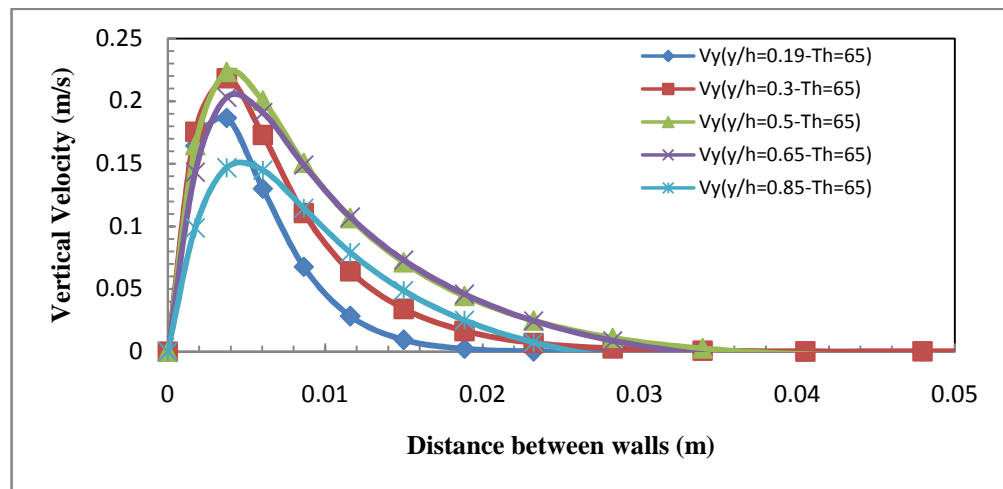
Figure A-2 Velocity profiles for aspect ratios a) 2.0, b) 1.0 and b) 0.5.



(a)

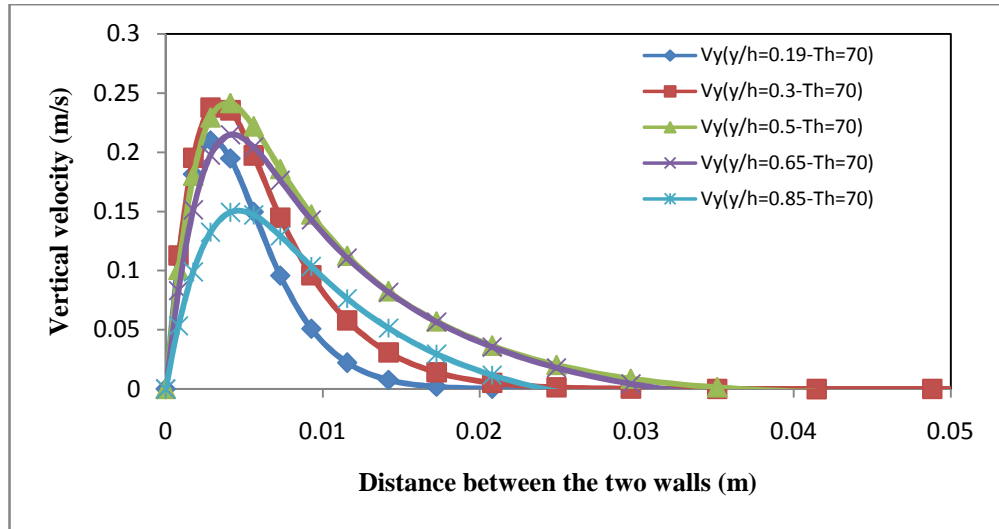


(b)

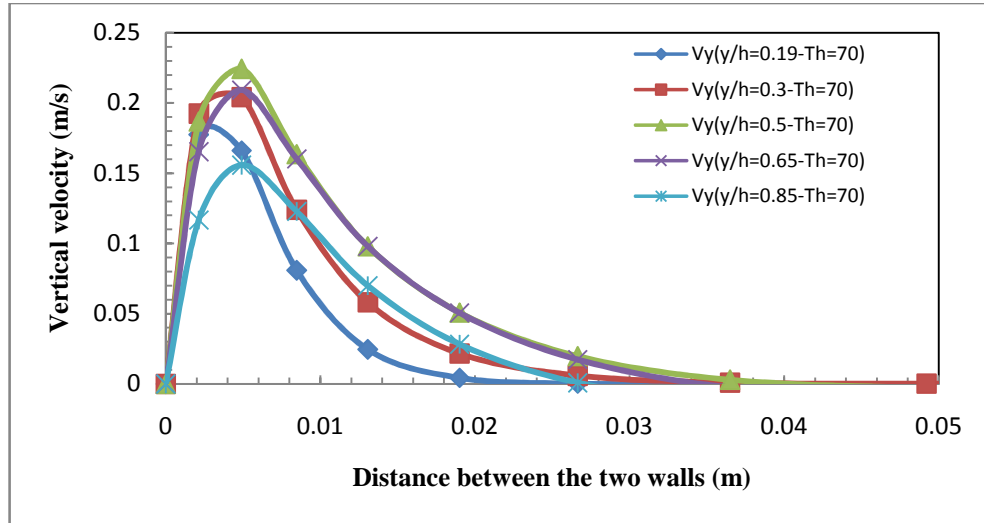


(c)

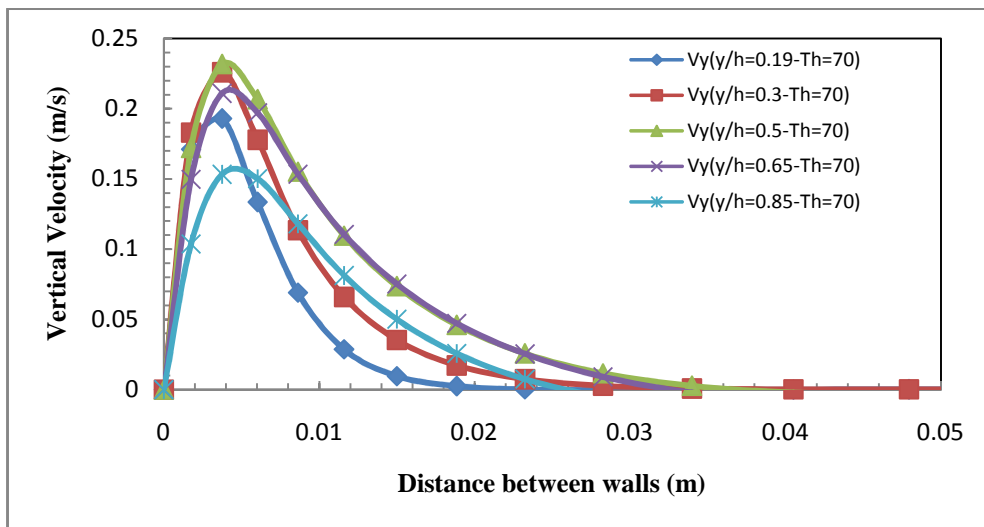
Figure A-3 Velocity profiles for aspect ratios a) 2.0, b) 1.0 and b) 0.5.



(a)



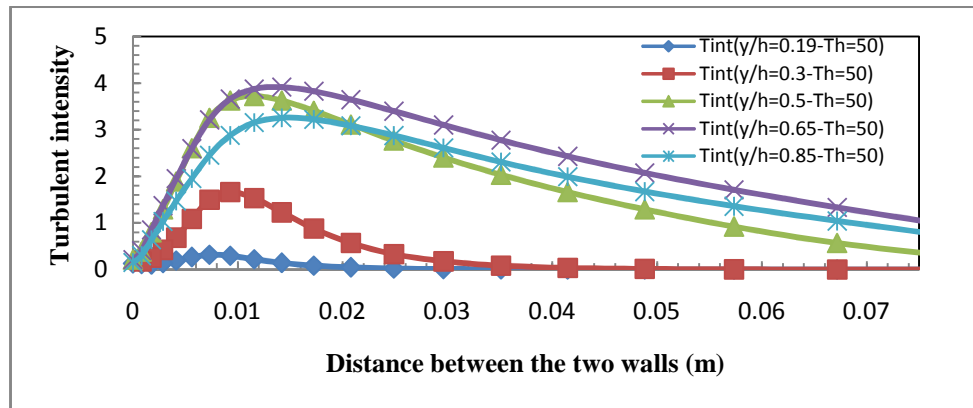
(b)



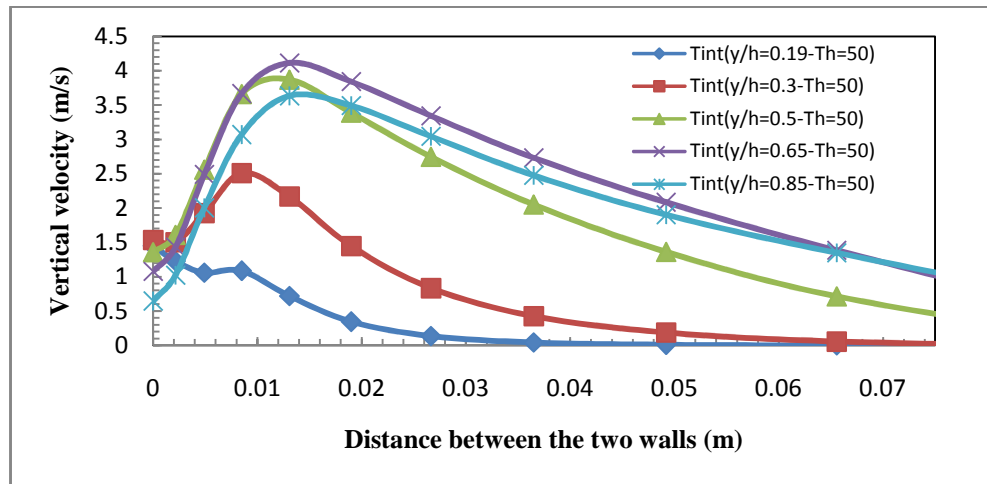
(c)

Figure A-4 Velocity profiles for aspect ratios a) 2.0, b) 1.0 and b) 0.5.

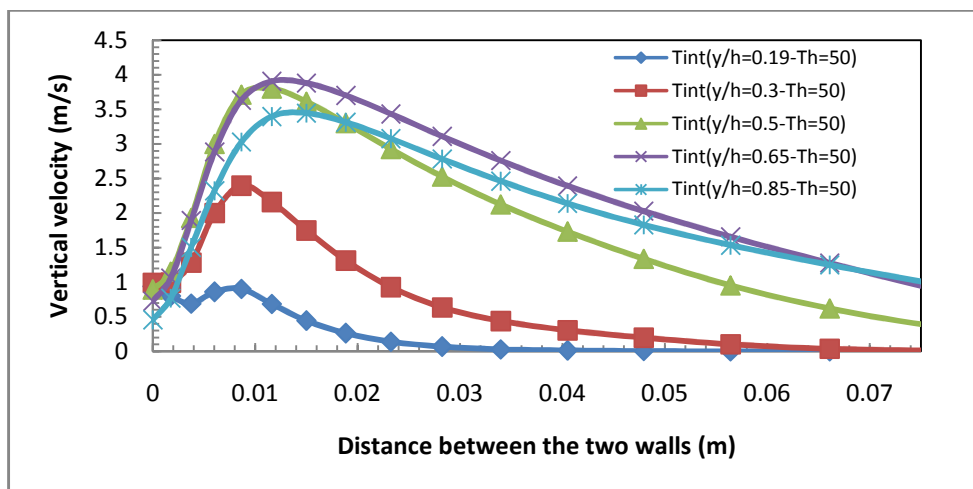
### A.3. Turbulence intensity for numerical results at hot wall temperatures 50°C, 55°C, 65°C and 70°C.



(a)

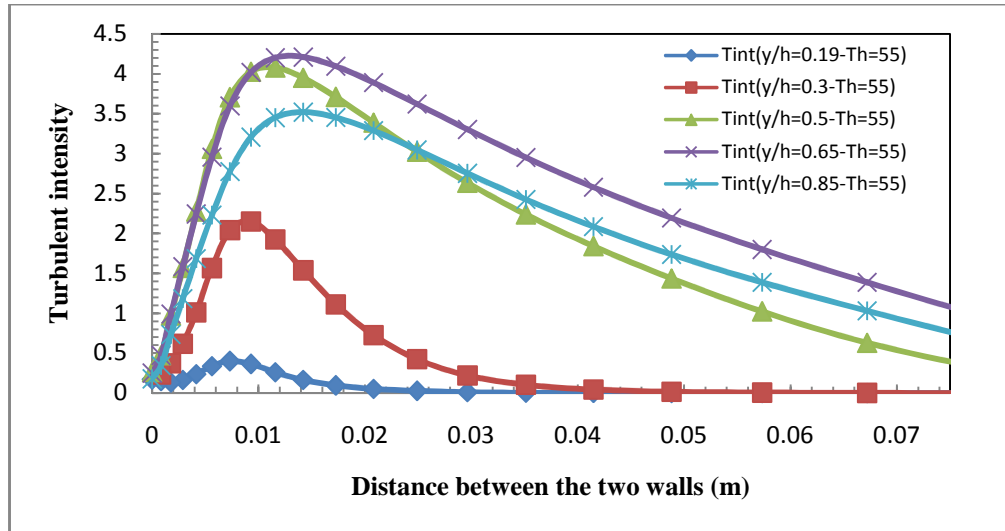


(b)

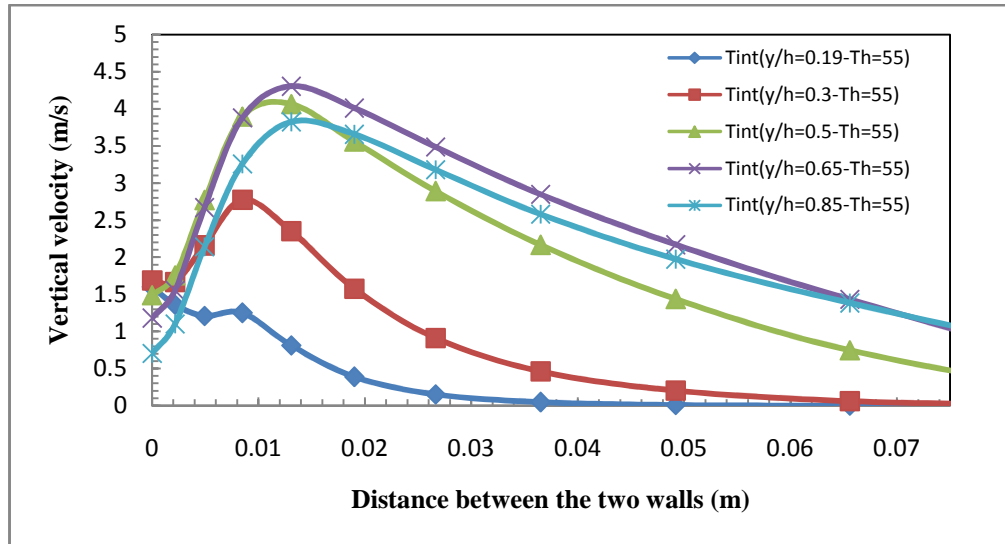


(c)

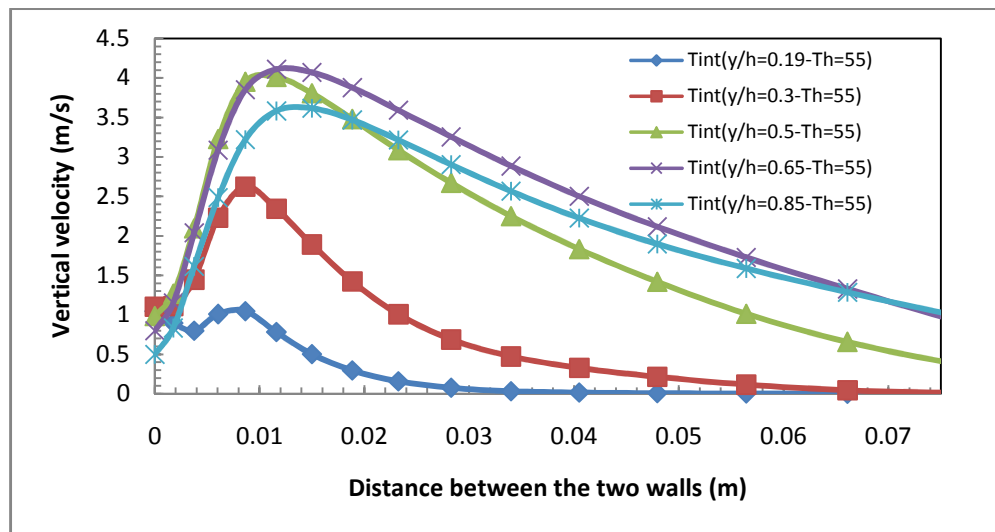
Figure A-5 Turbulent intensity profiles for aspect ratio a) 2.0, b) 1.0 and b) 0.5



(a)

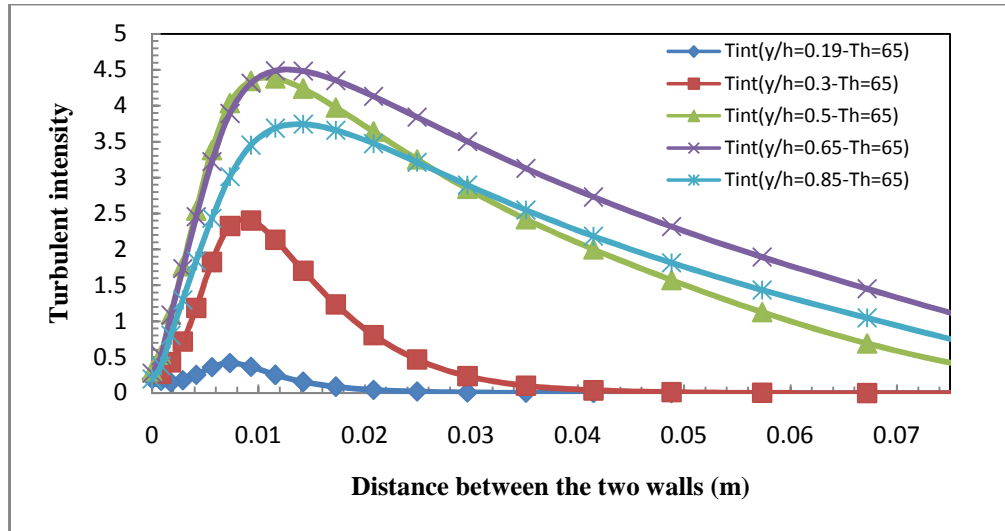


(b)

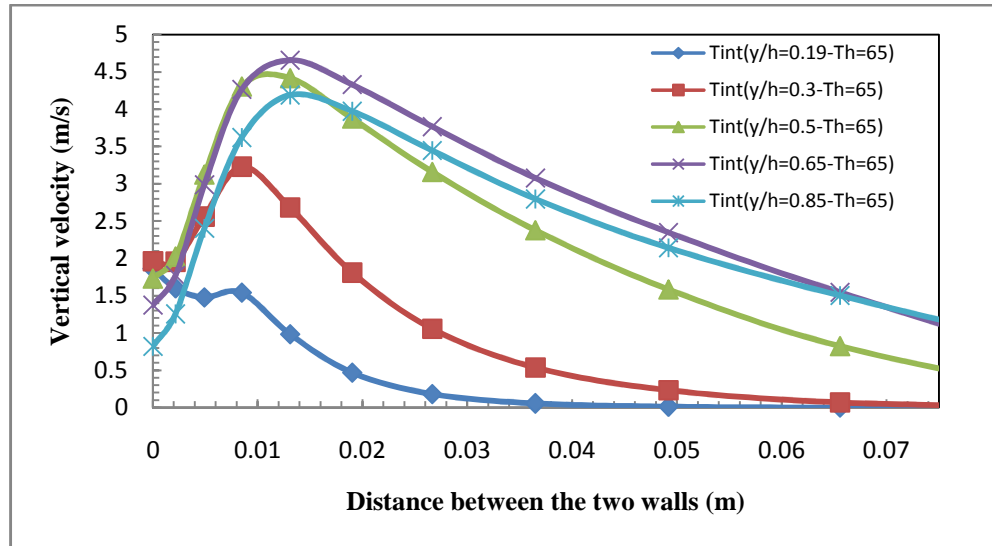


(c)

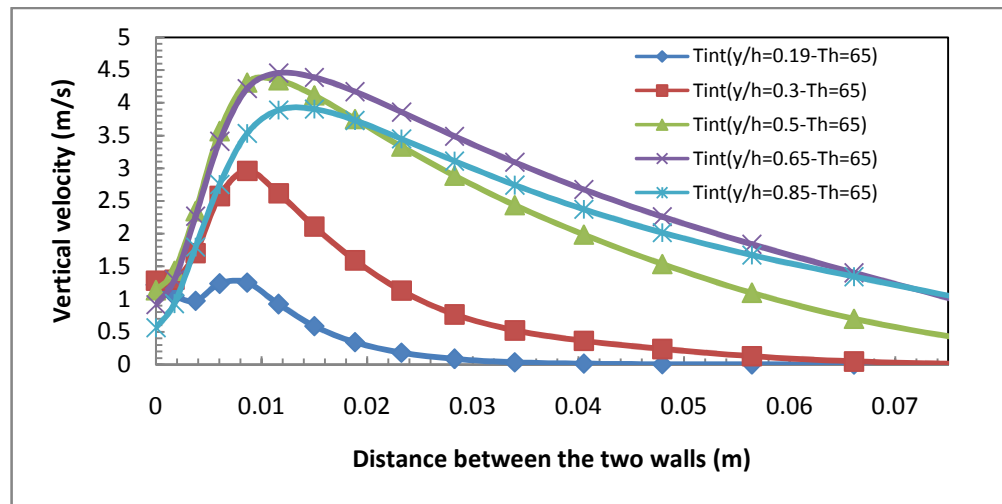
Figure A-6 Turbulent intensity profiles for aspect ratio a) 2.0, b) 1.0 and b) 0.5



(a)

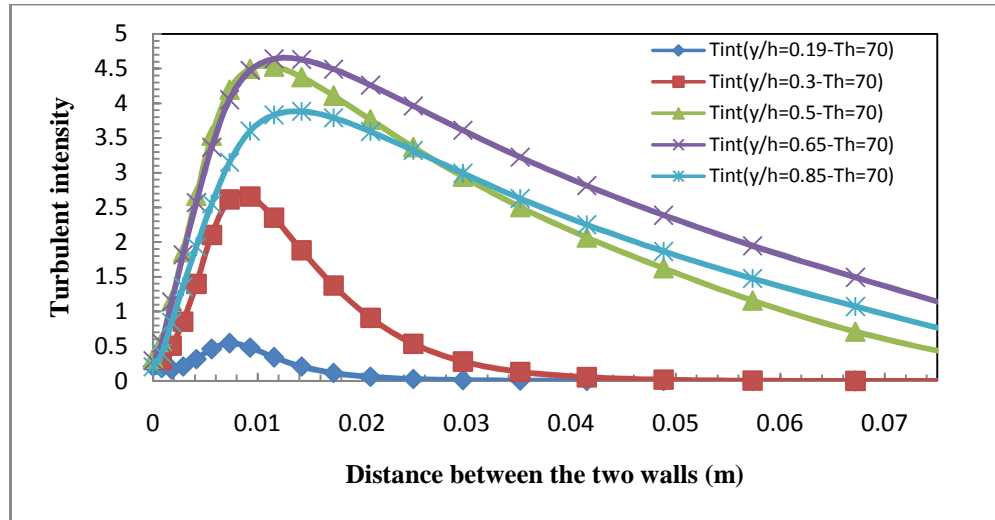


(b)

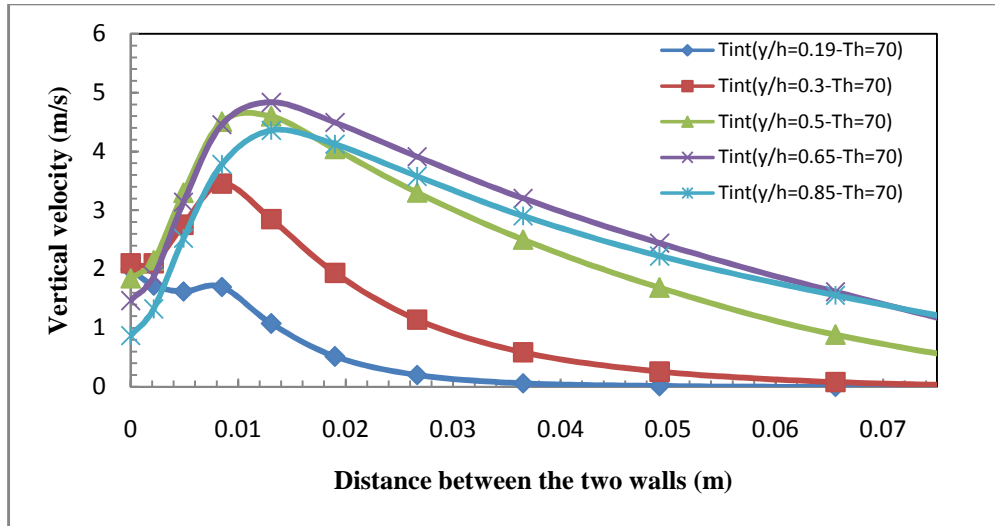


(c)

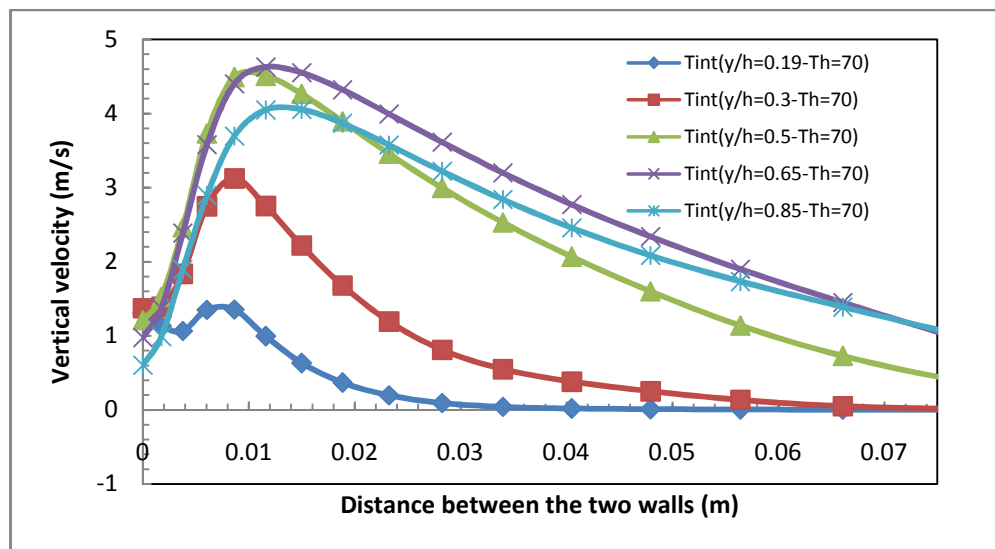
Figure A-7 Turbulent intensity profiles for aspect ratio a) 2.0, b) 1.0 and b) 0.5



(a)



(b)




(c)

Figure A-8 Turbulent intensity profiles for aspect ratio a) 2.0, b) 1.0 and b) 0.5


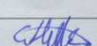
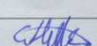
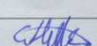


## Appendix-B

### B.1 Calibration certificate of the reference thermometer.

<b>CERTIFICATE OF CALIBRATION</b>		 <b>UKAS</b> <small>CALIBRATION</small> <b>0601</b>
<b>Date Of Issue</b> 22nd August 2012	<b>Certificate Number</b> 220812/N3	

<b>Certificate Issued By:</b> 	<b>Electronic Temperature Instruments Ltd</b> Easting Close, Worthing West Sussex BN14 8HQ England Telephone +44 01903 202151 Facsimile +44 01903 202445 email: sales@etilt.co.uk Website: www.etilt.co.uk	<table border="1" style="width: 100%; border-collapse: collapse;"> <tr> <td colspan="2" style="padding: 2px;">Page 1 of 1 pages</td> </tr> <tr> <td style="width: 60%; padding: 2px;">Approved Signatory</td> <td style="width: 40%; padding: 2px;">Signature</td> </tr> <tr> <td style="padding: 2px;">J. Carswell</td> <td style="padding: 2px;"></td> </tr> <tr> <td style="padding: 2px;">D. Carter</td> <td style="padding: 2px;"></td> </tr> <tr> <td style="padding: 2px;">G. Hills</td> <td style="padding: 2px; text-align: center;">  </td> </tr> </table>	Page 1 of 1 pages		Approved Signatory	Signature	J. Carswell		D. Carter		G. Hills	
Page 1 of 1 pages												
Approved Signatory	Signature											
J. Carswell												
D. Carter												
G. Hills												

<b>Customer Name:</b> THE UNIVERSITY OF SHEFFIELD <b>Address:</b> MECHANICAL ENGINEERING MD64 MAPPIN STREET SHEFFIELD S1 3JD	<b>Order Number:</b> XJ0/4500426930 <b>Ref Number:</b> 326/32474 <b>Date Received:</b> 21st August 2012 <b>Date Calibrated:</b> 22nd August 2012 <b>Ambient Temperature:</b> 22 °C ± 2 °C <b>Ambient Humidity:</b> < 60 %rh <b>Temperature Scale:</b> International Temperature Scale of 1990 <b>Inst Description:</b> ETI REFERENCE THERMOMETER <b>Sensor Type:</b> INTEGRAL 130mm PT100 LIQUID PROBE <b>Inst Serial Number:</b> D12260698 <b>Sensor Serial Number:</b> N/A <b>Calibrated Range/Scale:</b> - 18 °C to + 100 °C / 0.01 °C RESOLUTION <b>Procedure:</b> The Instrument was stabilised at ambient temperature, then calibrated by comparison with two traceable references in stirred liquid baths. Immersion depth 110mm <table style="width: 100%;"> <tr> <th style="width: 40%;">Results:</th> <th style="width: 30%;">Test Temperature °C</th> <th style="width: 30%;">Instrument Reading °C</th> </tr> <tr> <td></td> <td style="text-align: center;">-18.00</td> <td style="text-align: center;">-17.98</td> </tr> <tr> <td></td> <td style="text-align: center;">0.00</td> <td style="text-align: center;">0.00</td> </tr> <tr> <td></td> <td style="text-align: center;">40.00</td> <td style="text-align: center;">39.98</td> </tr> <tr> <td></td> <td style="text-align: center;">70.00</td> <td style="text-align: center;">70.00</td> </tr> <tr> <td></td> <td style="text-align: center;">100.00</td> <td style="text-align: center;">100.00</td> </tr> </table>	Results:	Test Temperature °C	Instrument Reading °C		-18.00	-17.98		0.00	0.00		40.00	39.98		70.00	70.00		100.00	100.00
Results:	Test Temperature °C	Instrument Reading °C																	
	-18.00	-17.98																	
	0.00	0.00																	
	40.00	39.98																	
	70.00	70.00																	
	100.00	100.00																	

Uncertainty of Measurement ± 0.04 °C + Instrument Resolution.

End of Report

---

The reported expanded uncertainty is based on a standard uncertainty multiplied by a coverage factor k=2, providing a level of confidence of approximately 95%.  
 The uncertainty evaluation has been carried out in accordance with UKAS requirements.  
 Results indicate performance of instrument at time of measurement, with no warranty as to specification, repeatability or long term stability.  
 This certificate is issued in accordance with the laboratory accreditation requirements of the United Kingdom Accreditation Service. It provides traceability of measurements to recognised national standards, and to units of measurement realised at the National Physical Laboratory and other recognised national standards laboratories, including the National Institute of Standards and Technology (NIST).  
 This certificate may not be reproduced other than in full, except with the prior written approval of the issuing laboratory.

Figure B-1 Calibration certificate of the reference thermometer.

## B.2. Calibration of thermocouples

All the thermocouples for the hot and cold sides were calibrated using an electronic reference thermometer which has a resolution of  $0.01^{\circ}\text{C}$ . This reference thermometer has been calibrated by the manufacturer using five reference points comes out with an uncertainty of measurement equal to  $\pm 0.05$ , the calibration certificate of this reference thermometer is included in appendix B. All the twelve thermocouples used for this work were calibrated using this reference thermometer at three reference points:  $0^{\circ}\text{C}$ , ambient temperature which was around  $23^{\circ}\text{C}$  and  $40^{\circ}\text{C}$  using a heater with a magnetic stirring device to keep the temperature constant. All the readings of the thermocouples had an error of  $\pm 0.2^{\circ}\text{C}$ .

All the thermocouples calibration tests for each cold and hot side are shown in the tables below:

Table B.1 Cold side for air temperature at about ( $23^{\circ}\text{C}$ )

Ref (Temp)	Time (s)	TC-OUT-1 Diff.	TC-OUT-2 Diff.	TC-OUT-3 Diff.	TC-IN-1 Diff.	TC-IN-2 Diff.	TC-IN-3 Diff.
23.26	450	0.58	0.17	0.31	-0.34	0.24	0.57
23.24	160	0.59	0.17	0.31	-0.30	0.23	0.56
23.205	120	0.63	0.19	0.30	-0.28	0.24	0.56
Average		+0.6	+0.18	+0.31	-0.31	+0.24	+0.56

Table B.2 Cold side for  $40^{\circ}\text{C}$  temperature

Ref (Temp)	Time (s)	TC-OUT-1 Diff.	TC-OUT-2 Diff.	TC-OUT-3 Diff.	TC-IN-1 Diff.	TC-IN-2 Diff.	TC-IN-3 Diff.
40.125	130	0.41	0.26	0.21	0.04	0.13	0.37
40.09	230	0.42	0.27	0.22	0.05	0.13	0.37
39.86	190	0.42	0.27	0.22	0.05	0.15	0.36
		+0.42	+0.27	+0.22	+0.05	+0.14	+0.37

Table B.3 Cold side for  $0.0^{\circ}\text{C}$  temperature

Ref (Temp)	Time (s)	TC-OUT-1 Diff.	TC-OUT-2 Diff.	TC-OUT-3 Diff.	TC-IN-1 Diff.	TC-IN-2 Diff.	TC-IN-3 Diff.
0.28	120	0.47	0.33	0.18	-0.14	0.15	0.43
0.25	1000	0.47	0.36	0.23	-0.08	0.14	0.40
0.28	320	0.46	0.35	0.22	-0.08	0.12	0.37
		+0.47	+0.36	+0.23	-0.08	+0.14	+0.4

Table B.4 Average values

Average values for the three temperatures at 0°C, 23°C and 40°C					
TC-OUT-1	TC-OUT-2	TC-OUT-3	TC-IN-1	TC-IN-2	TC-IN-3
+0.5	+0.27	+0.25	-0.11	+0.17	+0.44

Therefore as it can be seen from the tables above and the average value of the thermocouples readings, all the thermocouples have an uncertainty of  $\pm 0.2^\circ\text{C}$ .

Table B.5 Hot side for air temperature at about (23°C)

Ref (Temp)	Time (s)	TH-OUT-1 Diff.	TH-OUT-2 Diff.	TH-IN-1 Diff.	TH-IN-2 Diff.	TH-IN-3 Diff.	TH-OUT-3 Diff.
23.26	450	0.26	0.58	0.12	-0.55	-0.02	0.20
23.24	160	0.23	0.46	0.17	-0.49	-0.11	0.16
23.205	120	0.24	0.27	0.44	-0.56	-0.12	0.16
		+0.24	+0.52	+0.14	-0.52	-0.09	+0.18

Table B.6 Hot side for 40°C temperature

Ref (Temp)	Time (s)	TH-OUT-1 Diff.	TH-OUT-2 Diff.	TH-IN-1 Diff.	TH-IN-2 Diff.	TH-IN-3 Diff.	TH-OUT-3 Diff.
40.125	130	0.44	0.36	0.16	-0.21	0.02	0.16
40.09	230	0.44	0.37	0.17	-0.21	0.02	0.16
39.86	190	0.44	0.36	0.17	-0.21	0.02	0.15
		+0.44	+0.36	+0.17	-0.21	+0.02	+0.16

Table B.7 Hot side for about 0.0°C temperature

Ref (Temp)	Time (s)	TH-OUT-1 Diff.	TH-OUT-2 Diff.	TH-IN-1 Diff.	TH-IN-2 Diff.	TH-IN-3 Diff.	TH-OUT-3 Diff.
0.28	120	0.61	0.43	-0.02	-0.33	0.21	0.50
0.25	1000	0.59	0.45	0.02	-0.28	0.22	0.44
0.28	320	0.57	0.43	0.02	-0.28	0.20	0.41
		+0.59	+0.44	+0.02	-0.3	+0.21	+0.45

Table B.8 Average values

Average values for the three temperatures at 0°C, 23°C and 40°C					
TH-OUT-1	TH-OUT-2	TH-IN-1	TH-IN-2	TH-IN-3	TH-OUT-3
+0.42	+0.44	+0.11	-0.34	-0.03	+0.26

Therefore as it can be seen from the tables above and the average value of the thermocouples readings, all the thermocouples have an uncertainty of  $\pm 0.2^{\circ}\text{C}$ .

### B.3. Calibration of the rotameter for the hot wall side.

The rotameter is a glass tube graded from zero to 30cm, and these values are corresponding to a volumetric flow rates from zero to 1.2 L/min respectively, where the polynomial equation to calculate the volumetric flow rate was provided based on the data from the rotameter test as shown in table B.9 below. This data in the table produced using the calibration of the rotameter by recording the time using stop watch and weighing the water using a digital scale for the whole rotameter measuring range.

Table B.9

Test number	Tube scale measure(cm)	Weight (g)	Time (s)	Volumetric flow rate (l/min)
1	1.1	1168.6	407	0.172
2	7.1	1795.7	313	0.344
3	12.2	1980	226	0.526
4	17.45	2261.2	208	0.652
5	22.6	3246.9	230	0.847
6	30	4276.8	230	1.116

From the data provided in table B.9 the polynomial equation to calculate the volume flow rate for this rotameter has been produced as below:

$$Q_h = 1.628 \times 10^{-4} Q_o^2 + 2.738 \times 10^{-2} Q_o + 0.1448$$

The uncertainty of this flow meter will be equal to the minimum scale reading divided by two, which will be equal to about  $\pm 0.02$  l/min.

### B.4. Calibration of Rotameter for the cold side.

For the rotameter of the cold side it has been tested using the same procedure above for the hot side and the results are as follows:

Table B.10

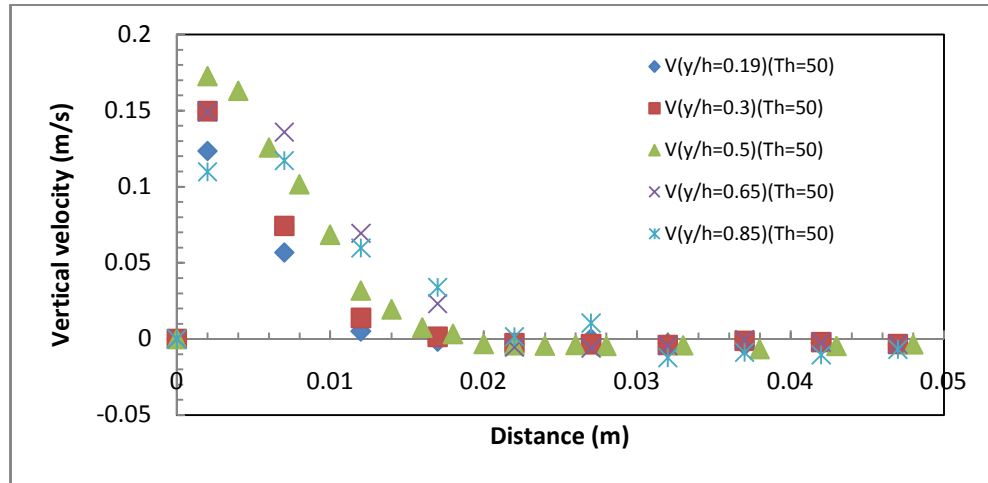
Test number	Tube scale measure(cm)	Weight (g)	Time (s)	Volumetric flow rate (l/min)
1	2.4	1168.6	407	0.172
2	6.9	1795.7	313	0.344
3	11	1980	226	0.526
4	14.65	2261.2	208	0.652
5	17.6	3246.9	230	0.847
6	23.1	4276.8	230	1.116

From the data provided in table B.10 the polynomial equation to calculate the volume flow rate for this rotameter has been produced as below:

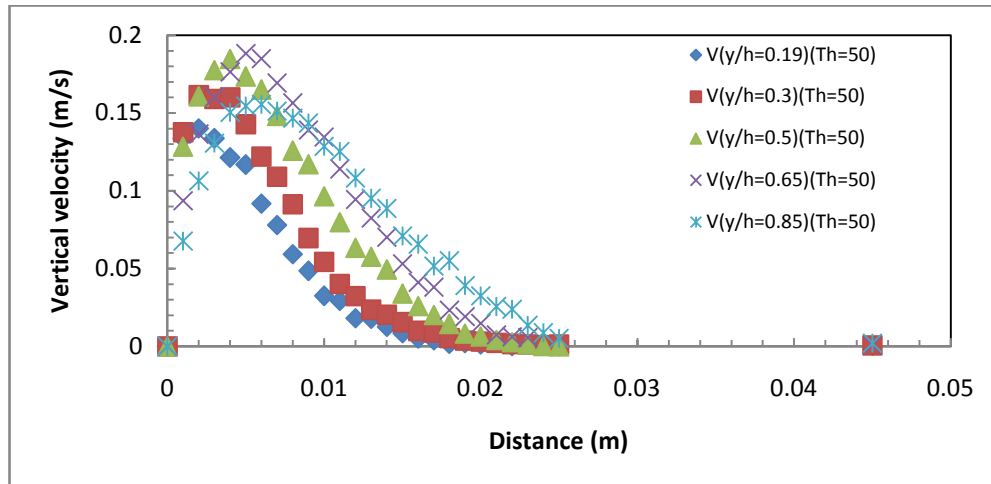
$$Q_c = 4.975 \times 10^{-4} Q_o^2 + 3.297 \times 10^{-2} Q_o + 0.0916$$

The uncertainty of this flow meter will be again equal to the minimum scale reading divided by two, which will be equal to about  $\pm 0.02$  l/min.

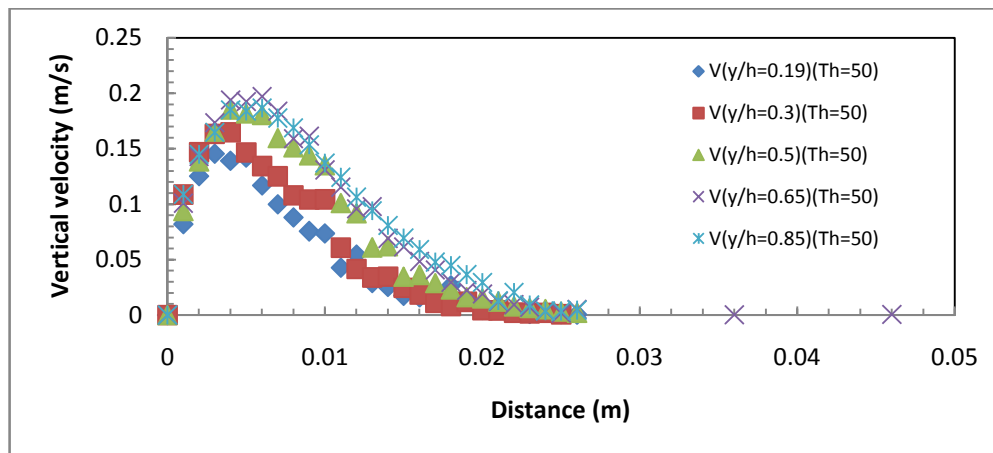
B.5. Velocity profiles for experimental results at hot wall temperatures 50°C, 55°C, 65°C and 70°C.



(a)

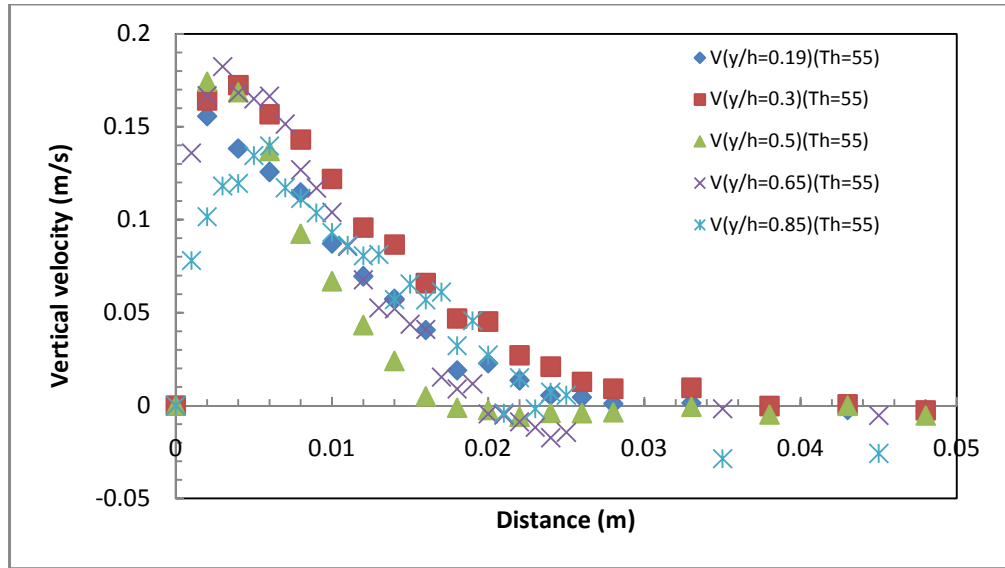


(b)

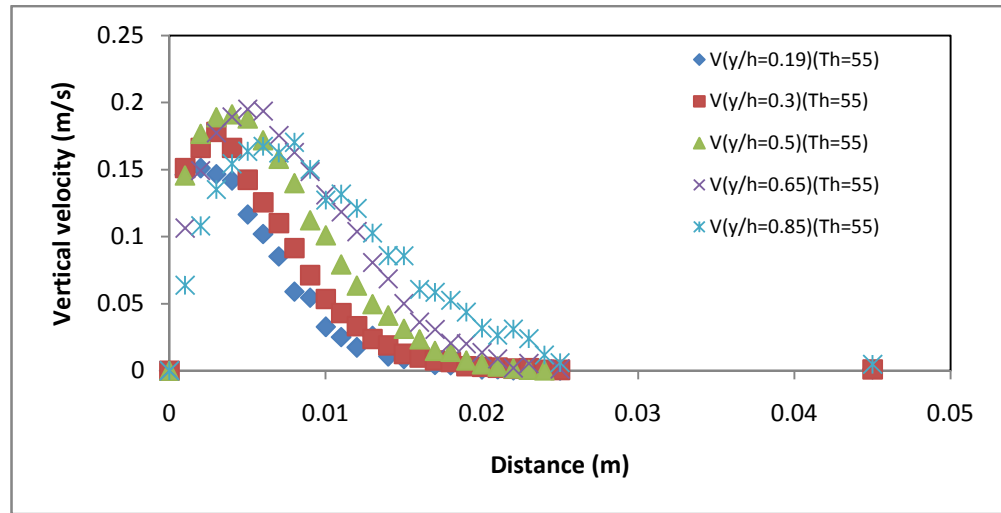


(c)

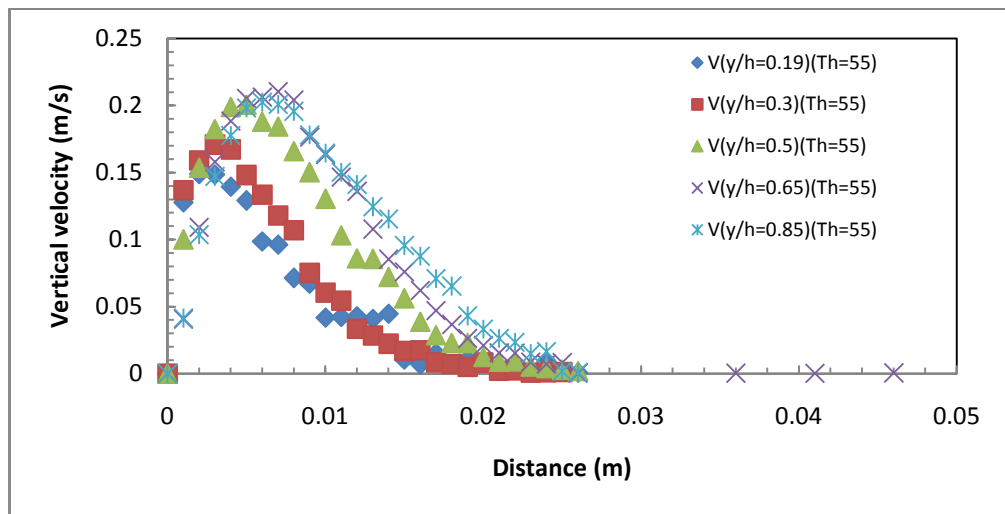
Figure B-2 Velocity profiles for aspect ratios a) 2.0, b) 1.0 and b) 0.5.



(a)

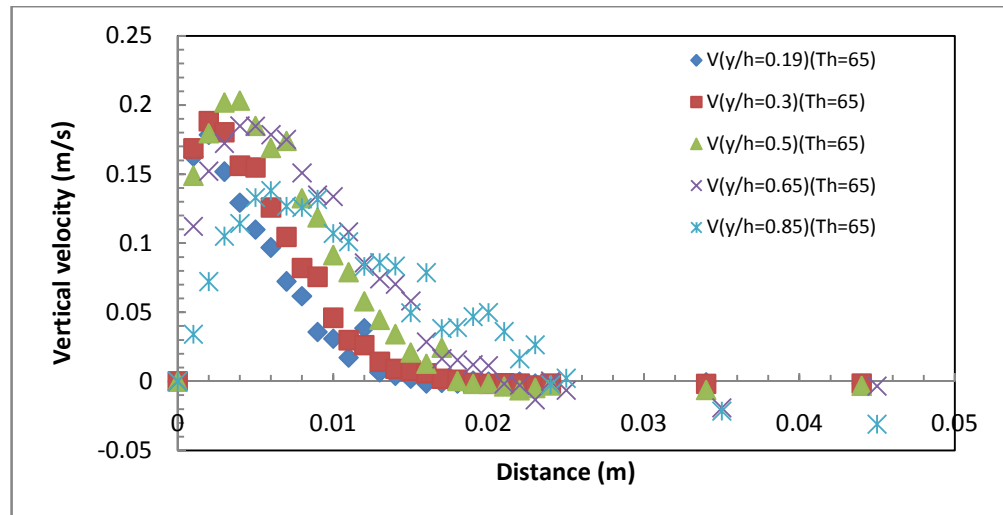


(b)

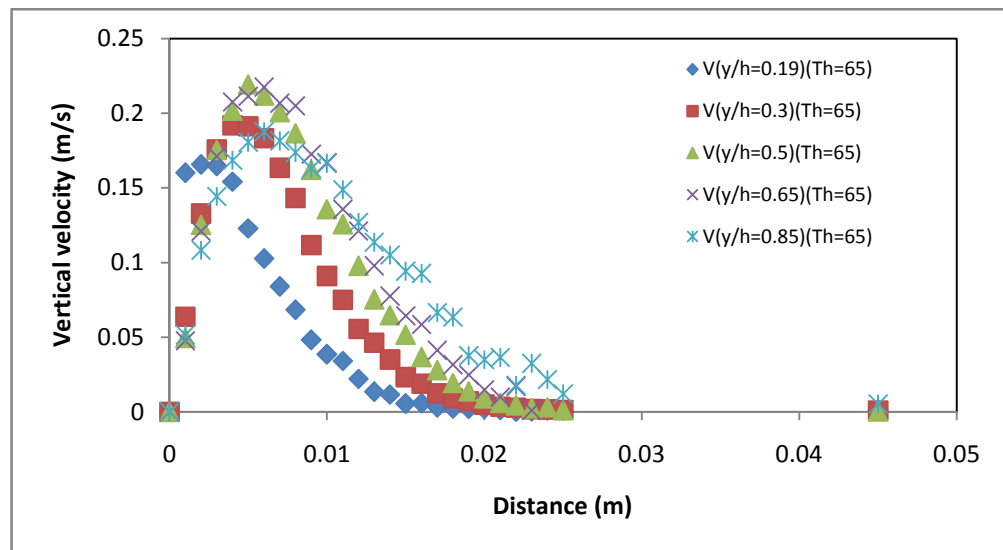


(c)

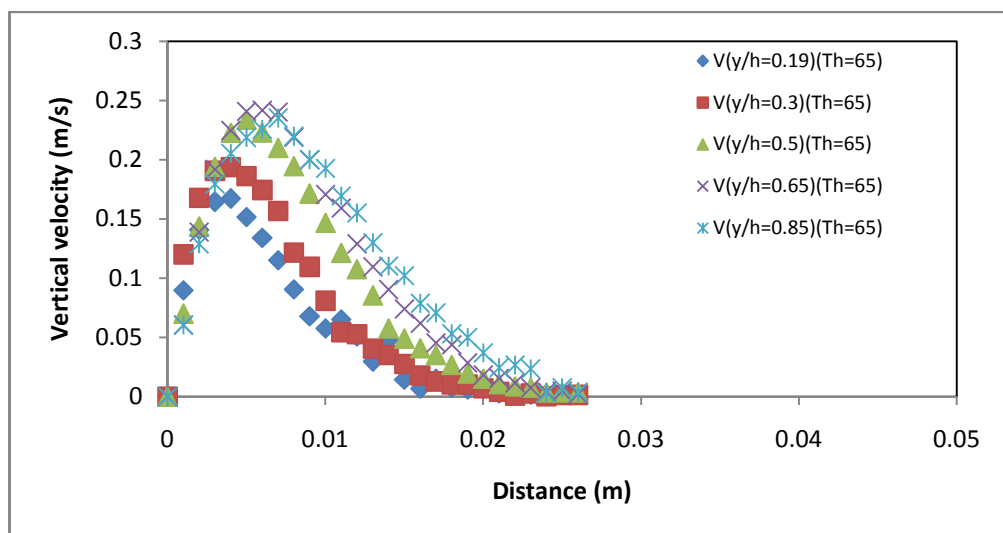
Figure B-3 Velocity profiles for aspect ratios a) 2.0, b) 1.0 and b) 0.5.



(a)



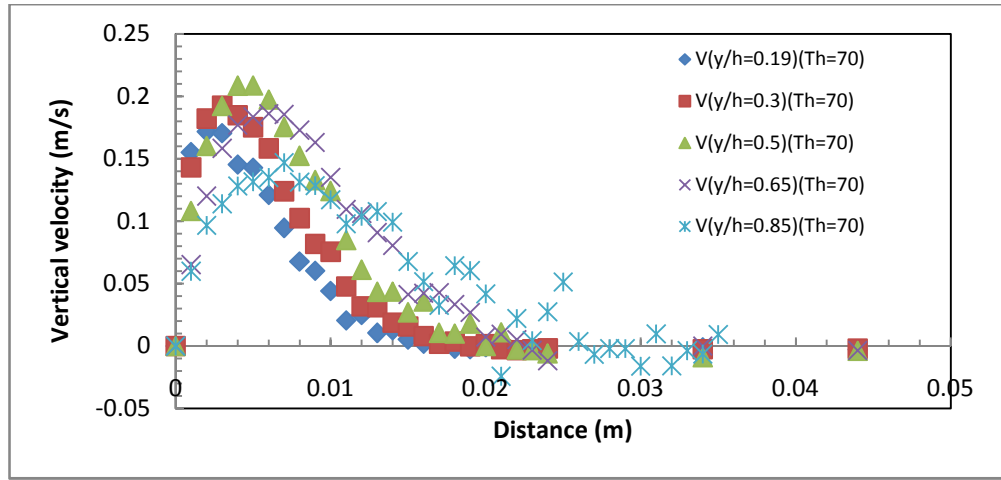
(b)



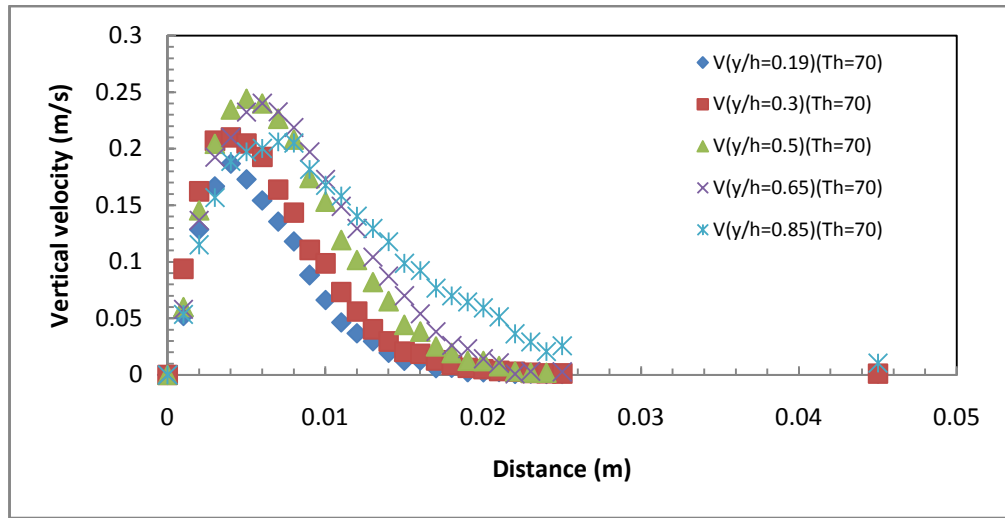
(c)

Figure B-4 Velocity profiles for aspect ratios a) 2.0, b) 1.0 and b) 0.5.

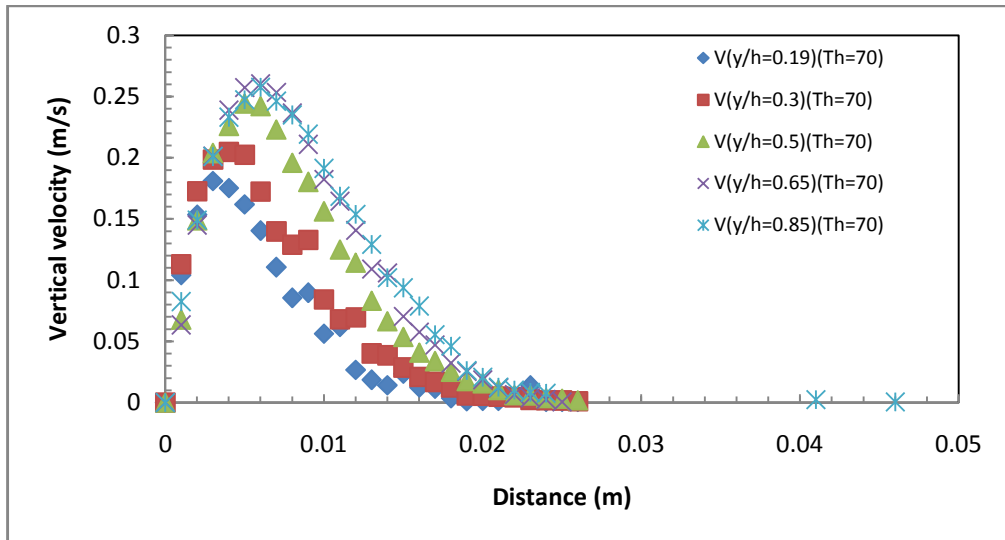




(a)



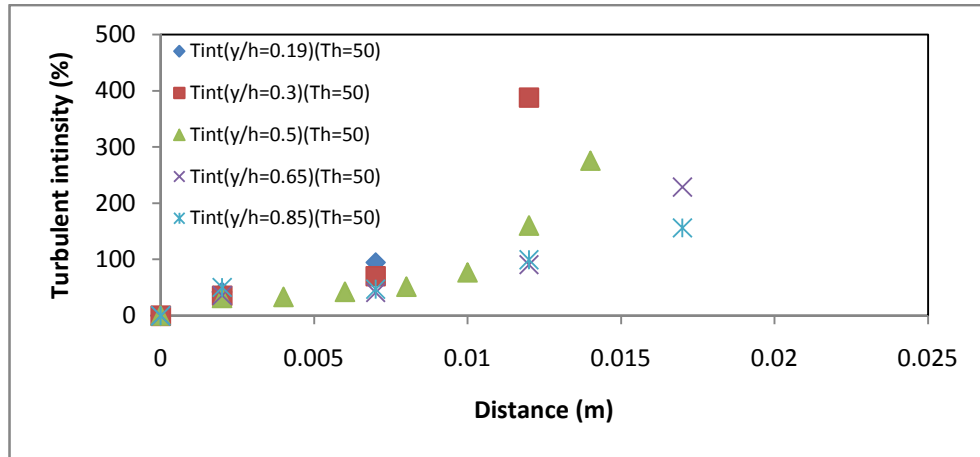
(b)



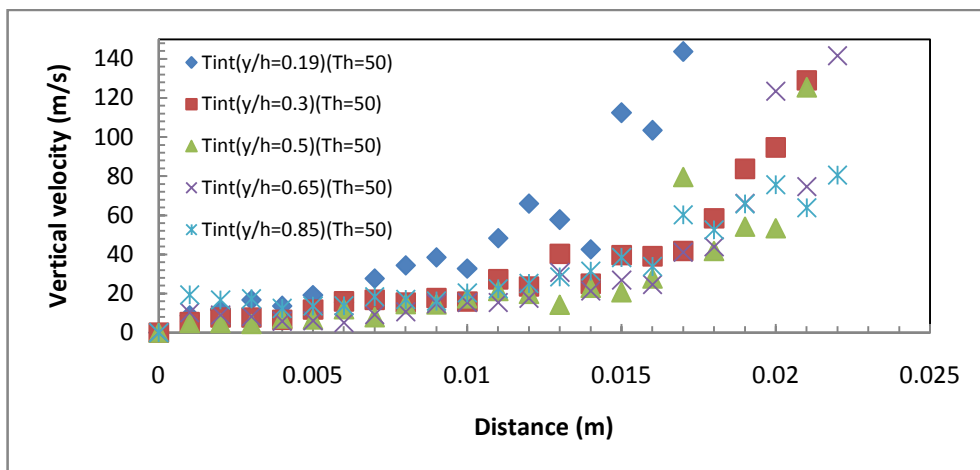
(c)

Figure B-5 Velocity profiles for aspect ratios a) 2.0, b) 1.0 and b) 0.5.

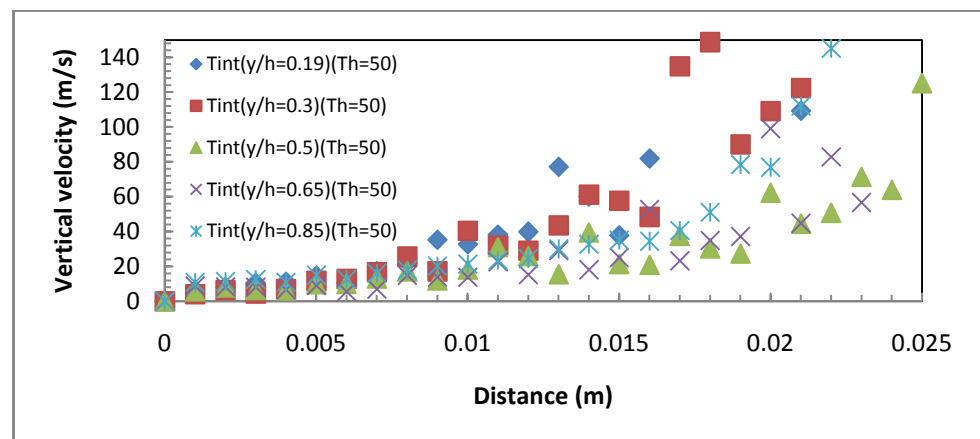
B.6. Turbulence intensity profiles for experimental results at hot wall temperatures 50°C, 55°C, 65°C and 70°C.



(a)

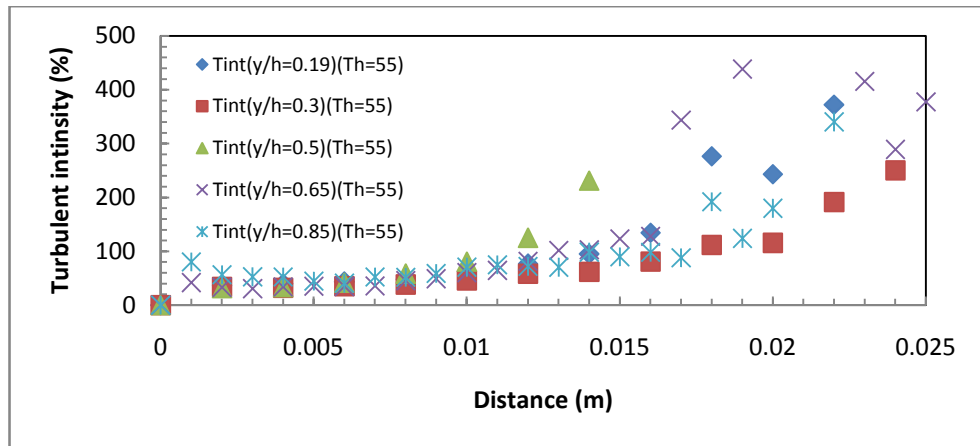


(b)

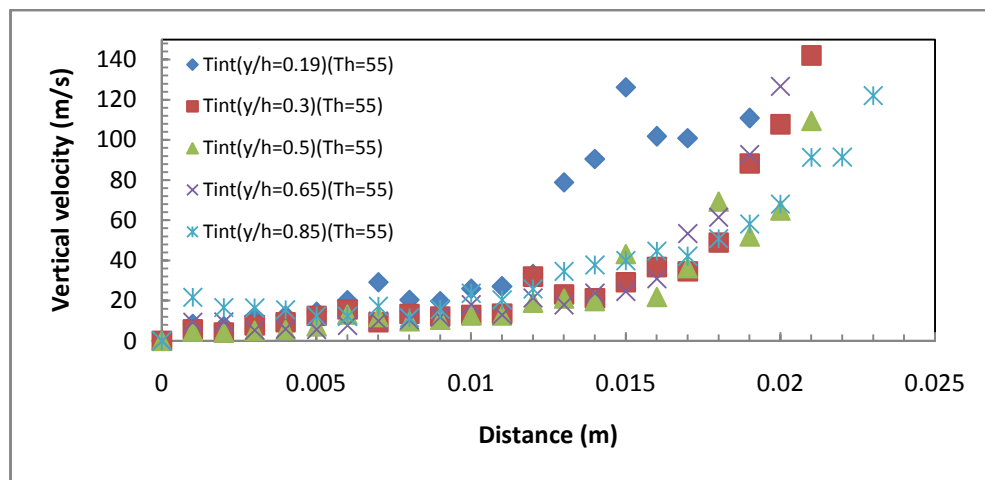


(c)

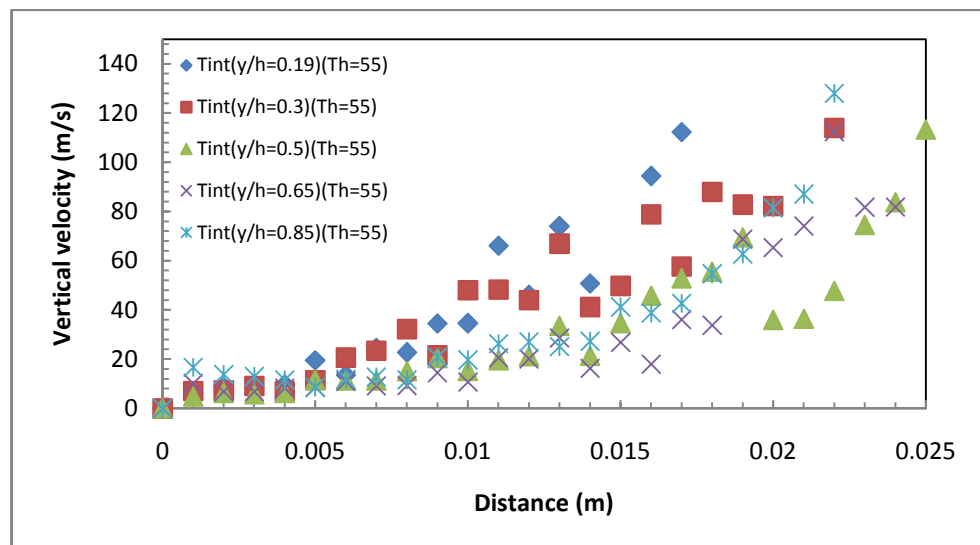
Figure B-6 Turbulent intensity profiles for aspect ratio a) 2.0, b) 1.0 and c) 0.5.



(a)

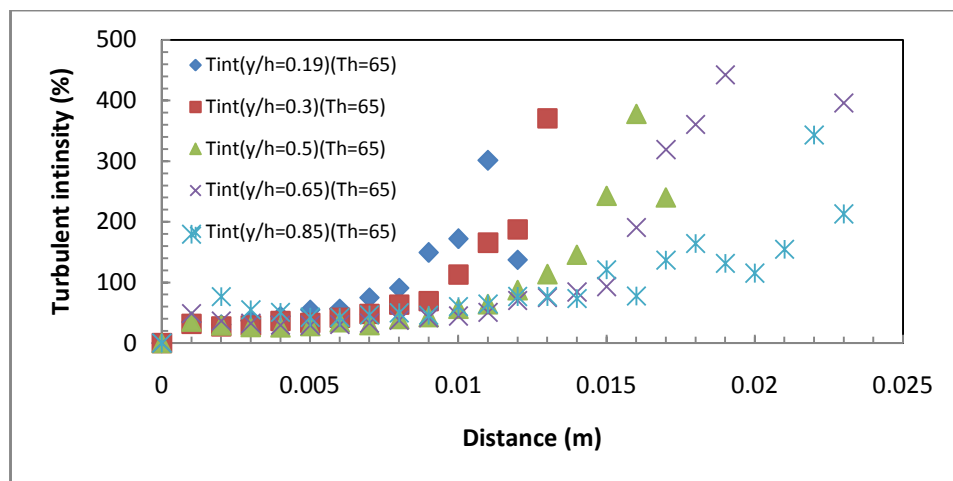


(b)

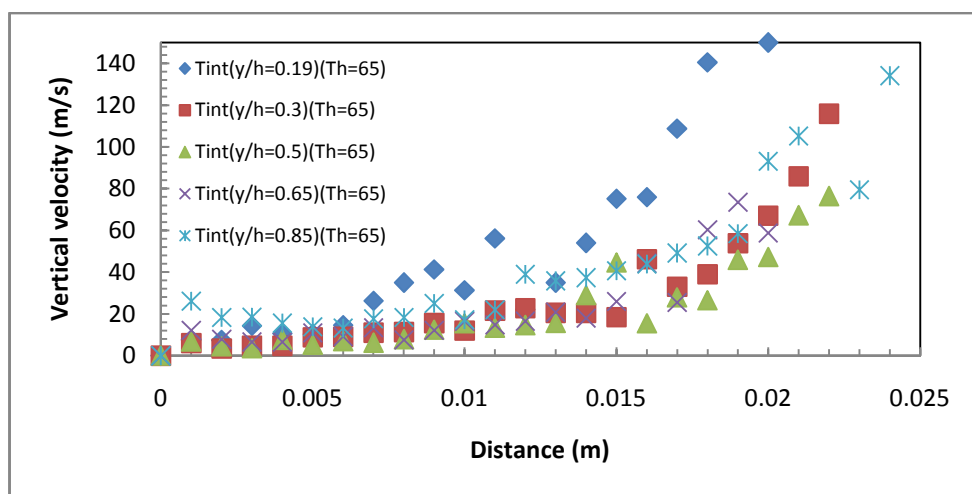


(c)

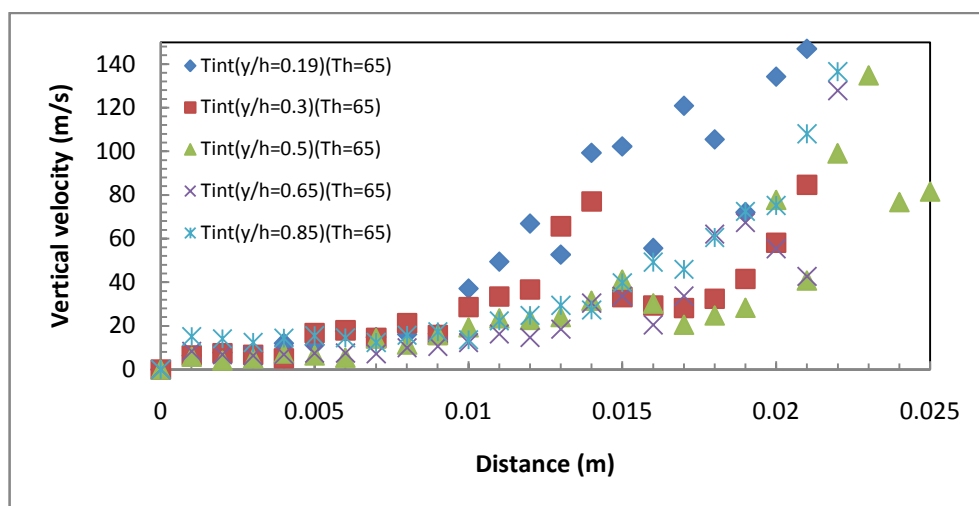
Figure B-7 Turbulent intensity profiles for aspect ratio a) 2.0, b) 1.0 and c) 0.5.



(a)

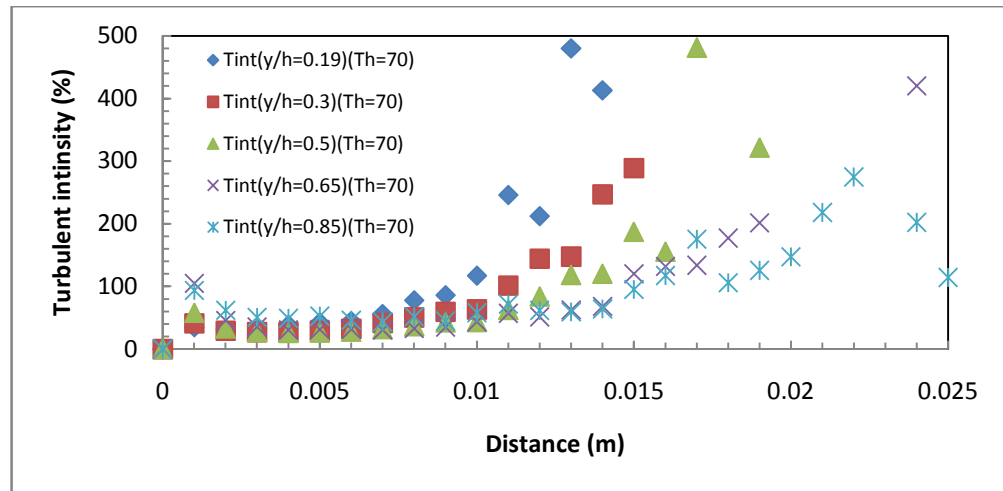


(b)

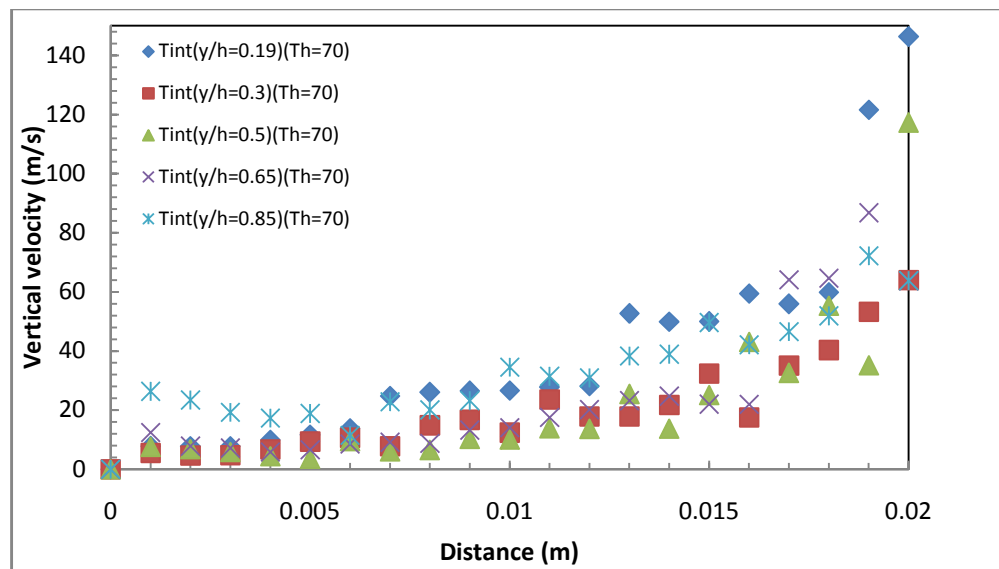


(c)

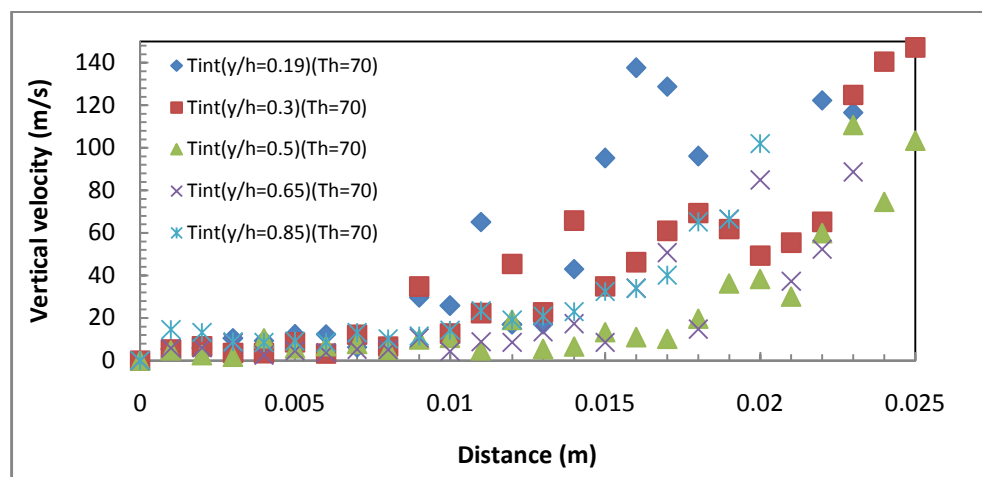
Figure B-8 Turbulent intensity profiles for aspect ratio a) 2.0, b) 1.0 and c) 0.5.



(a)



(b)

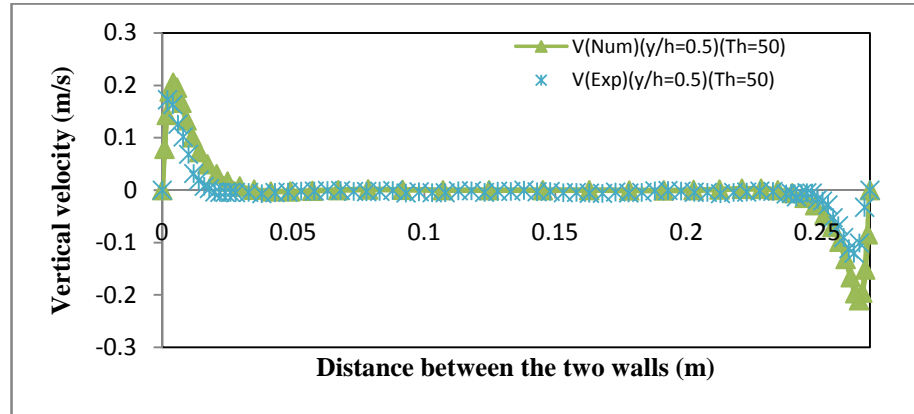


(c)

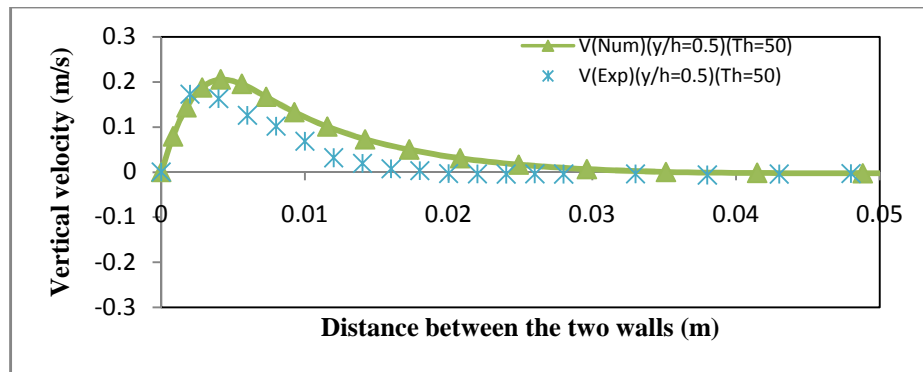
Figure B-9 Turbulent intensity profiles for aspect ratio a) 2.0, b) 1.0 and c) 0.5.

## Appendix-C

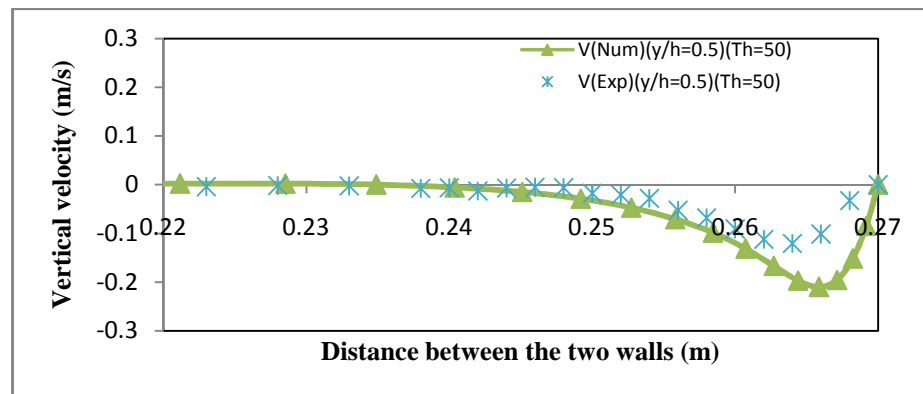
### C.1 Comparison of velocity profiles between experimental and numerical results for aspect ratio 2.0.



(a)

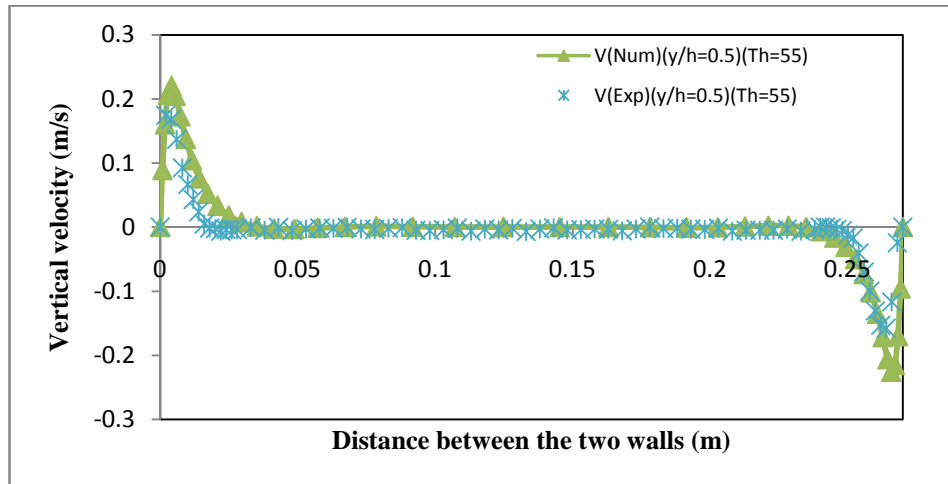


(b)

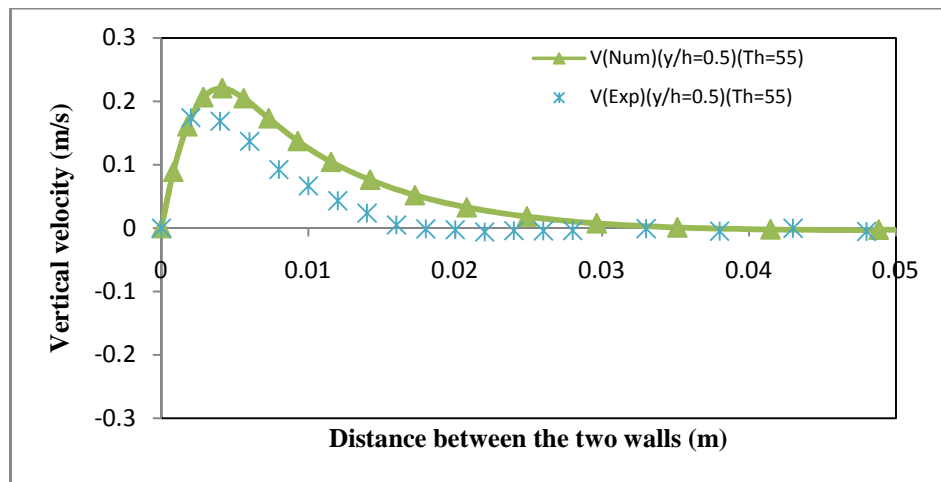


(c)

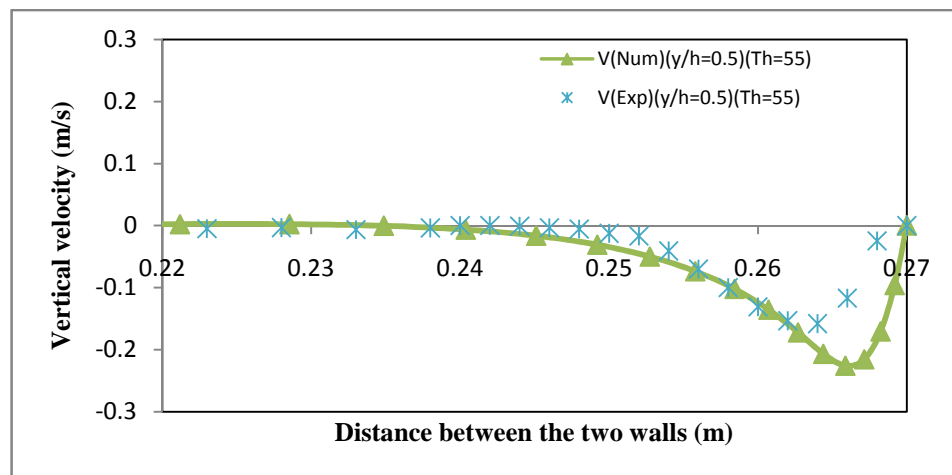
Figure C-1 Comparison of velocity profiles between experimental and numerical results for aspect ratio 2.0 and hot wall temperature 50 °C a) between the two walls b) near the hot side c) near the cold side



(a)

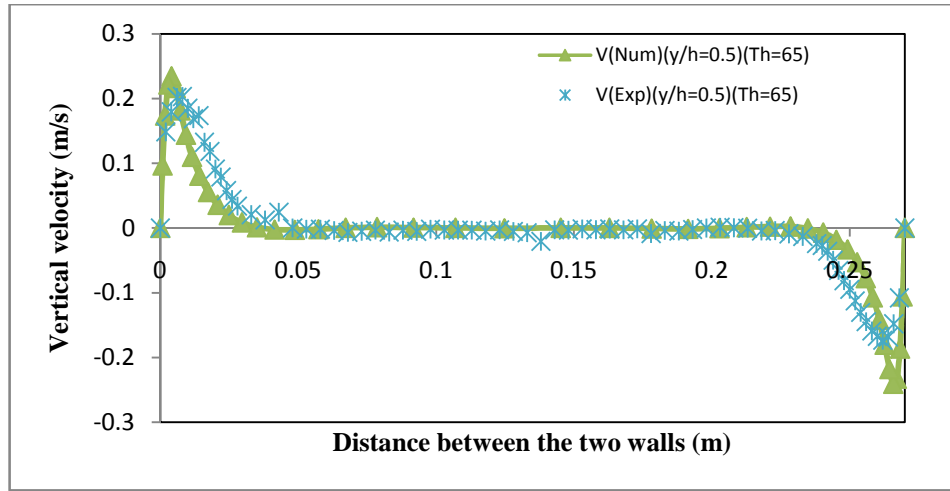


(b)

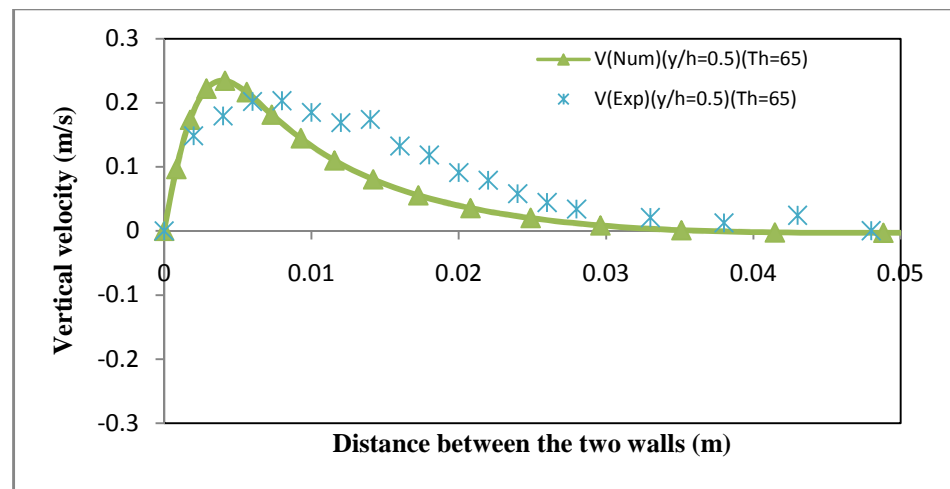


(c)

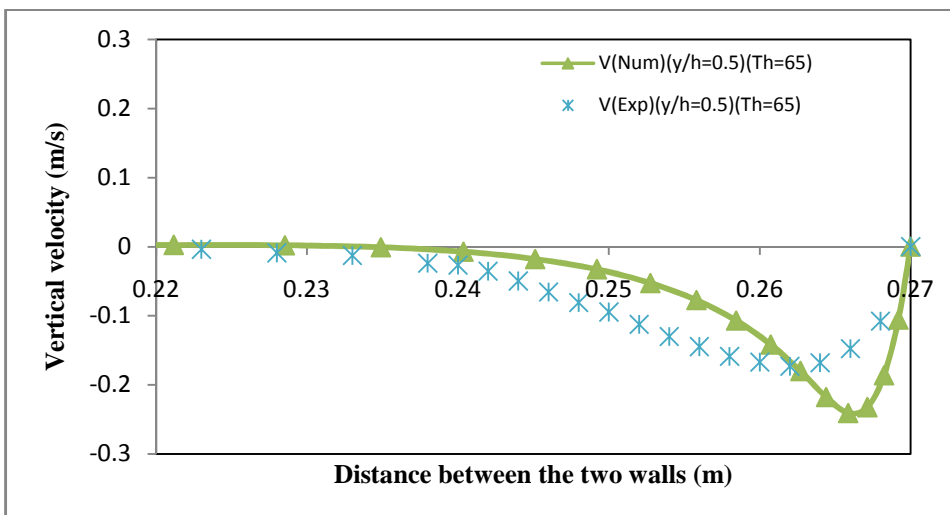
Figure C-2 Comparison of velocity profiles between experimental and numerical results for aspect ratio 2.0 and hot wall temperature 55 °C a) between the two walls b) near the hot side c) near the cold side



(a)



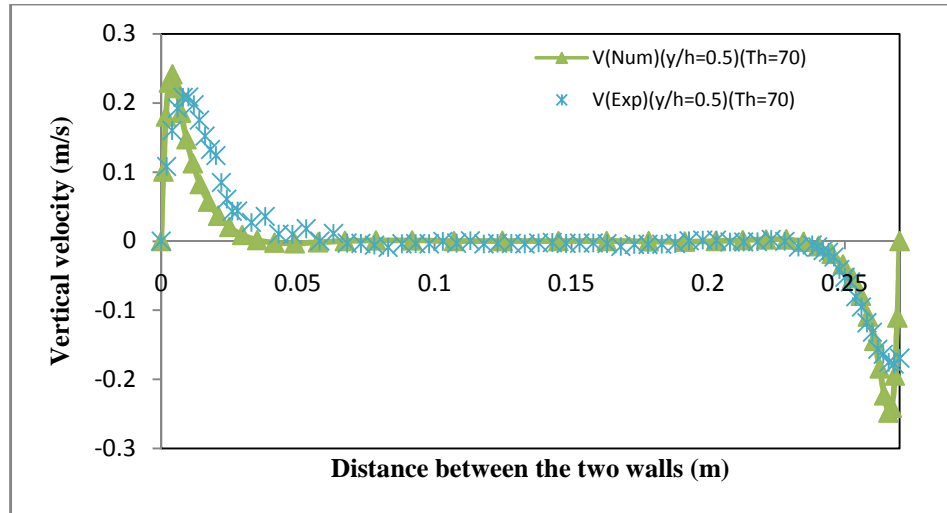
(b)



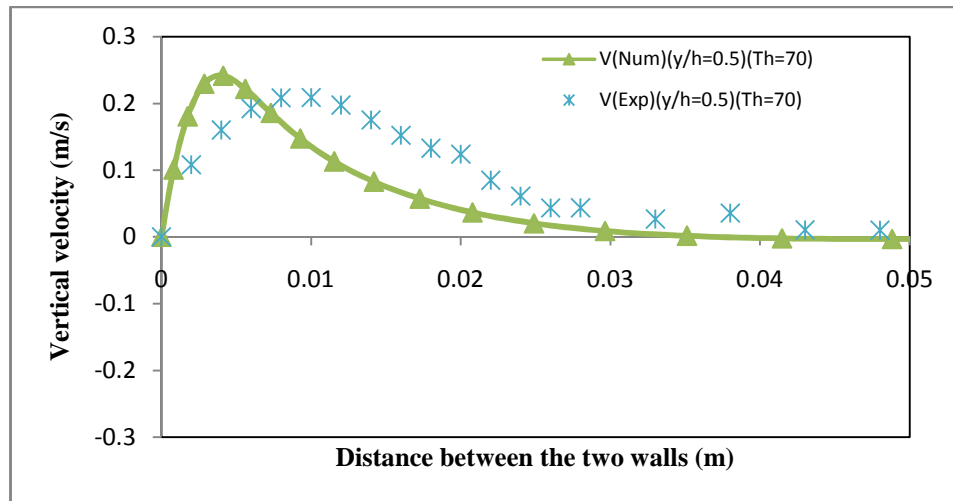
(c)

Figure C-3 Comparison of velocity profiles between experimental and numerical results for aspect ratio 2.0 and hot wall temperature 65 °C a) between the two walls b) near the hot side c) near the cold side

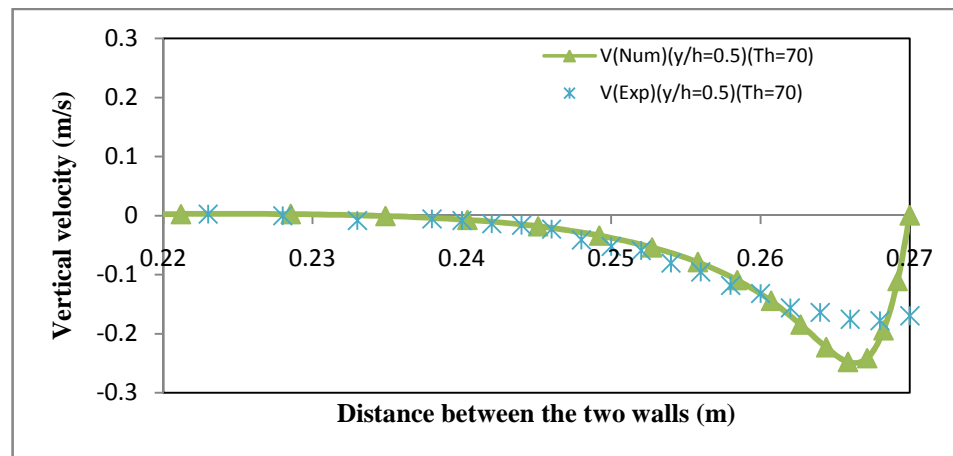




(a)



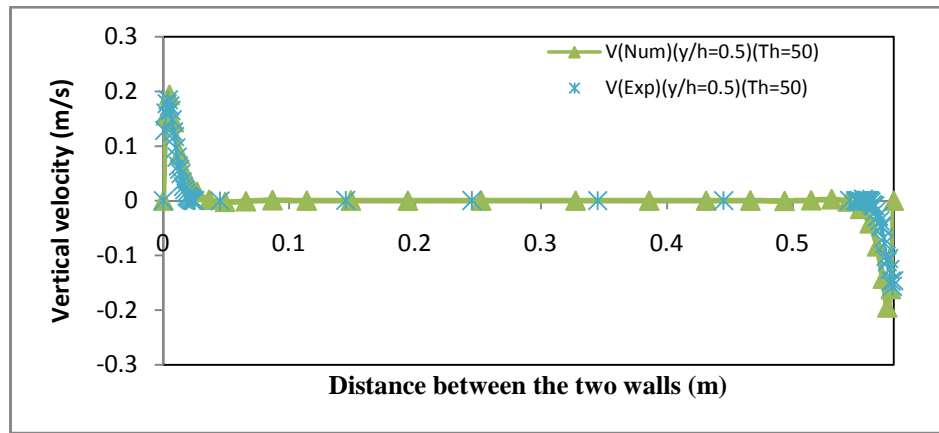
(b)



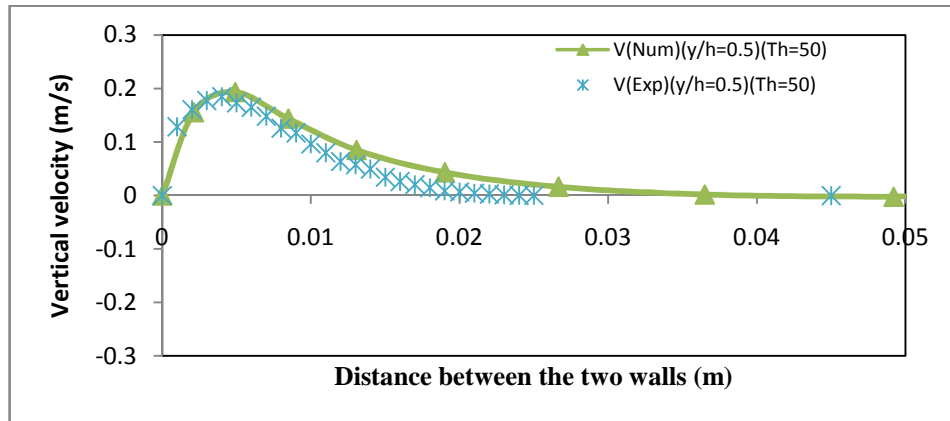
(c)

Figure C-4 Comparison of velocity profiles between experimental and numerical results for aspect ratio 2.0 and hot wall temperature 70 °C a) between the two walls b) near the hot side c) near the cold side

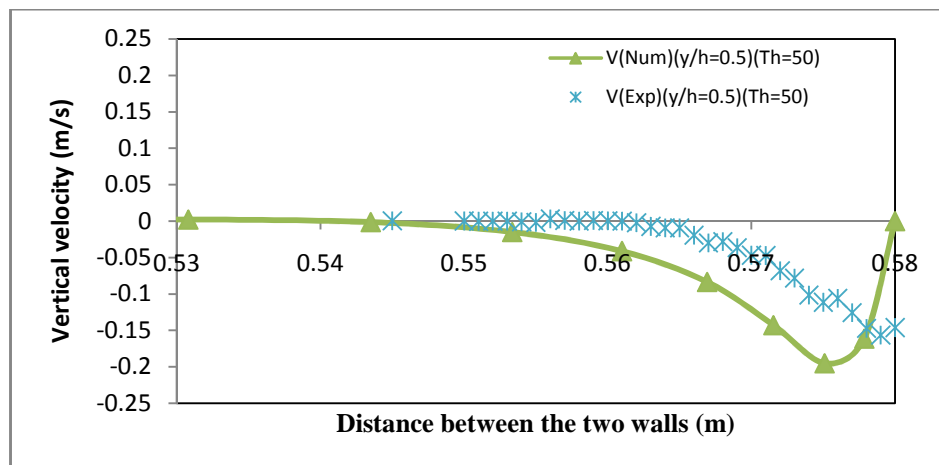
## C.2 Comparison of velocity profiles between experimental and numerical results for aspect ratio 1.0.



(a)

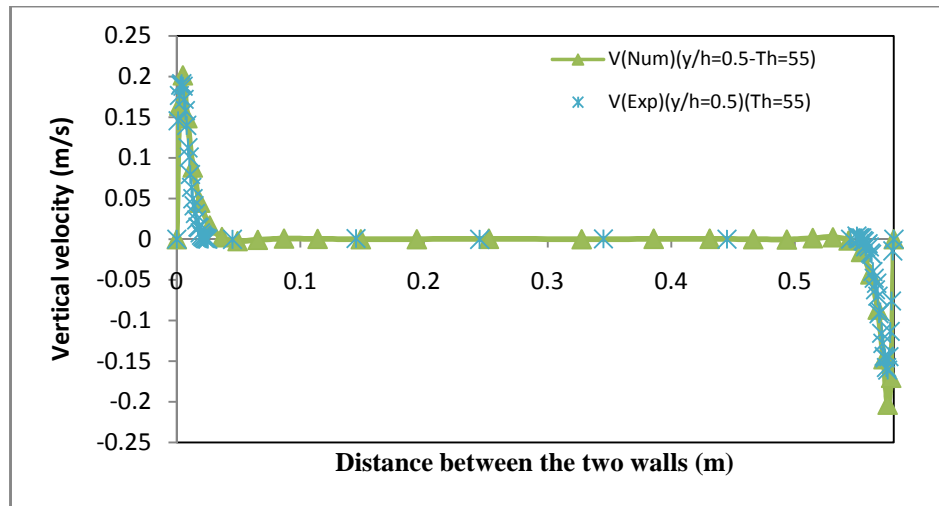


(b)

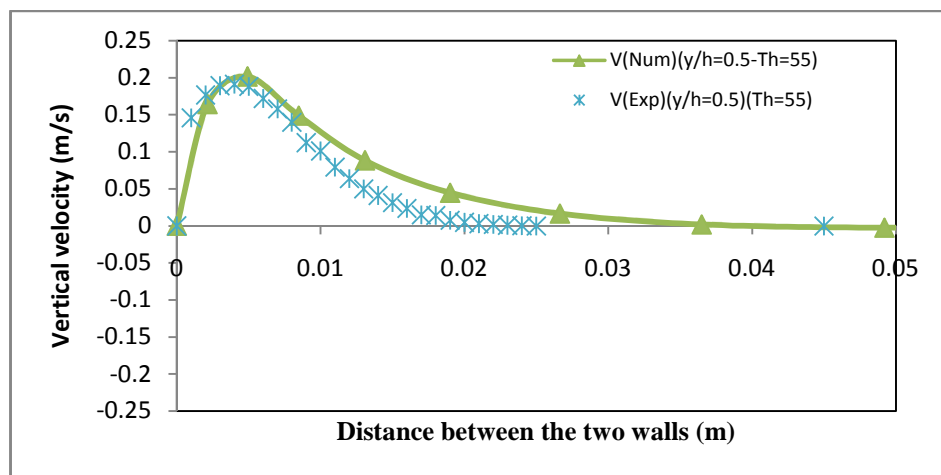


(c)

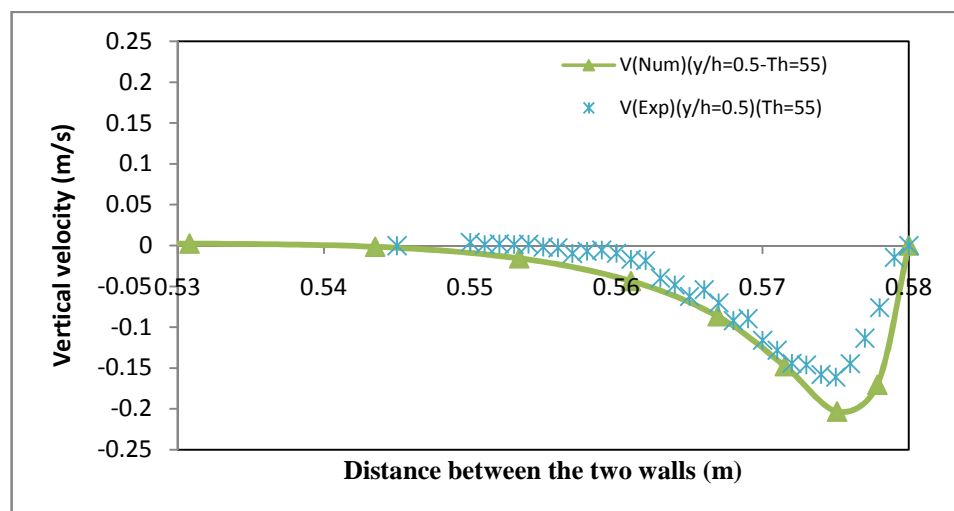
Figure C-5 Comparison of velocity profiles between experimental and numerical results for aspect ratio 1.0 and hot wall temperature 50 °C a) between the two walls b) near the hot side c) near the cold side



(a)

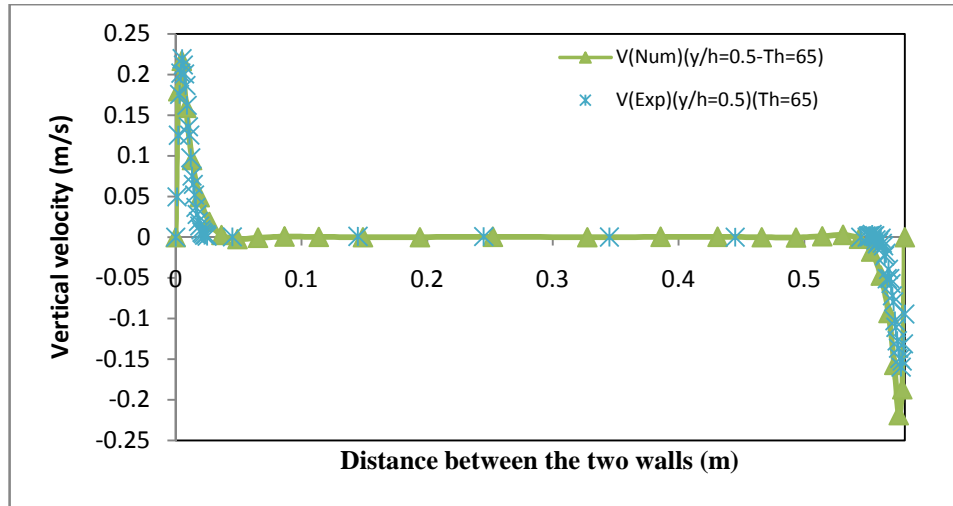


(b)

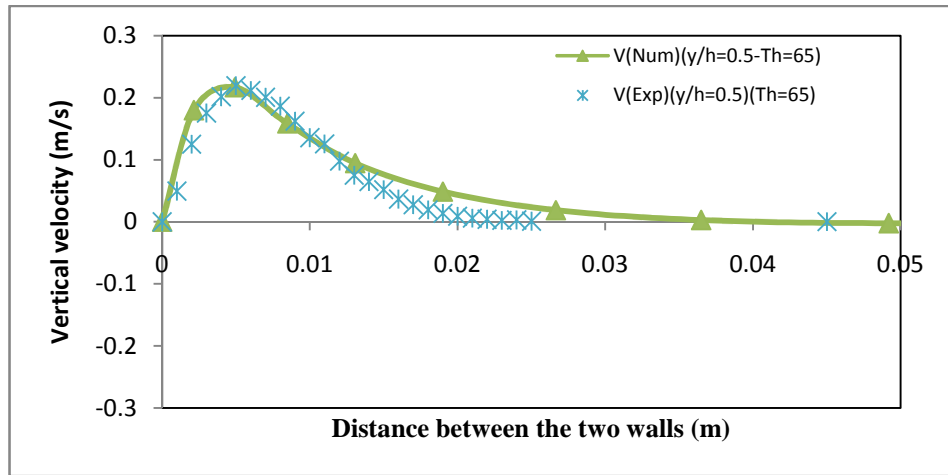


(c)

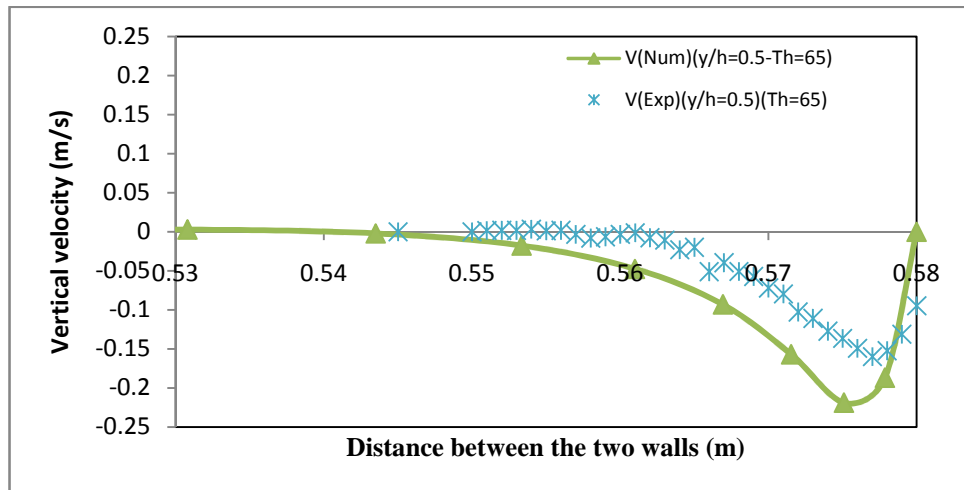
Figure C-6 Comparison of velocity profiles between experimental and numerical results for aspect ratio 1.0 and hot wall temperature 55°C a) between the two walls b) near the hot side c) near the cold side



(a)

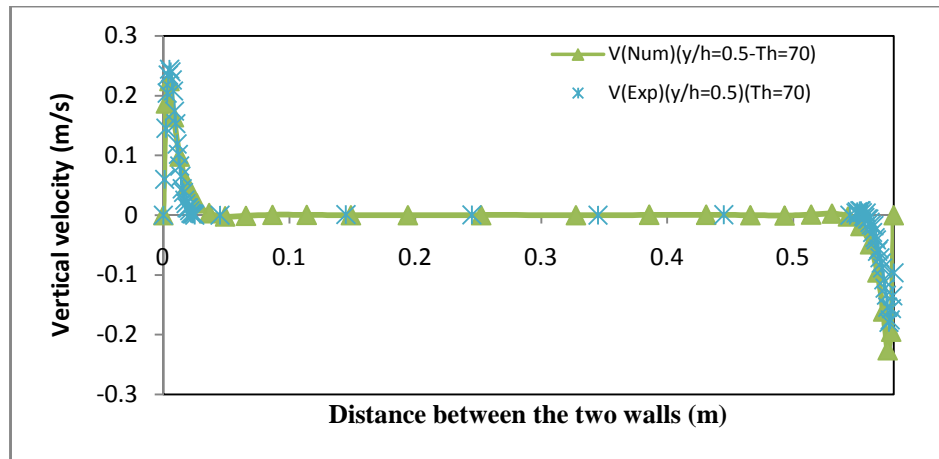


(b)

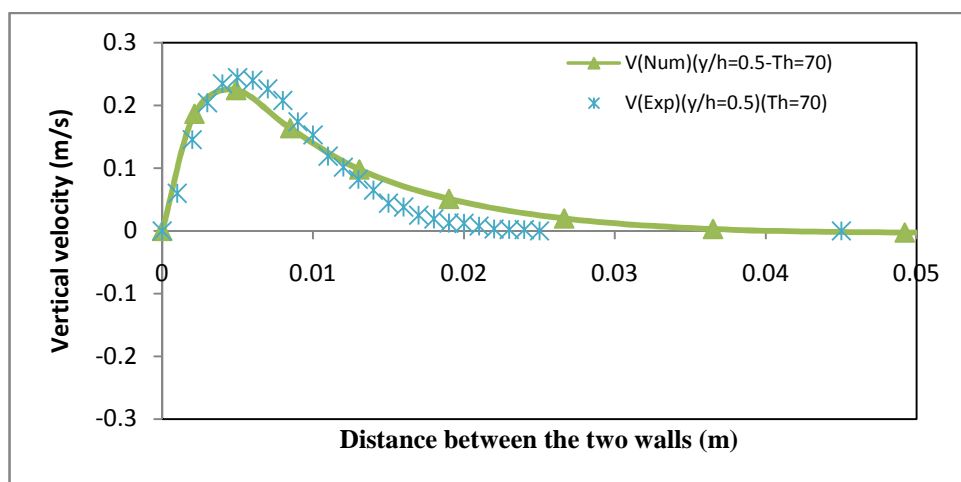


(c)

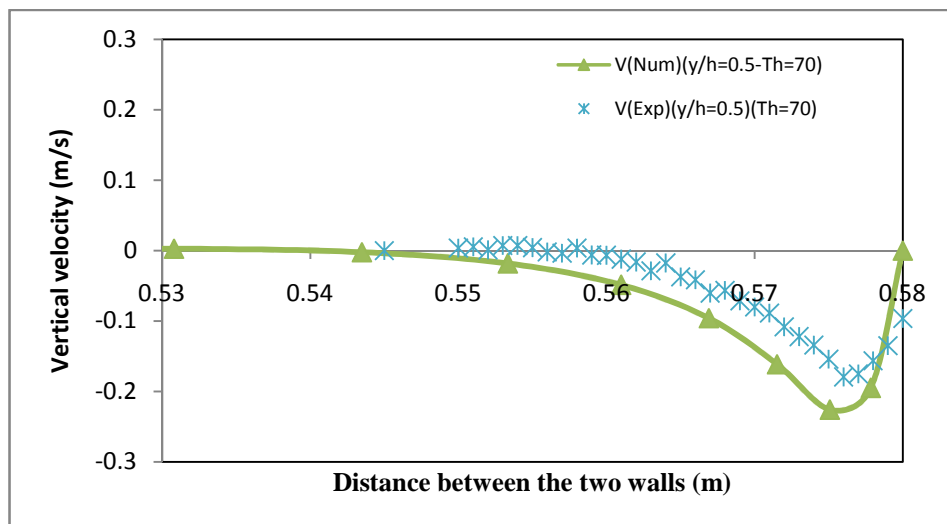
Figure C-7 Comparison of velocity profiles between experimental and numerical results for aspect ratio 1.0 and hot wall temperature 65 °C a) between the two walls b) near the hot side c) near the cold side



(a)



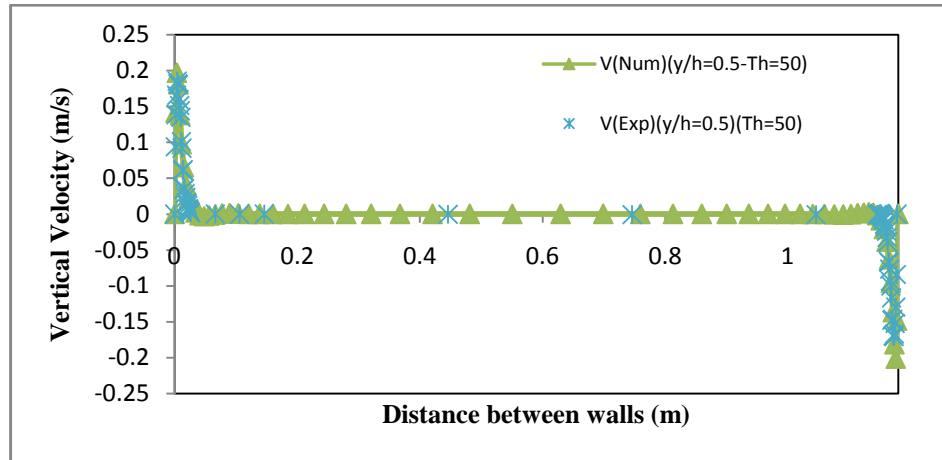
(b)



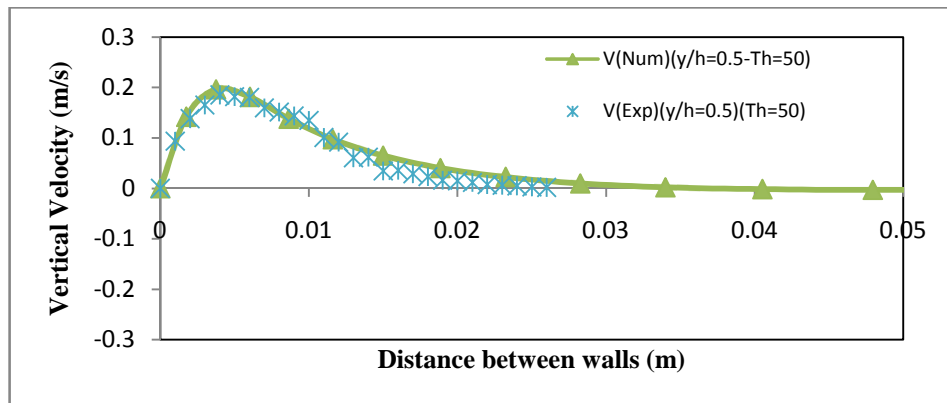
(c)

Figure C-8 Comparison of velocity profiles between experimental and numerical results for aspect ratio 1.0 and hot wall temperature 70 °C a) between the two walls b) near the hot side c) near the cold side

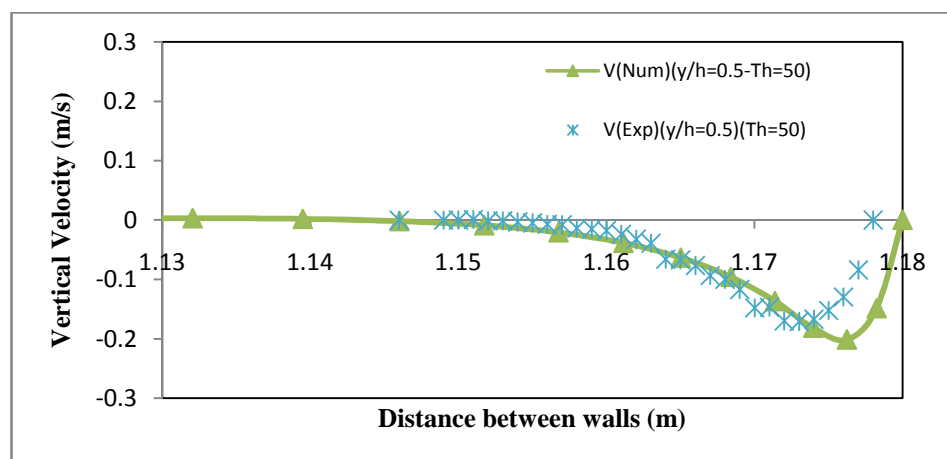
### C.3 Comparison of velocity profiles between experimental and numerical results for aspect ratio 0.5.



(a)

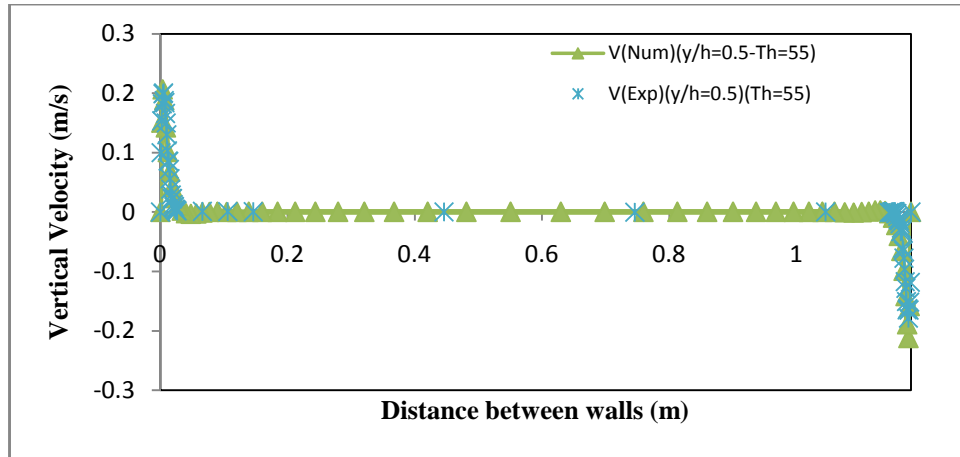


(b)

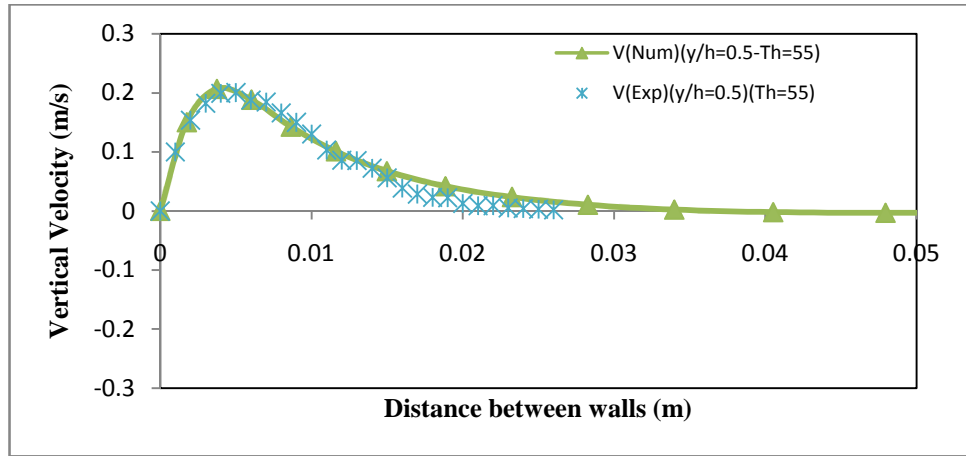


(c)

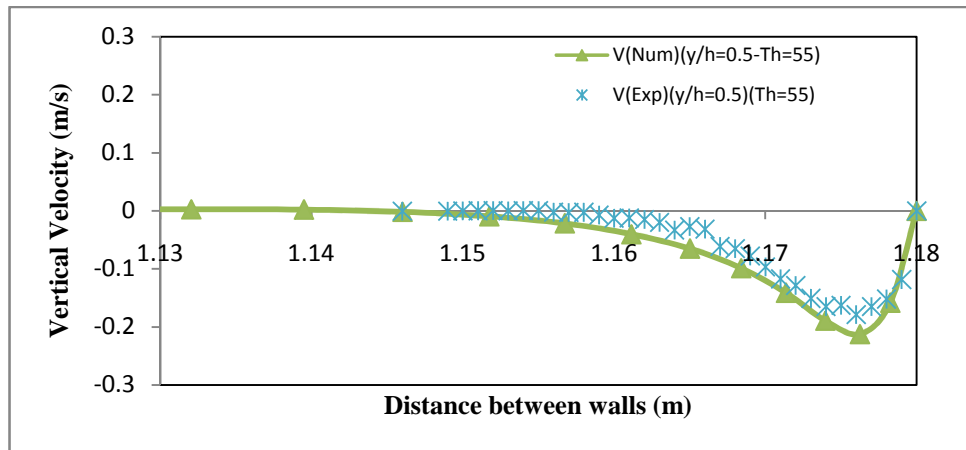
Figure C-9 Comparison of velocity profiles between experimental and numerical results for aspect ratio 0.5 and hot wall temperature 50 °C a) between the two walls b) near the hot side c) near the cold side



(a)

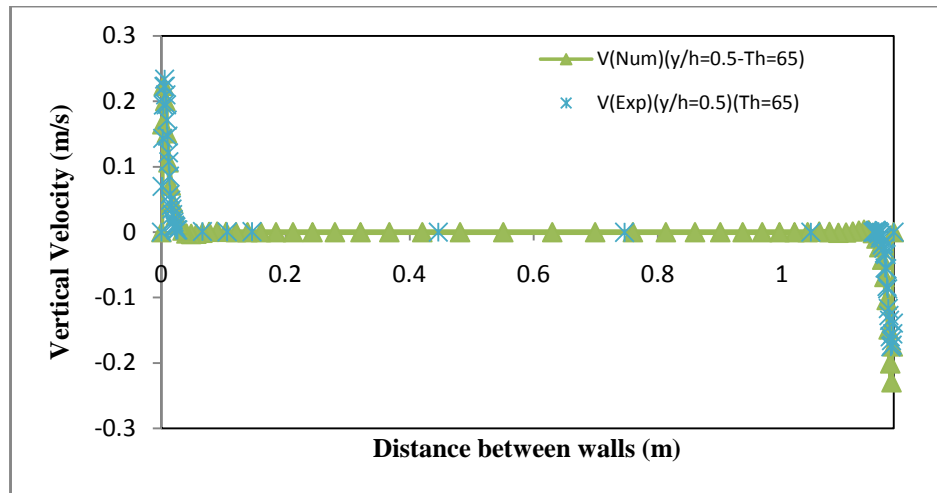


(b)

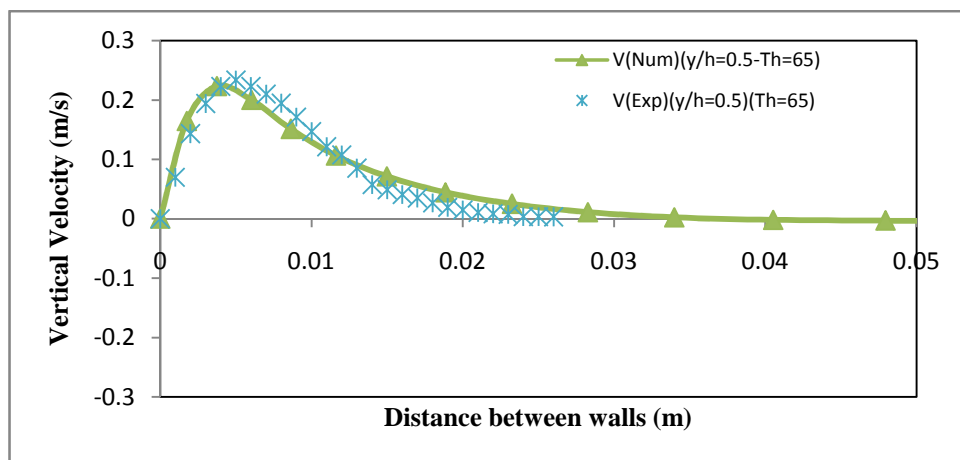


(c)

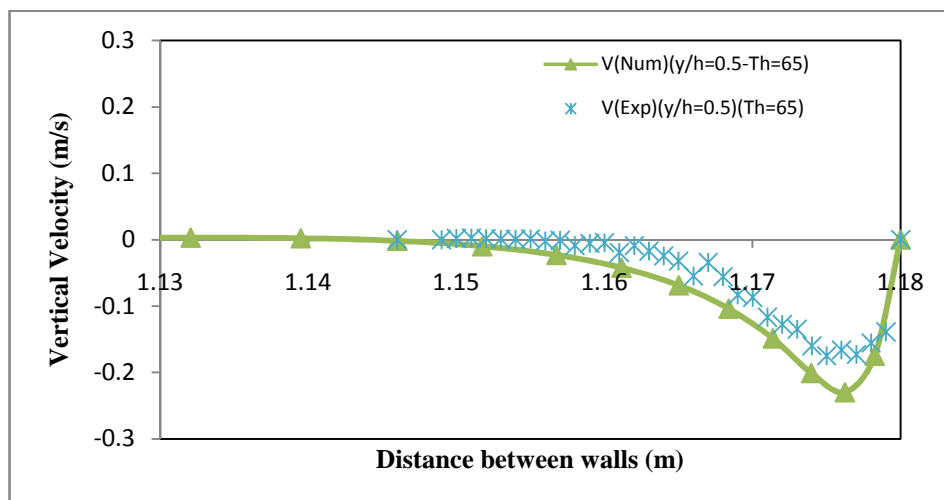
Figure C-10 Comparison of velocity profiles between experimental and numerical results for aspect ratio 0.5 and hot wall temperature 55 °C a) between the two walls b) near the hot side c) near the cold side



(a)



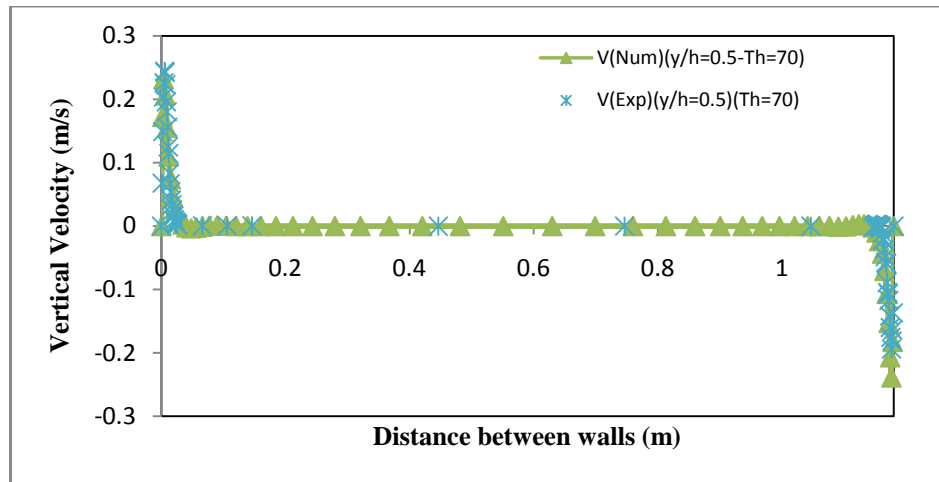
(b)



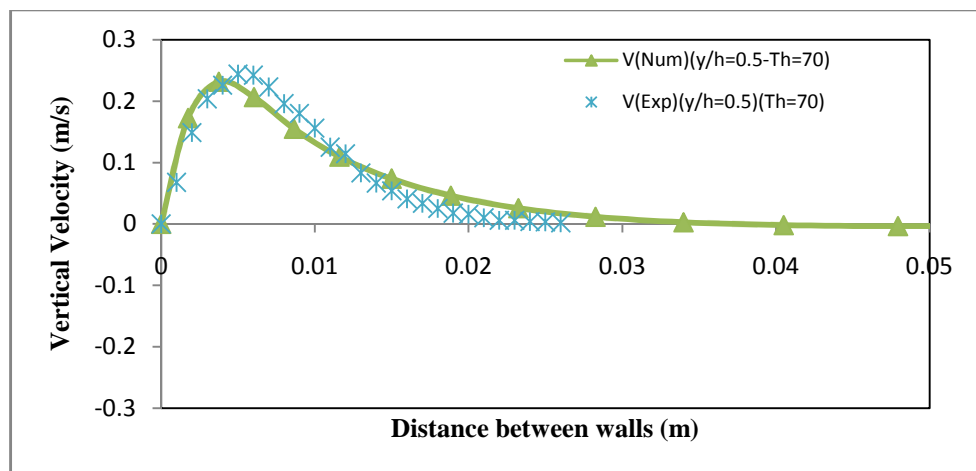
(c)

Figure C-11 Comparison of velocity profiles between experimental and numerical results for aspect ratio 0.5 and hot wall temperature 65 °C a) between the two walls b) near the hot side c) near the cold side

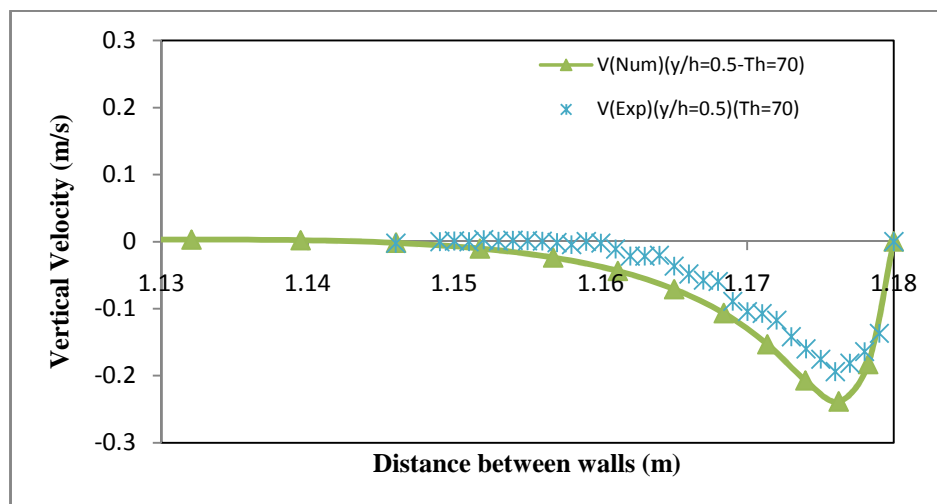




(a)



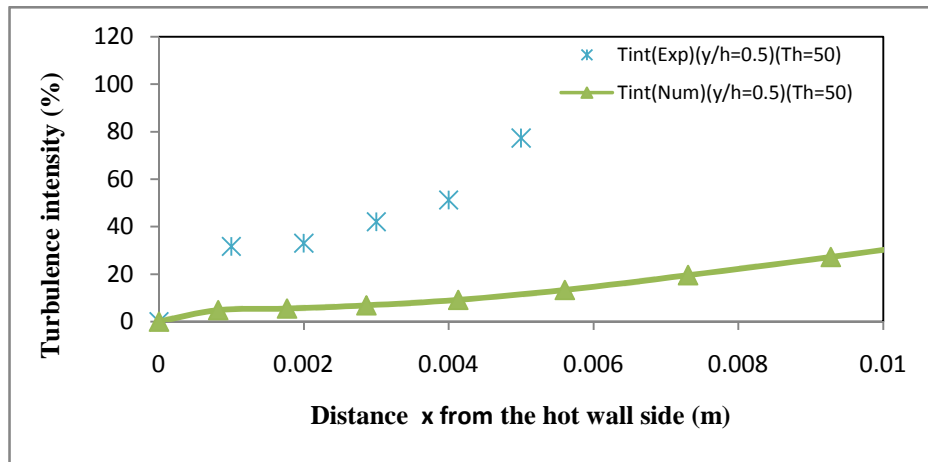
(b)



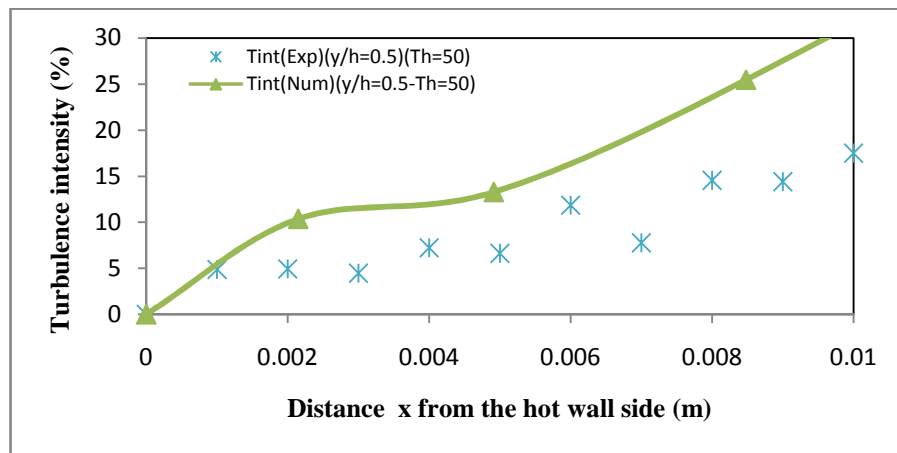
(c)

Figure C-12 Comparison of velocity profiles between experimental and numerical results for aspect ratio 0.5 and hot wall temperature 70 °C a) between the two walls b) near the hot side c) near the cold side.

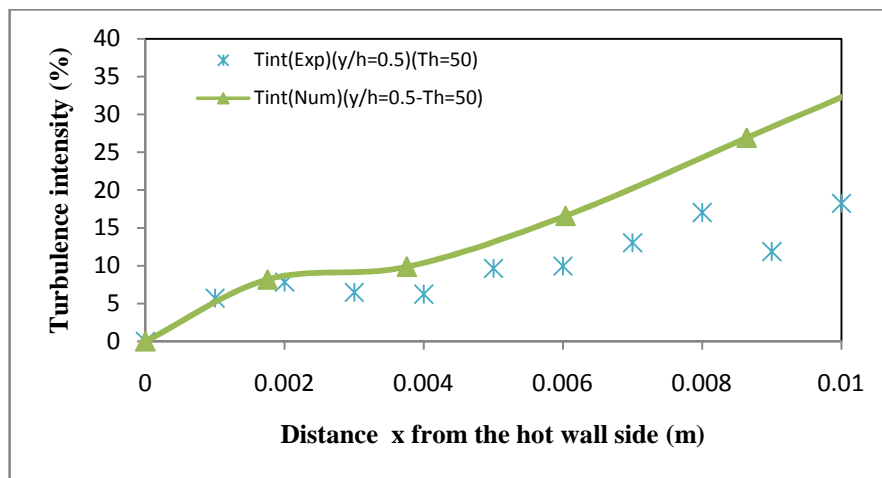
## C.4 Comparison of turbulence intensity between experimental and numerical results near the hot wall side



(a)

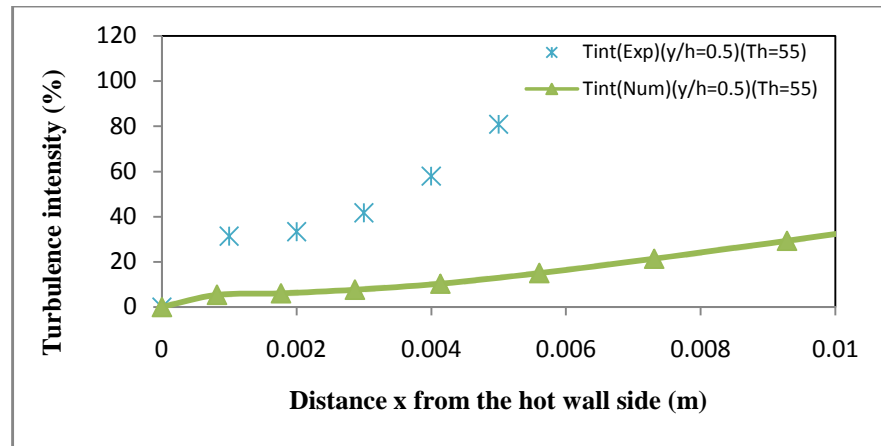


(b)

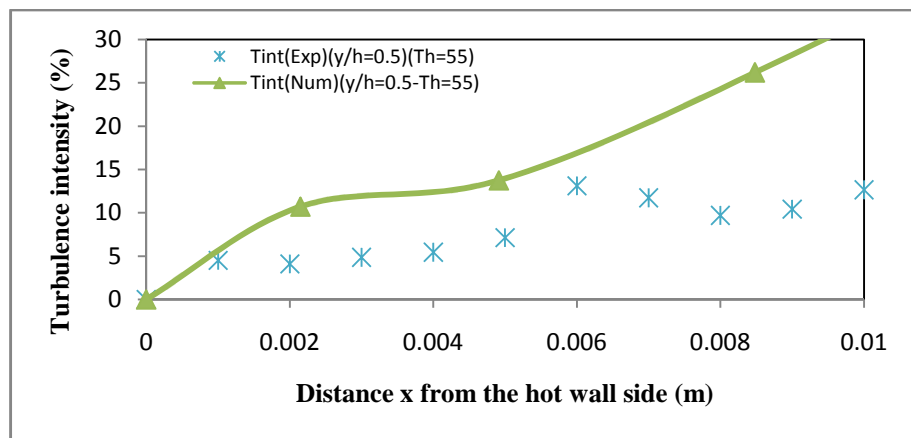


(c)

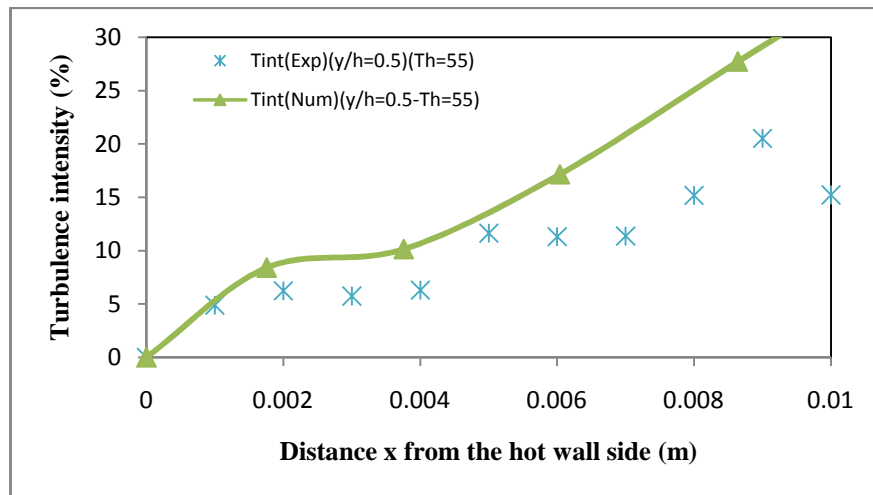
Figure C-13 Turbulence intensity near the hot wall side for 50°C and aspect ratio a) 2.0, b) 1.0 and c) 0.5



(a)

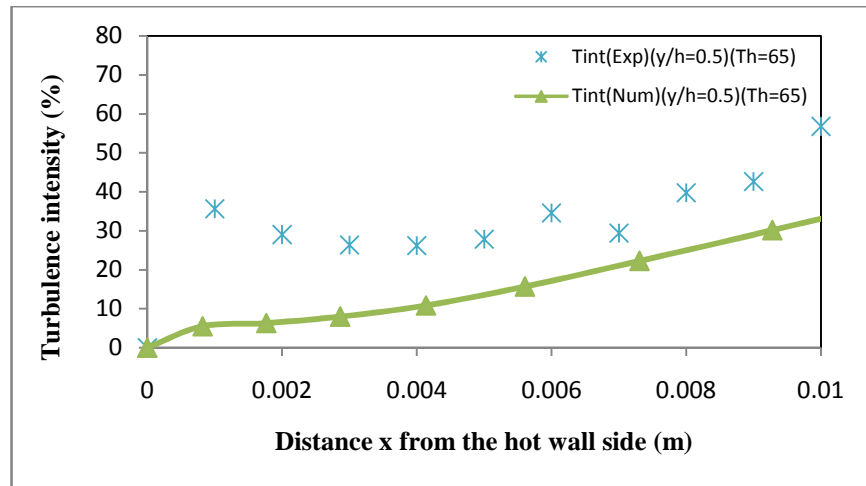


(b)

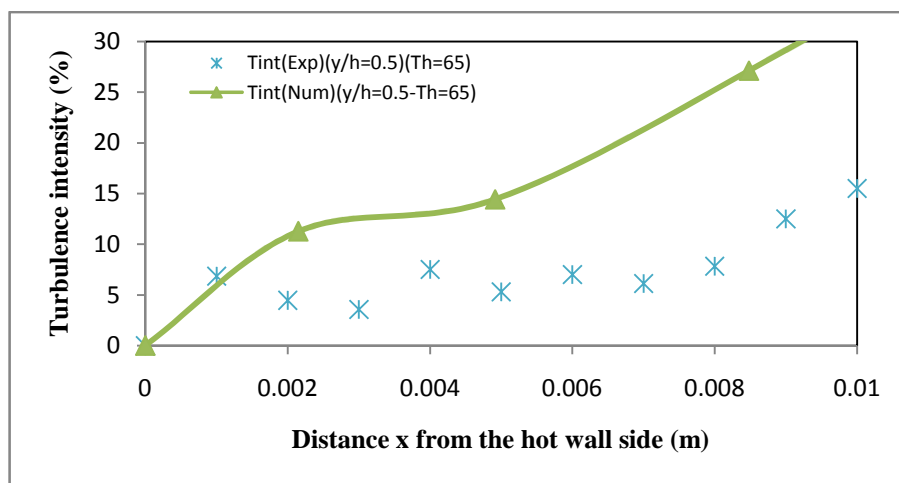


(c)

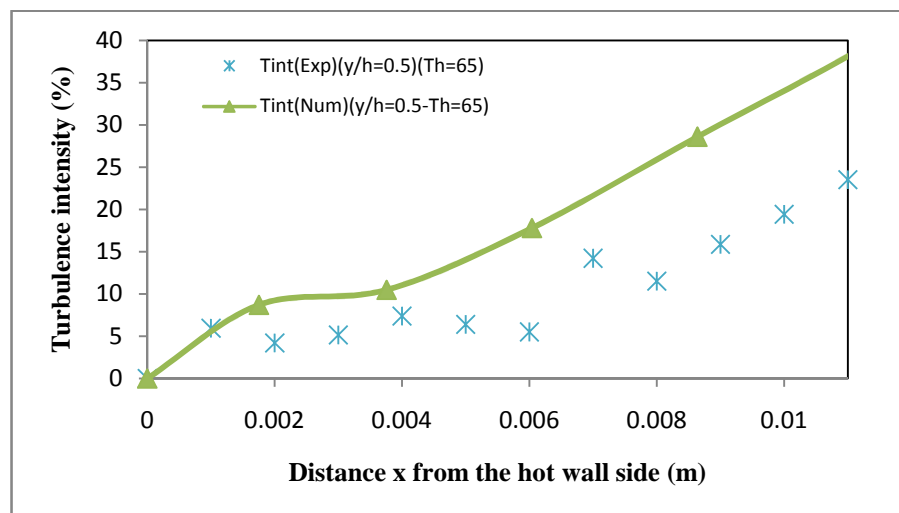
Figure C-14 Turbulence intensity near the hot wall side for 55°C and aspect ratio a) 2.0, b) 1.0 and c) 0.5



(a)

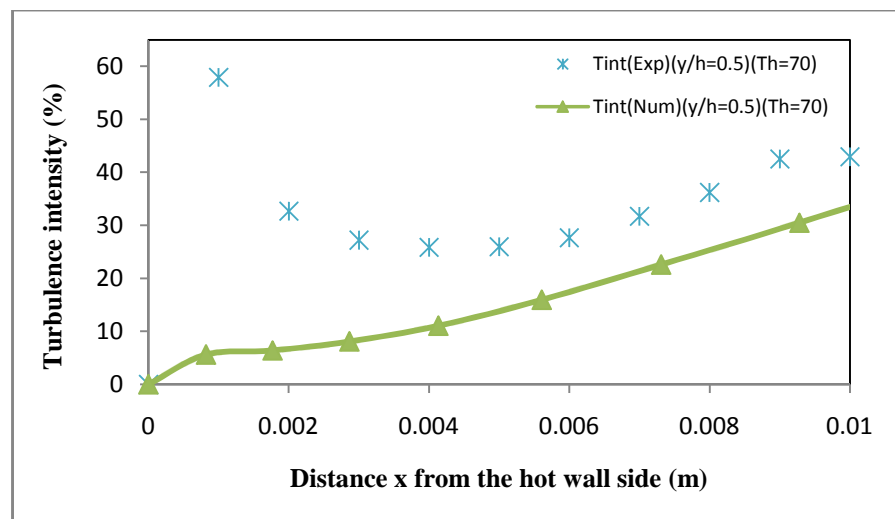


(b)

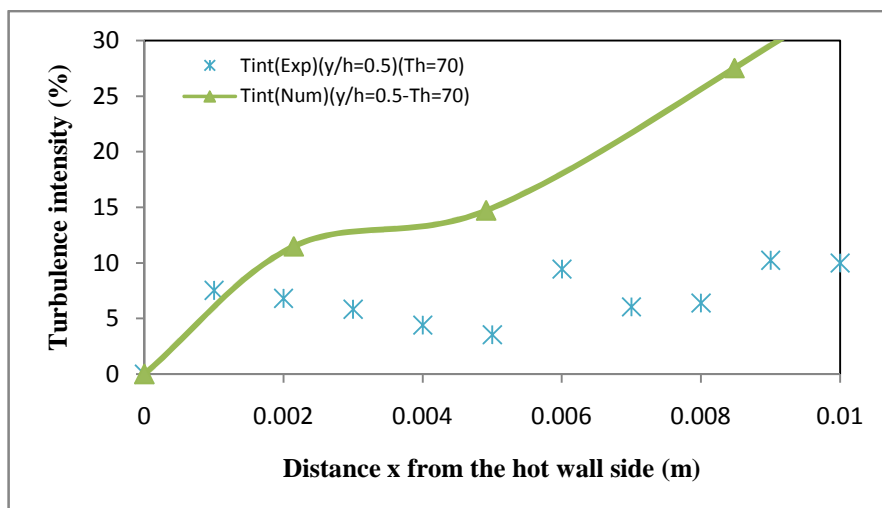


(c)

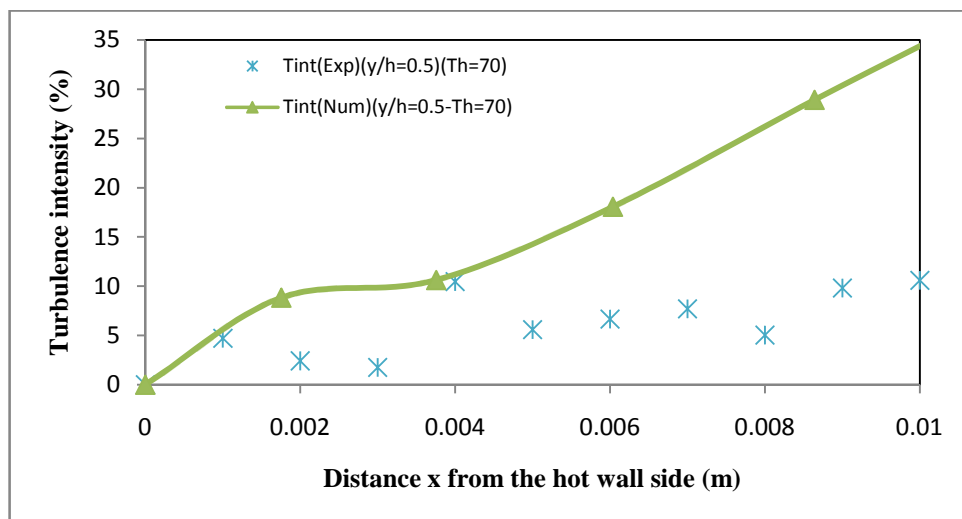
Figure C-15 Turbulence intensity near the hot wall side for 65°C and aspect ratio a) 2.0, b) 1.0 and c) 0.5



(a)



(b)



(c)

Figure C-16 Turbulence intensity near the hot wall side for 70°C and aspect ratio a) 2.0, b) 1.0 and c) 0.5

# **Appendix-D**

## **List of Publications**

1. Shati , A. K. A., Blakey, S. G., and Beck , S. B. M. (2011). The effect of surface roughness and emissivity on radiator output. *Energy and Buildings*, (43) 400-406.
2. Shati, A. K. A., Blakey, S. G., and Beck, S. B. M. (2011). Polynomial dimensionless equations to solve natural convection with radiation in rectangular enclosures. The 12<sup>th</sup> UK National Heat Transfer Conference 30 August to 1<sup>st</sup> September, Leeds.
3. Shati, A. K. A., Blakey, S. G., and Beck, S. B. M. (2012). A dimensionless solution to radiation and turbulent natural convection in square and rectangular enclosures. *Journal of Engineering Science and Technology*, (7) (2) 257-279.
4. Shati, A. K. A., Blakey, S. G., and Beck, S. B. M. (2013). An empirical solution to turbulent natural convection and radiation heat transfer in square and rectangular enclosures. *Applied Thermal Engineering*, (51) 364-370.